UNIVERSIDAD COMPLUTENSE DE MADRID

FACULTAD DE CIENCIAS QUÍMICAS

TESIS DOCTORAL

Funcionalización de nanomateriales en primer plano: análisis termodinámico y caracterización microscópica

Close-up on the functionalization of nanomaterials: thermodynamic analysis and microscopic characterization

MEMORIA PARA OPTAR AL GRADO DE DOCTORA

PRESENTADA POR

Sara Moreno Da Silva

DIRECTORES

María Luisa Ruiz González
Emilio Manuel Pérez Álvarez

UNIVERSIDAD COMPLUTENSE DE MADRID

FACULTAD DE CIENCIAS QUÍMICAS

TESIS DOCTORAL

Funcionalización de nanomateriales en primer plano: Análisis termodinámico y caracterización microscópica.

Close-up on the functionalization of nanomaterials: Thermodynamic analysis and microscopic characterization

MEMORIA PARA OPTAR AL GRADO DE DOCTOR

PRESENTADA POR

Sara Moreno Da Silva

DIRECTORES

María Luisa Ruiz González
Emilio Manuel Pérez Álvarez

This Ph.D. thesis has been developed at the institute IMDEA Nanoscience, the Faculty of Chemical Sciences of the UCM and the National Centre of Electron Microscopy (CNME), under the direction and the supervision of Prof. Dra. **María Luisa Ruiz González** and Prof. Dr. **Emilio M. Pérez Álvarez**.

A mis padres y a mi hermana.

INDEX

LIST OF ABBREVIATIONS

1D	One dimensional
2D	Two dimensional
3D	Three dimensional
Å	Angstrom
A/cm^2	Ampere per square centimetre
AFM	Atomic Force Microscopy
Bn-mal	Benzyl-maleimide
CNT	Carbon nanotube
CVD	Chemical Vapor Deposition
DFT	Density-Functional Theory
DMF	Dimethylformamide
EDS	Energy Dispersion Spectroscopy
EELS	Electron Energy Loss Spectroscopy
EM	Electron Microscopy
EPR	Electron Paramagnetic Resonance
eV	Electron-volt
EXAFS	Extended X-ray Absorption Fine Structure
FET	Field-effect transistor
Fk	Franckeite
GPa	Gigapascal
HiPCO	High Pressure Carbon Monoxide
HRTEM	High Resolution Transmission Electron Microscopy
HSQC	Heteronuclear Single Quantum Coherence
K	Kelvin degree
K_a	Association constant
M	Molar
MD	Molecular Dynamics
MIM	Mechanically Interlocked Molecule
MINT	Mechanically Interlocked Carbon Nanotube
MWNT	Multi-walled carbon nanotube
nm	Nanometre

NMR	Nuclear Magnetic Resonance
OCC	Organic colour centre
ORR	Oxygen reduction reaction
PLQY	Photoluminescence quantum yield
PTFE	Polytetrafluoroethylene
RBM	Radial Breathing Mode
RCM	Ring-closing metathesis
TCE	1,1,2,2-tetrachloroethane
TEM	Transmission Electron Microscopy
TGA	Thermogravimetric analysis
TPa	Terapascal
UV-vis-NIR	Ultraviolet, visible and near infrared
$Wm^{-1}K^{-1}$	Watts per meter-Kelvin
XANES	X-ray Absorption Near Edge Structure

ABSTRACT

Close-up on the functionalization of nanomaterials: Thermodynamic analysis and microscopic characterization

Nanomaterials have unique properties that make them highly attractive for many applications due to their small size, high surface area and quantum mechanical effects. However, these inherent features often need to be tuned to satisfy specific requirements. By functionalizing, scientists can carefully control and tailor nanomaterials to achieve the desired characteristics.

This thesis is based on previous works described in our group. Firstly, the synthesis of mechanically interlocked carbon nanotubes (MINTs),[1] which are the result of the supramolecular functionalization of single-walled carbon nanotubes (SWNTs) with macrocycles formed by ring-closing metathesis. Due to their insolubility of the carbon nanotubes, it was very difficult to quantify the affinity of different molecules for them. In 2015, we described a simple and direct procedure for the determination of the association constants of these structures based on thermogravimetric analysis.[2] The molecules used were previously shown to be good receptors for the non-covalent modification of SWNTs. In this context, the objectives have been the study of the best type of recognition motives for the supramolecular association between carbon nanotubes and organic molecules, the study of the MINT formation through direct encapsulation or with the previous synthesis of an organometallic macrocycle, the synthesis of several molecules for the functionalization of nanomaterials that will be used in different areas and the use of the electron microscopy for the characterization of the designed hybrids.

This thesis has been divided in five chapters:

- Chapter 1 presents an introduction of the functionalization of SWNTs to give a general idea of the history of their synthesis, as well as their modification via covalent, non-covalent or by forming interlocked species.
- In Chapter 2, the thermodynamics and dynamics in the supramolecular association of SWNTs and different organic molecules have been studied. In this chapter has been demonstrated that the higher the flexibility and

[1] de Juan, A.; Pouillon, Y.; Ruiz-González, L.; Torres-Pardo, A.; Casado, S.; Martín, N.; Rubio, Á.; Pérez, E. M. *Angew. Chem. Int. Ed.* **2014**, *53* (21), 5394–5400.

[2] de Juan, A.; López-Moreno, A.; Calbo, J.; Ortí, E.; Pérez, E. M. *Chem. Sci.* **2015**, *6* (12), 7008–7014.

aromaticity of the molecules, the higher the association with an increase in the entropy of the system.

- Chapter 3 and 4 have been dedicated to the synthesis of different MINTs. Magnetic MINTs (mMINTs) with porphyrins as recognition units for the nanotubes have been synthesized in Chapter 3. The choice of the metal placed at the centre of the heterocyclic macrocycle determines the orbital occupied by the spin and hence the interaction with the SWNTs. This is highly relevant to the design of mMINTs, as it provides a tool to modulate the interaction between the spin and the conduction electrons, which can be used to read the molecular spin. Finally, mMINTs have been suggested as a hybrid candidate for molecular spintronics and molecular spin qubits, since they could be placed on nanoscale devices using dielectrophoresis. Chapter 4 describes the synthesis of metallacycle-containing MINTs. This has been done either by template self-assembly of the palladium-based molecular building blocks around the SWNTs, or by direct encapsulation of the nanotube into the cavity of the preformed metallacycle. It has been shown that MINT formation is dependent on structural variations of the metallo-assemblies and that the metal atoms influence the electronic properties of these functionalized nanotubes, broadening the potential applications of MINTs.
- An important technique used to confirm the formation of MINTs is the transmission electron microscopy (TEM). Therefore, this spectroscopic technique has been the subject of Chapter 5, which in turn, has been divided into three parts. It starts with an introduction to the TEM, explaining how the beam interacts with the matter, how the image is formed, what aberrations are and how to correct them, and the basics of transmission electron microscopes. The other two parts have described the use of this tool to confirm the supramolecular functionalization of carbon nanotubes with nitrogen-rich macrocycles and the covalent functionalization of a 2D material, Franckeite, with a maleimide derivative.

In summary, in this thesis there have been synthesized different molecules to functionalized nanomaterials opening the possibility of using these hybrids in potential applications.

RESUMEN

Funcionalización de nanomateriales en primer plano: Análisis termodinámico y caracterización microscópica.

Los nanomateriales tienen propiedades únicas que los hacen muy atractivos para muchas aplicaciones debido a su pequeño tamaño, su elevada superficie y sus efectos mecánicos cuánticos. Sin embargo, estas cualidades inherentes a menudo deben ajustarse para satisfacer requisitos específicos. Mediante la funcionalización los científicos pueden controlar y adaptar cuidadosamente los nanomateriales para conseguir las características deseadas.

Esta tesis se ha basado en trabajos anteriores descritos en nuestro grupo. En primer lugar, la síntesis de nanotubos de carbono mecánicamente funcionalizados (MINTs),[1] los cuales son el resultado de la funcionalización supramolecular de nanotubos de carbono de pared simple (SWNT) con macrociclos formados por metátesis de cierre de anillo. Debido a la insolubilidad de los nanotubos de carbono, cuantificar la afinidad de moléculas orgánicas hacia estos materiales era un proceso complicado. En 2015 describimos un procedimiento sencillo y directo para la determinación de las constantes de asociación de estas estructuras basado en el análisis termogravimétrico.[2] Las moléculas utilizadas ya habían sido comprobadas previamente como adecuados receptores para la modificación no covalente de los SWNTs. En este contexto, los objetivos han sido el estudio del mejor tipo de motivos de reconocimiento para la asociación supramolecular entre nanotubos de carbono y moléculas orgánicas, el estudio de la formación de MINTs mediante la encapsulación de los nanotubos de manera directa o con la formación previa de macrociclos organometálicos, la síntesis de varias moléculas para lograr la funcionalización de nanomateriales que posteriormente se usarán para aplicaciones en diferentes áreas y el empleo de la microscopía electrónica para la caracterización de los híbridos diseñados.

Esta tesis se ha dividido en cinco capítulos.

- El Capítulo 1 consiste en una introducción a la funcionalización de los SWNTs para dar una idea general de la historia de su síntesis, así como de su modificación vía covalente, no covalente o mediante su encapsulación con macrociclos moleculares.

[1] de Juan, A.; Pouillon, Y.; Ruiz-González, L.; Torres-Pardo, A.; Casado, S.; Martín, N.; Rubio, Á.; Pérez, E. M. *Angew. Chem. Int. Ed.* **2014**, *53* (21), 5394–5400.

[2] de Juan, A.; López-Moreno, A.; Calbo, J.; Ortí, E.; Pérez, E. M. *Chem. Sci.* **2015**, *6* (12), 7008–7014.

- En el Capítulo 2 se han estudiado la termodinámica y la dinámica de la asociación supramolecular de los SWNT y diferentes moléculas orgánicas. En este capítulo se ha demostrado que cuanto mayor es la flexibilidad y aromaticidad de las moléculas, mayor es la asociación; con un aumento de la entropía del sistema.
- Los Capítulos 3 y 4 se han dedicado a la síntesis de diferentes MINTs. En el Capítulo 3 se han sintetizado MINTs magnéticos (mMINTs) con porfirinas como unidades de reconocimiento para los nanotubos. La elección del metal situado en el centro del macrociclo heterocíclico determina el orbital ocupado por el espín y, por tanto, la interacción con los SWNTs. Esto es muy relevante para el diseño de mMINTs ya que proporciona una herramienta para modular la interacción entre el espín y los electrones de conducción que puede utilizarse para leer el espín molecular. Por último, los mMINTs se han sugerido como candidatos híbridos para su uso en espintrónica molecular y como qubits de espín molecular puesto que podrían colocarse en dispositivos en nanoescala mediante dielectroforesis. En el Capítulo 4 se describe la síntesis de MINTs que contienen macrociclos organometálicos. Esta funcionalización se ha conseguido mediante el autoensamblaje de los bloques de construcción moleculares basados en paladio alrededor de los SWNTs, o bien mediante la encapsulación directa del nanotubo en la cavidad del macrociclo preformado. Se ha demostrado que la formación de MINTs depende de las variaciones estructurales de los macrociclos y que los átomos metálicos influyen en las propiedades electrónicas de estos nanotubos funcionalizados, ampliando así las aplicaciones potenciales de los MINTs.
- Una técnica importante utilizada para confirmar la formación de MINTs es la microscopía electrónica de transmisión (TEM), que ha sido explicada en el Capítulo 5 (a su vez dividido en tres partes). Se ha comenzado con una introducción al TEM, en la que se ha explicado cómo interactúa el haz con la materia, cómo se forma la imagen, qué son las aberraciones y cómo corregirlas, y los fundamentos de los microscopios electrónicos de transmisión. Las otras dos partes han centrado en el uso de esta herramienta para confirmar la funcionalización supramolecular de nanotubos de carbono con macrociclos ricos en nitrógeno y la funcionalización covalente de un material 2D, la Franckeita, con un derivado de maleimida.

En resumen, en esta tesis se han sintetizado diferentes moléculas para funcionalizar nanomateriales abriendo la posibilidad de utilizar estos híbridos en potenciales aplicaciones.

Chapter 1

Introduction

Carbon nanotubes (CNTs) are one dimensional structures that were discovered in 1991 by Sumio Iijima while studying the surfaces of graphite electrodes used in an electric arc discharge.[1] They were identified to be a concentric assembly of multi seamless graphite layers weakly bound together by van der Waals interactions in a hollow cylinder composition named as multi-walled carbon nanotubes (MWNTs). Then in 1993, the first single-walled carbon nanotube (SWNT) was successfully synthesized by the group of Tsang through oxidation of MWNTs.[2] The same year, Iijima and co-workers at NEC, parallel to Bethune at IBM, reported the direct synthesis of SWNTs.[3,4] These are narrower than the multiwall tubes, with diameters in the range of 0.3 to 2.0 nm and tend to be curved as a result of the presence of defects in their walls. In addition, nanotubes lengths range from less than 100 nm to several centimeters, thereby bridging molecular and macroscopic scales. Precedents to what is considered the official discovery of CNTs include the production of "filamentous carbon" through the decomposition of benzene.[5] The main reason why they had not have attracted much interest from the scientific community was the lack of interesting properties because of their imperfect structure.

Since the discovery of the CNTs, some techniques have been used to prepare them with different structures and morphologies.[6–8] The most common methods are electric arc discharge,[9] laser ablation[10] and chemical vapor deposition.[11] Arc discharge was the first method used to synthesize CNTs by Iijima and coworkers.[1] Graphite electrodes were evaporated in electric arcs at 4000 ºC resulting in the formation of pure carbon nanotubes, metal doped nanotubes and amorphous carbon. Laser ablation, developed by Guo *et al.*,[12] produces CNTs using high power laser in furnaces at high temperature. Even though both techniques enable the synthesis of nanotubes, their yields are low. Chemical vapor deposition (CVD) was firstly

[1] Iijima, S. *Nature* **1991**, *354* (6348), 56–58.
[2] Tsang, S. C.; Harris, P. J. F.; Green, M. L. H. *Nature* **1993**, *362* (6420), 520–522.
[3] Iijima, S.; Ichihashi, T. *Nature* **1993**, *363* (6430), 603–605.
[4] Bethune, D. S.; Kiang, C. H.; de Vries, M. S.; Gorman, G.; Savoy, R.; Vazquez, J.; Beyers, R. *Nature* **1993**, *363* (6430), 605–607.
[5] Oberlin, A.; Endo, M.; Koyama, T. *J. Cryst. Growth* **1976**, *32* (3), 335–349.
[6] Prasek, J.; Drbohlavova, J.; Chomoucka, J.; Hubalek, J.; Jasek, O.; Adam, V.; Kizek, R. *J. Mater. Chem.* **2011**, *21* (40), 15872–15884.
[7] Rathinavel, S.; Priyadharshini, K.; Panda, D. *Mater. Sci. Eng. B* **2021**, *268*, 115095.
[8] Zhu, Z.; Cui, C.; Bai, Y.; Gao, J.; Jiang, Y.; Li, B.; Wang, Y.; Zhang, Q.; Qian, W.; Wei, F. *Adv. Funct. Mat.* **2022**, *32* (11), 2109401.
[9] Arora, N.; Sharma, N. N. *Diam. Relat. Mater.* **2014**, *50*, 135–150.
[10] Yogesh, G. K.; Shukla, S.; Sastikumar, D.; Koinkar, P. *Appl. Phys. A* **2021**, *127* (11), 810.
[11] Gupta, N.; Gupta, S. M.; Sharma, S. K. *Carbon Lett.* **2019**, *29* (5), 419–447.
[12] Guo, T.; Nikolaev, P.; Thess, A.; Colbert, D. T.; Smalley, R. E. *Chem. Phys. Lett.* **1995**, *243* (1), 49–54.

employed for the synthesis of nanotubes in 1993.[13] Since then, it can be categorized as the most common process for CNT growth. It is a scalable, low cost, and low temperature synthetic method which uses a hydrocarbon source and a metallic catalyst. Two important methods based on CVD synthesis are high pressure CO (HiPCO)[14] and Co/Mo-catalyzed CVD (CoMoCAT).[15] Firstly, the hydrocarbon is dissociated and transported over the catalyst surface. Then, the diffusion and nucleation start building the new graphitic structure thanks to the carbon incorporation, since hydrogen atoms escape away. Finally, the nanotubes are collected once the reactor has cooled down. CVD can be assisted by plasma, water, oxygen, microwave and hot filaments, and radio frequency to increase the hydrocarbon gas decomposition, the final yield, quality, and purity.[16,17] Nonetheless, there are other less frequently used, yet relevant methods for CNTs production such as electrolysis,[18] or solar production.[19]

SWNTs are built from a cylindrical lattice of carbon atoms.[20–22] Depending on their position, the hexagons that form the nanotubes are aligned with or at some angle against one another. This alignment throughout the lattice infers the nanotube´s chirality. In this sense, CNTs are geometrically fully described, except for their length, by the chiral vector, which is defined by the relation $C_h = na_1 + ma_2$ (n and m being integers and a_1 and a_2 the unit cell vectors of the 2D lattice formed by the graphene sheets). Depending on how the graphene layer is rolled up, that it is to say, on the values of the integers, the carbon nanotubes can be categorized as follows: “armchair”, when m is equal to n, “zigzag”, in which m is equal to 0, and “chiral” tube, embracing all other configurations (Figure 1). The value of (n, m) determines the chirality of the nanotube, which directly affects mainly to the electronic, and optical properties. Regarding electronic properties, chirality affects

[13] José-Yacamán, M.; Miki-Yoshida, M.; Rendón, L.; Santiesteban, J. G. *Appl. Phys. Lett.* **1993**, *62* (6), 657–659.
[14] Nikolaev, P. *J. Nanosci. Nanotechnol.* **2004**, *4* (4), 307–316.
[15] Bachilo, S. M.; Balzano, L.; Herrera, J. E.; Pompeo, F.; Resasco, D. E.; Weisman, R. B. *J. Am. Chem. Soc.* **2003**, *125* (37), 11186–11187.
[16] Shah, K. A.; Tali, B. A. *Mater. Sci. Semicond. Process.* **2016**, *41*, 67–82.
[17] Szabó, A.; Perri, C.; Csató, A.; Giordano, G.; Vuono, D.; Nagy, J. B. *Materials (Basel)* **2010**, *3* (5), 3092–3140.
[18] Chen, G. Z.; Fan, X.; Luget, A.; Shaffer, M. S. P.; Fray, D. J.; Windle, A. H. *J. Electroanal. Chem.* **1998**, *446* (1), 1–6.
[19] Guillard, T.; Cetout, S.; Flamant, G.; Laplaze, D. *J. Mater. Sci.* **2000**, *35* (2), 419–425.
[20] Ferreira, F. V.; Franceschi, W.; Menezes, B. R. C.; Biagioni, A. F.; Coutinho, A. R.; Cividanes, L. S. Elsevier, **2019**, 1–45.
[21] Ganesh, E. N. *Int. J. Innov. Technol. Explor. Eng.* **2013**, *2* (4), 2278–3075.
[22] Yao, F.; Yu, W.; Liu, C.; Su, Y.; You, Y.; Ma, H.; Qiao, R.; Wu, C.; Ma, C.; Gao, P.; Xiao, F.; Zhao, J.; Bai, X.; Sun, Z.; Maruyama, S.; Wang, F.; Zhang, J.; Liu, K. *Nat. Nanotechnol.* **2021**, *16* (10), 1073–1078.

the size of the band gap between conduction and valence bands. In general, if the integers are equal, there is no band gap. The nanotubes are metallic with conducting behavior. When the integers are different and their subtraction (n-m) is a multiple of 3, the nanotubes are quasi-metallic with a very small bandgap. For all other possibilities, the nanotubes have a moderate semiconducting behavior. In terms of optical properties, the chirality influences the electronic states and the energy levels allowed. Thus, the absorption and emission peaks of carbon nanotubes vary based on different (n,m) values due to distinct energy band gaps. Those with smaller band gaps absorb light in the infrared region of the spectrum, while the ones with larger band gaps tend to absorb light in the visible range. Related to this, nanotubes with smaller band gaps emit light at longer wavelengths while the opposite emit at shorter wavelengths (higher energy).

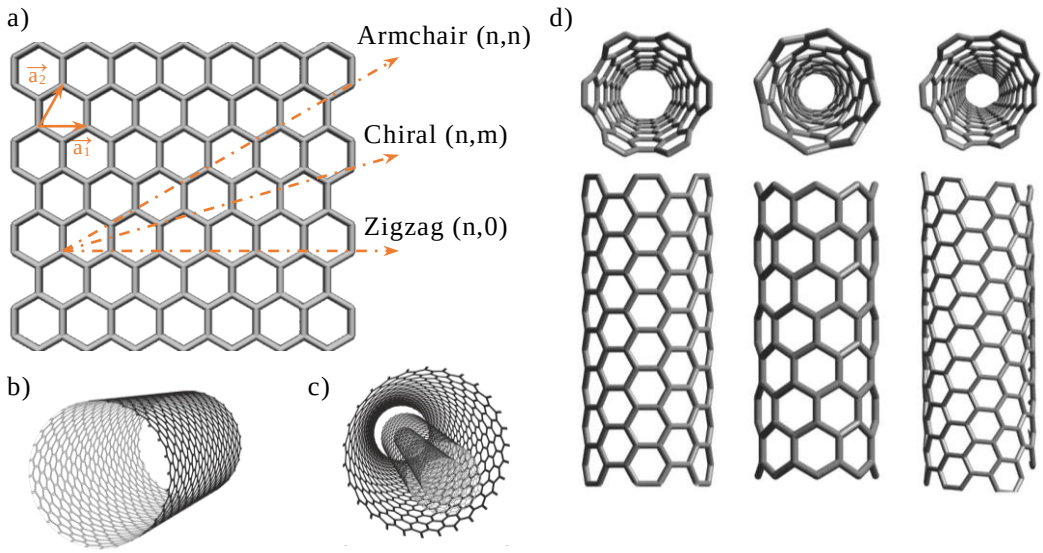

Figure 1. Schematic model of a) Graphene layer, b) SWNT, c) MWNT, and d) armchair nanotube (left), zig-zag nanotube (center), and chiral nanotube (right).

The uniqueness of the carbon nanotubes arises from their structure. The carbon-carbon sp^2 bonding is the direct responsible of providing extraordinary mechanical properties to the SWNTs. They are the stiffest known fibre with a tensile strength around 100 GPa,[23] and a Young´s modulus up to 1 TPa to 1.8 TPa.[7,24] The aspect ratio (length/diameter) can be greater than 10^4,[25] leading to a 1D system. Their one-

[7] Rathinavel, S.; Priyadharshini, K.; Panda, D. *Mater. Sci. Eng. B* **2021**, *268*, 115095.
[23] Xiao, J. R.; Gama, B. A.; Gillespie, J. W. *Int. J. Solids Struct.* **2005**, *42* (11), 3075–3092.
[24] Yu, M.-F.; Files, B. S.; Arepalli, S.; Ruoff, R. S. *Phys. Rev. Lett.* **2000**, *84* (24), 5552–5555.
[25] Ma, P.-C.; Siddiqui, N. A.; Marom, G.; Kim, J.-K. *Composites Part A: Appl. Sci. Manuf.* **2010**, *41* (10), 1345–1367.

dimensional structure, added to the electronic structure of graphite, endow the CNTs with unique electrical properties. They show extremely low electrical resistance, superconductivity below 20 K,[26] and the highest current density of any known material measured, 10^9 Acm^2.[27] CNTs can be either metals or semiconductors with different size energy gaps depending on their geometry (bandgaps in the range of 0.4 to about 2 eV).[28] Additionally, they have best thermal conductivity, as high as 6000 $Wm^{-1}K^{-1}$ in the axial direction.[29] Finally, they also have excellent chemical stability; they are chemically inert.

As a result of their extraordinary properties, the use of the CNTs as building blocks of nanotechnology has been growing in the last few years. The applications have been extensively studied in many reviews. For instance, they can be used in photovoltaic devices, sensors, polymer composites, transmission electron microscopy grids, data storage devices, biomedicine, catalysis, or field-effect transistors.[7,11,30,31]

1.1. FUNCTIONALIZATION OF CARBON NANOTUBES.

The research on SWNTs has been in continuous evolution because of their outstanding properties and their application in nanotechnology. However, their lack of solubility, the difficulties of manipulation processes, the necessity of their purification, or the modulation of their properties, have imposed great limitations to their use. Because of that, their chemical modification is required as a previous step. Nowadays, there are three main approaches for the functionalization of carbon nanotubes: covalent functionalization of the sp^2 structure, non-covalent functionalization through supramolecular interactions between them and different chemical entities, and the formation of mechanically interlocked carbon nanotubes.

[7] Rathinavel, S.; Priyadharshini, K.; Panda, D. *Mater. Sci. Eng. B* **2021**, *268*, 115095.
[11] Gupta, N.; Gupta, S. M.; Sharma, S. K. *Carbon Lett.* **2019**, *29* (5), 419–447.
[26] Tang, Z. K.; Zhang, L.; Wang, N.; Zhang, X. X.; Wen, G. H.; Li, G. D.; Wang, J. N.; Chan, C. T.; Sheng, P. *Science* **2001**, *292* (5526), 2462–2465.
[27] Wei, B. Q.; Vajtai, R.; Ajayan, P. M. *Appl. Phys. Lett.* **2001**, *79* (8), 1172–1174.
[28] Hamada, N.; Sawada, S.; Oshiyama, A. *Phys. Rev. Lett.* **1992**, *68* (10), 1579–1581.
[29] Hone, J.; Whitney, M.; Piskoti, C.; Zettl, A. *Phys. Rev. B* **1999**, *59* (4), 3.
[30] Qiu, H.; Yang, J. Elsevier: Boston, **2017**, 47–69.
[31] Jain, N.; Gupta, E.; Kanu, N. J. *Smart Sci.* **2022**, *10* (1), 1–24.

1.1.1. Covalent functionalization.

Covalent functionalization is employed to enhance SWNTs dispersion in the target medium (solvent or polymer), improving wetting or adhesion characteristics and reducing their agglomeration. This approach relies on the formation of chemical bonds either on the sidewalls or at the ends of the carbon nanotubes. The linkage is formed between the carbon skeleton of the nanotubes and different functional entities. In this type of functionalization, the carbon atoms change from sp^2 to sp^3 hybridization losing the π-conjugation system on the graphene layer. Even though the structure of the nanotubes changes, hence their properties, this modification results in a very stable chemical bond, generally irreversible.

The covalent functionalization of carbon nanotubes can be achieved via oxidative treatment as a previous step of derivatization with functional groups, or by direct covalent sidewall reactions. The oxidation helps in the removal of metal particles or amorphous carbon generated in the synthesis process. The nanotubes are processed with oxidizing agents like oxygen air, nitric acid, sulfuric acid, aqueous hydrogen peroxide, etc.[32–35] The chemical modification results in the opening of the tubes´ caps, the formation of defects, and the incorporation of functional groups such as ketone, carboxyl, carbonyl, or hydroxyl on their sidewalls as well as at their ends.

[32] Ajayan, P. M.; Ebbesen, T. W.; Ichihashi, T.; Iijima, S.; Tanigaki, K.; Hiura, H. *Nature* **1993**, *362* (6420), 522–525.
[33] Lavagna, L.; Musso, S.; Pavese, M. *Mater. Lett.* **2021**, *283*, 128816.
[34] Lavagna, L.; Bartoli, M.; Suarez-Riera, D.; Cagliero, D.; Musso, S.; Pavese, M. *ACS Appl. Nano Mater.* **2022**, *5* (5), 6671–6678.
[35] Zhang, J.; Zou, H.; Qing, Q.; Yang, Y.; Li, Q.; Liu, Z.; Guo, X.; Du, Z. *J. Phys. Chem. B* **2003**, *107* (16), 3712–3718.

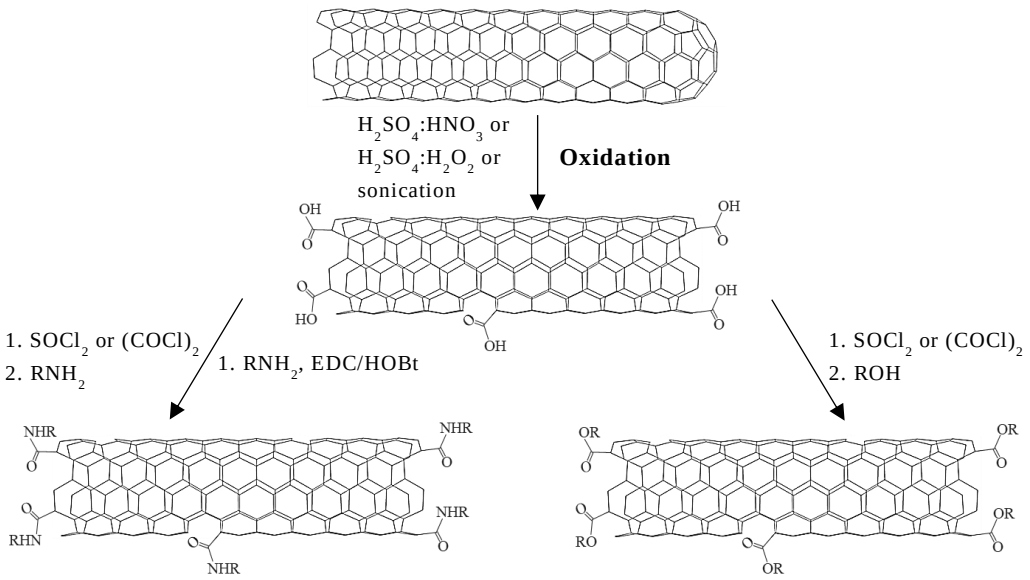

Scheme 1. Covalent functionalization through amidation and esterification reactions.

After the oxidation, the nanotubes could be derivatized employing acyl chlorides or carbodiimides to form amides or esters (Scheme 1). The amidation or esterification of oxidized carbon nanotubes results in the production of nanotubes suspendable either in organic solvents or in water. For instance, derivatization of SWNTs with ethylenediamine (EDA) via acylation allows the binding with proteins,[36] insulin can be conjugated with SWNTs through the formation of amide bonds,[37] amidation of a carboxylic SWNCTs results in a conjugated hybrid of C_{60}-fullerene and a SWNT,[38] and carboxylic acid groups reacts with hydroxyl or amine groups of dendron species.[39] Examples of esterifications are also reported. Carboxylate CNTs can be soluble in polar organic solvents by esterification reactions with porphyrin units,[40] electropolymerizable nanotubes are obtained through a ester reaction between oxidized SWNTs and pyrrole alcohol.[41] Phthalocyanine(Pc)-SWNTs hybrid was synthesized by esterification reaction

[36] Li, L.; Lin, R.; He, H.; Sun, M.; Jiang, L.; Gao, M. *J. Lumin.* **2014**, *145*, 125–131.
[37] Ng, C. M.; Loh, H.-S.; Muthoosamy, K.; Sridewi, N.; Manickam, S. *Int J Nanomed.* **2016**, *11*, 1607–1614.
[38] Delgado, J. L.; de la Cruz, P.; Urbina, A.; López Navarrete, J. T.; Casado, J.; Langa, F. *Carbon* **2007**, *45* (11), 2250–2252.
[39] Sun, Y.-P.; Huang, W.; Lin, Y.; Fu, K.; Kitaygorodskiy, A.; Riddle, L. A.; Yu, Y. J.; Carroll, D. L. *Chem. Mater.* **2001**, *13* (9), 2864–2869.
[40] Baskaran, D.; Mays, J. W.; Zhang, X. P.; Bratcher, M. S. *J. Am. Chem. Soc.* **2005**, *127* (19), 6916–6917.
[41] Cosnier, S.; Holzinger, M. *Electrochim. Acta.* **2008**, *53* (11), 3948–3954.

between metallized Pc and carboxylated nanotubes,[42] and acyl chloride coupled to hydroxyl modified SWNTs.[43]

The second approach of covalent functionalization of carbon nanotubes is the direct functionalization with very reactive species towards alkenes. Some examples are halogenation, hydrogenation, nucleophilic and electrophilic additions, and cycloadditions (Scheme 2).[44,45] Fluorination of carbon nanotubes emerged in 1998 when Margrave´s group developed a method with elemental fluorine.[46] At elevated temperatures, the linking of fluorine atoms modifies the sp^2 structure of the carbon nanotube giving rise to an insulating material.[47] The fluorination is also possible by thermal decomposition of fluoride derivatives, gases or plasmas,[48–52] and it can be reversed with hydrazine,[46] and by thermal annealing.[49] Chlorination[53,54] and bromination[55] reactions use the appropriate inorganic salts via electrochemical oxidation for the addition of halogen atoms onto the nanotubes. Hydrogenation[56] is achieved via Birch reduction, reducing the carbon nanotubes with lithium and methanol in ammonia,[57] or with atomic hydrogen, using a gas phase technique at low temperatures.[58] In 2008, it was demonstrated that the maximum value of hydrogenation (close to 100%) was obtained for SWNTs of around 2.0 nm.[59]

---

[42] d'Ambrosio, P.; Carchesio, M.; d'Alessandro, N.; Torre, G. de la; Torres, T. *Dalton Trans.* **2014**, *43* (20), 7473–7479.
[43] Xie, X.; Gao, L.; Sun, J. Trans. Tech. Publications Ltd: Stafa-Zurich, **2011**, 695, 373–376.
[44] Dubey, R.; Dutta, D.; Sarkar, A.; Chattopadhyay, P. *Nanoscale Adv.* **2021**, *3* (20), 5722–5744.
[45] Syrgiannis, Z.; Melchionna, M.; Prato, M. Springer: Berlin, Heidelberg, **2021**; 1–8.
[46] Mickelson, E. T.; Huffman, C. B.; Rinzler, A. G.; Smalley, R. E.; Hauge, R. H.; Margrave, J. L. *Chem. Phys. Lett.* **1998**, *296* (1), 188–194.
[47] Elavarasi, S. B.; Divya, S.; Vishnu Priya, M.; Sheik Sirajuddeen, M. *Chem. Phys. Lett.* **2020**, *742*, 137142.
[48] Zhang, W.; Bonnet, P.; Dubois, M.; Ewels, C. P.; Guérin, K.; Petit, E.; Mevellec, J.-Y.; Vidal, L.; Ivanov, D. A.; Hamwi, A. *Chem. Mater.* **2012**, *24* (10), 1744–1751.
[49] Yokoyama, K.; Mamiya, I.; Morita, H.; Sato, Y.; Sato, K.; Nishida, T.; Sato, Y. *J. Colloid Interface Sci.* **2022**, *627*, 168–179.
[50] Plank, N. O. V.; Cheung, R. *Microelectron. Eng.* **2004**, *73–74*, 578–582.
[51] Adamska, M.; Narkiewicz, U. *J. Fluor. Chem.* **2017**, *200*, 179–189.
[52] Khabashesku, V. N.; Billups, W. E.; Margrave, J. L. *Acc. Chem. Res.* **2002**, *35* (12), 1087–1095.
[53] Erbahar, D.; Berber, S. *Phys. Rev. B* **2012**, *85* (8), 085426.
[54] Oliveira, L.; Lu, F.; Andrews, L.; Takacs, G. A.; Mehan, M.; Debies, T. *J. Mater. Res.* **2014**, *29* (2), 239–246.
[55] Zarska, S.; Kulawik, D.; Drabowicz, J.; Ciesielski, W. *Fuller. Nanotub. Carbon Nanostruct.* **2017**, *25* (10), 563–569.
[56] Khalil, Rana. M. A.; Hussain, F.; Imran, M.; Rana, A. M.; Murtaza, G. *Phys. B: Condens.* **2019**, *552*, 124–129.
[57] Pekker, S.; Salvetat, J.-P.; Jakab, E.; Bonard, J.-M.; Forró, L. *J. Phys. Chem. B* **2001**, *105* (33), 7938–7943.
[58] Khare, B. N.; Meyyappan, M.; Cassell, A. M.; Nguyen, C. V.; Han, J. *Nano Lett.* **2002**, *2* (1), 73–77.
[59] Nikitin, A.; Li, X.; Zhang, Z.; Ogasawara, H.; Dai, H.; Nilsson, A. *Nano Lett.* **2008**, *8* (1), 162–167.

Nucleophilic addition is another alternative for the covalent functionalization of SWNTs where electron rich nucleophiles attack the moderately electrophilic alkenes of the SWNTs. Using diethyl bromomalonate and 1,8-diazabicyclo[5.4.0]undecene, Coleman and co-workers performed the cyclopropanation of SWNTs.[60] The surface of SWNTs can also be covalently modified by two-stage nucleophilic addition using boron-based agents.[61] Electrophilic addition was reported via gas-phase method by N. Tagmatarchis *et al.*[62] The addition of chloroform followed by a hydrolysis reaction ends up with the addition of hydroxyl groups to the nanotube sidewalls. A computational study on polyyne systems under electric fields also support this kind of functionalization.[63]

Cycloadditions are the most used family of reactions for the direct functionalization of nanotubes. Representative examples are the addition of carbenes and nitrenes, 1,3-dipolar cycloadditions, and Diels-Alder reactions. Carbene addition is one of the first methods explored. The surface modification of SWNTs with carbenes was studied theoretically. By DFT calculations Yumura *et al.* found a cooperative interaction in the first and second CH_2 adsorbent binding sites.[64] Additionally, Luksitikul group functionalized SWNTs using the high reactivity of carbenes derived from diazo compounds.[65] Nitrenes were reported as reagents to functionalise SWNTs by Hirsch and co-workers.[66] The thermal decomposition of alkyl azidoformate results in the formation or alkozycarbonylaziridinio, which reacts with the SWNT affording alkoxycarbonylaziridino-SWNT.[66] 1,3-Dipolar cycloadditions were yielded by Prato *et al.* for fullerenes.[67] Later, this reaction, known as Prato reaction, extended its use for carbon nanotubes. In situ condensation of α-amino acids and aldehydes results in the synthesis of azomethine ylides which react with the double bonds of the nanotubes forming pyrrolidine-fused CNTs.[68] Ammonia sensors can be achieved by covalent modification of SWNTs with coumarin derivatives.[69] Diels-Alder

[60] Coleman, K. S.; Bailey, S. R.; Fogden, S.; Green, M. L. H. *J. Am. Chem. Soc.* **2003**, 125 (29), 8722–8723.
[61] Desmecht, A.; Sheet, D.; Poleunis, C.; Hermans, S.; Riant, O. *Chem.-Eur. J.* **2019**, *25* (6), 1436–1440.
[62] Tagmatarchis, N.; Georgakilas, V.; Prato, M.; Shinohara, H. *Chem. Commun.* **2002**, 18, 2010–2011.
[63] Yosipof, A.; Basch, H.; Hoz, S. *J. Phys. Chem. A* **2013**, *117* (24), 5023–5027.
[64] Yumura, T.; Kertesz, M. *Chem. Mater.* **2007**, *19* (5), 1028–1034.
[65] Luksirikul, P.; Ballesteros, B.; Tobias, G.; Moloney, M. G.; Green, M. L. H. *J. Mater. Chem.* **2011**, *21* (47), 19080–19085.
[66] Holzinger, M.; Abraham, J.; Whelan, P.; Graupner, R.; Ley, L.; Hennrich, F.; Kappes, M.; Hirsch, A. *J. Am. Chem. Soc.* **2003**, *125* (28), 8566–8580.
[67] Maggini, M.; Scorrano, G.; Prato, M. *J. Am. Chem. Soc.* **1993**, *115* (21), 9798–9799.
[68] Rabti, A.; Raouafi, N.; Merkoçi, A. *Carbon* **2016**, *108*, 481–514.
[69] Polyakov, M. S.; Ivanova, V. N.; Basova, T. V.; Saraev, A. A.; Köksoy, B.; Şenocak, A.; Demirbaş, E.; Durmuş, M. *Appl. Surf. Sci.* **2020**, *504*, 144276.

cycloaddition can also be performed onto the sidewalls of CNTs. The reactivity of several SWNTs with 1,3-butadiene was investigated by DFT calculations showing that a decrease of the diameter results in an enhancement of the reactivity.[70] [4+2] cycloaddition of benzyne was studied for zigzag and armchair SWNTs.[71]

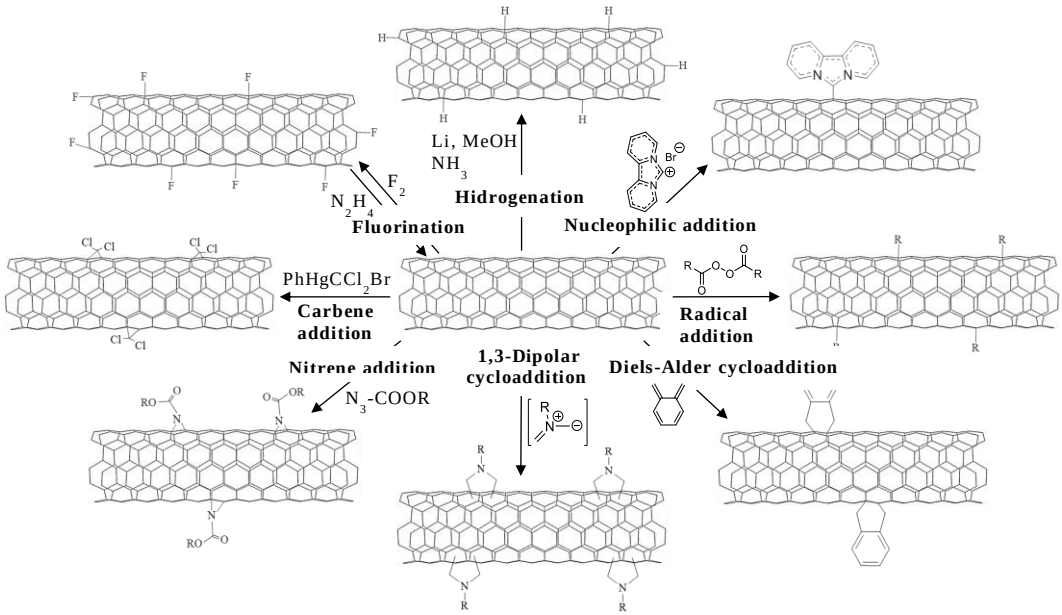

Scheme 2. Examples of direct covalent functionalization.

On account of all the above, it has been demonstrated that the covalent functionalization of carbon nanotubes enhances their solubility and modifies their hybridization. This type of chemistry is suitable for applications which require changes in their characteristics. An emerging field is the formation of quantum defects.[72,73] In contrast with the usual defects, which normally quench the photoluminescence, this type allows the transitions between the electronic states enhancing it. For example, Piao and co-workers have demonstrated that by covalently modifying SWNTs with aryl functional groups, the creation of an optically allowed state below the energy levels of dark excitons, alters their optical and electronic properties.[74] This makes them suitable for use in optoelectronic and

[70] Li, Y.; Osuna, S.; Garcia-Borras, M.; Qi, X.; Liu, S.; Houk, K. N.; Lan, Y. *Chem. Eur. J.* **2016**, *22* (36), 12819–12824.
[71] Martínez, J. P.; Langa, F.; Bickelhaupt, F. M.; Osuna, S.; Solà, M. *J. Phys. Chem. C* **2016**, *120* (3), 1716–1726.
[72] Brozena, A. H.; Kim, M.; Powell, L. R.; Wang, Y. Nat. Rev. Chem. **2019**, 3 (6), 375–392.
[73] Zaumseil, J. Adv. Opt. Mater. **2022**, 10 (2), 2101576.
[74] Piao, Y.; Meany, B.; Powell, L. R.; Valley, N.; Kwon, H.; Schatz, G. C.; Wang, Y. *Nat. Chem.* **2013**, *5* (10), 840–845.

photovoltaic applications. Nanotubes were functionalized at room temperature with aryl diazonium salts in water or deuterium. In this fashion, the emission energy and maximum photoluminescence brightness could be chemically controlled by forming quantum defects using electron donor/acceptor substituents on the aryl group. Based on this research, in 2019 it was developed a method to create luminescent aryl defects in polymer-wrapped SWNTs solubilizing diazonium salts in organic non-halogenated solvents.[75] The work revealed the dependence of the photoluminescence quantum yield (PLQY) and the relative brightening factor upon the introduction of luminescent defects according to the length and quality of the SWNTs. Long SWNTs with high PLQYs yielded the highest values after functionalization. However, the shortest nanotubes with the lowest initial PLQYs showed maximum relative brightening. Furthermore, this approach could be used to produce brighter carbon nanotube-based NIR-emitting devices such as light-emitting diodes and field-effect transistors.

It is also possible to detect high-grade serous ovarian carcinoma (HGSOC) from patient serum samples by taking the effect of quantum defects into account. In 2022, Kim *et al.* developed a nanosensor array coupled to a computational model that led to the perception-based recognition of this type of cancer.[76] They synthesized a matrix functionalizing SWNTs with organic colour centers (OCCs) which were then encapsulated with single-stranded DNA (ssDNA) (Figure 2). Several factors are responsible for the fluorescence modulation of SWNTs. However, OCC fluorescence is molecularly specific and highly sensitive to the local chemical environment of atomic defect sites, responding differently to serum samples from HGSOC patients, other non-HGSOC diseases and healthy individuals. The accuracy of this approach is 95%, exceeding the results of the best clinical screening test currently available.

[75] Berger, F. J.; Lüttgens, J.; Nowack, T.; Kutsch, T.; Lindenthal, S.; Kistner, L.; Müller, C. C.; Bongartz, L. M.; Lumsargis, V. A.; Zakharko, Y.; Zaumseil, J. ACS Nano **2019**, 13 (8).

[76] Kim, M.; Chen, C.; Wang, P.; Mulvey, J. J.; Yang, Y.; Wun, C.; Antman-Passig, M.; Luo, H.-B.; Cho, S.; Long-Roche, K.; Ramanathan, L. V.; Jagota, A.; Zheng, M.; Wang, Y.; Heller, D. A. *Nat. Biomed. Eng.* **2022**, *6* (3), 267–275.

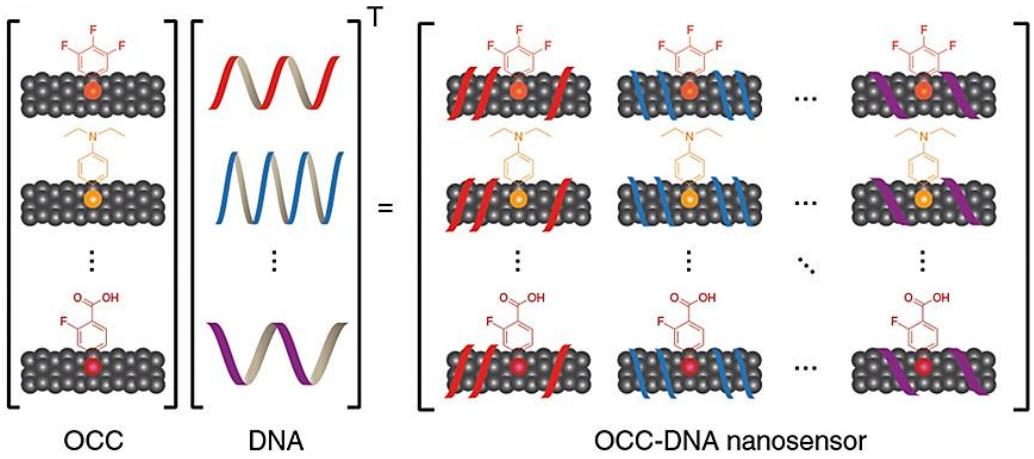

Figure 2. Construction of an OCC-DNA nanosensor array from OCC and ssDNA components. Adapted from ref. 76.

1.1.2. Non-covalent functionalization.

Non-covalent functionalization relies on the use of van der Waals forces, hydrogen bonds, electrostatic interactions, and π-π stacking interactions. These adsorption forces allow the supramolecular adsorption, wrapping, and/or endohedral filling of the nanotubes with numerous functional groups without disturbing their sp^2-hybrid structure in such a way that their intrinsic properties are maintained. The main disadvantage of this type of chemical modification is that the individual forces between the nanotube and the molecules are weak. The reactions occur under relatively soft conditions and in equilibrium becoming reversible processes. The non-covalent functionalization is based on the physisorption of chemicals and can be mainly performed by the supramolecular addition of aromatic compounds, surfactants, and polymers onto the walls of the carbon nanotubes, or in their inner empty cavity. The use of this molecules improves the dispersion of CNTs in solvents, as well as enable their separation by metallicity and chirality, and their isolation from carbonaceous and metal impurities.[77–80]

[76] Kim, M.; Chen, C.; Wang, P.; Mulvey, J. J.; Yang, Y.; Wun, C.; Antman-Passig, M.; Luo, H.-B.; Cho, S.; Long-Roche, K.; Ramanathan, L. V.; Jagota, A.; Zheng, M.; Wang, Y.; Heller, D. A. *Nat. Biomed. Eng.* **2022**, *6* (3), 267–275.

[77] Fagan, J. A.; Hároz, E. H.; Ihly, R.; Gui, H.; Blackburn, J. L.; Simpson, J. R.; Lam, S.; Hight Walker, A. R.; Doorn, S. K.; Zheng, M. *ACS Nano* **2015**, *9* (5), 5377–5390.

[78] Subbaiyan, N. K.; Cambré, S.; Parra-Vasquez, A. N. G.; Hároz, E. H.; Doorn, S. K.; Duque, J. G. *ACS Nano* **2014**, *8* (2), 1619–1628.

[79] Defillet, J.; Avramenko, M.; Martinati, M.; López Carrillo, M. Á.; Van der Elst, D.; Wenseleers, W.; Cambré, S. *Carbon* **2022**, *195*, 349–363.

[80] Park, M.; Choi, I.-S.; Ju, S.-Y. *Nanoscale Adv.* **2022**, *4* (17), 3537–3548.

Endohedral doping is a special type of functionalization in which molecular-sized entities are introduced into the hollow interior of carbon nanotubes, providing them with space for storage and protection. As the subject of this thesis is the functionalization of the outer surface of the nanotubes, we will not go into further detail. For more information on the encapsulation process, we recommend reading Kharlamova[81] and Cadena.[82]

Aromatic molecules, such as pyrene, porphyrin, phthalocyanine, anthracene, and their derivatives, can interact with the sidewalls of CNTs by means of π-π stacking interactions. Supramolecular modification of carbon nanotubes began with the pioneering works of Dai's and Nakashima's groups. Dai and co-workers reported the earliest example of functionalization using a pyrene derivative in 2001.[83] SWNTs were non-covalently modified with the succinimidyl ester of 1-pyrenebutanoic acid (Figure 3a). The nanotubes were functionalized via π-π interactions through the pyrene moieties. The terminal amines in various biological molecules were used to anchor them to the succinimidyl ester of the pyrene derivative forming amide bonds. The result is a protein immobilization with high efficiency and specificity, showing good stability against desorption in solution. The following year, Nakashima *et al.* were able to disperse SWNTs in water for the first time using 1-(trimethylammonium-acetyl)pyrene, a water soluble salt (Figure 3b).[84]

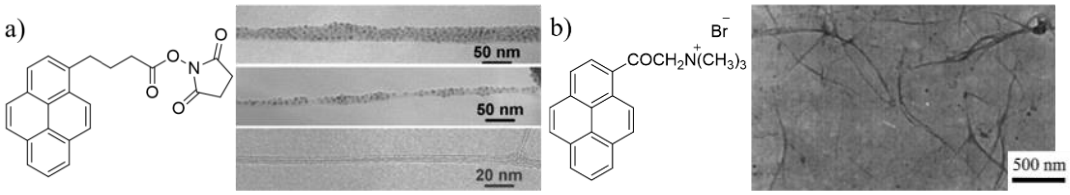

Figure 3. a) Left: structure of succinimidyl ester of 1-pyrenebutanoic acid, right: TEM of a SWNTs´ bundle functionalized with the succinimidyl ester bonded to a ferritin protein (up), TEM of single SWNT functionalized with ferritin (centre), and TEM of a pristine SWNT (down). b) Left: structure of trimethyl-(2-oxo-2-pyren-1-yl-ethyl)-ammonium bromide, right: TEM of an aqueous dispersion of functionalized SWNTs. Adapted with permission from ref. 83,84, respectively.

Taking into account the electron-accepting nature of SWNTs, an interesting study on the individualisation of SWNTs by liquid phase exfoliation under

[81] Kharlamova, M. V.; Kramberger, C. *Nanomater.* **2023**, *13* (2), 314.
[82] Cadena, A.; Botka, B.; Kamarás, K. *Oxf. Open Mater. Sci.* **2021**, *1* (1), itab009.
[83] Chen, R. J.; Zhang, Y.; Wang, D.; Dai, H. *J. Am. Chem. Soc.* **2001**, *123* (16), 3838–3839.
[84] Nakashima, N.; Tomonari, Y.; Murakami, H. *Chem. Lett.* **2002**, *31* (6), 638–639.

ultrasound irradiation was carried out.[85] Free base and zinc porphyrins were synthesized and covalently bonded to monopodal or tripodal pyrene molecules (Figure 4a,b). These architectures were then used as excited state electron donors through the pyrene moieties for non-covalent modification of carbon nanotubes. Several techniques were used for a complete characterization of the new materials. It should be noted that Raman spectroscopy revealed the n-doping effect in the solid state due to the shift of the G and 2D bands of the functionalized nanotubes towards lower wavenumbers compared to the pristine nanotubes (Figure 4c). The final properties were determined by the number of pyrene anchors, the oxidative potential of the free base and metalated porphyrins, and the alignments of the mono- and tripodal structures on the SWNTs. Finally, tripodal porphyrins gave the best individualization of SWNTs.

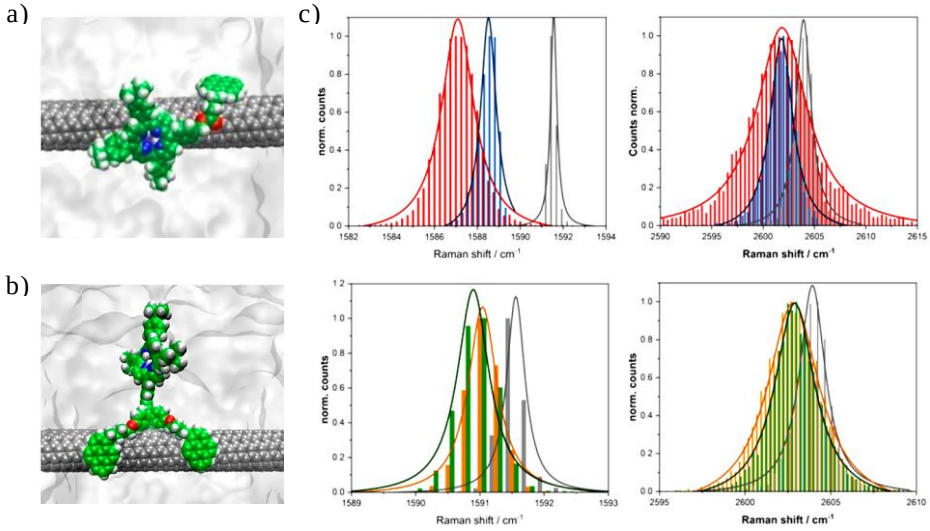

Figure 4. Representative snapshots of MD simulations for a) monopodal porphyrin, and b) tripodal porphyrin functionalization. c) Histogram of the G band position (top left) and the 2D band position (top right) of SWNT functionalization with monopodal pyrene covalently linked to free metal porphyrin (red), and zinc porphyrin (blue), and the SWNT reference (grey). Histogram of the G band position (bottom left) and the 2D band position (bottom right) of SWNT functionalization with tripodal pyrene covalently linked to free metal porphyrin (orange), and zinc porphyrin (green), and the SWNT reference (grey). Adapted with permission from ref. 85.

The isolation of SWNTs is an important factor for their subsequent use in various applications. However, it is also important to know how the organic molecules

[85] Garrido, M.; Volland, M. K.; Münich, P. W.; Rodríguez-Pérez, L.; Calbo, J.; Ortí, E.; Herranz, M. Á.; Martín, N.; Guldi, D. M. *J. Am. Chem. Soc.* **2020**, *142* (4), 1895–1903.

associated supramolecularly with carbon nanotubes. In 2015, our group developed a simple method for quantifying the non-covalent functionalization of SWNTs.[86] Association constants of five molecules with two types of SWNTs in four different solvents were calculated using thermogravimetric measurements. The values of K_a obtained were in the range of $1\text{-}10^4$ M^{-1}. This is due to structural changes in the soluble molecules and carbon nanotubes, as well as to the influence of the different solvents. DFT calculations confirmed the experimental results. Later in 2019, Komatsu and collaborators synthesized several porphyrins and pyrene molecules that were assembled to form nanotweezers and nanocalipers.[87] After isolating the CNTs by diameter, they studied the association constants of the complexes, establishing a correlation with the component and shape of the organic entities. Porphyrin structures showed higher constants than the pyrene analogues. In addition, the more contact, the higher the constants, i.e., the larger the contact area between the organic molecules and the SWNTs, the greater the value of the constants. Summarizing, the order of association constant was: nanocalipers > nanotweezers > monoporphyrins > monopyrenes. Finally, they extraction ability was also investigated. It was found that there was no correlation between the two analyses, as it is necessary to take into account the stability of the complex in solution. In other words, the cavity size of the organic structure must be adapted to the diameter of the carbon nanotubes.

In 2008, Grüner's group functionalized CdSe nanoparticles (NPs) with pyrene derivatives, which were the anchor point for the supramolecular functionalization of SWNTs.[88] They proved an effective charge transfer process from the pyrene/CdSe NPs to the SWNTs, opening up the possibility of incorporating this type of hybrid into organic photovoltaic devices owing to the controllable bandgap of the NPs and the 1D electronic transport of the SWNTs. Bionano donor-acceptor hybrids that are able to perform photoinduced electron transfer were created by Ito *et al.*[89] First, they wrapped single-stranded DNA (ssDNA) around SWNTs, and subsequently different porphyrins (free base and zinc metalated porphyrin) were added to the dispersion to obtain the final supramolecules in water by ion-pair bonding. The results showed that both hybrids use the ssDNA as an electron

[86] de Juan, A.; López-Moreno, A.; Calbo, J.; Ortí, E.; Pérez, E. M. *Chem. Sci.* **2015**, *6* (12), 7008–7014.

[87] López-Moreno, A.; Jiang, Y.; Cheng, G.; Komatsu, N. *J. Porphyrins Phthalocyanines* **2020**, *24* (01n03), 314–319.

[88] Hu, L.; Zhao, Y.-L.; Ryu, K.; Zhou, C.; Stoddart, J. F.; Grüner, G. *Adv. Mater.* **2008**, *20* (5), 939–946.

[89] D'Souza, F.; Das, S. K.; Zandler, M. E.; Sandanayaka, A. S. D.; Ito, O. *J. Am. Chem. Soc.* **2011**, *133* (49), 19922–19930.

mediator. However, there is a better charge stabilization ability when the porphyrin used has zinc in its core. Therefore, higher photocurrents can be expected in photoelectrochemical solar cells constructed with these supramolecular hybrids. Another potential application of non-covalently modified SWNT is their use as sensors. In 2011, Zhang and coworkers developed a gas sensing device using SWNTs supramolecularly functionalized with cobalt phthalocyanine (CoPc) derivatives by π-π interactions. They built a dimethyl methylphosphonate (DMMP) sensor that was more sensitive and selective than the original sensors using SWNTs. This was made possible by attaching hexafluoroisopropanol (HFIP) substituents to the CoPc. The HFIP moiety broadens the pi system, improving the electron-withdrawing effect, establishes strong hydrogen bonds with the DMMP, helping its adsorption, and enhances the dispersion of the nanotubes to facilitate their processability due to its superior solubility.[90] So far, examples have been given of carbon nanotubes being functionalized with only one type of motif. However, it is possible to dope them with multiple molecules. Cosnier et. al. developed polyvalent biosensors modifying the surface of the SWNTs with pyrene derivatives through π-stacking interactions by dip coating.[91] SWNTs were non-covalent functionalized with adamantane–pyrene, biotin–pyrene, and nitrilotriacetic acid–pyrene molecules which were used to immobilized different biomolecules via affinity interactions. In a sequential process, the resulting electrodes were incubated in several solutions to create distinct systems: biotin/avidin/biotin, adamantane/b-cyclodextrin, and NTA/Cu^{2+}/histidine.

Surfactants are amphiphilic organic compounds, which means that each molecule has both a hydrophilic group (the head), and hydrophobic group (the tail). In general, the hydrophobic tails are oriented towards the surface of CNTs, while the polar parts interact with the solvent. These interactions may result in different surfactant-SWNT structures.[92] The dispersion of CNTs with detergents turns out in stable dispersions. To prevent re-bundling, the strong inter-tube van der Waals forces are compensated with solvent-SWNT and surfactant-SWNTs interactions.[93] Both ionic and non-ionic surfactants have been used (see examples in Figure 5). The most well-known in aqueous media are sodium dodecyl sulphate (SDS), sodium dodecyl benzene sulfonate (SDBS), Tween, cetyltrimethyl ammonium bromide

[90] Wang, Y.; Hu, N.; Zhou, Z.; Xu, D.; Wang, Z.; Yang, Z.; Wei, H.; Kong, E. S.-W.; Zhang, Y. *J. Mater. Chem.* **2011**, *21* (11), 3779–3787.
[91] Holzinger, M.; Baur, J.; Haddad, R.; Wang, X.; Cosnier, S. *Chem. Commun.* **2011**, *47* (8), 2450–2452.
[92] Fatemi, S. M.; Foroutan, M. *J. Nanostruct. Chem.* **2016**, *6* (1), 29–40.
[93] Gillen, A. J.; Boghossian, A. A. *Front. Chem.* **2019**, *7* (612).

(CTAB), polyoxyethylene octylphenylether (Triton X-100), and a non-ionic triblock copolymer of polyethylene oxide-polypropylene oxide-polyethylene oxide (PEO-PPO-PEO, also known as pluronic).[94–97]

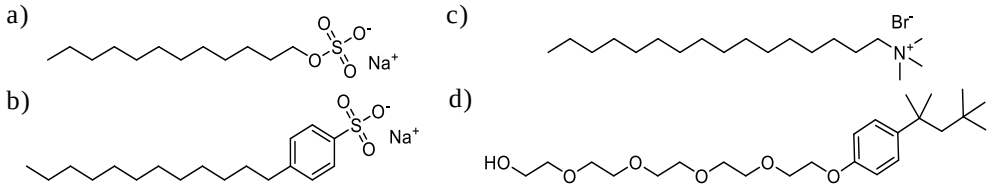

Figure 5. Examples of surfactants used for non-covalent functionalization of CNTs. a) SDS, b) SDBS, c) CTAB, and d) Triton.

The stability of CNTs dispersions depends on the ability of the emulsifiers to adsorb on their walls, i.e., depends on the presence of aromatic ring residues, charged groups, and alkyl chains. A comparative study of SDS, SDBS, and Triton X-100 for the dispersion of SWNTs, showed a superior scattering capacity of SDBS compared to the other two. The interaction of SDS with the nanotube surface is weaker than that of SDBS and Triton X-100, as it has no benzene ring. In addition, the dispersion capacity of SDBS is higher than the one of Triton X-100. This is because the smaller head group, and the presence of sulfur trioxide anions (which stabilize the dispersion via Coulomb interactions) in SDBS.[98] Besides their nature, their concentration must also be taken into account. As an example, in 2020, Blanch *et al.* determined the optimal concentration of several anionic (1.6% sodium deoxycholate (DOC) and 0.5% SDBS) and non-ionic (3% Triton-X 405, 2% Brij S-100, 5% Pluronic F-127, and 3% polyvinyl pyrrolidone, PVP-55) surfactants to get better nanotube dispersion. They showed than the tensioactive concentration is the most important parameter to consider, as opposed to the surfactant/nanotube ratio, mainly to control micelle formation and avoid the CNTs aggregation.[99]

Polymers are materials formed by repetitive units of monomeric species. Polymer wrapping of SWNTs works via π-π stacking and van der Waals interactions

[94] Bergler, F. F.; Stahl, S.; Goy, A.; Schöppler, F. *Langmuir* **2016**, *32* (37), 9598–9603.
[95] Zhang, X.; Song, K.; Liu, J.; Zhang, Z.; Wang, C.; Li, H. *Colloids Surf. A: Physicochem. Eng.* **2019**, *562*, 280–288.
[96] Kato, H.; Nakamura, A.; Horie, M. *RSC Adv.* **2014**, *4* (5), 2129–2136.
[97] Liu, L.; Wei, X.; Yao, Z.; Li, X.; Wang, W.; Wang, Y.; Zhou, W.; Xiong, F.; Kataura, H.; Xie, S.; Liu, H. *J. Phys. Chem. C* **2022**, *126* (7), 3787–3795.
[98] Islam, M. F.; Rojas, E.; Bergey, D. M.; Johnson, A. T.; Yodh, A. G. *Nano Lett.* **2003**, *3* (2), 269–273.
[99] Blanch, A. J.; Lenehan, C. E.; Quinton, J. S. *J. Phys. Chem. B* **2010**, *114* (30), 9805–9811.

between the surfaces of the nanotubes, and the conjugated chains of the dispersants forming supramolecular complexes. The advantage over the surfactants is that they reduce the entropic penalty of micelle formation.[100] Apart from that, they form thermodynamically stable coatings, which enables the removal of the unbound polymers from the bulk solution by different methods such as precipitation,[101] filtration,[102] and ultracentrifugation[103] without disturbing the supramolecular complex. The use of polyvinyl pyrrolidone (PVP),[104] polyvinylidene fluoride (PVDF),[104] tetraethylene polyfluorene bypyridine copolymer with tetraglycol side chains (TEG-PF-BPy),[105] etc polymers for non-covalent functionalization of carbon nanotubes have been extensively reviewed.[106–110] Water-soluble polymers, such as, polyethylene glycol derivatives, were used to functionalize SWNTs via a Diels-Alder click reaction creating effective nanocarrier materials for doxorubicin delivery.[111] In another interesting example, Gan *et al.* functionalized carbon nanotubes with tannins making adsorbent materials to easily remove cationic pollutants from aqueous solutions.[112]

1.1.3. Mechanically Interlocked carbon nanotubes, MINTs.

Mechanically interlocked molecules (MIMs)[113] are composed for two or more fragments which are not connected by covalent bonds, but cannot be separated without breaking a covalent bond. The archetypal examples are catenates,

[100] Bilalis, P.; Katsigiannopoulos, D.; Avgeropoulos, A.; Sakellariou, G. *RSC Adv.* **2013**, *4* (6), 2911–2934.
[101] Stranks, S. D.; Habisreutinger, S. N.; Dirks, B.; Nicholas, R. *J. Adv. Mater.* **2013**, *25* (31), 4365–4371.
[102] Izard, N.; Kazaoui, S.; Hata, K.; Okazaki, T.; Saito, T.; Iijima, S.; Minami, N. *Appl. Phys. Lett.* **2008**, *92* (24), 243112.
[103] Bisri, S. Z.; Gao, J.; Derenskyi, V.; Gomulya, W.; Iezhokin, I.; Gordiichuk, P.; Herrmann, A.; Loi, M. A. *Adv. Mater.* **2012**, *24* (46), 6147–6152.
[104] Namasivayam, M.; Andersson, M. R.; Shapter, J. G. *Polym.* **2021**, *13* (15), 2447.
[105] Heimfarth, D.; Balcı Leinen, M.; Klein, P.; Allard, S.; Scherf, U.; Zaumseil, J. *ACS Appl. Mater. Interfaces* **2022**, *14* (6), 8209–8217.
[106] Wang, J.; Lei, T. *Polym.* **2020**, *12* (7), 1548.
[107] Chik, M. W.; Hussain, Z.; Zulkefeli, M.; Tripathy, M.; Kumar, S.; Majeed, A. B. A.; Byrappa, K. *Drug Deliv. Transl. Res.* **2019**, *9* (2), 578–594.
[108] Lei, T.; Pochorovski, I.; Bao, Z. *Acc. Chem. Res.* **2017**, *50* (4), 1096–1104.
[109] Samanta, S. K.; Fritsch, M.; Scherf, U.; Gomulya, W.; Bisri, S. Z.; Loi, M. A. *Acc. Chem. Res.* **2014**, *47* (8), 2446–2456.
[110] Fujigaya, T.; Nakashima, N. *Sci. Technol. Adv. Mater.* **2015**, *16* (2), 024802.
[111] Cao, X. T.; Patil, M. P.; Phan, Q. T.; Le, C. M. Q.; Ahn, B.-H.; Kim, G.-D.; Lim, K. T. *J. Ind. Eng. Chem.* **2020**, *83*, 173–180.
[112] Gan, D.; Liu, M.; Huang, H.; Chen, J.; Dou, J.; Wen, Y.; Huang, Q.; Yang, Z.; Zhang, X.; Wei, Y. *J. Mol. Liq.* **2018**, *271*, 246–253.
[113] Stoddart, J. F. *Angew. Chem. Int. Ed.* **2017**, *56* (37), 11094–11125.

molecules in which two or more macrocycles are interlocked, and rotaxanes, molecules made up of at least one macrocycle threaded onto a linear component with bulky end-groups (stoppers) to prevent the de-threading of the macrocycle(s). The aspect ratio of the SWNTs allows supramolecular modification with macrocycles to form rotaxane-like species. The hybrids formed have a stability equivalent to their weakest covalent bond, without changing their structure or properties.

In 2014, our group reported the synthesis of mechanically interlocked carbon nanotubes (MINTs).[114] The MINT formation relies on a "clipping" strategy where U-shaped molecules (which feature two recognition motifs with high affinity for nanotubes connected through a spacer and alkene-terminated alkyl chains) are mechanically interlocked around SWNTs. The new rotaxane-type structures combine the advantages of covalent and non-covalent functionalization, they are kinetically stable products which maintain intact the sp^2 structure of the SWNTs. The U-shaped molecule design was based on π-extended derivatives of tetrathiafulvalene (exTTF) because their well-known non-covalent interactions with fullerenes[115,116] and SWNTs.[117] Firstly, the derivative exTTF was supramolecularly associated with an individual SWNT (supramolecular equilibrium governed by an association constant, K_a). Secondly, the U-shaped molecule is closed forming rotaxane-type specie by ring-closing metathesis (RCM, leaded by a pseudo-first order kinetics, k_{RCM}) (Figure 6).[118] Techniques as Raman or UV-vis-NIR spectroscopies demonstrated that there was not change in the graphitic structure of the SWNTs. Furthermore, the high stability of the MINTs, that is the lack of macrocycle de-threading, was verified subjecting the samples to reflux in tetrachloroethane for 30 min.

[114] de Juan, A.; Pouillon, Y.; Ruiz-González, L.; Torres-Pardo, A.; Casado, S.; Martín, N.; Rubio, Á.; Pérez, E. M. *Angew. Chem. Int. Ed* **2014**, *53* (21), 5394–5400.
[115] Canevet, D.; Gallego, M.; Isla, H.; de Juan, A.; Pérez, E. M.; Martín, N. *J. Am. Chem. Soc.* **2011**, *133* (9), 3184–3190.
[116] Isla, H.; Gallego, M.; Pérez, E. M.; Viruela, R.; Ortí, E.; Martín, N. *J. Am. Chem. Soc.* **2010,** 132 (6), 1772–1773.
[117] Romero-Nieto, C.; García, R.; Herranz, M. Á.; Ehli, C.; Ruppert, M.; Hirsch, A.; Guldi, D. M.; Martín, N. *J. Am. Chem. Soc.* **2012**, *134* (22), 9183–9192.
[118] de Juan, A.; Mar Bernal, M.; Pérez, E. M. *ChemPlusChem* **2015**, *80* (7), 1153–1157.

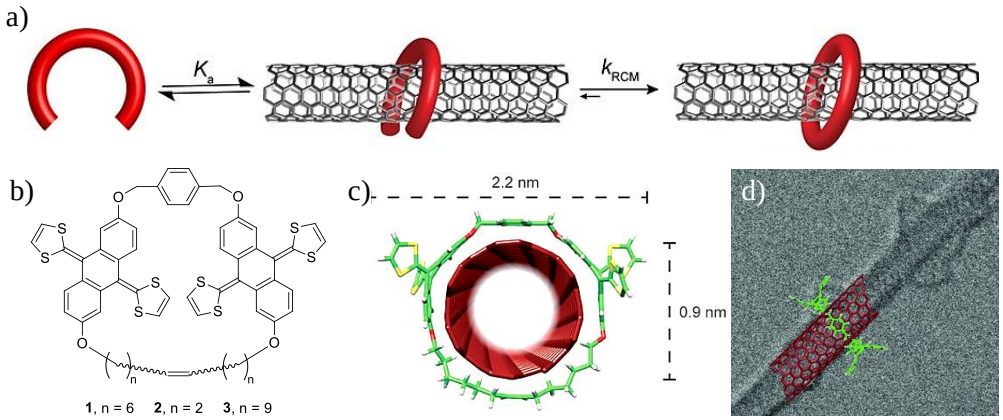

Figure 6. a) General scheme of MINTs synthesis: Supramolecular equilibrium followed by the ring-closing metathesis. b) Chemical structure of exTTF macrocycle. c) Energy-minimized (MMDD94) molecular model of a pseudorotaxane formed by exTTF and SWNTs. d) HR-STEM bright-field image of a exTTF MINT with an energy minimized (DFT) structure for its comparison. Macrocycle of 2.2 nm of diameter surrounds a SWNT of 0.8 nm. Scale bar: 1 nm.[114] Adapted with permission from ref. 119 (a) and ref. 114 (b, c).

The MINT functionalization can be modulated changing the chemical structure of the U-shaped molecules, their relative concentration with respect to the nanotubes, and the catalyst concentration. It has been shown that the optimum conditions for MINT synthesis are a concentration of exTTF U-shape of at least 1 mM, reaction times of not less than 48 h, and a ratio of catalyst concentration to U-shaped molecule of less than 1 equivalent.[118] Thermogravimetric analysis (TGA) was used as a reliable technique to quantify it since the degree of functionalization is given by the observed weight loss as a function of the temperature. For example, weight losses of MINTs synthesized with exTTF U-shaped molecules vary from 23 to 37% depending on the length of the macrocycle alkyl chains and the diameter of the SWNTs.[114] The same is applicable for pyrene MINTs, where the range of functionalization is between 24 and 28%.[120] The potential chiral selectivity of the MINT-forming reaction is another important aspect. In a 2016 paper, MINTs with exTTF macrocycles showed preferred functionalization for the smaller diameter (6,5)-SWNT instead of (7,6)-SWNTs.[121] The differences between the charge

[114] de Juan, A.; Pouillon, Y.; Ruiz-González, L.; Torres-Pardo, A.; Casado, S.; Martín, N.; Rubio, Á.; Pérez, E. M. *Angew. Chem. Int. Ed* **2014**, *53* (21), 5394–5400.

[118] de Juan, A.; Mar Bernal, M.; Pérez, E. M. *ChemPlusChem* **2015**, *80* (7), 1153–1157.

[119] Pérez, E. M. *Chem. Eur. J.* **2017**, *23* (52), 12681–12689.

[120] López-Moreno, A.; Pérez, E. M. *Chem. Commun.* **2015**, *51* (25), 5421–5424.

[121] Martínez-Periñán, E.; Juan, A. de; Pouillon, Y.; Schierl, C.; Strauss, V.; Martín, N.; Rubio, Á.; Guldi, D. M.; Lorenzo, E.; Pérez, E. M. *Nanoscale* **2016**, *8* (17), 9254–9264.

transfer rates of MINTs and their supramolecular counterparts due to the different nature of the interactions in the presence and absence of mechanical bonding were also confirmed.

The synthesis of MINTs requires bisalkene molecules to perform the RCM around SWNTs. Therefore, the in-situ formation of oligomers/polymers of the U-shaped molecule is a possible side reaction. Acyclic diene metathesis polymerization (ADMP) of naphthalene diimide (NDI) with nanotubes was studied and compared to the NDI-MINT formation (Figure 7).[122] In this study, the synthesis of NDI-MINT was performed using tetrachloroethane (TCE) and dimethylformamide (DMF). The results proved that when TCE is the solvent used for the synthesis, the NDI precursors have minor affinity for the SWNTs lowering the kinetics of the reaction and favoring the formation of stable MINTs. In this case, the MINT formation is strongly affected by the size of the macrocycle and the nanotube´s diameter. Whereas if DMF is used, the oligomeric reaction is faster than the templated reaction creating oligomers which wrap the SWNTs. The reaction is diameter-independent and leads to a higher NDI supramolecular loading.

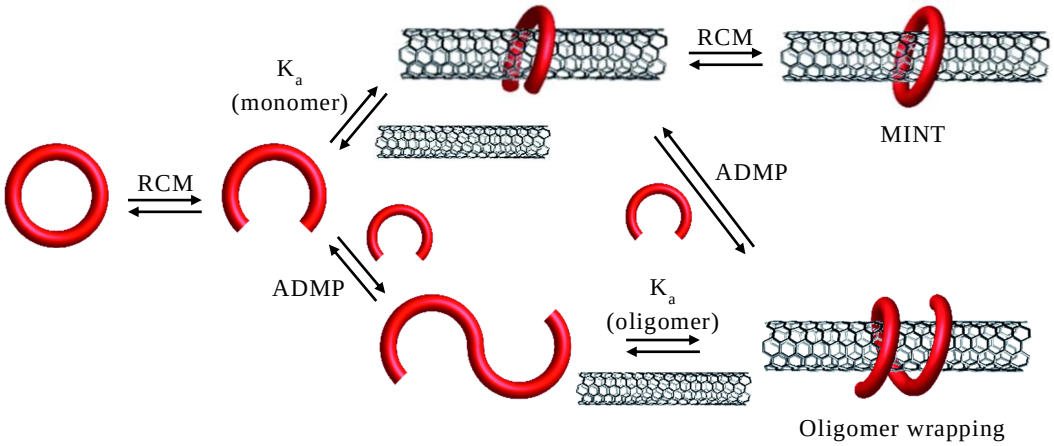

Figure 7. Reaction pathways for the bimodal supramolecular functionalization of SWNTs. Reproduced from ref. 122 with permission from the Royal Society of Chemistry.

The functionalization of SWNTs as MINTs via ring-closing metathesis has proven to be a versatile method. From the very first attempt with exTTF[114], several

[114] de Juan, A.; Pouillon, Y.; Ruiz-González, L.; Torres-Pardo, A.; Casado, S.; Martín, N.; Rubio, Á.; Pérez, E. M. *Angew. Chem. Int. Ed* **2014**, *53* (21), 5394–5400.
[122] Leret, S.; Pouillon, Y.; Casado, S.; Navío, C.; Rubio, Á.; Pérez, E. M. *Chem. Sci.* **2017**, *8* (3), 1927–1935.

molecules such as pyrene,[120] naphthalene diimides,[122] anthraquinone,[123] porphyrins,[124] benzophenones and diphenylmethane have been used as a recognition motives for SWNTs.[125] Arguably the most prominent feature of MIMs is the ability of one component to move with respect to the other(s) in a controlled fashion, which has been thoroughly studied in the context of synthetic molecular machinery (Stoddart y Sauvage NP lectures in Angewandte), the dynamic properties of MINTs were not explored until a few years ago.[126] In 2020, our group studied the shuttling and pirouetting movements of four type of macrocycles with different affinities for the SWNTs. Molecular dynamic simulations showed that the sub-molecular kinetics of the macrocycles along and around the single-walled carbon nanotubes do not rely on the interaction energy between the two species. In other words, there is no correlation between the interaction energy between the two species and their ability with respect to one another. The minor differences found among the MINTs were justified on the basis of macrocycle-SWNT compatibility.

Other approaches for the mechanically interlocking of carbon nanotubes have been also described. In 2018, González-Rodríguez and co-workers synthesized MINTs using self-assembled hydrogen-bonded macrocycles.[127] A dinucleoside monomer capable of self-assembly into nanorings (*via* Watson-Crick base-pairing) was mixed with single-walled carbon nanotubes, allowing an efficient debundling of SWNTs and long-lasting dispersions in apolar solvents. This was the result of the H-bonded rings, which can closely associate with the nanotubes. In addition, the interaction of more than one monomer with the surface of the SWNTs increased the stability of the nanorings. This approach relied on dynamic macrocycle interlocking around the nanotube sidewalls, which provides the reversibility for the pristine material to be easily and effectively recover by the addition of a polar solvent or by heating the apolar suspension (Figure 8). By combining theoretical methods based on DFT, spectroscopic techniques and atomic force and transmission

[120] López-Moreno, A.; Pérez, E. M. *Chem. Commun.* **2015**, *51* (25), 5421–5424.
[122] Leret, S.; Pouillon, Y.; Casado, S.; Navío, C.; Rubio, Á.; Pérez, E. M. *Chem. Sci.* **2017**, *8* (3), 1927–1935.
[123] Blanco, M.; Nieto-Ortega, B.; de Juan, A.; Vera-Hidalgo, M.; López-Moreno, A.; Casado, S.; González, L. R.; Sawada, H.; González-Calbet, J. M.; Pérez, E. M. *Nat. Commun.* **2018**, *9* (1), 2671.
[124] de Juan-Fernández, L.; Münich, P. W.; Puthiyedath, A.; Nieto-Ortega, B.; Casado, S.; Ruiz-González, L.; Pérez, E. M.; Guldi, D. M. *Chem. Sci.* **2018**, *9* (33), 6779–6784.
[125] Zhang, W.; Guillén-Soler, M.; Silva, S. M.-D.; López-Moreno, A.; González, L. R.; Giménez-López, M. del C.; Pérez, E. M. *Chem. Sci.* **2022**, *13* (33), 9706–9712.
[126] Villalva, J.; Nieto-Ortega, B.; Melle-Franco, M.; Pérez, E. M. *J. Phys. Chem. C* **2020**, *124* (28), 15541–15546.
[127] Chamorro, R.; Juan-Fernández, L. de; Nieto-Ortega, B.; Mayoral, M. J.; Casado, S.; Ruiz-González, L.; Pérez, E. M.; González-Rodríguez, D. *Chem. Sci.* **2018**, *9* (17), 4176–4184.

electron microscopies, robust evidence was established for a preferred mode of association in which the H-bonded nanorings embrace the tube (mode IV in Figure 8).

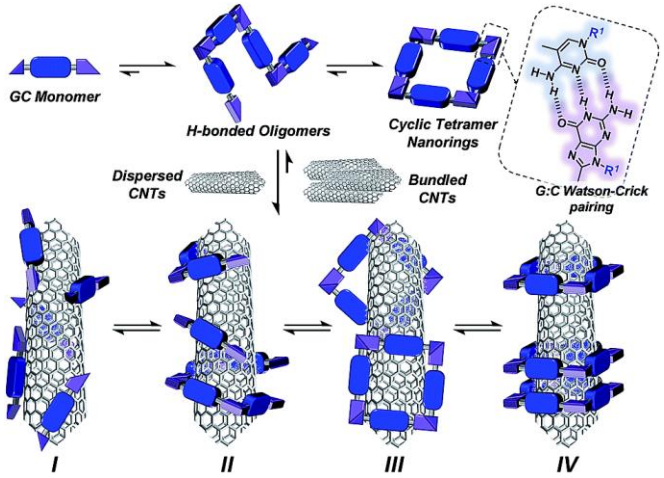

Figure 8. Global equilibria established for the H-bonding strategy between the GC monomers and the SWNTs. Self-assembly of the cyclic tetramers using G-C base pairing and different feasible modes of nanotube dispersion stabilization mediated by monomers, oligomers, and cyclic tetramers. Adapted from ref. 127 with permission from the Royal Society of Chemistry.

Miki, Ohe *et al.* described an effective approach for the direct preparation of interlocked carbon nanotubes using π-conjugated carbon nanorings.[128] The "ring toss" method was based on the mixing of [8]-, [9]-, and [10]-cycloparaphenyleneacetylene (CPPA) macrocycles with SWNTs, yielding tube-in-ring and tube-on-ring complexes (Figure 9). It was found that the complexation rate depended on the size of the CPPAs as well as the diameter of the nanotubes. CPPAs with both larger and smaller ring sizes predominantly formed "ring-on-tube" hybrids with CNTs, whereas when the fit is particularly tight, such as between the [9] CPPA (1.89 nm cavity) and SWNTs of 1.1–1.4 nm diameter, the tube-in-ring predominated.

[127] Chamorro, R.; Juan-Fernández, L. de; Nieto-Ortega, B.; Mayoral, M. J.; Casado, S.; Ruiz-González, L.; Pérez, E. M.; González-Rodríguez, D. *Chem. Sci.* **2018**, *9* (17), 4176–4184.
[128] Miki, K.; Saiki, K.; Umeyama, T.; Baek, J.; Noda, T.; Imahori, H.; Sato, Y.; Suenaga, K.; Ohe, K. *Small* **2018**, *14* (26), 1800720.

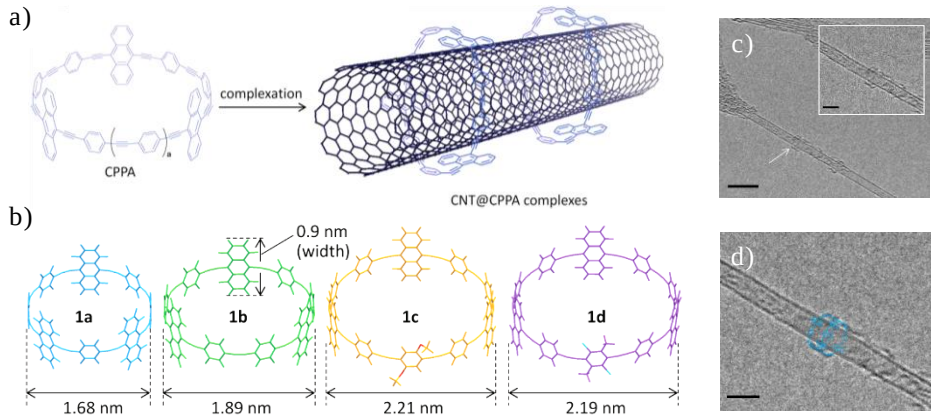

Figure 9. a) Example of "Ring-toss" method. b) Structure of CPPAs 1a-d optimized at the B3LYP/6-31G. c) Representative TEM image of a CNT@CPPA complex. Scale bar, 5nm. The inset is it enlarge image. Scale bar, 2nm. d) Capped stick model of CNT@CPPA complex of the inset of Figure 9c. Scale bar, 2nm. Adapted with permission from ref. 128.

Von Delius *et al.* reported another strategy based on dynamic covalent macrocyclization.[129] Guided by computational modelling, they synthesized two macrocycles with exTTF binding motives and alkyl thiol residues to build reversible interlocking SWNTs. To gain a better understanding of the results, the irreversible and supramolecular functionalization experiments were also carried out resulting into different functionalization ratios (Figure 10). It was shown that the dynamic covalent bonds favour the opening and closing of the macrocycles under mild basic conditions, thereby enhancing the rotaxane-like functionalisation of SWNTs. Raman and 3D fluorescence characterisation revealed the selective functionalization of the smaller diameter (6,4)- and (6,5)-SWNTs in contrast to the larger (7,5)- and (8,3)-SWNTs. The found chirality selectivity is different for the studied macrocycles due to a combination of size matching and ground state charge transfer. This methodology had two advantages over previous studies: i) the dithiol building blocks made possible the comparative evaluation of three types of functionalization: reversible, irreversible, and supramolecular; ii) the disulphide bonds allowed the quantitative reductive dissociation, which facilitated the purification of mixtures of SWNTs by diameter-selective solubilization in organic

[128] Miki, K.; Saiki, K.; Umeyama, T.; Baek, J.; Noda, T.; Imahori, H.; Sato, Y.; Suenaga, K.; Ohe, K. *Small* **2018**, *14* (26), 1800720.

[129] Balakrishna, B.; Menon, A.; Cao, K.; Gsänger, S.; Beil, S. B.; Villalva, J.; Shyshov, O.; Martin, O.; Hirsch, A.; Meyer, B.; Kaiser, U.; Guldi, D. M.; von Delius, M. *Angew. Chem. Int. Ed* **2020**, *59* (42), 18774–18785.

solvents. This was achieved simply by means of ultracentrifugation and the subsequent cleavage of the macrocycles.

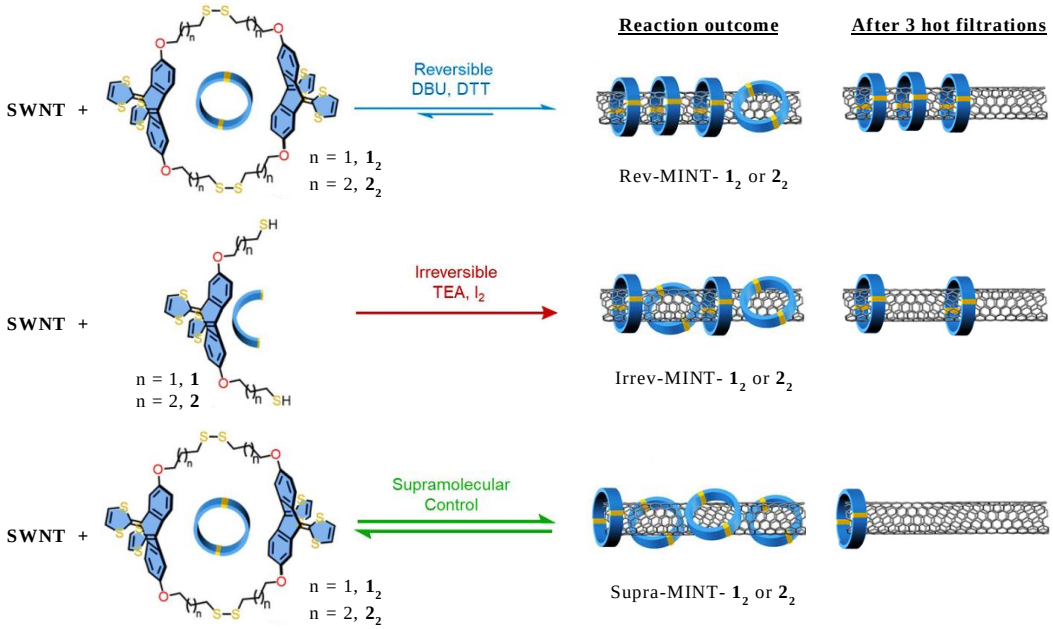

Figure 10. Schematic representation of the three different approaches of SWNTs functionalization. Adapted with permission from Ref. 129.

The last strategy to synthesize MINTs was explored simultaneously and independently by our group, in collaboration with the Peris group,[130] and the group led by Komatsu,[131] using coordination chemistry. The first example will be explained in depth in Chapter 4. In the case of Komatsu and co-workers, they synthesized U-shaped molecules with dipyrrin ligands at each end for their use as supramolecular coordination complexes. After the addition of metallic centres and through them, two units coordinate *in situ* around the carbon nanotubes forming interlocked hybrids (Figure 11). Due to the rigid structure of the Cu-tethered tetragonal nanobrackets, they were used to separate SWNTs with a diameter range of 0.90 to 0.92 nm. This allowed the isolation of (7,6)-, (8,5)-, and (9,4)-SWNTs. In addition to strictly discriminating SWNT diameters, this functionalization opens

[129] Balakrishna, B.; Menon, A.; Cao, K.; Gsänger, S.; Beil, S. B.; Villalva, J.; Shyshov, O.; Martin, O.; Hirsch, A.; Meyer, B.; Kaiser, U.; Guldi, D. M.; von Delius, M. *Angew. Chem. Int. Ed* **2020**, *59* (42), 18774–18785.

[130] López-Moreno, A.; Ibáñez, S.; Moreno-Da Silva, S.; Ruiz-González, L.; Sabanés, N. M.; Peris, E.; Pérez, E. M. *Angew. Chem. Int. Ed.* **2022**, *61* (35), e202208189.

[131] Cheng, G.; Hayashi, T.; Miyake, Y.; Sato, T.; Tabata, H.; Katayama, M.; Komatsu, N. *ACS Nano* **2022**, *16* (8), 12500–12510.

the possibility of using Cu-nanobrackets to interlock of SWNTs, as well as the recovery of pristine carbon nanotubes and the square nanobrackets easily removing the mental centre.

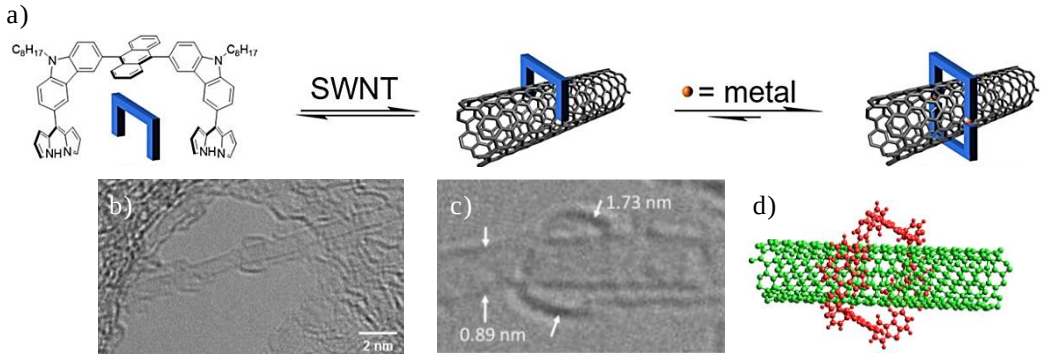

Figure 11. a) Reaction scheme for the synthesis of MINTs. b) Representative TEM image of a MINT. c) Zoom of TEM image in (b). d) Corresponding model structure of (8,5)-SWNT interlocked with Cu-nanobrackets. Adapted with permission from ref. 131.

As we have seen, chemically modifying SWNTs using mechanical bonding combines the best of the covalent and non-covalent worlds. This has led to the development of mechanically interlocked SWNT derivatives with high stability and structural integrity, making them ideal for different applications.

1.1.3.1. Potential applications of MINTs.

With the synthetic and characterization pathways towards MINTs firmly established, our group started exploring potential fields of application for these SWNT derivatives. In 2016, MINTs were used to reinforce polymers. The mechanical properties of electrospun polystyrene fibres doped with 0.01% MINTs were characterized and compared with composites made from polystyrene fibres with pristine SWNTs and with supramolecular complexes of equal chemical composition of MINT. By mixing two different macrocycles and three types of SWNTs, different MINTs were prepared. The results showed that the tensile strength and Young's modulus of the fibres were improved by up to 200% at very low concentrations (0.01 % w/w) of MINTs (Figure 12). On the other hand, insignificant or even negative effects were observed in the polystyrene fibres filled with the identical chemical composition but without the interlocked species. This was the result of the use of electrospinning, which forced the alignment of the

[131] Cheng, G.; Hayashi, T.; Miyake, Y.; Sato, T.; Tabata, H.; Katayama, M.; Komatsu, N. *ACS Nano* **2022**, *16* (8), 12500–12510.

polymer fibres parallel to the carbon nanotubes, and the use of macrocycles, which prevented the nanotubes from self-aggregating, thereby enhancing their interaction with the polymer matrix. [132]

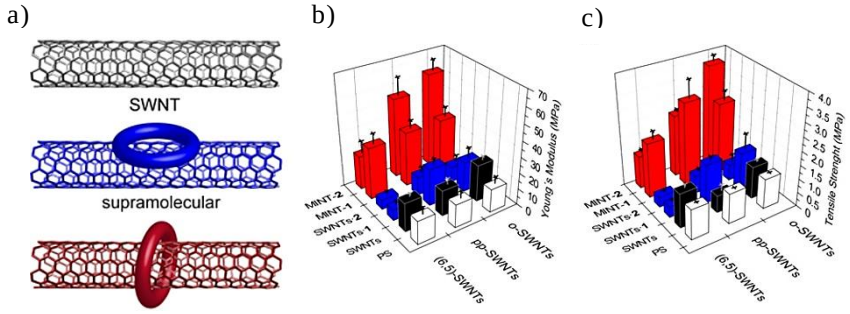

Figure 12. a) Schematic representation of the three types of fillers studied. b) Young's modulus; and c) Tensile strength of polystyrene (white), SWNTs (black), supramolecular complexes (blue), and MINTs (red) with (6,5)-SWNTs (left), pp-SWNTs (center), and o-SWNTs (right). Adapted from ref. 132.

Another potential application of MINTs is their use as catalysts. Our group studied the catalytic effect of different types of MINTs in the reduction of nitroaromatic compounds.[123] They were able to regulate the reduction process using electron donor (MINT-exTTF), acceptor (MINT-anthraquinone, MINT-AQ), or electronically neutral (MINT-pyrene, MINT-pyr) U-shaped molecules positively or negatively due to their n- or p-doping effect. They clarified that the effect of the macrocycles is the result of several factors like the degree of aggregation or de the binding stability. However, it was the electronic effect that was mainly responsible for the enhanced or decreased catalytic activity. Compared to pristine SWNTs, electron-donating exTTF macrocycles exhibit the highest activity. Pyrene macrocycles showed similar activity, while electron-accepting anthraquinone macrocycles significantly slowed down the reaction rates. This approach has allowed the synthesis of stable and recyclable catalysts. The effector (macrocycle) is linked to the catalyst (SWNT) by non-covalent but robust mechanical bonds, and its action is long-range rather than allosteric, as it does not affect the 3D structure of the active site of the catalyst.

[123] Blanco, M.; Nieto-Ortega, B.; de Juan, A.; Vera-Hidalgo, M.; López-Moreno, A.; Casado, S.; González, L. R.; Sawada, H.; González-Calbet, J. M.; Pérez, E. M. *Nat. Commun.* **2018**, *9* (1), 2671.

[132] López-Moreno, A.; Nieto-Ortega, B.; Moffa, M.; de Juan, A.; Bernal, M. M.; Fernández-Blázquez, J. P.; Vilatela, J. J.; Pisignano, D.; Pérez, E. M. *ACS Nano* **2016**, *10* (8), 8012–8018.

In 2020, MINTs made with anthraquinone macrocycles demonstrated their potential application as stable electrocatalytic platform for oxygen reduction reactions (ORR)[133] Compared to physiosorbed AQ-based electrodes, AQ-MINTs showed an enhancement of stability of adsorbed organic molecules upon electrochemical reduction while maintaining the electrochemical properties of the macrocycle. In addition, the potential of MINTs as immobilization carriers was demonstrated by improving the H_2O_2 production rate. Cyclic voltammogram (CV) of AQ-MINT reveals the representative AQ peak at around -0.68V for all conditions and a reduction broad peak at -0.12V resulting from oxygen reduction under O_2 saturation. However, the pristine SWNT only showed the broad capacitive current with a small reducing step as O_2 reduced (Figure 13).

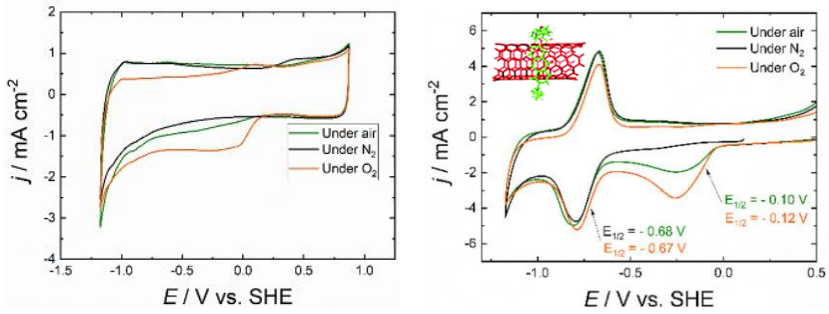

Figure 13. Cyclic voltammogram of SWNTs in 0.1M Na_2SO_4 aqueous solution (left) and AQ-MINT in 0.1M NaOH solution (right) under air (green line), N_2 (black line) and O_2 (orange line) conditions. Adapted with permission from ref. 133.

A novel strategy for the application of MINTs as electrocatalyst in the ORR was described in 2022.[125] Our group synthesized mechanically interlocked species using SWNTs and N-rich macrocycles containing triphenylamine (TPA) groups to display electroactive sites on the carbon nanotube surfaces. A comparison between the MINTs doped with nitrogen atoms, MINTs without the heteroatoms in their structure, and pristine carbon nanotubes, showed that the nitrogen atoms present on the TPA fragments allowed the improvement of the ORR activity. Moreover, with the electrochemical characterization, it was also possible to discover that the carbonyl groups presented in benzophenone macrocycles also acted as electroactive sites improving ever more the ORR performance. Finally, better activity and stability respect to the ORR performance was developed with (7,6)-SWNTs than

[125] Zhang, W.; Guillén-Soler, M.; Silva, S. M.-D.; López-Moreno, A.; González, L. R.; Giménez-López, M. del C.; Pérez, E. M. *Chem. Sci.* **2022**, *13* (33), 9706–9712.
[133] Wielend, D.; Vera-Hidalgo, M.; Seelajaroen, H.; Sariciftci, N. S.; Pérez, E. M.; Whang, D. R. *ACS Appl. Mater. Interfaces* **2020**, *12* (29), 32615–32621.

(6,5)-SWNTs due to a tighter interlocking fit which resulted in more effective intermolecular charge-transfer (Figure 14).

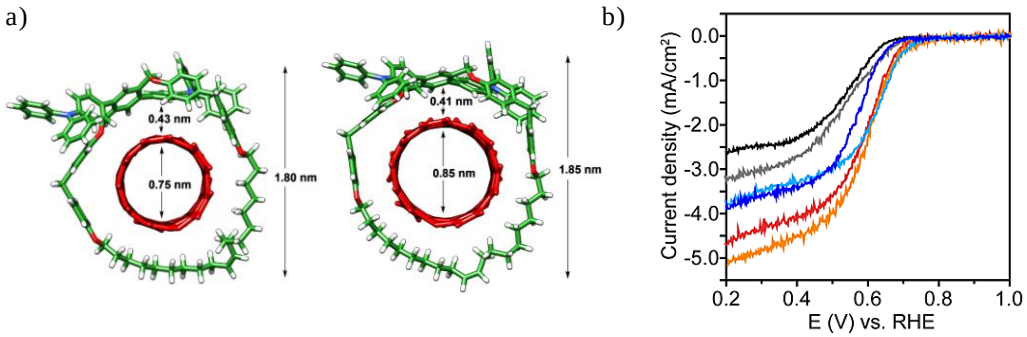

Figure 14. a) Energy-minimized (MM94) model of MINT(6,5)-**1** (left) and MINT(7,6)-**1** (right) b) Comparison of the ohmic drop corrected ORR polarization curves of (6,5)-SWNT in black, (7,6)-SWNT in grey, (6,5)-MINT-**1** in dark blue, (7,6)-MINT-**1** in red, (6,5)-MINT-**2** in light blue and (7,6)-MINT-**2** in orange. Adapted from ref. and ref. 125.

1.2. BIBLIOGRAPHY

(1) Iijima, S. Helical Microtubules of Graphitic Carbon. *Nature* **1991**, *354* (6348), 56–58.

(2) Tsang, S. C.; Harris, P. J. F.; Green, M. L. H. Thinning and Opening of Carbon Nanotubes by Oxidation Using Carbon Dioxide. *Nature* **1993**, *362* (6420), 520–522.

(3) Iijima, S.; Ichihashi, T. Single-Shell Carbon Nanotubes of 1-Nm Diameter. *Nature* **1993**, *363* (6430), 603–605.

(4) Bethune, D. S.; Kiang, C. H.; de Vries, M. S.; Gorman, G.; Savoy, R.; Vazquez, J.; Beyers, R. Cobalt-Catalysed Growth of Carbon Nanotubes with Single-Atomic-Layer Walls. *Nature* **1993**, *363* (6430), 605–607.

(5) Oberlin, A.; Endo, M.; Koyama, T. Filamentous Growth of Carbon through Benzene Decomposition. *J. Cryst. Growth* **1976**, *32* (3), 335–349.

(6) Prasek, J.; Drbohlavova, J.; Chomoucka, J.; Hubalek, J.; Jasek, O.; Adam, V.; Kizek, R. Methods for Carbon Nanotubes Synthesis—Review. *J. Mater. Chem.* **2011**, *21* (40), 15872–15884.

(7) Rathinavel, S.; Priyadharshini, K.; Panda, D. A Review on Carbon Nanotube: An Overview of Synthesis, Properties, Functionalization, Characterization, and the Application. *Mater. Sci. Eng. B* **2021**, *268*, 115095.

[125] Zhang, W.; Guillén-Soler, M.; Silva, S. M.-D.; López-Moreno, A.; González, L. R.; Giménez-López, M. del C.; Pérez, E. M. *Chem. Sci.* **2022**, *13* (33), 9706–9712.

(8) Zhu, Z.; Cui, C.; Bai, Y.; Gao, J.; Jiang, Y.; Li, B.; Wang, Y.; Zhang, Q.; Qian, W.; Wei, F. Advances in Precise Structure Control and Assembly toward the Carbon Nanotube Industry. *Adv. Funct. Mat.* **2022**, *32* (11), 2109401.

(9) Arora, N.; Sharma, N. N. Arc Discharge Synthesis of Carbon Nanotubes: Comprehensive Review. *Diam. Relat.* **2014**, *50*, 135–150.

(10) Yogesh, G. K.; Shukla, S.; Sastikumar, D.; Koinkar, P. Progress in Pulsed Laser Ablation in Liquid (PLAL) Technique for the Synthesis of Carbon Nanomaterials: A Review. *Appl. Phys. A* **2021**, *127* (11), 810.

(11) Gupta, N.; Gupta, S. M.; Sharma, S. K. Carbon Nanotubes: Synthesis, Properties and Engineering Applications. *Carbon Lett.* **2019**, *29* (5), 419–447.

(12) Guo, T.; Nikolaev, P.; Thess, A.; Colbert, D. T.; Smalley, R. E. Catalytic Growth of Single-Walled Manotubes by Laser Vaporization. *Chem. Phys. Lett.* **1995**, *243* (1), 49–54.

(13) José-Yacamán, M.; Miki-Yoshida, M.; Rendón, L.; Santiesteban, J. G. Catalytic Growth of Carbon Microtubules with Fullerene Structure. *Appl. Phys. Lett.* **1993**, *62* (6), 657–659.

(14) Nikolaev, P. Gas-Phase Production of Single-Walled Carbon Nanotubes from Carbon Monoxide: A Review of the HiPco Process. *J. Nanosci. Nanotechnol.* **2004**, *4* (4), 307–316.

(15) Bachilo, S. M.; Balzano, L.; Herrera, J. E.; Pompeo, F.; Resasco, D. E.; Weisman, R. B. Narrow (n,m)-Distribution of Single-Walled Carbon Nanotubes Grown Using a Solid Supported Catalyst. *J. Am. Chem. Soc.* **2003**, *125* (37), 11186–11187.

(16) Shah, K. A.; Tali, B. A. Synthesis of Carbon Nanotubes by Catalytic Chemical Vapour Deposition: A Review on Carbon Sources, Catalysts and Substrates. *Mater. Sci. Semicond. Process.* **2016**, *41*, 67–82.

(17) Szabó, A.; Perri, C.; Csató, A.; Giordano, G.; Vuono, D.; Nagy, J. B. Synthesis Methods of Carbon Nanotubes and Related Materials. *Materials (Basel)* **2010**, *3* (5), 3092–3140.

(18) Chen, G. Z.; Fan, X.; Luget, A.; Shaffer, M. S. P.; Fray, D. J.; Windle*, A. H. Electrolytic Conversion of Graphite to Carbon Nanotubes in Fused Salts. *J. Electroanal. Chem.* **1998**, *446* (1), 1–6.

(19) Guillard, T.; Cetout, S.; Flamant, G.; Laplaze, D. Solar Production of Carbon Nanotubes; Structure Evolution with Experimental Conditions. *J. Mater. Sci.* **2000**, *35* (2), 419–425.

(20) Ferreira, F. V.; Franceschi, W.; Menezes, B. R. C.; Biagioni, A. F.; Coutinho, A. R.; Cividanes, L. S. Chapter One - Synthesis, Characterization, and Applications of Carbon Nanotubes. In *Carbon-Based Nanofillers and Their Rubber Nanocomposites*; Yaragalla, S., Mishra, R., Thomas, S., Kalarikkal, N., Maria, H. J., Eds.; Elsevier, **2019**; 1–45.

(21) Ganesh, E. N. Single Walled and Multi Walled Carbon Nanotube Structure, Synthesis and Applications. *Int. J. Innov. Technol. Explor. Eng.* **2013**, *2* (4), 2278–3075.

(22) Yao, F.; Yu, W.; Liu, C.; Su, Y.; You, Y.; Ma, H.; Qiao, R.; Wu, C.; Ma, C.; Gao, P.; Xiao, F.; Zhao, J.; Bai, X.; Sun, Z.; Maruyama, S.; Wang, F.; Zhang, J.; Liu, K. Complete Structural Characterization of Single Carbon Nanotubes by Rayleigh Scattering Circular Dichroism. *Nat. Nanotechnol.* **2021**, *16* (10), 1073–1078.

(23) Xiao, J. R.; Gama, B. A.; Gillespie, J. W. An Analytical Molecular Structural Mechanics Model for the Mechanical Properties of Carbon Nanotubes. *Int. J. Solids Struct.* **2005**, *42* (11), 3075–3092.

(24) Yu, M.-F.; Files, B. S.; Arepalli, S.; Ruoff, R. S. Tensile Loading of Ropes of Single Wall Carbon Nanotubes and Their Mechanical Properties. *Phys. Rev. Lett.* **2000**, *84* (24), 5552–5555.

(25) Ma, P.-C.; Siddiqui, N. A.; Marom, G.; Kim, J.-K. Dispersion and Functionalization of Carbon Nanotubes for Polymer-Based Nanocomposites: A Review. *Composites Part A: Appl. Sci. Manuf.* **2010**, *41* (10), 1345–1367.

(26) Tang, Z. K.; Zhang, L.; Wang, N.; Zhang, X. X.; Wen, G. H.; Li, G. D.; Wang, J. N.; Chan, C. T.; Sheng, P. Superconductivity in 4 Angstrom Single-Walled Carbon Nanotubes. *Science* **2001**, *292* (5526), 2462–2465.

(27) Wei, B. Q.; Vajtai, R.; Ajayan, P. M. Reliability and Current Carrying Capacity of Carbon Nanotubes. *Appl. Phys. Lett.* **2001**, *79* (8), 1172–1174.

(28) Hamada, N.; Sawada, S.; Oshiyama, A. New One-Dimensional Conductors: Graphitic Microtubules. *Phys. Rev. Lett.* **1992**, *68* (10), 1579–1581.

(29) Hone, J.; Whitney, M.; Piskoti, C.; Zettl, A. Thermal Conductivity of Single-Walled Carbon Nanotubes. *Phys. Rev. B* **1999**, *59* (4), 3.

(30) Qiu, H.; Yang, J. Chapter 2 - Structure and Properties of Carbon Nanotubes. In *Industrial Applications of Carbon Nanotubes*; Peng, H., Li, Q., Chen, T., Eds.; Micro and Nano Technologies; Elsevier: Boston, **2017**; 47–69.

(31) Jain, N.; Gupta, E.; Kanu, N. J. Plethora of Carbon Nanotubes Applications in Various Fields – A State-of-the-Art-Review. *Smart Sci.* **2022**, *10* (1), 1–24.

(32) Ajayan, P. M.; Ebbesen, T. W.; Ichihashi, T.; Iijima, S.; Tanigaki, K.; Hiura, H. Opening Carbon Nanotubes with Oxygen and Implications for Filling. *Nature* **1993**, *362* (6420), 522–525.

(33) Lavagna, L.; Musso, S.; Pavese, M. A Facile Method to Oxidize Carbon Nanotubes in Controlled Flow of Oxygen at 350 °C. *Mater. Lett.* **2021**, *283*, 128816.

(34) Lavagna, L.; Bartoli, M.; Suarez-Riera, D.; Cagliero, D.; Musso, S.; Pavese, M. Oxidation of Carbon Nanotubes for Improving the Mechanical and Electrical Properties of Oil-Well Cement-Based Composites. : *ACS Appl. Nano Mater.* **2022**, *5* (5), 6671–6678.

(35) Zhang, J.; Zou, H.; Qing, Q.; Yang, Y.; Li, Q.; Liu, Z.; Guo, X.; Du, Z. Effect of Chemical Oxidation on the Structure of Single-Walled Carbon Nanotubes. *J. Phys. Chem. B* **2003**, *107* (16), 3712–3718.

(36) Li, L.; Lin, R.; He, H.; Sun, M.; Jiang, L.; Gao, M. Interaction of Amidated Single-Walled Carbon Nanotubes with Protein by Multiple Spectroscopic Methods. *J. Lumin.* **2014**, *145*, 125–131.

(37) Ng, C. M.; Loh, H.-S.; Muthoosamy, K.; Sridewi, N.; Manickam, S. Conjugation of Insulin onto the Sidewalls of Single-Walled Carbon Nanotubes through Functionalization and Diimide-Activated Amidation. *Int J Nanomed.* **2016**, *11*, 1607–1614.

(38) Delgado, J. L.; de la Cruz, P.; Urbina, A.; López Navarrete, J. T.; Casado, J.; Langa, F. The First Synthesis of a Conjugated Hybrid of C60–Fullerene and a Single-Wall Carbon Nanotube. *Carbon* **2007**, *45* (11), 2250–2252.

(39) Sun, Y.-P.; Huang, W.; Lin, Y.; Fu, K.; Kitaygorodskiy, A.; Riddle, L. A.; Yu, Y. J.; Carroll, D. L. Soluble Dendron-Functionalized Carbon Nanotubes: Preparation, Characterization, and Properties,. *Chem. Mater.* **2001**, *13* (9), 2864–2869.

(40) Baskaran, D.; Mays, J. W.; Zhang, X. P.; Bratcher, M. S. Carbon Nanotubes with Covalently Linked Porphyrin Antennae: Photoinduced Electron Transfer. *J. Am. Chem. Soc.* **2005**, *127* (19), 6916–6917.

(41) Cosnier, S.; Holzinger, M. Design of Carbon Nanotube-Polymer Frameworks by Electropolymerization of SWCNT-Pyrrole Derivatives. *Electrochim. Acta.* **2008**, *53* (11), 3948–3954.

(42) d'Ambrosio, P.; Carchesio, M.; d'Alessandro, N.; Torre, G. de la; Torres, T. Linking Pd(II) and Ru(II) Phthalocyanines to Single-Walled Carbon Nanotubes. *Dalton Trans.* **2014**, *43* (20), 7473–7479.

(43) Xie, X.; Gao, L.; Sun, J. Esterification of Chemical Functional Single-Wall Carbon Nanotubes. In *Eco-Materials Processing and Design Xii*; Kim, H. S., Yang, J. F., Han, C. H., Thongtem, S. C., Lee, S. W., Eds.; Trans Tech Publications Ltd: Stafa-Zurich, **2011**, 695, 373–376.

(44) Dubey, R.; Dutta, D.; Sarkar, A.; Chattopadhyay, P. Functionalized Carbon Nanotubes: Synthesis, Properties and Applications in Water Purification, Drug Delivery, and Material and Biomedical Sciences. *Nanoscale Adv.* **2021**, *3* (20), 5722–5744.

(45) Syrgiannis, Z.; Melchionna, M.; Prato, M. Covalent Carbon Nanotube Functionalization. In *Encyclopedia of Polymeric Nanomaterials*; Kobayashi, S., Müllen, K., Eds.; Springer: Berlin, Heidelberg, **2021**, 1–8.

(46) Mickelson, E. T.; Huffman, C. B.; Rinzler, A. G.; Smalley, R. E.; Hauge, R. H.; Margrave, J. L. Fluorination of Single-Wall Carbon Nanotubes. *Chem. Phys. Lett.* **1998**, *296* (1), 188–194.

(47) Elavarasi, S. B.; Divya, S.; Vishnu Priya, M.; Sheik Sirajuddeen, M. NMR, Magnetic and Electronic Investigations of Fluorinated Nanotubes with Different Coverage of Fluorine. *Chem. Phys. Lett.* **2020**, *742*, 137142.

(48) Zhang, W.; Bonnet, P.; Dubois, M.; Ewels, C. P.; Guérin, K.; Petit, E.; Mevellec, J.-Y.; Vidal, L.; Ivanov, D. A.; Hamwi, A. Comparative Study of SWCNT Fluorination by Atomic and Molecular Fluorine. *Chem. Mater.* **2012**, *24* (10), 1744–1751.

(49) Yokoyama, K.; Mamiya, I.; Morita, H.; Sato, Y.; Sato, K.; Nishida, T.; Sato, Y. Controlled Introduction of Defects into Single-Walled Carbon Nanotubes via a Fluorination–Defluorination Strategy Using Xenon Difluoride and Their Alkaline Oxygen Reduction Reaction Catalytic Activity. *J. Colloid Interface Sci.* **2022**, *627*, 168–179.

(50) Plank, N. O. V.; Cheung, R. Functionalisation of Carbon Nanotubes for Molecular Electronics. *Microelectron. Eng.* **2004**, *73–74*, 578–582.

(51) Adamska, M.; Narkiewicz, U. Fluorination of Carbon Nanotubes − A Review. *J. Fluor. Chem.* **2017**, *200*, 179–189.

(52) Khabashesku, V. N.; Billups, W. E.; Margrave, J. L. Fluorination of Single-Wall Carbon Nanotubes and Subsequent Derivatization Reactions. *Acc. Chem. Res.* **2002**, *35* (12), 1087–1095.

(53) Erbahar, D.; Berber, S. Chlorination of Carbon Nanotubes. *Phys. Rev. B* **2012**, *85* (8), 085426.

(54) Oliveira, L.; Lu, F.; Andrews, L.; Takacs, G. A.; Mehan, M.; Debies, T. UV Photo-Chlorination and -Bromination of Single-Walled Carbon Nanotubes. *J. Mater. Res.* **2014**, *29* (2), 239–246.

(55) Zarska, S.; Kulawik, D.; Drabowicz, J.; Ciesielski, W. A Review of Procedures of Purification and Chemical Modification of Carbon Nanotubes with Bromine. *Fuller. Nanotub. Carbon Nanostruct.* **2017**, *25* (10), 563–569.

(56) Khalil, Rana. M. A.; Hussain, F.; Imran, M.; Rana, A. M.; Murtaza, G. Ab Initio Study of the Exo-Hydrogenated Single Wall Carbon Nanotubes. *Phys. B: Condens.* **2019**, *552*, 124–129.

(57) Pekker, S.; Salvetat, J.-P.; Jakab, E.; Bonard, J.-M.; Forró, L. Hydrogenation of Carbon Nanotubes and Graphite in Liquid Ammonia. *J. Phys. Chem. B* **2001**, *105* (33), 7938–7943.

(58) Khare, B. N.; Meyyappan, M.; Cassell, A. M.; Nguyen, C. V.; Han, J. Functionalization of Carbon Nanotubes Using Atomic Hydrogen from a Glow Discharge. *Nano Lett.* **2002**, *2* (1), 73–77.

(59) Nikitin, A.; Li, X.; Zhang, Z.; Ogasawara, H.; Dai, H.; Nilsson, A. Hydrogen Storage in Carbon Nanotubes through the Formation of Stable C−H Bonds. *Nano Lett.* **2008**, *8* (1), 162–167.

(60) Coleman, K. S.; Bailey, S. R.; Fogden, S.; Green, M. L. H. Functionalization of Single-Walled Carbon Nanotubes via the Bingel Reaction. *J. Am. Chem. Soc.* **2003**, *125* (29), 8722–8723.

(61) Desmecht, A.; Sheet, D.; Poleunis, C.; Hermans, S.; Riant, O. Covalent Grafting of BPin Functions on Carbon Nanotubes and Chan-Lam-Evans Post-Functionalization. *Chem.-Eur. J.* **2019**, *25* (6), 1436–1440.

(62) Tagmatarchis, N.; Georgakilas, V.; Prato, M.; Shinohara, H. Sidewall Functionalization of Single-Walled Carbon Nanotubes through Electrophilic Addition. *Chem. Commun.* **2002**, 18, 2010–2011.

(63) Yosipof, A.; Basch, H.; Hoz, S. Nucleophilic and Electrophilic Reactions of Polyynes Catalyzed by an Electric Field: Toward Barcoding of Carbon Nanotubes Like Long Homogeneous Substrates. *J. Phys. Chem. A* **2013**, *117* (24), 5023–5027.

(64) Yumura, T.; Kertesz, M. Cooperative Behaviors in Carbene Additions through Local Modifications of Nanotube Surfaces. *Chem. Mater.* **2007**, *19* (5), 1028–1034.

(65) Luksirikul, P.; Ballesteros, B.; Tobias, G.; Moloney, M. G.; Green, M. L. H. Sidewall Functionalisation of Carbon Nanotubes by Addition of Diarylcarbene Derivatives. *J. Mater. Chem.* **2011**, *21* (47), 19080–19085.

(66) Holzinger, M.; Abraham, J.; Whelan, P.; Graupner, R.; Ley, L.; Hennrich, F.; Kappes, M.; Hirsch, A. Functionalization of Single-Walled Carbon Nanotubes with (R-)Oxycarbonyl Nitrenes. *J. Am. Chem. Soc.* **2003**, *125* (28), 8566–8580.

(67) Maggini, M.; Scorrano, G.; Prato, M. Addition of Azomethine Ylides to C60: Synthesis, Characterization, and Functionalization of Fullerene Pyrrolidines. *J. Am. Chem. Soc.* **1993**, *115* (21), 9798–9799.

(68) Rabti, A.; Raouafi, N.; Merkoçi, A. Bio(Sensing) Devices Based on Ferrocene–Functionalized Graphene and Carbon Nanotubes. *Carbon* **2016**, *108*, 481–514.

(69) Polyakov, M. S.; Ivanova, V. N.; Basova, T. V.; Saraev, A. A.; Köksoy, B.; Şenocak, A.; Demirbaş, E.; Durmuş, M. 3D, Covalent and Noncovalent Hybrid Materials Based on 3-Phenylcoumarin Derivatives and Single Walled Carbon Nanotubes as Gas Sensing Layers. *Appl. Surf. Sci.* **2020**, *504*, 144276.

(70) Li, Y.; Osuna, S.; Garcia-Borras, M.; Qi, X.; Liu, S.; Houk, K. N.; Lan, Y. Reactivity of Single-Walled Carbon Nanotubes in the Diels-Alder Cycloaddition Reaction: Distortion-Interaction Analysis along the Reaction Pathway. *Chem. Eur. J.* **2016**, *22* (36), 12819–12824.

(71) Martínez, J. P.; Langa, F.; Bickelhaupt, F. M.; Osuna, S.; Solà, M. (4 + 2) and (2 + 2) Cycloadditions of Benzyne to C60 and Zig-Zag Single-Walled Carbon Nanotubes: The Effect of the Curvature. *J. Phys. Chem. C* **2016**, *120* (3), 1716–1726.

(72) Brozena, A. H.; Kim, M.; Powell, L. R.; Wang, Y. Controlling the Optical Properties of Carbon Nanotubes with Organic Colour-Centre Quantum Defects. *Nat Rev Chem* **2019**, *3* (6), 375–392.

(73) Zaumseil, J. Luminescent Defects in Single-Walled Carbon Nanotubes for Applications. *Adv. Opt. Mater.* **2022**, *10* (2), 2101576.

(74) Piao, Y.; Meany, B.; Powell, L. R.; Valley, N.; Kwon, H.; Schatz, G. C.; Wang, Y. Brightening of Carbon Nanotube Photoluminescence through the Incorporation of Sp3 Defects. *Nat. Chem.* **2013**, *5* (10), 840–845.

(75) Berger, F. J.; Lüttgens, J.; Nowack, T.; Kutsch, T.; Lindenthal, S.; Kistner, L.; Müller, C. C.; Bongartz, L. M.; Lumsargis, V. A.; Zakharko, Y.; Zaumseil, J. Brightening of Long, Polymer-Wrapped Carbon Nanotubes by Sp3 Functionalization in Organic Solvents. *ACS Nano* **2019**, *13* (8), 9259–9269.

(76) Kim, M.; Chen, C.; Wang, P.; Mulvey, J. J.; Yang, Y.; Wun, C.; Antman-Passig, M.; Luo, H.-B.; Cho, S.; Long-Roche, K.; Ramanathan, L. V.; Jagota, A.; Zheng, M.; Wang, Y.; Heller, D. A. Detection of Ovarian Cancer via the Spectral Fingerprinting of Quantum-Defect-Modified Carbon Nanotubes in Serum by Machine Learning. *Nat. Biomed. Eng.* **2022**, *6* (3), 267–275.

(77) Fagan, J. A.; Hároz, E. H.; Ihly, R.; Gui, H.; Blackburn, J. L.; Simpson, J. R.; Lam, S.; Hight Walker, A. R.; Doorn, S. K.; Zheng, M. Isolation of >1 Nm Diameter Single-Wall Carbon Nanotube Species Using Aqueous Two-Phase Extraction. *ACS Nano* **2015**, *9* (5), 5377–5390.

(78) Subbaiyan, N. K.; Cambré, S.; Parra-Vasquez, A. N. G.; Hároz, E. H.; Doorn, S. K.; Duque, J. G. Role of Surfactants and Salt in Aqueous Two-Phase Separation of Carbon Nanotubes toward Simple Chirality Isolation. *ACS Nano* **2014**, *8* (2), 1619–1628.

(79) Defillet, J.; Avramenko, M.; Martinati, M.; López Carrillo, M. Á.; Van der Elst, D.; Wenseleers, W.; Cambré, S. The Role of the Bile Salt Surfactant Sodium Deoxycholate in Aqueous Two-Phase Separation of Single-Wall Carbon Nanotubes Revealed by Systematic Parameter Variations. *Carbon* **2022**, *195*, 349–363.

(80) Park, M.; Choi, I.-S.; Ju, S.-Y. Quantification and Removal of Carbonaceous Impurities in a Surfactant-Assisted Carbon Nanotube Dispersion and Its Implication on Electronic Properties. *Nanoscale Adv.* **2022**, *4* (17), 3537–3548.

(81) Kharlamova, M. V.; Kramberger, C. Phemenology of Filling, Investigation of Growth Kinetics and Electronic Properties for Applications of Filled Single-Walled Carbon Nanotubes. *Nanomater.* **2023**, *13* (2), 314.

(82) Cadena, A.; Botka, B.; Kamarás, K. Organic Molecules Encapsulated in Single-Walled Carbon Nanotubes. *Oxf. Open Mater. Sci.* **2021**, *1* (1), itab009.

(83) Chen, R. J.; Zhang, Y.; Wang, D.; Dai, H. Noncovalent Sidewall Functionalization of Single-Walled Carbon Nanotubes for Protein Immobilization. *J. Am. Chem. Soc.* **2001**, *123* (16), 3838–3839.

(84) Nakashima, N.; Tomonari, Y.; Murakami, H. Water-Soluble Single-Walled Carbon Nanotubes via Noncovalent Sidewall-Functionalization with a Pyrene-Carrying Ammonium Ion. *Chem. Lett.* **2002**, *31* (6), 638–639.

(85) Garrido, M.; Volland, M. K.; Münich, P. W.; Rodríguez-Pérez, L.; Calbo, J.; Ortí, E.; Herranz, M. Á.; Martín, N.; Guldi, D. M. Mono- and Tripodal Porphyrins: Investigation on the Influence of the Number of Pyrene Anchors in Carbon Nanotube and Graphene Hybrids. *J. Am. Chem. Soc.* **2020**, *142* (4), 1895–1903.

(86) Juan, A. de; López-Moreno, A.; Calbo, J.; Ortí, E.; Pérez, E. M. Determination of Association Constants towards Carbon Nanotubes. *Chem. Sci.* **2015**, *6* (12), 7008–7014.

(87) López-Moreno, A.; Jiang, Y.; Cheng, G.; Komatsu, N. Extraction of Carbon Nanotubes with Porphyrin- and Pyrene-Based Nanotweezers and Nanocalipers: Insight from the Association Constants. *J. Porphyrins Phthalocyanines* **2020**, *24* (01n03), 314–319.

(88) Hu, L.; Zhao, Y.-L.; Ryu, K.; Zhou, C.; Stoddart, J. F.; Grüner, G. Light-Induced Charge Transfer in Pyrene/CdSe-SWNT Hybrids. *Adv. Mater.* **2008**, *20* (5), 939–946.

(89) D'Souza, F.; Das, S. K.; Zandler, M. E.; Sandanayaka, A. S. D.; Ito, O. Bionano Donor–Acceptor Hybrids of Porphyrin, ssDNA, and Semiconductive Single-Wall Carbon Nanotubes for Electron Transfer via Porphyrin Excitation. *J. Am. Chem. Soc.* **2011**, *133* (49), 19922–19930.

(90) Wang, Y.; Hu, N.; Zhou, Z.; Xu, D.; Wang, Z.; Yang, Z.; Wei, H.; Kong, E. S.-W.; Zhang, Y. Single-Walled Carbon Nanotube/Cobalt Phthalocyanine Derivative Hybrid Material: Preparation, Characterization and Its Gas Sensing Properties. *J. Mater. Chem.* **2011**, *21* (11), 3779–3787.

(91) Holzinger, M.; Baur, J.; Haddad, R.; Wang, X.; Cosnier, S. Multiple Functionalization of Single-Walled Carbon Nanotubes by Dip Coating. *Chem. Commun.* **2011**, *47* (8), 2450–2452.

(92) Fatemi, S. M.; Foroutan, M. Recent Developments Concerning the Dispersion of Carbon Nanotubes in Surfactant/Polymer Systems by MD Simulation. *J. Nanostruct. Chem.* **2016**, *6* (1), 29–40.

(93) Gillen, A. J.; Boghossian, A. A. Non-Covalent Methods of Engineering Optical Sensors Based on Single-Walled Carbon Nanotubes. *Front. Chem.* **2019**, *7* (612).

(94) Bergler, F. F.; Stahl, S.; Goy, A.; Schöppler, F.; Hertel, T. Substrate-Mediated Cooperative Adsorption of Sodium Cholate on (6,5) Single-Wall Carbon Nanotubes. *Langmuir* **2016**, *32* (37), 9598–9603.

(95) Zhang, X.; Song, K.; Liu, J.; Zhang, Z.; Wang, C.; Li, H. Sorption of Triclosan by Carbon Nanotubes in Dispersion: The Importance of Dispersing Properties Using Different Surfactants. *Colloids Surf. A: Physicochem. Eng.* **2019**, *562*, 280–288.

(96) Kato, H.; Nakamura, A.; Horie, M. Behavior of Surfactants in Aqueous Dispersions of Single-Walled Carbon Nanotubes. *RSC Adv.* **2014**, *4* (5), 2129–2136.

(97) Liu, L.; Wei, X.; Yao, Z.; Li, X.; Wang, W.; Wang, Y.; Zhou, W.; Xiong, F.; Kataura, H.; Xie, S.; Liu, H. Separation of Metallic and Semiconducting Single-Wall Carbon Nanotubes Using Sodium Hyodeoxycholate Surfactant. *J. Phys. Chem. C* **2022**, *126* (7), 3787–3795.

(98) Islam, M. F.; Rojas, E.; Bergey, D. M.; Johnson, A. T.; Yodh, A. G. High Weight Fraction Surfactant Solubilization of Single-Wall Carbon Nanotubes in Water. *Nano Lett.* **2003**, *3* (2), 269–273.

(99) Blanch, A. J.; Lenehan, C. E.; Quinton, J. S. Optimizing Surfactant Concentrations for Dispersion of Single-Walled Carbon Nanotubes in Aqueous Solution. *J. Phys. Chem. B* **2010**, *114* (30), 9805–9811.

(100) Bilalis, P.; Katsigiannopoulos, D.; Avgeropoulos, A.; Sakellariou, G. Non-Covalent Functionalization of Carbon Nanotubes with Polymers. *RSC Adv.* **2013**, *4* (6), 2911–2934.

(101) Stranks, S. D.; Habisreutinger, S. N.; Dirks, B.; Nicholas, R. J. Novel Carbon Nanotube-Conjugated Polymer Nanohybrids Produced by Multiple Polymer Processing. *Adv. Mater.* **2013**, *25* (31), 4365–4371.

(102) Izard, N.; Kazaoui, S.; Hata, K.; Okazaki, T.; Saito, T.; Iijima, S.; Minami, N. Semiconductor-Enriched Single Wall Carbon Nanotube Networks Applied to Field Effect Transistors. *Appl. Phys. Lett.* **2008**, *92* (24), 243112.

(103) Bisri, S. Z.; Gao, J.; Derenskyi, V.; Gomulya, W.; Iezhokin, I.; Gordiichuk, P.; Herrmann, A.; Loi, M. A. High Performance Ambipolar Field-Effect Transistor of Random Network Carbon Nanotubes. *Adv. Mater.* **2012**, *24* (46), 6147–6152.

(104) Namasivayam, M.; Andersson, M. R.; Shapter, J. G. A Comparative Study on the Role of Polyvinylpyrrolidone Molecular Weight on the Functionalization of Various Carbon Nanotubes and Their Composites. *Polym.* **2021**, *13* (15), 2447.

(105) Heimfarth, D.; Balcı Leinen, M.; Klein, P.; Allard, S.; Scherf, U.; Zaumseil, J. Enhancing Electrochemical Transistors Based on Polymer-Wrapped (6,5) Carbon Nanotube Networks with Ethylene Glycol Side Chains. *ACS Appl. Mater. Interfaces* **2022**, *14* (6), 8209–8217.

(106) Wang, J.; Lei, T. Separation of Semiconducting Carbon Nanotubes Using Conjugated Polymer Wrapping. *Polym.* **2020**, *12* (7), 1548.

(107) Chik, M. W.; Hussain, Z.; Zulkefeli, M.; Tripathy, M.; Kumar, S.; Majeed, A. B. A.; Byrappa, K. Polymer-Wrapped Single-Walled Carbon Nanotubes: A Transformation toward Better Applications in Healthcare. *Drug Deliv. Transl. Res.* **2019**, *9* (2), 578–594.

(108) Lei, T.; Pochorovski, I.; Bao, Z. Separation of Semiconducting Carbon Nanotubes for Flexible and Stretchable Electronics Using Polymer Removable Method. *Acc. Chem. Res.* **2017**, *50* (4), 1096–1104.

(109) Samanta, S. K.; Fritsch, M.; Scherf, U.; Gomulya, W.; Bisri, S. Z.; Loi, M. A. Conjugated Polymer-Assisted Dispersion of Single-Wall Carbon

Nanotubes: The Power of Polymer Wrapping. *Acc. Chem. Res.* **2014**, *47* (8), 2446–2456.

(110) Fujigaya, T.; Nakashima, N. Non-Covalent Polymer Wrapping of Carbon Nanotubes and the Role of Wrapped Polymers as Functional Dispersants. *Sci. Technol. Adv. Mater.* **2015**, *16* (2), 024802.

(111) Cao, X. T.; Patil, M. P.; Phan, Q. T.; Le, C. M. Q.; Ahn, B.-H.; Kim, G.-D.; Lim, K. T. Green and Direct Functionalization of Poly (Ethylene Glycol) Grafted Polymers onto Single Walled Carbon Nanotubes: Effective Nanocarrier for Doxorubicin Delivery. *J. Ind. Eng. Chem.* **2020**, *83*, 173–180.

(112) Gan, D.; Liu, M.; Huang, H.; Chen, J.; Dou, J.; Wen, Y.; Huang, Q.; Yang, Z.; Zhang, X.; Wei, Y. Facile Preparation of Functionalized Carbon Nanotubes with Tannins through Mussel-Inspired Chemistry and Their Application in Removal of Methylene Blue. *J. Mol. Liq.* **2018**, *271*, 246–253.

(113) Stoddart, J. F. Mechanically Interlocked Molecules (MIMs)—Molecular Shuttles, Switches, and Machines (Nobel Lecture). *Angew. Chem. Int. Ed* **2017**, *56* (37), 11094–11125.

(114) de Juan, A.; Pouillon, Y.; Ruiz-González, L.; Torres-Pardo, A.; Casado, S.; Martín, N.; Rubio, Á.; Pérez, E. M. Mechanically Interlocked Single-Wall Carbon Nanotubes. *Angew. Chem. Int. Ed* **2014**, *53* (21), 5394–5400.

(115) Canevet, D.; Gallego, M.; Isla, H.; de Juan, A.; Pérez, E. M.; Martín, N. Macrocyclic Hosts for Fullerenes: Extreme Changes in Binding Abilities with Small Structural Variations. *J. Am. Chem. Soc.* **2011**, *133* (9), 3184–3190.

(116) Isla, H.; Gallego, M.; Pérez, E. M.; Viruela, R.; Ortí, E.; Martín, N. A Bis-exTTF Macrocyclic Receptor That Associates C60 with Micromolar Affinity. *J. Am. Chem. Soc.* **2010**, *132* (6), 1772–1773.

(117) Romero-Nieto, C.; García, R.; Herranz, M. Á.; Ehli, C.; Ruppert, M.; Hirsch, A.; Guldi, D. M.; Martín, N. Tetrathiafulvalene-Based Nanotweezers—Noncovalent Binding of Carbon Nanotubes in Aqueous Media with Charge Transfer Implications. *J. Am. Chem. Soc.* **2012**, *134* (22), 9183–9192.

(118) de Juan, A.; Mar Bernal, M.; Pérez, E. M. Optimization and Insights into the Mechanism of Formation of Mechanically Interlocked Derivatives of Single-Walled Carbon Nanotubes. *ChemPlusChem* **2015**, *80* (7), 1153–1157.

(119) Pérez, E. M. Putting Rings around Carbon Nanotubes. *Chem. Eur. J.* **2017**, *23* (52), 12681–12689.

(120) López-Moreno, A.; Pérez, E. M. Pyrene-Based Mechanically Interlocked SWNTs. *Chem. Commun.* **2015**, *51* (25), 5421–5424.

(121) Martínez-Periñán, E.; Juan, A. de; Pouillon, Y.; Schierl, C.; Strauss, V.; Martín, N.; Rubio, Á.; Guldi, D. M.; Lorenzo, E.; Pérez, E. M. The Mechanical Bond on Carbon Nanotubes: Diameter-Selective

Functionalization and Effects on Physical Properties. *Nanoscale* **2016**, *8* (17), 9254–9264.

(122) Leret, S.; Pouillon, Y.; Casado, S.; Navío, C.; Rubio, Á.; Pérez, E. M. Bimodal Supramolecular Functionalization of Carbon Nanotubes Triggered by Covalent Bond Formation. *Chem. Sci.* **2017**, *8* (3), 1927–1935.

(123) Blanco, M.; Nieto-Ortega, B.; de Juan, A.; Vera-Hidalgo, M.; López-Moreno, A.; Casado, S.; González, L. R.; Sawada, H.; González-Calbet, J. M.; Pérez, E. M. Positive and Negative Regulation of Carbon Nanotube Catalysts through Encapsulation within Macrocycles. *Nat. Commun.* **2018**, *9* (1), 2671.

(124) de Juan-Fernández, L.; Münich, P. W.; Puthiyedath, A.; Nieto-Ortega, B.; Casado, S.; Ruiz-González, L.; Pérez, E. M.; Guldi, D. M. Interfacing Porphyrins and Carbon Nanotubes through Mechanical Links. *Chem. Sci.* **2018**, *9* (33), 6779–6784.

(125) Zhang, W.; Guillén-Soler, M.; Silva, S. M.-D.; López-Moreno, A.; González, L. R.; Giménez-López, M. del C.; Pérez, E. M. Mechanical Interlocking of SWNTs with N-Rich Macrocycles for Efficient ORR Electrocatalysis. *Chem. Sci.* **2022**, *13* (33), 9706–9712.

(126) Villalva, J.; Nieto-Ortega, B.; Melle-Franco, M.; Pérez, E. M. Quasi-Barrierless Submolecular Motion in Mechanically Interlocked Carbon Nanotubes. *J. Phys. Chem. C* **2020**, *124* (28), 15541–15546.

(127) Chamorro, R.; Juan-Fernández, L. de; Nieto-Ortega, B.; Mayoral, M. J.; Casado, S.; Ruiz-González, L.; Pérez, E. M.; González-Rodríguez, D. Reversible Dispersion and Release of Carbon Nanotubes via Cooperative Clamping Interactions with Hydrogen-Bonded Nanorings. *Chem. Sci.* **2018**, *9* (17), 4176–4184.

(128) Miki, K.; Saiki, K.; Umeyama, T.; Baek, J.; Noda, T.; Imahori, H.; Sato, Y.; Suenaga, K.; Ohe, K. Unique Tube–Ring Interactions: Complexation of Single-Walled Carbon Nanotubes with Cycloparaphenyleneacetylenes. *Small* **2018**, *14* (26), 1800720.

(129) Balakrishna, B.; Menon, A.; Cao, K.; Gsänger, S.; Beil, S. B.; Villalva, J.; Shyshov, O.; Martin, O.; Hirsch, A.; Meyer, B.; Kaiser, U.; Guldi, D. M.; von Delius, M. Dynamic Covalent Formation of Concave Disulfide Macrocycles Mechanically Interlocked with Single-Walled Carbon Nanotubes. *Angew. Chem. Int. Ed* **2020**, *59* (42), 18774–18785.

(130) López-Moreno, A.; Ibáñez, S.; Moreno-Da Silva, S.; Ruiz-González, L.; Sabanés, N. M.; Peris, E.; Pérez, E. M. Single-Walled Carbon Nanotubes Encapsulated within Metallacycles. *Angew. Chem. Int. Ed* **2022**, *61* (35), e202208189.

(131) Cheng, G.; Hayashi, T.; Miyake, Y.; Sato, T.; Tabata, H.; Katayama, M.; Komatsu, N. Interlocking of Single-Walled Carbon Nanotubes with Metal-Tethered Tetragonal Nanobrackets to Enrich a Few Hundredths of a Nanometer Range in Their Diameters. *ACS Nano* **2022**, *16* (8), 12500–12510.

(132) López-Moreno, A.; Nieto-Ortega, B.; Moffa, M.; de Juan, A.; Bernal, M. M.; Fernández-Blázquez, J. P.; Vilatela, J. J.; Pisignano, D.; Pérez, E. M. Threading through Macrocycles Enhances the Performance of Carbon Nanotubes as Polymer Fillers. *ACS Nano* **2016**, *10* (8), 8012–8018.

(133) Wielend, D.; Vera-Hidalgo, M.; Seelajaroen, H.; Sariciftci, N. S.; Pérez, E. M.; Whang, D. R. Mechanically Interlocked Carbon Nanotubes as a Stable Electrocatalytic Platform for Oxygen Reduction. *ACS Appl. Mater. Interfaces* **2020**, *12* (29), 32615–32621.

Chapter 2

Enthalpy vs Entropy in the Supramolecular Association of SWNTs by U-shaped Molecules

Supramolecular functionalization of carbon nanotubes involves the non-covalent attachment of molecular species to the surface of CNTs through van der Waals forces or π-π interactions (among others). Therefore, it is important to choose a suitable molecule to achieve the best interaction. We have studied the non-covalent functionalization of SWNTs with six different organic species at various temperatures. The experiments showed that the molecules with higher flexibility and aromaticity have the higher values of the association constants, as well as an increase of the entropy of the system after the association. Furthermore, this modification is independent of the temperature. To support the experimental data, computational measurements proved the high flexibility of the guest, exhibiting them in three different conformations, embraced to the carbon nanotube, unfolded and semi-folded. There was also evidence of the importance of the alkyl chains for the success of the association.

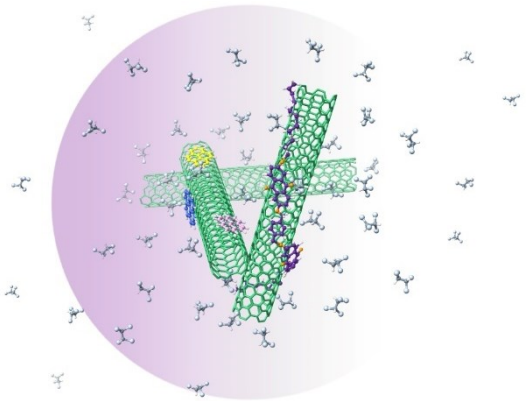

2.1. INTRODUCTION

Since their discovery, single-walled carbon nanotubes (SWNTs) have been chemically modified to improve their solubility and to tune their properties for being used in different potential applications. The mechanical bond is a one-off methodology used to connect two or more component parts in a way that they cannot be separated without breaking chemical bonds between atoms. With this in mind, we described the synthesis of mechanically interlocked carbon nanotubes (MINTs).[1] MINTs are rotaxane-like species where SWNTs are encapsulated within organic macrocycles. They show remarkable stability compared to covalently modified nanotubes maintaining the native structure of the SWNTs. We relied on a clipping strategy wherein carbon nanotubes act as a template for a ring-closing metathesis (RCM) of linear molecules with two SWNT-recognition motives in a such way that they associate supramolecularly. MINTs could be used for many applications such as fillers in polymer-MINT composites,[2] catalysts,[3–5] or as molecular spintronics and molecular spin qubits.[6]

To determine the driven energies which lead the association, it has been necessary to know the association constants between binding soluble molecules and insoluble carbon nanotubes. The diverse structure of the carbon nanotubes and their characteristic insolubility block the determination of the molar concentration of SWNTs in solution and therefore the majority of publications on supramolecular chemistry of carbon nanotubes use approximation or do not report quantitative data. In 2015, we described a simple procedure for the quantitative determination of association constants of supramolecular systems based on titration experiments using thermogravimetric analysis.[7] We reported binding constants between different hosts and several types of SWNTs in four solvents in a range of $1–10^4$

[1] de Juan, A.; Pouillon, Y.; Ruiz-González, L.; Torres-Pardo, A.; Casado, S.; Martín, N.; Rubio, Á.; Pérez, E. M. *Angew. Chem. Int. Ed.* **2014**, *53* (21), 5394–5400.

[2] López-Moreno, A.; Nieto-Ortega, B.; Moffa, M.; de Juan, A.; Bernal, M. M.; Fernández-Blázquez, J. P.; Vilatela, J. J.; Pisignano, D.; Pérez, E. M. *ACS Nano* **2016**, *10* (8), 8012–8018.

[3] Blanco, M.; Nieto-Ortega, B.; de Juan, A.; Vera-Hidalgo, M.; López-Moreno, A.; Casado, S.; González, L. R.; Sawada, H.; González-Calbet, J. M.; Pérez, E. M. *Nat. Commun.* **2018**, *9* (1), 2671.

[4] Wielend, D.; Vera-Hidalgo, M.; Seelajaroen, H.; Sariciftci, N. S.; Pérez, E. M.; Whang, D. R. *ACS Appl. Mater. Interfaces* **2020**, *12* (29), 32615–32621.

[5] Zhang, W.; Guillén-Soler, M.; Silva, S. M.-D.; López-Moreno, A.; González, L. R.; Giménez-López, *Chem. Sci.* **2022**, *13* (33), 9706–9712.

[6] Moreno-Da Silva, S.; Martínez, J. I.; Develioglu, A.; Nieto-Ortega, B.; de Juan-Fernández, L.; Ruiz-Gonzalez, L.; Picón, A.; Oberli, S.; Alonso, P. J.; Moonshiram, D.; Pérez, E. M.; Burzurí, E. *J. Am. Chem. Soc.* **2021**, *143* (50), 21286–21293.

[7] Juan, A. de; López-Moreno, A.; Calbo, J.; Ortí, E.; Pérez, E. M. *Chem. Sci.* **2015**, *6* (12), 7008–7014.

M^{-1}. The results obtained experimentally were validated through state-of-the-art DFT calculations. In 2017, we studied the association to SWNTs of a set of pyrene derivatives with different surface area and electronic properties, in different solvents and we performed both DFT and MD calculations, demonstrating that solvophobic interactions govern the self-assembly of small molecules with SWNTs.[8]

In our previous studies we have synthesized MINTs using organic molecules that exhibit high affinity for SWNTs like pyrene,[9] π-extended derivatives of tetrathiafulvalene,[1] naphthalene diimides,[10] anthraquinone,[4] or porphyrins.[6,11] In order to verify if it is necessary to have recognition units with high affinity for SWNTs, in this work we have performed titration experiments towards organic molecules varying their degree of aromaticity at different temperatures. The association constants that lead the supramolecular equilibrium were measured, and the thermodynamics governing chemical association processes were also explored. Computational measurements were also done to complement the experimental data.

2.2. RESULTS AND DISCUSSION

The non-covalent functionalization (summarized in Figure 1) is dispersion-type interaction, and it can be conceptually split into three steps: 1. Desolvation of the binding partners. That is, the disruption of interactions between solvent, organic molecules and carbon nanotubes that translates into a favourable entropy of the system. 2. Association, i.e., conformational rearrangement of the binding partners and the solvent, and 3. Re-solvation. The formation of the non-covalent functionalization establishes hydrogen bonds, π-π stacking interactions, van der

---

[1] de Juan, A.; Pouillon, Y.; Ruiz-González, L.; Torres-Pardo, A.; Casado, S.; Martín, N.; Rubio, Á.; Pérez, E. M. *Angew. Chem. Int. Ed.* **2014**, *53* (21), 5394–5400.

[4] Wielend, D.; Vera-Hidalgo, M.; Seelajaroen, H.; Sariciftci, N. S.; Pérez, E. M.; Whang, D. R. *ACS Appl. Mater. Interfaces* **2020**, *12* (29), 32615–32621.

[6] Moreno-Da Silva, S.; Martínez, J. I.; Develioglu, A.; Nieto-Ortega, B.; de Juan-Fernández, L.; Ruiz-Gonzalez, L.; Picón, A.; Oberli, S.; Alonso, P. J.; Moonshiram, D.; Pérez, E. M.; Burzurí, E. *J. Am. Chem. Soc.* **2021**, *143* (50), 21286–21293.

[8] Calbo, J.; López-Moreno, A.; de Juan, A.; Comer, J.; Ortí, E.; Pérez, E. M. *Chem. Eur. J.* **2017**, *23* (52), 12909–12916.

[9] López-Moreno, A.; Pérez, E. M. *Chem. Commun.* **2015**, *51* (25), 5421–5424.

[10] Leret, S.; Pouillon, Y.; Casado, S.; Navío, C.; Rubio, Á.; Pérez, E. M. *Chem. Sci.* **2017**, *8* (3), 1927–1935.

[11] de Juan-Fernández, L.; Münich, P. W.; Puthiyedath, A.; Nieto-Ortega, B.; Casado, S.; Ruiz-González, L.; Pérez, E. M.; Guldi, D. M. *Chem. Sci.* **2018**, *9* (33), 6779–6784.

Waals and electrostatic interactions that imply favourable enthalpy and unfavourable entropy energies.

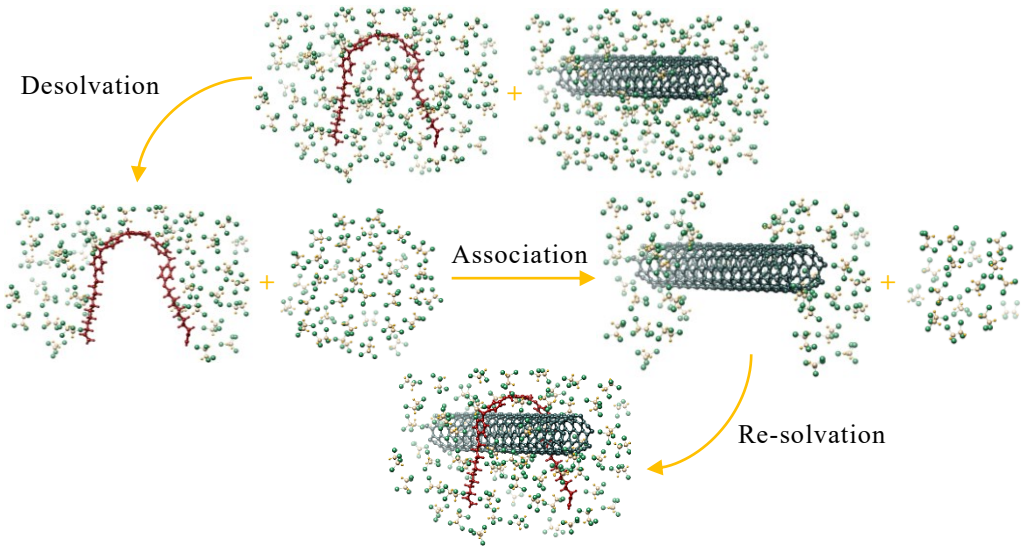

Figure 1. Association equilibrium scheme.

Pyrene has been widely used in supramolecular chemistry to introduce a variety of functionalities to carbon nanotubes via π-π stacking.[12] For this reason, we compare the association of SWNTs with pyrene and some derivatives against other organic molecules endowed with lower electron density. Figure 2 shows the chemical structure of the guests for SWNTs used in the present work.

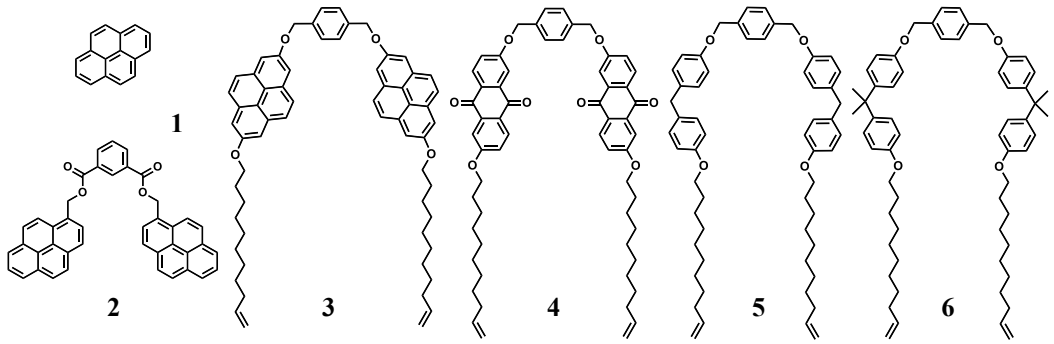

Figure 2. Organic molecules with different recognition units used in this work.

[12] Chen, R. J.; Zhang, Y.; Wang, D.; Dai, H. *J. Am. Chem. Soc.* **2001**, *123* (16), 3838–3839.

The experimental procedure can be summarized as follows: over a solution of known concentration of the organic molecules, carbon nanotubes (6,5-SWNTs, >95% purity, 0.78 nm in diameter, 1 $mgmL^{-1}$) were suspended and mixed for two hours at different temperatures, allowing to reach the equilibrium of the system. Then, the suspension was filtered through a 0.2 µm-pore polytetrafluorethylene (PTFE) membrane and the complex was analyzed by thermogravimetric analysis (N_2, $30ºC \cdot min^{-1}$). We measured the weight loss up to 600 ºC where all the associated hosts had been desorbed. Finally, the association constants were obtained by plotting the degree of functionalization against the concentration of free host using a standard 1:1 isotherm, assuming that maximum of functionalization is equivalent to saturation of the binding equilibrium:

$$\theta = \frac{S \cdot K_a \cdot [H]_{free}}{1 + K_a \cdot [H]_{free}}$$

where θ is the fraction of occupied binding sites, S is the maximum functionalization at saturation, K_a is the association constant, and $[H]_{free}$ is the concentration of free species.

The titration reactions were repeated for several initial concentrations of the guest molecules, ranging from zero to near saturation at four different temperatures. A blank experiment to determine the encapsulated or adsorbed solvent was run in all cases, and the data was subtracted. Figure 3 shows an example of the results for four guest molecules where each data point is the average of three separate experiments (see SI S4 for all experiments). The electron-rich conjugated compounds with alkyl chains showed the major association constants values proving that their affinity with the SWNTs is higher. The association constants of molecules **3** and **4** towards 6,5-SWNTs at room temperature are $K_a = 820 \pm 79\ M^{-1}$ and $K_a = 725 \pm 167\ M^{-1}$, respectively. However, these values are one order of magnitude smaller for molecules **2**, **5**, and **6** with $K_a = 63 \pm 12\ M^{-1}$, $K_a = 33 \pm 10\ M^{-1}$, and $K_a = 10 \pm 2\ M^{-1}$, respectively and two order of magnitude smaller for **1** , with $K_a = 7 \pm 4\ M^{-1}$ (Summary table with all calculated constants in SI S5). According to this, we can say that supramolecular experiments are very influenced by non-covalent intermolecular interactions. In line with the graphs, there is no influence of temperature when only the interactions of the molecules with the wall of the nanotubes are taken into account.

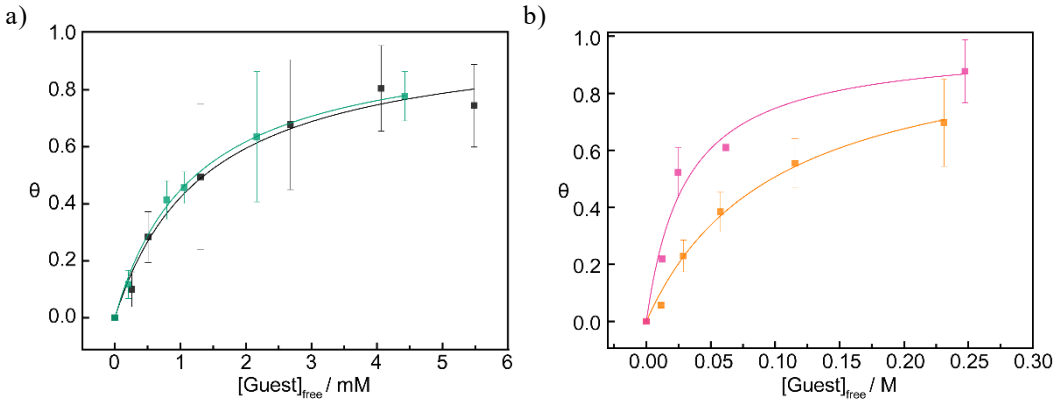

Figure 3. Titration experiments with 6,5-SWNTs (1 mg·mL^{-1}) in TCE at 298.15 K. a) Fitting with guest **3** (K_a = 820.01 ± 78.91 M^{-1}, r^2 = 0.996 - green) and guest **4** (K_a = 725.07 ± 166.59 M^{-1}, r^2 = 0.979 – black); b) Fitting with guest **5** (K_a = 32.93 ± 9.67 M^{-1}, r^2 = 0.962 – pink) and guest **6** (K_a = 10.03 ± 1.72 M^{-1}, r^2 = 0.991 – orange). The error bars represent the standard deviation.

The solubility at saturation (S_{max}) was calculated for each molecule at different temperatures to determine their relationship with the binding constant. As expected, these calculations showed that the higher the association constant, the lower the amount of molecule to reach saturation (Summary table with all S_{max} values are in SI S5). A linear relationship between log K_a and log S_{max} is observed in Figure 4. This proves that the contribution of the solvation enthalpy is predominant in these supramolecular systems, the solubility of the guests influences the association process. The organic molecule establishes better interactions with the SWNT compared to those with solvent.

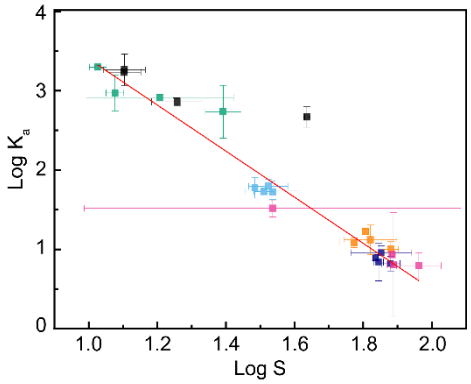

Figure 4. Logarithm of association constant vs logarithm of maximum solubility of guest molecules. Guest code: **1**-dark blue; **2**-light blue; **3**-green; **4**-black; **5**-pink; and **6**-orange.

Van´t Hoff equation has been used to analyze the variations in the thermodynamic functions. It studies the relation between the equilibrium constant (K_a) of chemical reactions and the temperature (T):

$$\ln(K_a) = -\frac{\Delta H^\circ}{R}\frac{1}{T} + \frac{\Delta S^\circ}{R}$$

where ΔH° and ΔS° are the standard enthalpy and entropy energies, and R is the gas constant (8.314 $J \cdot mol^{-1}K^{-1}$). The enthalpic component quantifies the change in heat associated with binding and reflects specific interactions (organic molecule - SWNT, organic molecule – solvent, and SWNT - solvent). The entropic component quantifies the change in the disorder of the overall system and reflects unspecific interactions (hydrophobicity, shape complementarity, and conformational flexibility). Figure 5 shows the plot of ln K_a versus the inverse of T, which allow us to estimate the change in enthalpy and entropy of a reaction.

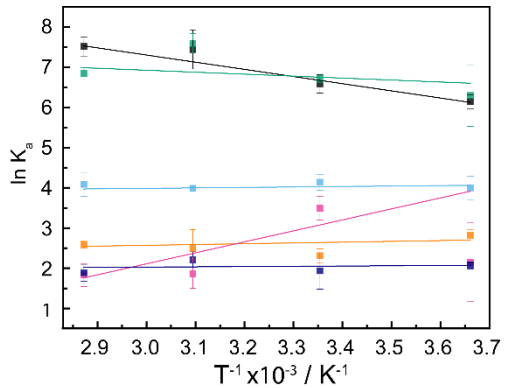

Figure 5. Plot of the natural logarithm of the association constant against the inverse of the temperature for guests **1** (dark blue), **2** (light blue), **3** (green), **4** (black), **5** (pink), and **6** (orange).

Free or binding energy (ΔG) of an equilibrium process can be used to predict the feasibility of a reaction. This function is temperature dependent and may be quantified by two approximations:

Considering the association constant value:

$$\Delta G = -RT \ln K_a$$

Considering the enthalpy and entropy energies:

$$\Delta G = \Delta H - T\Delta S$$

where R is the gas constant, T is the temperature, and ΔH plus ΔS are the enthalpy and entropy energies of the process.

Table 1 shows the thermodynamic functions summary of the supramolecular processes studied in this work. All the chemical processes studied are exergonic. Moreover, they are spontaneous reactions regardless of the temperature of the association. The enthalpy is the result of the host-guest formation in aqueous media. The association is endothermic for molecules **4** and **5** generating higher-energy products which are usually more reactive and, therefore less stable. This unfavourable energy change could be associated with the organic molecules conformational changes needed to their template over the nanotubes. Meanwhile, this process is exothermic and energetically favourable for molecules **1**, **2**, **5** and, **6**. On the other hand, entropy arises from the randomness of a system. A positive ΔS indicates a decrease in system order, and this is entropically favourable. Because of that, these reactions are more likely to occur. The entropy change tends to be affected by the solvent contribution as a result of the realignment of molecules.[13] In turn, solvation effects are the main factors contributing to ΔS in host-guest formation. It is then, it is positive for all guests except number **5**.

Table 1. Summary of the thermodynamic functions. ΔG_1 corresponds with the free energies obtained when approximation 1 was used. ΔG_2 matches with the Gibb´s energies calculated employing the approach number 2.

Guest n°	T / K	ΔG_1 ± error / J·mol^{-1}	ΔG_2 ± error / J·mol^{-1}	ΔH ± error / J·mol^{-1}	ΔS ± error / J·mol^{-1}
1	273.15	$(-4.68 \pm 0.20)10^3$	$(-4.68 \pm 3.29)10^3$	$(-0.70 \pm 2.46)10^3$	$(1.45 \pm 0.80)10^1$
	298.15	$(-4.79 \pm 1.12)10^3$	$(-5.04 \pm 3.42)10^3$		
	323.15	$(-5.93 \pm 0.53)10^3$	$(-5.40 \pm 3.56)10^3$		
	348.15	$(-5.46 \pm 0.61)10^3$	$(-5.77 \pm 3.71)10^3$		
2	273.15	$(-9.07 \pm 0.67)10^3$	$(-9.15 \pm 1.68)10^3$	$(-0.38 \pm 1.25)10^3$	$(3.49 \pm 0.41)10^1$
	298.15	$(-1.02 \pm 0.05)10^4$	$(-1.00 \pm 0.17)10^4$		
	323.15	$(-1.07 \pm 0.02)10^4$	$(-1.09 \pm 0.18)10^4$		
	348.15	$(-1.18 \pm 0.09)10^4$	$(-1.18 \pm 0.19)10^4$		
3	273.15	$(-1.43 \pm 0.17)10^4$	$(-1.46 \pm 0.96)10^4$	$(8.51 \pm 7.17)10^3$	$(8.46 \pm 2.34)10^1$
	298.15	$(-1.66 \pm 0.02)10^4$	$(-1.67 \pm 1.00)10^4$		
	323.15	$(-2.04 \pm 0.07)10^4$	$(-1.88 \pm 1.04)10^4$		
	348.15	$(-1.98 \pm 0.04)10^4$	$(-2.10 \pm 1.08)10^4$		
4	273.15	$(-1.39 \pm 0.04)10^4$	$(-1.39 \pm 0.39)10^4$	$(1.58 \pm 0.29)10^4$	$(1.09 \pm 0.09)10^2$
	298.15	$(-1.63 \pm 0.06)10^4$	$(-1.66 \pm 0.40)10^4$		
	323.15	$(-2.00 \pm 0.13)10^4$	$(-1.93 \pm 0.42)10^4$		
	348.15	$(-2.17 \pm 0.07)10^4$	$(-2.21 \pm 0.44)10^4$		
5	273.15	$(-4.88 \pm 2.22)10^3$	$(-0.61 \pm 1.68)10^4$	$(-0.74 \pm 1.26)10^4$	$(-0.46 \pm 4.09)10^1$
	298.15	$(-8.66 \pm 0.73)10^3$	$(-0.60 \pm 1.75)10^4$		

[13] Murphy, K. P.; Xie, D.; Thompson, K. S.; Amzel, L. M.; Freire, E. *Proteins* **1994**, *18* (1), 63–67.

	323.15	$(-5.00 \pm 0.98)10^3$	$(-0.59 \pm 1.82)10^4$	
	348.15	$(-5.30 \pm 0.82)10^3$	$(-0.58 \pm 1.90)10^4$	
6	273.15	$(-6.40 \pm 0.30)10^3$	$(-6.01 \pm 4.58)10^3$	$(-2.00 \pm 3.42)10^3$ $(1.47 \pm 1.11)10^1$
	298.15	$(-5.71 \pm 0.42)10^3$	$(-6.38 \pm 4.77)10^3$	
	323.15	$(-6.69 \pm 1.26)10^3$	$(-6.75 \pm 4.96)10^3$	
	348.15	$(-7.47 \pm 0.25)10^3$	$(-7.12 \pm 5.17)10^3$	

To support the experimental data collection, computational measurements were also performed. The supramolecular recognition properties of the six guest molecules **1-6**, whose structures are shown in Figure 2, towards the 6,5-SWNT has been studied through computational simulations to unveil the role of the different side chains in the formation of the mechanically interlocked derivatives of carbon nanotubes. Given the structural differences between the guests and the tendencies observed in their association constants, this study aims to understand the dominant non-covalent interactions for each supramolecular complex. As such, a special focus is given to the π-conjugation of the guests and their conformational flexibility, mainly for those with equally long alkyl chains (**3**, **4**, **5**, **6**), but also to the influence of the alkyl chains upon binding (when going from **2** to **3**), to the affinity of pyrene as a single guest (**1**) and in a larger system (**2** and **3**), to how it compares to another π-conjugated system, as anthraquinone (difference between **3** and **4**) and to whether the affinity is increased when a *u*-shaped molecule is formed with two pyrene rings (**2**).

First, the minimum energy structures of the supramolecular complexes formed by **1-6** and 6,5-SWNT were calculated in gas phase at the GFN2-xTB[14] level of theory using the xTB program[15] (Figure 6). From the structures, it can be concluded that the aromatic regions of the guests, including the pyrene, anthraquinone and benzene rings, are oriented almost in parallel to the surface of the nanotube to maximize the extent of the π–π interactions, with an average distance between them of 3.2 Å. Nonetheless, the influence of the alkyl chains on the coordination of the guests should not be neglected as they embrace the nanotube and form contacts at distances around 3.5 Å. The distances between the surface of the host and the O atoms vary from 3.2 to 3.4 Å, hence denoting strong interactions for all the guests **1-6** and the 6,5-SWNT.

[14] Bannwarth, C.; Ehlert, S.; Grimme, S. *J. Chem. Theory Comput.* **2019**, *15* (3), 1652–1671.
[15] Bannwarth, C.; Caldeweyher, E.; Ehlert, S.; Hansen, A.; Pracht, P.; Seibert, J.; Spicher, S.; Grimme, S. E. *Comput. Mol. Sci.* **2021**, *11* (2), e1493.

In order to estimate the magnitude of the interaction for a given MINT, the association energy E_a, the interaction energy E_i and the deformation energy E_d were computed at the GFN2-xTB level of theory for each guest as follows.

$$E_{a,n} = E_{N+n} - E_N - E_n$$

$$E_{i,n} = E_{N+n} - E_{N,di} - E_{n,di}$$

$$E_{d,n} = E_{a,n} - E_{i,n}$$

where E_{N+n}, E_N and E_n are the energies of the supramolecular complex (N+n), the 6,5-SWNT (N) and the guest molecule (n) corresponding to their minimum energy structures, while $E_{N,di}$ and $E_{n,di}$ correspond to those of the guest and the nanotube, respectively, at the minimum energy structure of the dimer.

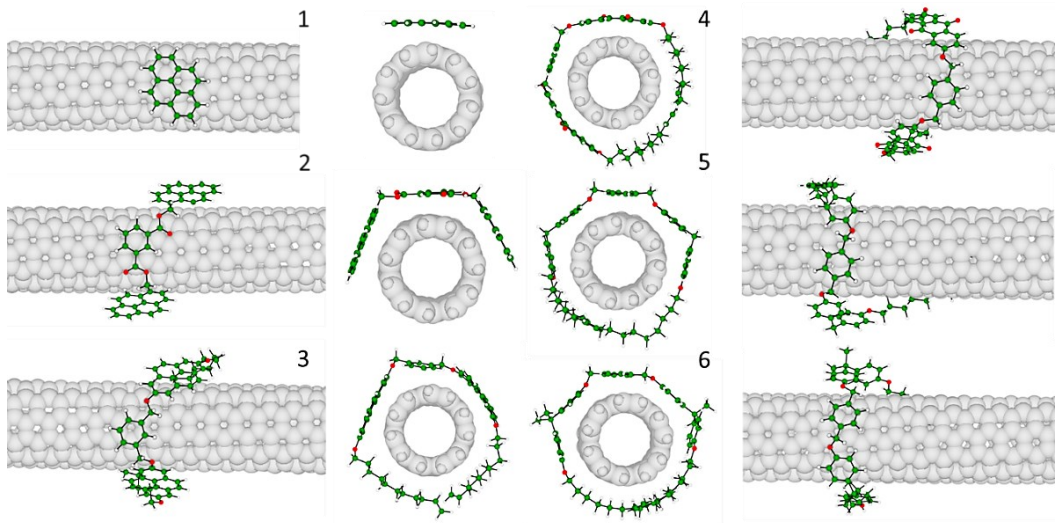

Figure 6. GFN2-Xtb-optimized structures calculated in vacuum for the MINTs formed between the guests **1-6** (shown as sticks and balls) and the 6,5-SWNT (shown as a gray van der Waals surface). Atom color coding: C (green), O (red), H (white).

The results listed in Table 2 indicate that the absolute values of the association and interaction energies become larger as the size of the conjugated regions that are available in the guest to stablish π–π interactions with the surface of the nanotube increases. Especially remarkable is the difference in the E_i calculated for **1** and the rest of guests, which is in all cases larger than 30 kcalmol^{-1}. The presence of long alkyl chains clearly contributes to a stronger interaction between the guests and the host, as it can be concluded when comparing the values computed for **2** and **3** are compared, but also by the similar values found for **3**-**6**. The extension of the aromatic moieties of guests **3**-**6** also plays a significant role in the association energies, as the energies obtained for **5** and **6**, with a broken π-conjugation, are

reduced by ca. 5 kcal mol^{-1} compared to **3** and **4**, with a larger π-conjugated system. From the values of the deformation energies, it can be concluded that pyrene is the most rigid backbone, since it undergoes almost no deformation in forming the supramolecular complex, and that the presence of long alkyl chains increases the flexibility of the molecules, which are significantly rearranged to interact with the 6,5-SWNT, compared to their minimum energy structures shown in Figure 7.

Table 2. Association (E_a), interaction (E_i) and deformation (E_d) energies (kcal mol^{-1}) calculated at the GFN2-xTB level of theory in vacuum for the supramolecular complexes formed by guests **1**-**6** and 6,5-SWNT.

	1	**2**	**3**	**4**	**5**	**6**
E_a	–20.0	–52.0	–61.1	–59.2	–55.8	–53.3
E_i	–20.3	–54.1	–71.8	–77.7	–70.7	–71.8
E_d	0.3	2.1	10.7	18.6	14.9	18.5

The association energies theoretically calculated are in good correlation with the association constants ($K_{a,n}$) determined experimentally. Theoretical calculations indicate that **3** and **4** are the guests with the strongest interaction with 6,5-SWNT, in agreement with the experimental results ($K_{a,\mathbf{3}}$ = 820 M^{-1} and $K_{a,\mathbf{4}}$ = 725 M^{-1}) due to the large extent of their π-conjugated region, followed by **2** ($K_{a,\mathbf{2}}$ = 63 M^{-1}), **5** ($K_{a,\mathbf{5}}$ = 33 M^{-1}) and **6** ($K_{a,\mathbf{6}}$ = 10 M^{-1}), with an association energy around –53 kcal mol^{-1}. The difference in both the values of the association constants and energies might be the result of the absence of the alkyl chains in the case of **2** and the breaking of the π-conjugation in the case of **5** and **6**, thus highlighting the importance of these two factors for a large affinity in the resulting supramolecular complexes. The subtle differences found between the experimental and the computational results concerning guests **2**, **5** and **6** could be due to the absence of solvent effects in the calculations, which may affect the relative position of the benzene rings of **5** and **6**, hence reducing the interaction with the nanotube. In the case of **1**, both the experimental result ($K_{a,1}$ = 7 M^{-1}) and the theoretical association and interaction energies predict the weakest interaction with the nanotube compared to the rest of guests.

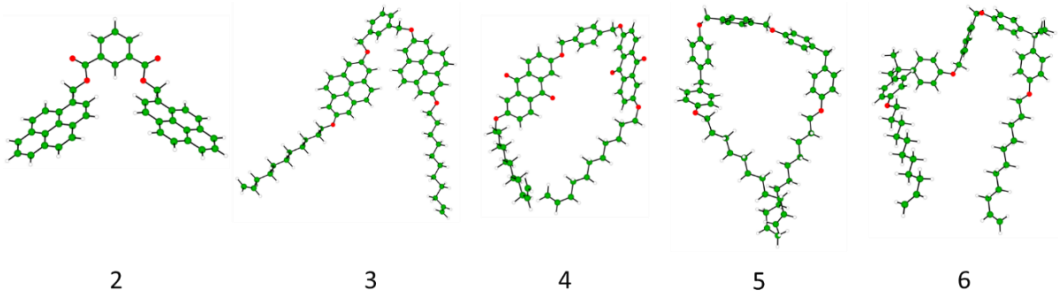

Figure 7. GFN2-xTB-optimized structures computed in vacuum for guests **2–6**. Atom color coding: C (green), O (red), H (white).

In order to validate the theoretical calculations at the cheap, semiempirical, yet accurate GFN2-xTB level of theory, the association energies of guests **1-6** were computed using *ab initio* Density Functional Theory [16](DFT) calculations with the B97D3 functional,[17–19] that includes D3 dispersion corrections,[19] and the Pople's 6-31G(d,p) basis set.[20] The calculations were performed using Gaussian-16.A.03.[21] As GFN2-xTB includes the D4 dispersion correction,[22] the DFT values were corrected by subtracting the effect of the D3 correction and including the former in the calculations. From the association energy values given in Table 3, it can be concluded that the GFN2-xTB methodology is accurate enough to evaluate the energies of the different conformations of the monomers and the supramolecular complexes as the absolute errors obtained for the association energy values when comparing with the DFT values are in all cases smaller than 5 kcal mol^{-1}, except for **4** (6.4 kcal mol^{-1}).

[16] Becke, A. D. *J. Chem. Phys.* **2014**, *140* (18), 18A301.
[17] Becke, A. D. *J. Chem. Phys.* **1997**, *107* (20), 8554–8560.
[18] Schmider, H. L.; Becke, A. D. *J. Appl. Phys.* **1998**, *108* (23), 9624–9631.
[19] Grimme, S.; Antony, J.; Ehrlich, S.; Krieg, H. *J. Chem. Phys.* **2010**, *132* (15), 154104.
[20] Rassolov, V. A.; Ratner, M. A.; Pople, J. A.; Redfern, P. C.; Curtiss, L. A. *J. Comp. Chem.* **2001**, *22* (9), 976–984.
[21] Gaussian 16, Revision A.03, Frisch, M. J.; Trucks, G. W.; Schlegel, H. B.; Scuseria, G. E.; Robb, M. A.; Cheeseman, J. R.; Scalmani, G.; Barone, V.; Petersson, G. A.; Nakatsuji, H.; Li, X.; Caricato, M.; Marenich, A. V.; Bloino, J.; Janesko, B. G.; Gomperts, R.; Mennucci, B.; Hratchian, H. P.; Ortiz, J. V.; Izmaylov, A. F.; Sonnenberg, J. L.; Williams-Young, D.; Ding, F.; Lipparini, F.; Egidi, F.; Goings, J.; Peng, B.; Petrone, A.; Henderson, T.; Ranasinghe, D.; Zakrzewski, V. G.; Gao, J.; Rega, N.; Zheng, G.; Liang, W.; Hada, M.; Ehara, M.; Toyota, K.; Fukuda, R.; Hasegawa, J.; Ishida, M.; Nakajima, T.; Honda, Y.; Kitao, O.; Nakai, H.; Vreven, T.; Throssell, K.; Montgomery, J. A., Jr.; Peralta, J. E.; Ogliaro, F.; Bearpark, M. J.; Heyd, J. J.; Brothers, E. N.; Kudin, K. N.; Staroverov, V. N.; Keith, T. A.; Kobayashi, R.; Normand, J.; Raghavachari, K.; Rendell, A. P.; Burant, J. C.; Iyengar, S. S.; Tomasi, J.; Cossi, M.; Millam, J. M.; Klene, M.; Adamo, C.; Cammi, R.; Ochterski, J. W.; Martin, R. L.; Morokum
[22] Caldeweyher, E.; Bannwarth, C.; Grimme, S. *J. Chem. Phys.* **2017**, *147* (3), 034112.

Table 3. Values of the association energies between guests **1-6** and 6,5-SWNT computed at the GFN2-xTB ($E_{a,xTB}$) and B97D4/6-31G(d,p) ($E_{a,DFT}$) levels of theory, and absolute error (Δ_{EA}) of GFN2-xTB values with respect to the DFT values, all in kcal mol^{-1}.

	1	**2**	**3**	**4**	**5**	**6**
$E_{a,xTB}$	–20.0	–52.0	–61.1	–59.2	–55.8	–53.3
$E_{a,DFT}$	–17.8	–47.5	–58.4	–52.7	–53.4	–50.1
Δ_{EA}	2.2	4.5	2.7	6.4	2.4	3.2

With the purpose of rationalizing the influence of the aromatic and aliphatic regions of guests **1-6** into their affinity for 6,5-SWNT, the GFN2-xTB interaction energies were evaluated for the different fragments of the molecules. The guests were decomposed into one (**1**), two (**2**) or three (**3-6**) molecular fragments, corresponding to their π-conjugated region (and the analogue in the case of **5** and **6**), the central benzene ring and the aliphatic chains, as is shown in Figure 8. The results of the interaction energies for each fragment of guests **1-6** are listed in Table 4. The largest interaction for all the guests arises from their aromatic region, due to π–π stacking interactions, with values that almost amount up to 50 kcal mol^{-1}, followed by interaction of the alkyl chains, with values around 25 kcal mol^{-1}, and the interaction of the central benzene ring, with a small contribution of about 9 kcal mol^{-1}, for guests **2-6**. However, significant differences are found between the guests for the aromatic regions. On the one hand, the differences between **2** and **3** when compared to **1** might be due to the presence of O atoms and alkyl groups in the former guests that clearly increase the interaction energy. On the other hand, the larger interaction energies for **3** and **4** compared to **5** and **6** showcases the importance of a larger, non-broken π-conjugated system for the formation of the supramolecular complex. The interaction energies calculated for pyrene (**3**) and anthraquinone (**4**) moieties are similar (–45.6 and –47.2 kcal mol^{-1}), therefore suggesting that both aromatic systems could be used to design guests with prominent affinities for 6,5-SWNT. The analysis based on the decomposition is correct as small deviations up to 6.3 kcal mol^{-1} are found when comparing the sum of the values of the interaction energies with those obtained without decomposing the molecules (Table 4). These deviations might correspond to changes in the polarity that arise from the addition of H atoms to terminate the fragments and from the change in length of the ether chains.

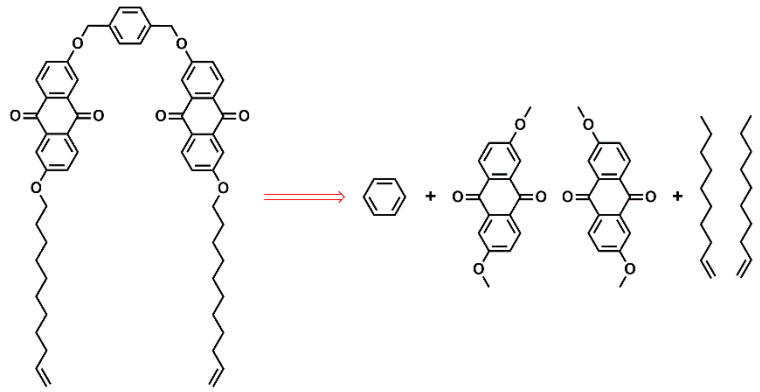

Figure 8. Example of the fragmentation of the guests, applied to **4**, into their components: central benzene ring, aromatic region, and long aliphatic chains.

Table 4. Interaction energies (kcal mol^{-1}) calculated for the different molecular fragments of guests **1–6**: aromatic region ($E_{i,arom.}$), central benzene ring ($E_{i,benz.}$), alkyl chains ($E_{i,alkyl}$), the sum of the values ($E_{i,sum}$), and the interaction energies as computed without the fragmentation ($E_{i,tot.}$).

	1	**2**	**3**	**4**	**5**	**6**
$E_{i,arom.}$	–20.3	–48.2	–45.6	–47.2	–40.9	–41.7
$E_{i,benz.}$		–9.3	–8.3	–9.4	–9.4	–9.1
$E_{i,alkyl}$			–23.6	–27.2	–26.1	–27.3
$E_{i,sum}$	–20.3	–57.5	–77.5	–83.8	–76.4	–78.1
$E_{i,tot.}$	–20.3	–54.1	–71.8	–77.7	–70.7	–71.8

As the experiments were performed in TCE and DMF, the GFN2-xTB interaction energies for the supramolecular complexes between 6,5-SWNT and molecules **1–6** were also computed considering the effects of the solvent upon aggregation. For this purpose, the ALPB[23] (*Analytical linearized Poisson-Boltzmann*) implicit solvation method was used, as available in the xTB program. While the dielectric constant for DMF was readily available in the xTB program, it was not the case for TCE and chloroform ($CHCl_3$) was therefore selected in order to explore the differences observed when varying the experimental conditions. The trends in the interaction energy values computed in the solvent, which show differences up to 30 and 40 kcal mol^{-1} compared to those in the gas phase for DMF and $CHCl_3$, respectively, are shown in Figure 9. All the supramolecular complexes are less stable in the presence of solvent, but the trends in the interaction energies are preserved compared to those previously discussed in vacuum: **4** is the guest with the strongest affinity for the nanotube, while the interaction with **1** is the most unfavored. The decrease of the interaction energy found when the solvent is introduced might be due to the reduction of the accessible area for both the nanotube

[23] Ehlert, S.; Stahn, M.; Spicher, S.; Grimme, S. *J. Chem. Theory Comput.* **2021**, *17* (7), 4250–4261.

and the guests to interact, thus stabilizing the monomers. The variation of the interaction energy depending on the solvent results from the large difference in the dielectric constant of $CHCl_3$ (ε = 4.81) and DMF (ε = 37.0). Nonetheless, to further understand the effect of the solvent in the coordination of the guests and the nanotube, calculations treating the solvent molecules explicitly should be performed.

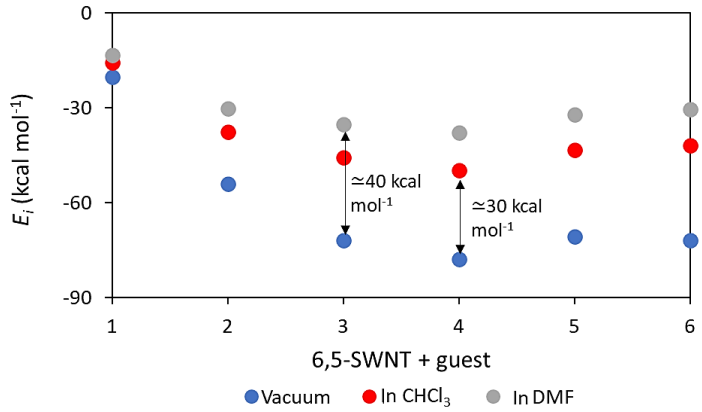

Figure 9. Interaction energy (E_i) for the supramolecular complexes between 6,5-SWNT and molecules **1–6** in gas phase, and in the presence of chloroform and dimethylformamide.

The intermolecular contact area (ICA)[24] was calculated to rationalize the non-covalent interactions of the different supramolecular complexes. This index, which was computed using Chimera,[25] is computed as follows

$$ICA = \frac{A_N + A_n + A_{N+n}}{2}$$

where A_N is the 6,5-SWNT area, A_n is the area of the guest n and A_{N+n} is the area of the complex, all of them obtained from the GFN2-xTB-optimized structures in vacuum. The ICA values were compared to those of the interaction energies, as a good correlation between them would correspond to a large net stabilization of the complexes as the result of the intermolecular contacts formed upon aggregation. As it can be concluded from Figure 10, there is a strong relationship between these two magnitudes, and it shows the importance of the alkyl chains and the conjugated regions of the guests **3–6** for their larger affinity for 6,5-SWNT.

[24] Ribeiro, J.; Ríos-Vera, C.; Melo, F.; Schüller, A. *Bioinformatics* **2019**, *35* (18), 3499–3501.
[25] Pettersen, E. F.; Goddard, T. D.; Huang, C. C.; Couch, G. S.; Greenblatt, D. M.; Meng, E. C.; Ferrin, T. E. *J. Comput. Chem.* **2004**, *25* (13), 1605–1612.

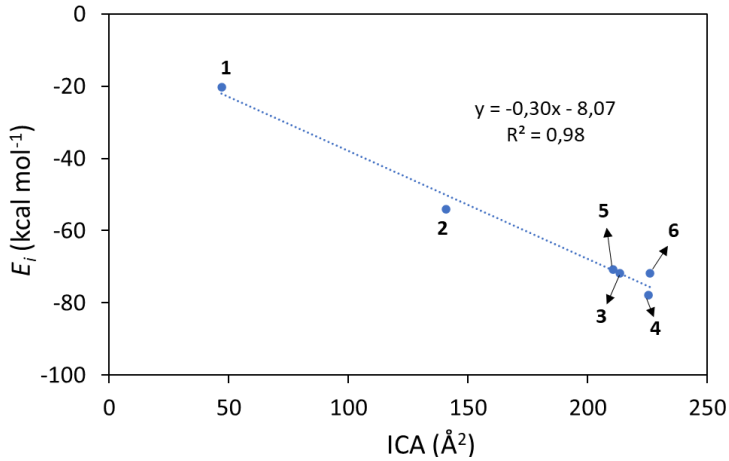

Figure 10. Correlation between the intermolecular contact area (ICA) and the interaction energies computed for guests **1–6** at the GFN2-xTB level of theory in vacuum.

A way to visualize the non-covalent interactions and to see the formation of contacts within a supramolecular complex consists on analyzing the topology of its electron density, as it can be done by using NCIplot.[26] More precisely, the reduced electron density, its reduced gradient and its hessian can be used to graphically represent those regions in which attractive and repulsive interactions take place. The non-covalent interaction surfaces calculated for the complexes between 6,5-SWNT and **1–6** are shown in Figure 11. The results confirm the trends previously discussed on the basis of association energies and ICA index. The non-covalent interaction surfaces calculated for guests **3–6**, with a larger area to interact with the nanotube, largely spread over both the nanotube and the guests, hence explaining their good affinity for the 6,5-SWNT.

In order to characterize the conformational flexibility of the supramolecular complexes, molecular dynamics simulations were performed at the GFN2-xTB level of theory in the gas phase. The simulations were propagated for 500 ns with a time step of 2 fs to ensure that a large population of different conformations could be generated. The mobility of the molecules was assessed by analyzing the distance (*d*) between the axis of the nanotube and the centroid of the pyrene ring for **1** and the centroid of the central benzene ring for **2–6**. The results, shown in , denote a strong tendency for all the guests to remain extended over the surface of the nanotube. The values of *d* slightly fluctuate around 7 Å, and considering that the diameter of 6,5-SWNT is 7.6 Å,[27] in all cases the aromatic rings stand at 3.2 Å. As

[26] Boto, R. A.; Peccati, F.; Laplaza, R.; Quan, C.; Carbone, A.; Piquemal, J.-P.; Maday, Y.; Contreras-García, J. *J. Chem. Theory Comput.* **2020**, *16* (7), 4150–4158.
[27] Ozawa, H.; Ide, N.; Fujigaya, T.; Niidome, Y.; Nakashima, N. *Chem. Lett.* **2011**, *40* (3), 239–241.

it can be seen from some relevant conformations along the dynamics in , the flexible alkyl chains show a large mobility, and they easily lose the contacts with the nanotube. This could favour the interaction of guests **3–6** with more than one nanotube if they are sufficiently close in the experimental conditions. In some cases, as shown for **6**, the interaction between the central benzene ring and the surface of the nanotube is lost, increasing its distance in almost 6 Å. Nonetheless, and even if that contact is lost, the alkyl chains, which could remain interacting with the nanotube, contribute to ensure the formation of the supramolecular complex.

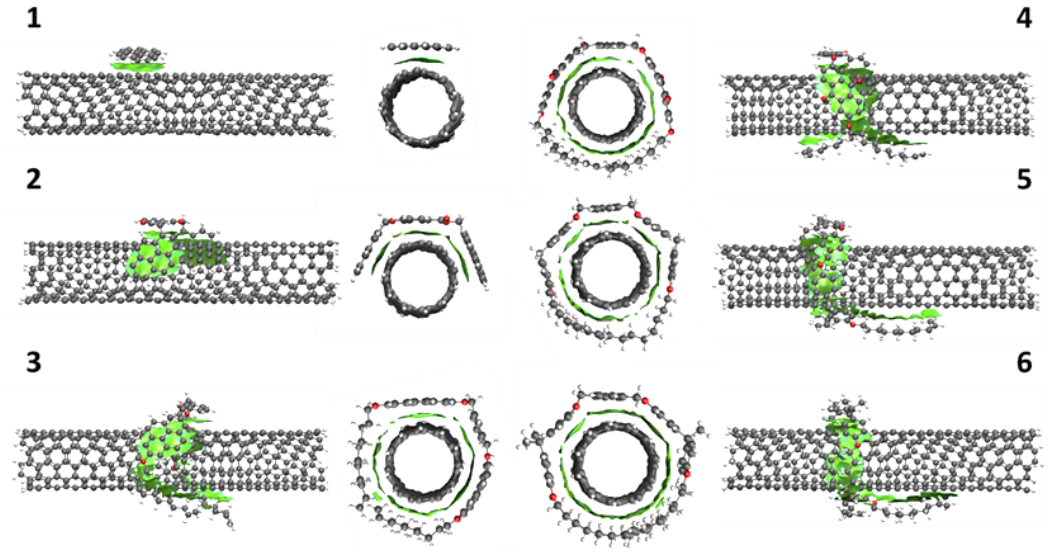

Figure 11. Non-covalent interaction surface (in green) calculated for the supramolecular complexes formed by 6,5-SWNT and guests **1-6**. Atom colour coding: C (grey), O (red), H (white).

Additionally, a similar analysis was performed to estimate the flexibility of the large alkyl chains for **3–6** by inspecting the distances between the extremes (e_1 and e_2) of the chains and the axis of the nanotube. As it can be seen in Figure 13, the distances generally fluctuate in the range between 7 and 9 Å, but in some cases distances of more than 20 Å are reached thus losing the interaction with the nanotube. As the simulation is not performed using periodic boundary conditions and the nanotube is terminated with H atoms, the alkyl chains are able to reach its extremes and distances below the radius of the nanotube are obtained for **3** and **4**.

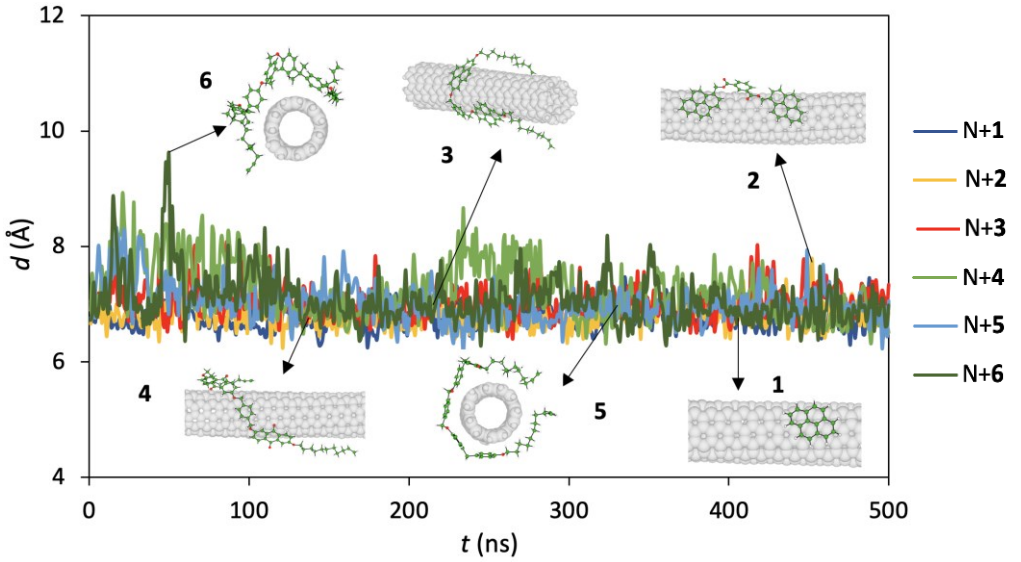

Figure 12. Evolution of the distance between the axis of the 6,5-SWNT (N) and the centroid of the central benzene ring for **2–6** and the central atom of the pyrene ring for **1**, with some relevant structures found along the simulation.

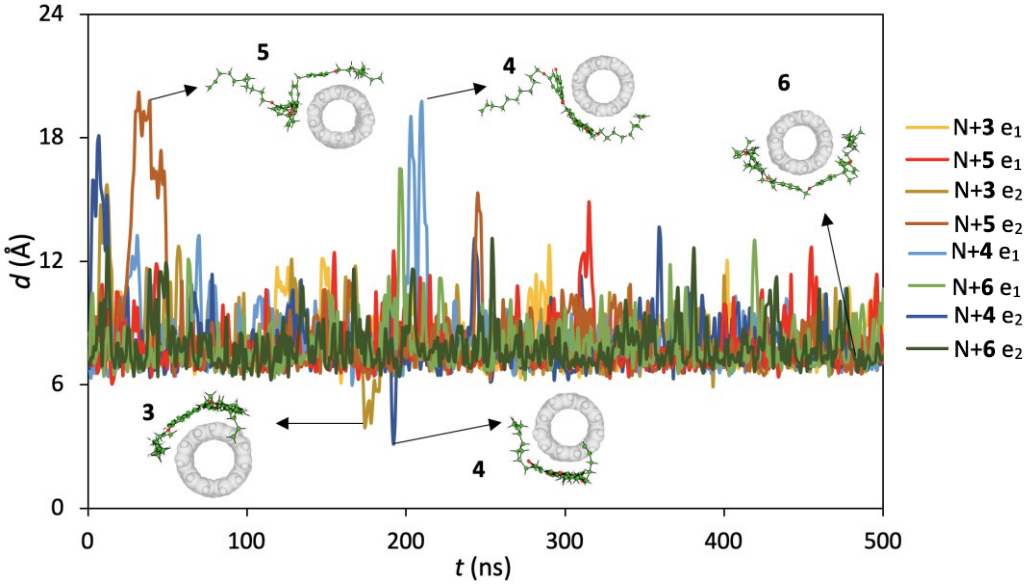

Figure 13. Evolution of the distance between the axis of the 6,5-SWNT (N) and the extremes of the alkyl chains of the molecules **3–6** along the simulation.

2.3. CONCLUSIONS

The supramolecular functionalization of SWNTs is a spontaneous reaction which needs electron rich conjugated compounds for a strong π-π interaction. A greater number of non-covalent interactions between association partners results in a tight binding, enhancing the stability of the resulting supramolecular complexes. Solvation forces are particularly important for determining the thermodynamic energies of the systems. The low solubility of the nanotubes translates into positive solvophobic interactions. In this sense, there is a preference of carbon nanotube surfaces to interact with the surfaces of the organic molecules, and thereby to displace solvent molecules from the interacting surfaces increasing the entropy of the system. Because of that the solubility of the organic molecules plays an important role in the association process.

Therefore, the dynamics show huge flexibility of the guests, which explore embraced, unfolded and semi-folded conformations when forming the supramolecular complexes with 6,5-SWNT. It has been shown that the interactions between guests **1**–**6** and the 6,5-SWNT are mostly driven by the aromatic regions of the guests but the alkyl chains also play an important role in the coordination process of **3**–**6**, thus explaining their augmented affinity for 6,5-SWNT. Up to this point, the effect of the solvent has been neglected in the dynamics, but it would certainly modify the conformational freedom of the guests in forming the supramolecular complexes. Advanced simulations are currently being performed to calculate the adsorption free energies including solvation effects and they will be part of a future publication, alongside with the results shown in this report.

In conclusion, the thermodynamic energies (and therefore the association constants) depend on the organic molecules attached to the carbon nanotubes as well as the reaction's solvent. They are a consequence of the molecules 'conformational changes and variations in the amount of solvent immobilized or released on forming the systems.

2.4. SUPPORTING INFORMATION

S1. Experimental section.

Reagents were obtained from usual commercial sources and used without further purification. Analytical thin layer chromatographies (TLC) were performed using

aluminium-coated Merck Kiesel silica gel 60 F254 plates. Column chromatography purification was performed using silica gel (Scharlau 60, 70-230 mesh).

NMR spectra were recorded on a BrukerAvance 400 (^{1}H: 400 MHz; ^{13}C: 400 MHz) at 298K, using partially deuterated solvents as internal standards. Coupling constants (J) are denoted in Hz and chemical shifts (δ) in ppm. Multiplicities are denoted as follows: s = singlet, d = doublet, t = triplet, m = multiplet, b = broad, dd = doublet of doublets. Ge-2D multiplicity-edited 1H-13C HSQC* (400 MHz) is a simple modification in the ge-2D HSQC experiment in which the carbon multiplicity can be directly extracted from the resulting spectra in addition to the conventional heteronuclear correlations by simple analysis of the cross-peaks sign. Methine and methyl protons will appear with different phase signals to methylene protons. Thermogravimetric Analyses (TGA) were performed using a TA Instruments TGAQ500 with a ramp of 10 °C/min under nitrogen conditions from 100 to 1000 °C. Mass spectra were recorder through electrospray (ESI) and matrix-assisted laser desorption ionization (coupled to a Time-Of-Flight analyser) (MALDI-TOF) experiments were recorded on a maXis II spectrometer and a Ultraflex III Bruker spectrometer, respectively.

S2. Synthetic details and characterization.

1. General scheme for the synthesis of guest **2**

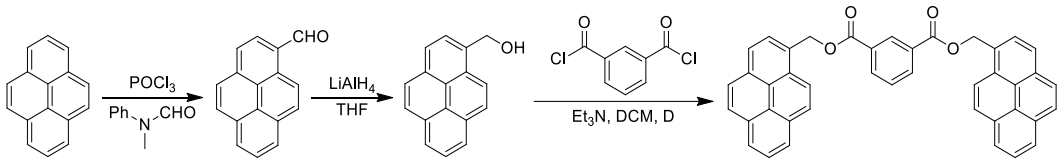

Synthesis of compound **2** described in *Chem. Sci*. **2015**, 6 (12), 7008-7014.[7]

[7] Juan, A. de; López-Moreno, A.; Calbo, J.; Ortí, E.; Pérez, E. M. *Chem. Sci.* **2015**, *6* (12), 7008–7014

2. General scheme for the synthesis of guest **3**

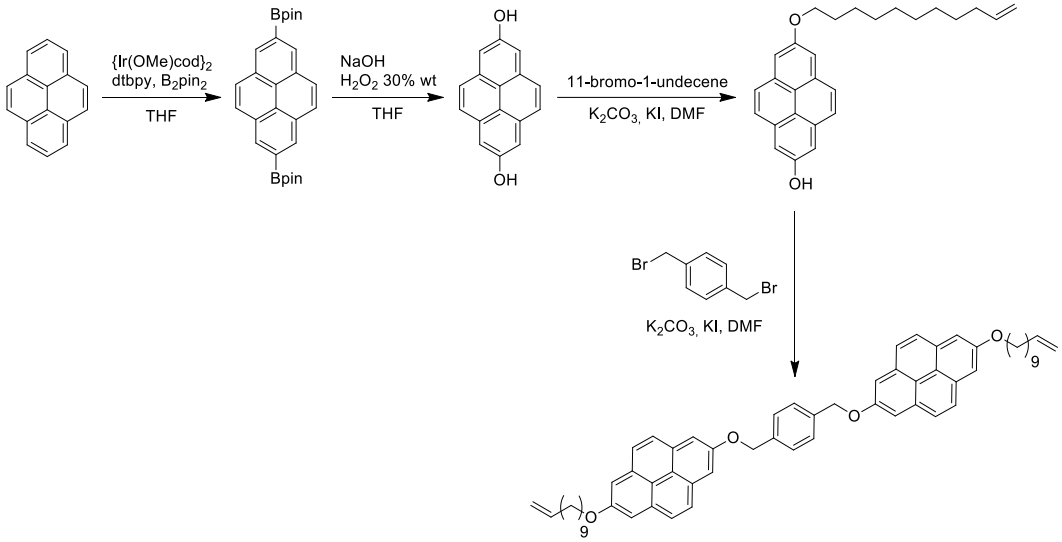

Synthesis of compound **3** described in *Chem. Commun*. **2015**, 51 (25), 5421-5424.[9]

3. General scheme for the synthesis of guest **4**

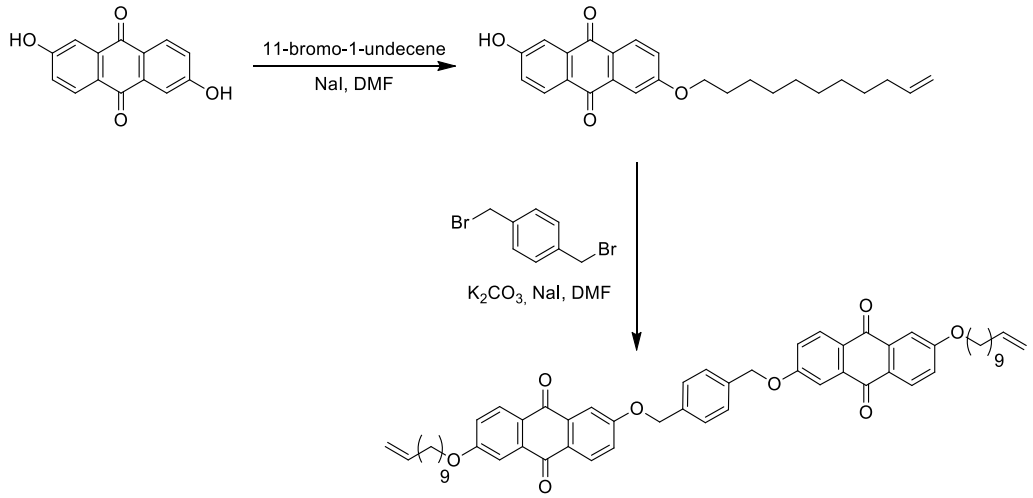

Synthesis of compound **4** described in *J. Am. Chem. Soc.* **2011**, 133 (9), 3184–3190.[28]

[9] López-Moreno, A.; Pérez, E. M. *Chem. Commun.* **2015**, *51* (25), 5421–5424.
[28] Canevet, D.; Gallego, M.; Isla, H.; de Juan, A.; Pérez, E. M.; Martín, N. *J. Am. Chem. Soc.* **2011**, *133* (9), 3184–3190.

4. General scheme for the synthesis of guest **5**

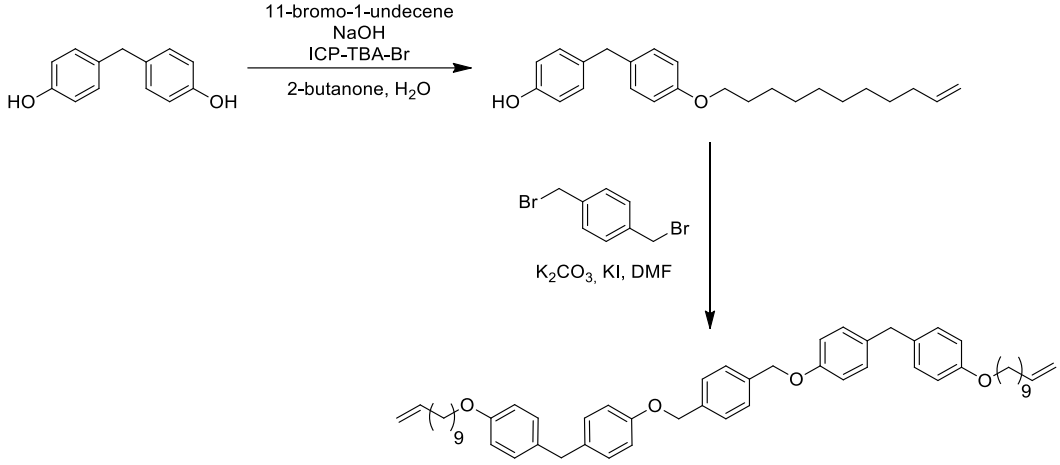

Synthesis of monoalkylated product: 4,4'-methylenediphenol (3 g, 14.98 mmol) was dissolved in a 1:1 mixture of 2-butanone/water (80 mL: 80 mL). Sodium hydroxide (598.4 mg, 14.98 mmol), 11-bromo-1-undecene (3.74 g, 16.03 mmol), and tetrabutylammonium bromide (4.83 g, 14.98 mmol) were added. The reaction mixture was stirred under reflux for 1 h. Then, the crude reaction was cooled down and poured onto ice-cold 1 M aqueous hydrochloric acid. The solution was extracted with ethyl acetate, the organic phase was dried over Na_2SO_4, and filtered. Solvent was removed by evaporation under reduced pressure. The crude solid was washed with hexane to remove the traces of starting material. The hexane was removed under vacuum and the precipitate was purified by column chromatography (silica gel, hexane/ethyl acetate 9:1) giving a pale yellow oil (2.54 mg, 7.21 mmol, 48 %). **^{1}H NMR (400 MHz, $CDCl_3$) δ (ppm)**: 7.05 (m, J = 11.2, 8.5 Hz, 4H, H_o, H_m), 6.81 (m, J = 8.6 Hz, 2H, H_p), 6.78 – 6.71 (m, 2H, H_l), 5.81 (ddt, J = 16.9, 10.1, 6.7 Hz, 1H, H_b), 5.04 – 4.89 (m, 2H, H_a), 4.60 (s, 1H, H_q), 3.91 (t, J = 6.6 Hz, 2H, H_k), 3.84 (s, 2H, H_n), 2.04 (q, J = 6.9 Hz, 2H, H_c), 1.75 (dt, J = 14.5, 6.7 Hz, 2H, H_j), 1.47 – 1.27 (m, 12H, H_d, H_e, H_f, H_g, H_h, H_i). **^{13}C NMR (400 MHz, CDCl3) δ (ppm)**: 157.63, 153.86, 139.39, 134.11, 133.56, 130.08, 129.84, 115.37, 114.61, 114.26, 77.48, 77.16, 76.84, 68.16, 40.27, 33.95, 29.66, 29.57, 29.47, 29.26, 29.07, 26.20. **MS m/z**: calculated for $C_{24}H_{32}O_2$ [M] 352.24, found ESI 351.23.

^{1}H NMR (400 MHz, $CDCl_3$)

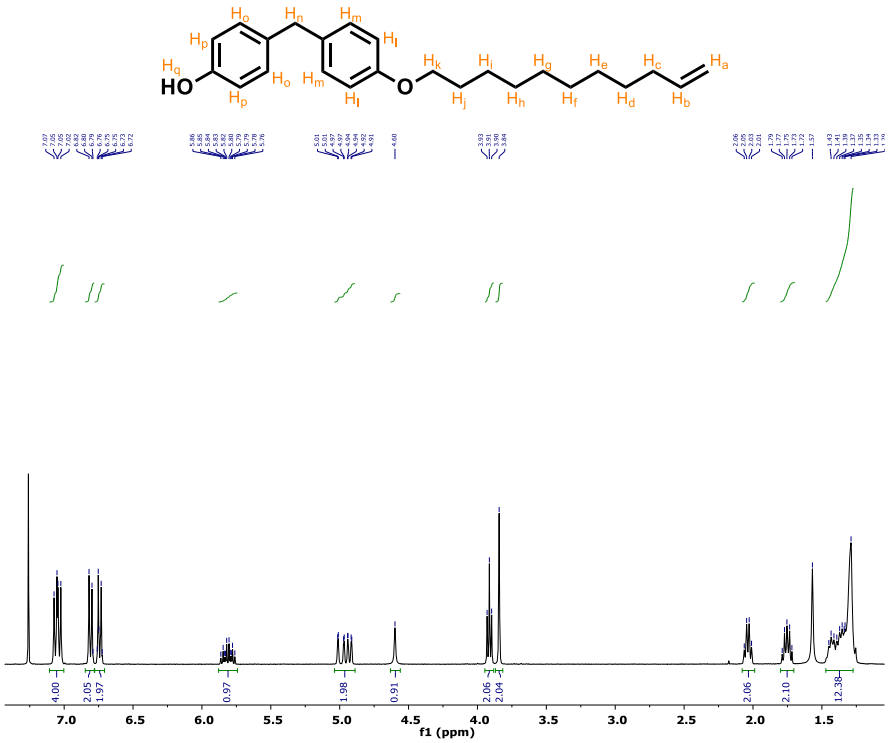

^{13}C NMR (400 MHz, $CDCl_3$)

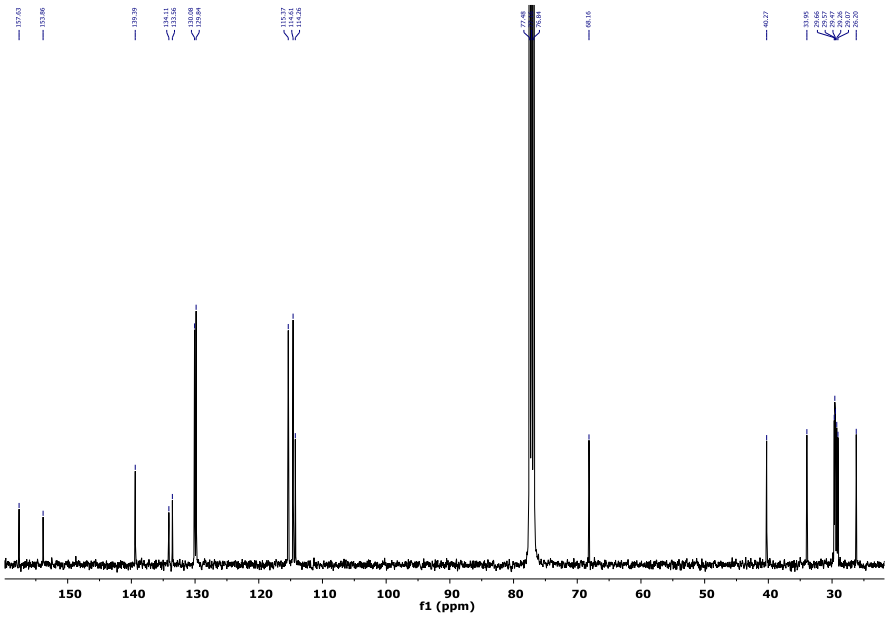

Ge-2D multiplicity-edited ^{1}H-^{13}C HSQC * (400 MHz, $CDCl_3$)

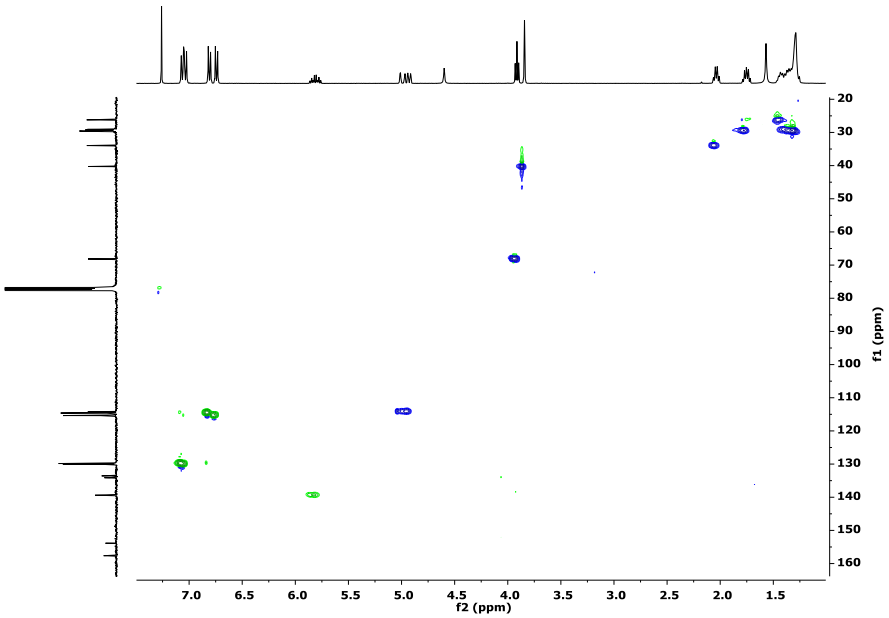

MS ESI negative (MeOH as ionising phase)

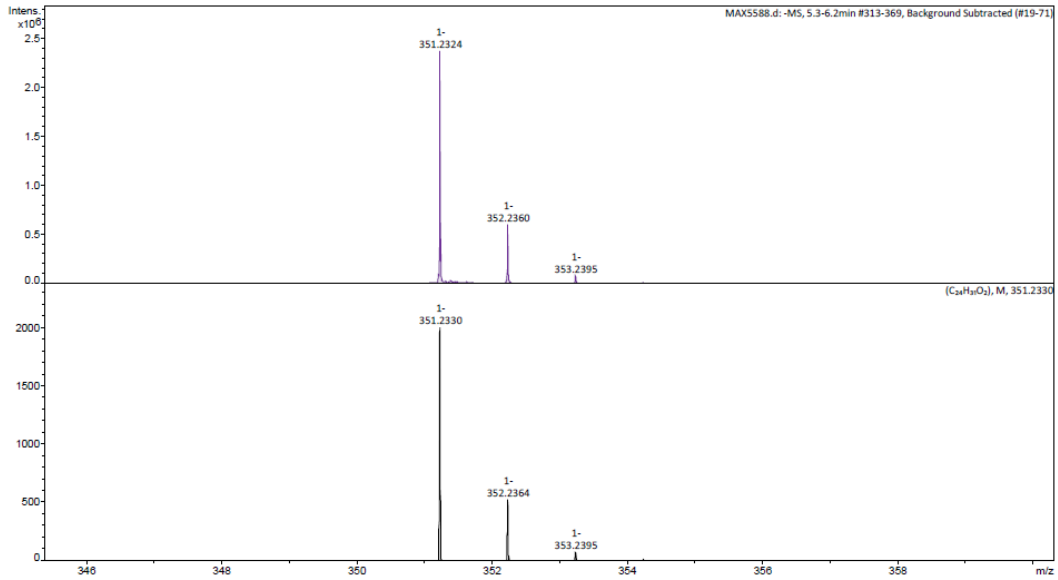

Synthesis of U-shaped product: 4-(4-(undec-10-en-1-yloxy)benzyl)phenol (1 g, 2.84 mmol) was dissolved in 30 mL of DMF. Potassium carbonate (0.78 g, 5.68 mmol) and a catalytic amount of potassium iodide were added to the previous solution. Then, α,α'-dibromo-p-xylene (2 g, 5.68 mmol) were added and the reaction mixture was refluxed overnight. The crude reaction was cooled to room temperature and hydrolysed with an aqueous hydrochloric acid (1 M) solution. The precipitate obtained was isolated by filtration and washed with methanol giving a white powder. (692.40 mg, 0.86 mmol, 60 %). **^{1}H NMR (400 MHz, $CDCl_3$) δ (ppm):** 7.43 (s, 4H, H_r), 7.07 (m, J = 8.5, 5.2 Hz, 8H, H_o, H_m), 6.88 (m, 4H, H_l), 6.81 (m, J = 8.6 Hz, 4H, H_p), 5.89 – 5.74 (m, 2H, H_b), 5.03 (s, 4H, H_q), 5.02 – 4.90 (m, 4H, H_a), 3.91 (t, J = 6.5 Hz, 4H, H_k), 3.86 (s, 4H, H_n), 2.04 (q, J = 7.0 Hz, 4H, H_c), 1.75 (dt, J = 14.5, 6.6 Hz, 4H, H_c), 1.55 – 1.29 (m, 24H, H_d, H_e, H_f, H_g, H_h, H_i). **^{13}C NMR (400 MHz, $CDCl_3$) δ (ppm):** 157.49, 157.08, 139.25, 136.91, 134.14, 133.42, 129.77, 129.72, 127.67, 114.79, 114.47, 114.13, 77.34, 77.02, 76.70, 69.78, 68.01, 40.16, 33.81, 29.52, 29.39, 29.33, 29.12, 28.93, 26.07. **MS m/z:** calculated for $C_{56}H_{70}O_4$ [M] 806.53, found MALDI 805.5.

^{1}H NMR (400 MHz, $CDCl_3$)

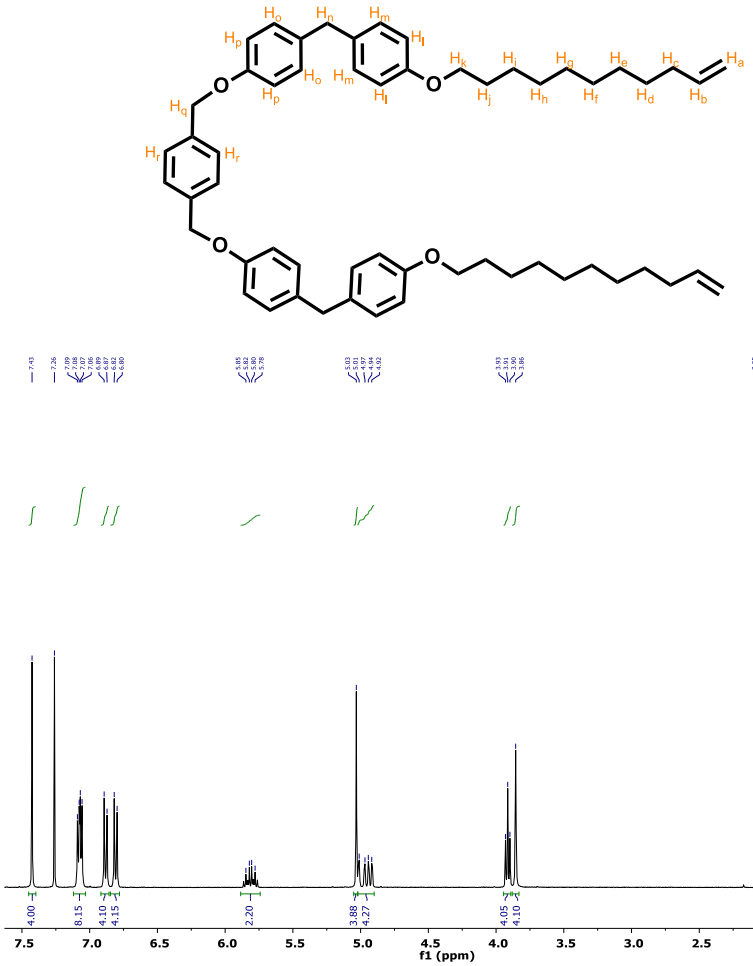

^{13}C NMR (400 MHz, $CDCl_3$)

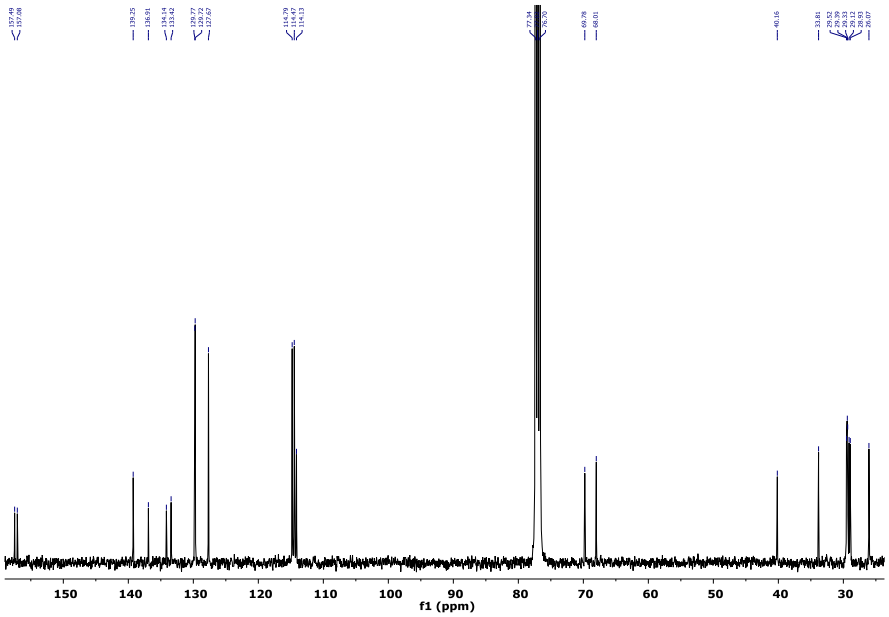

Ge-2D multiplicity-edited ^{1}H-^{13}C HSQC * (400 MHz, $CDCl_3$)

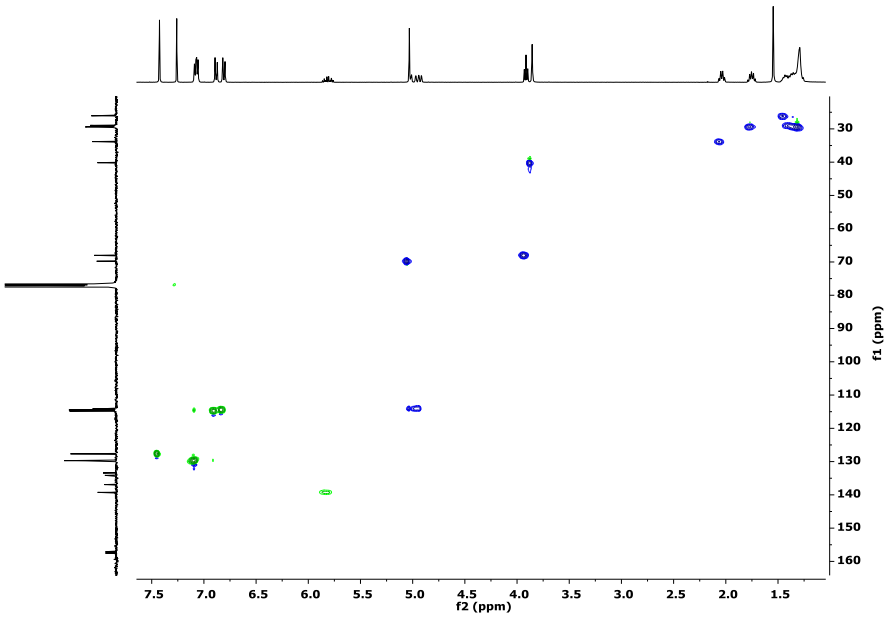

MS MALDI (Matrix DCTB)

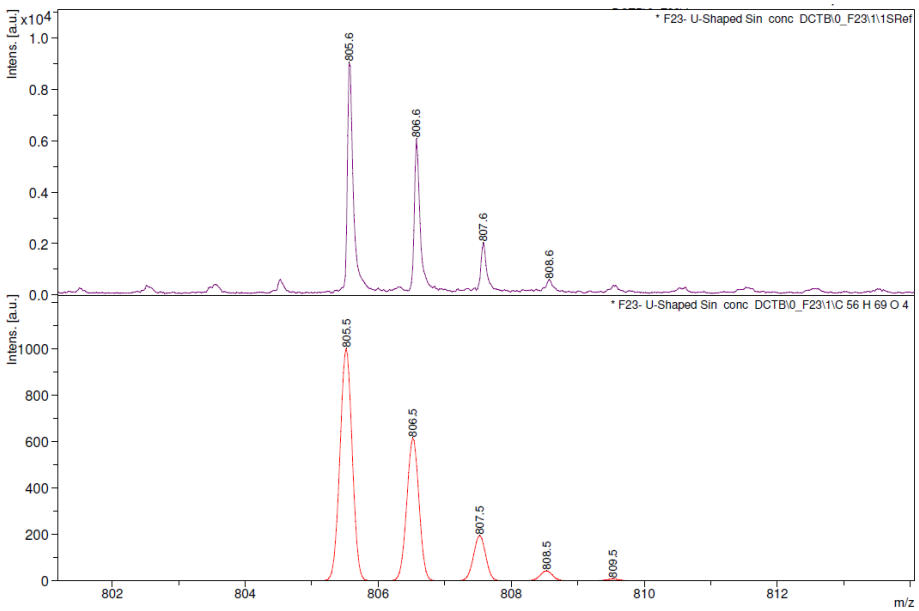

5. General scheme for the synthesis of guest **6**

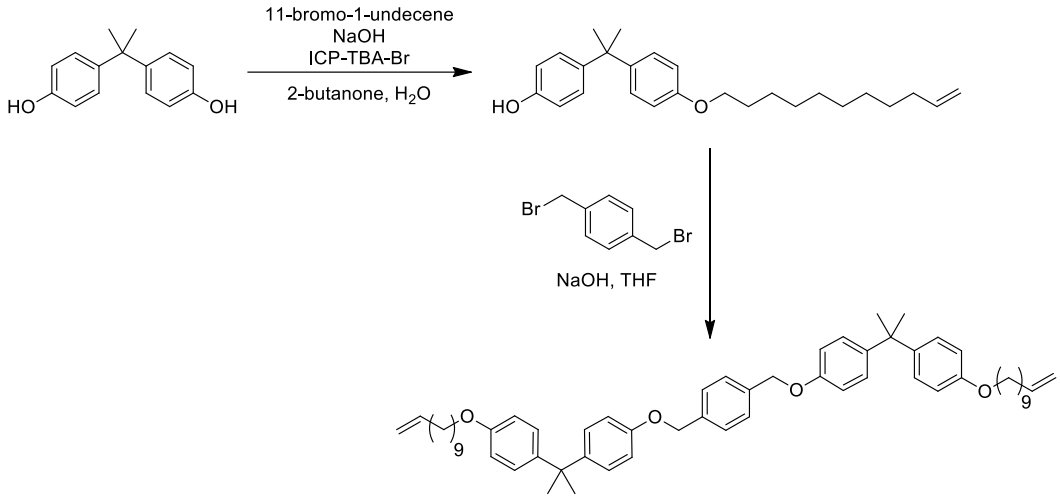

Synthesis of monoalkylated product: 4, 4'-(propane-2, 2-diyl) diphenol (5 g, 21.90 mmol) was dissolved in a 1:1 mixture of 2-butanone/water (131 mL: 131 mL). Sodium hydroxide (876.00 mg, 21.90 mmol), 11-bromo-1-undecene (5.46 g, 23.44 mmol), and tetrabutylammonium bromide (7.06 g, 21.90 mmol) were added. The reaction mixture was stirred under reflux for 1 h. Then, the crude reaction was

cooled down and poured onto ice-cold 1 M aqueous hydrochloric acid. The solution was extracted with ethyl acetate, the organic phase was dried over Na_2SO_4, and filtered. Solvent was removed by evaporation under reduced pressure. The precipitate was purified by column chromatography (silica gel, DCM) giving a white solid (2.75 g, 7.23 mmol, 66 %). **^{1}H NMR (400 MHz, $CDCl_3$) δ (ppm)**: 7.15 – 7.07 (m, 4H, H_o, H_m), 6.82 – 6.76 (m, J = 8.8 Hz 2H, H_p), 6.75 – 6.70 (m, 2H, H_l), 5.82 (ddt, *J* = 16.9, 10.2, 6.7 Hz, 1H, H_b), 5.04 – 4.89 (m, 2H, H_a), 4.60 (s, 1H, H_q), 3.92 (t, *J* = 6.6 Hz, 2H, H_k), 2.04 (q, *J* = 6.8 Hz, 2H, H_c), 1.76 (dt, *J* = 14.5, 6.6 Hz, 2H, H_j), 1.63 (s, 6H, H_n), 1.47-1.27 (m, 12H, H_d, H_e, H_f, H_g, H_h, H_i). **^{13}C NMR (101 MHz, $CDCl_3$) δ (ppm)**: 157.01, 153.38, 143.45, 143.06, 139.36, 128.05, 127.80, 114.82, 114.27, 113.98, 77.48, 77.16, 76.84, 68.11, 41.78, 33.93, 31.20, 29.64, 29.55, 29.51, 29.46, 29.24, 29.05, 26.19. **MS m/z**: calculated for $C_{26}H_{36}O_2$ [M] 380.27, found ESI 379.26.

^{1}H NMR (400 MHz, $CDCl_3$)

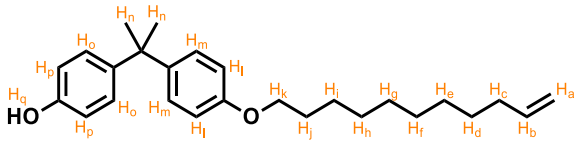

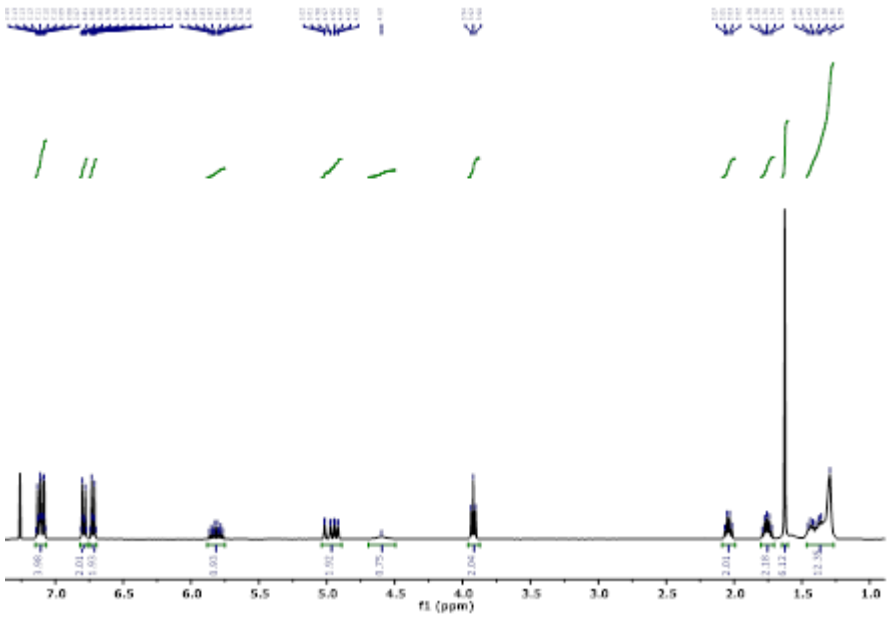

^{13}C NMR (400 MHz, $CDCl_3$)

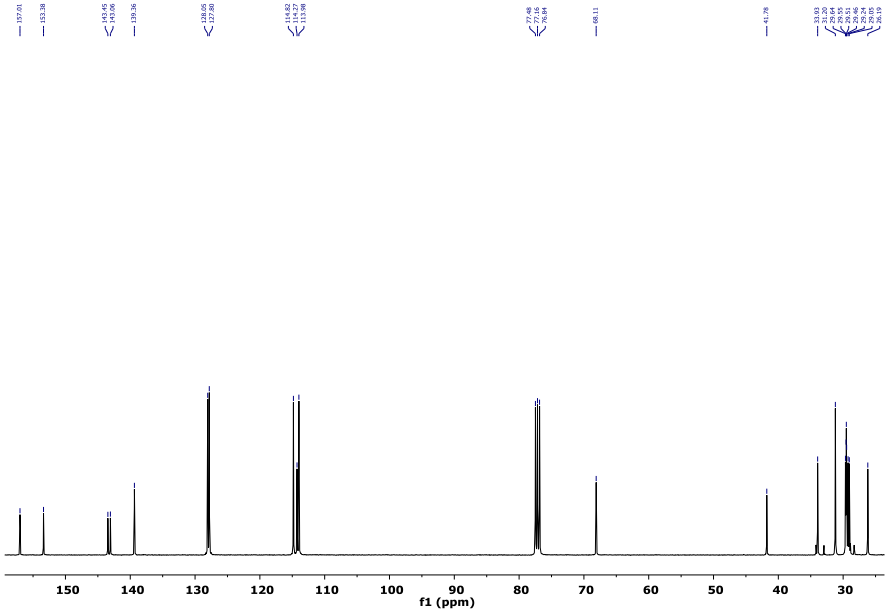

Ge-2D multiplicity-edited ^{1}H-^{13}C HSQC * (400 MHz, $CDCl_3$)

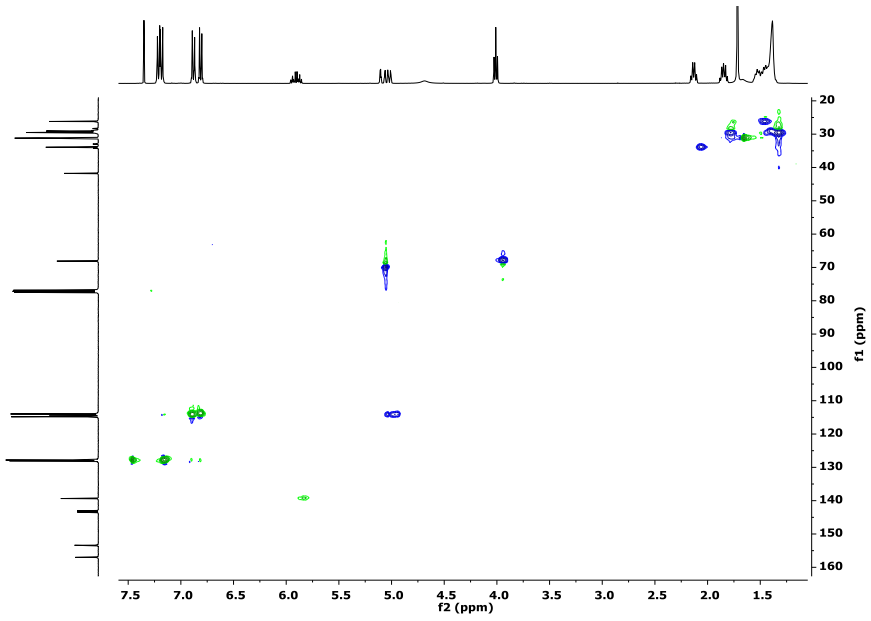

MS ESI negative (MeOH as ionising phase)

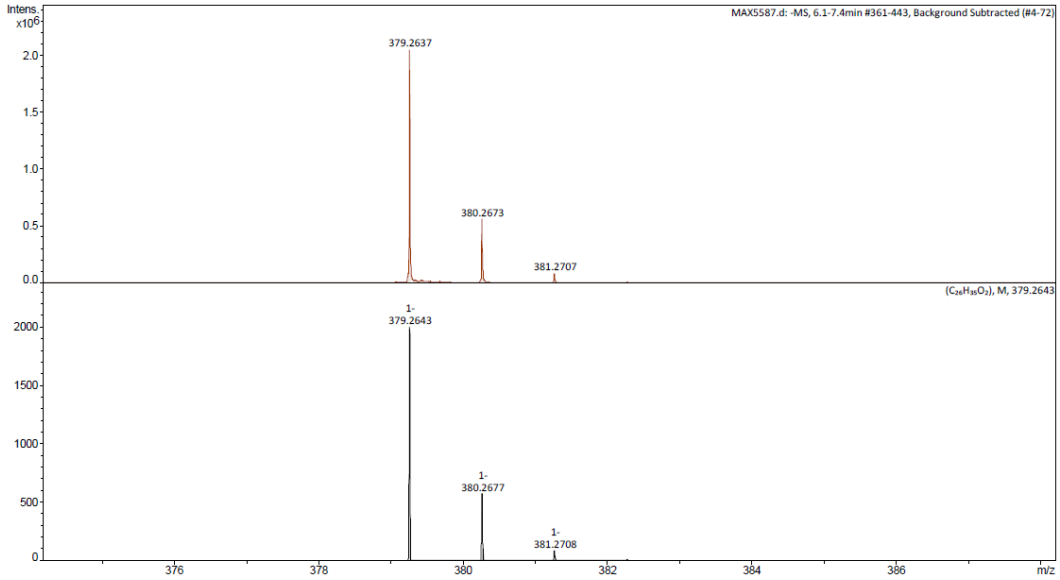

Synthesis of U-shaped product: 4-(2-(4-(undec-10-en-1-yloxy)phenyl)propan-2-yl)phenol (20 mg, 0.05 mmol) and sodium hydroxide (2 mg, 0.05 mmol) were dissolved in 0.5 mL of THF. Over that reaction mixture, a solution of α,α'-dibromo-p-xylene (5.3 mg, 0.02 mmol) in 0.3 mL of THF was added dropwise. The crude reaction was stirred under reflux for 12 h, cooled to room temperature, and hydrolysed with an aqueous hydrochloric acid (1 M) solution. Then, the mixture was extracted with dichloromethane, the organic phase was dried over sodium sulfate, and filtered. The solvent was removed under vacuum and the precipitated obtained was purified by column chromatography (silica gel, hexane/ ethyl acetate 9:1) giving a white powder (13.30 mg, 0.015mmol, 62 %). **^{1}H NMR (400 MHz, $CDCl_3$) δ (ppm):** 7.44 (s, 4H, H_r), 7.16 – 7.11 (m, 8H, H_o, H_m), 6.90 – 6.84 (m, 4H, H_l), 6.82 – 6.76 (m, 4H, H_p), 5.88 – 5.75 (m, 2H, H_b), 5.03 (s, 4H, H_q), 5.02 – 4.91 (m, 4H, H_a), 3.92 (t, J = 6.5 Hz, 4H, H_k), 2.04 (q, J = 6.9 Hz, 4H, H_c), 1.75 (dt, J = 14.6, 6.8 Hz, 4H, H_j), 1.63 (s, 12H, H_n), 1.46 – 1.28 (m, 24H, H_d, H_e, H_f, H_g, H_h, H_i). **^{13}C NMR (101MHz, $CDCl_3$) δ (ppm):** 157.12, 156.74, 143.69, 142.97, 139.39, 137.10, 127.86, 114.27, 113.95, 77.48, 77.16, 76.84, 69.86, 68.04, 41.83, 33.95, 31.21, 29.66, 29.57, 29.54, 29.51, 29.26, 29.07, 26.23. **MS m/z:** calculated for $C_{60}H_{78}O_4$ [M] 862.59, found MALDI 862.6.

^{1}H NMR (400 MHz, $CDCl_3$)

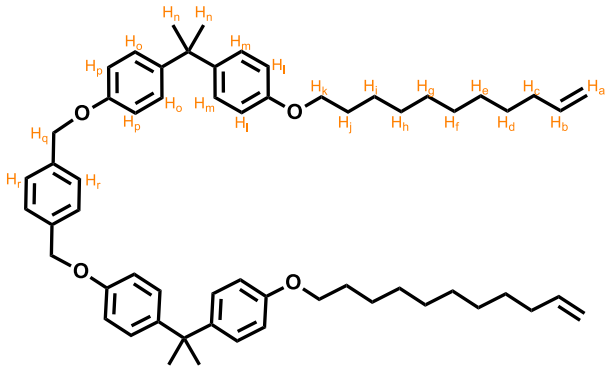

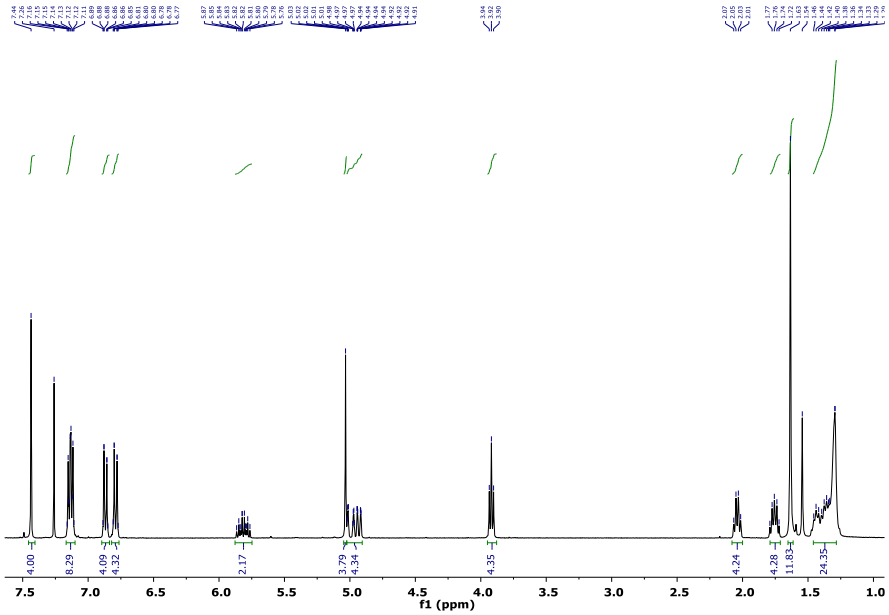

^{13}C NMR (400 MHz, $CDCl_3$)

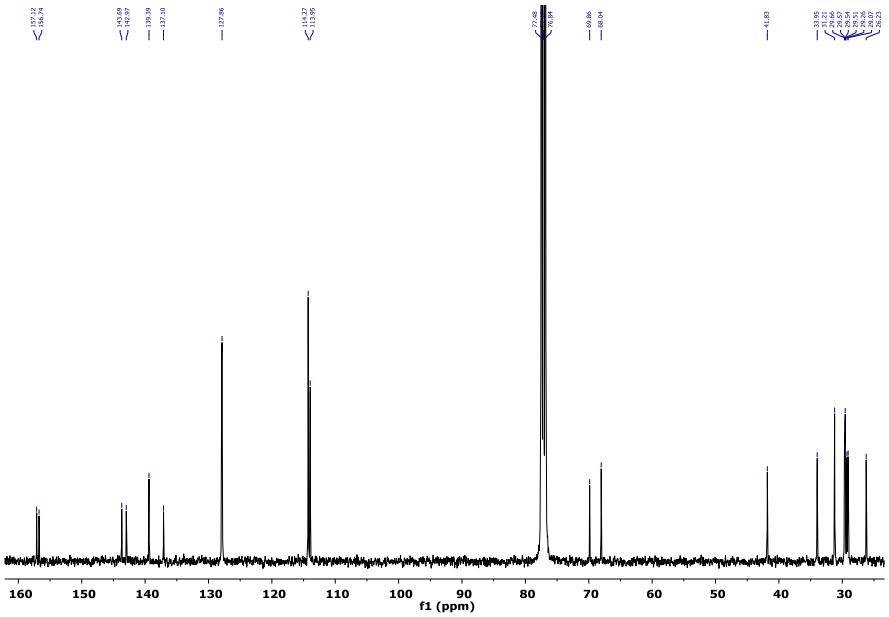

Ge-2D multiplicity-edited ^{1}H-^{13}C HSQC * (400 MHz, $CDCl_3$)

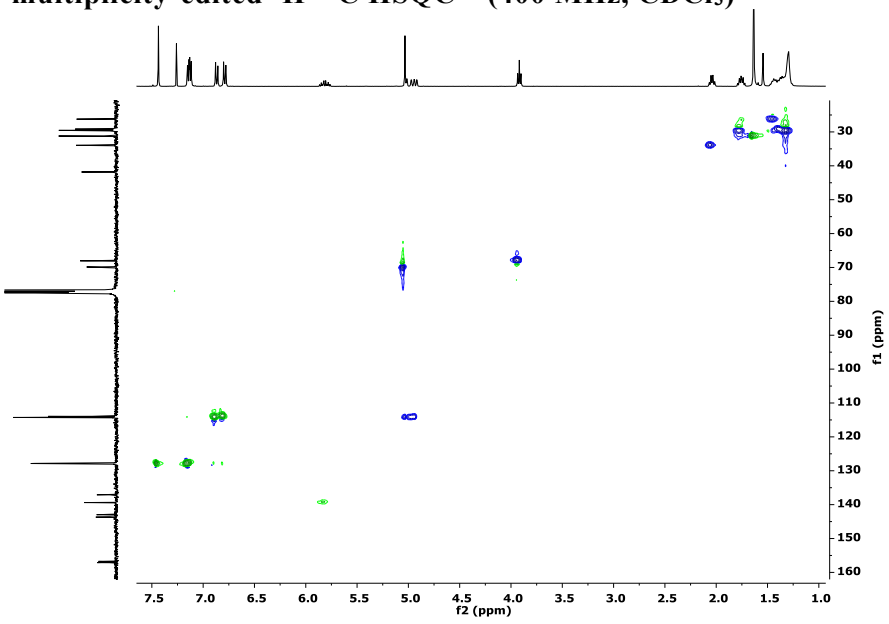

MS MALDI (Matrix DCTB + NaI)

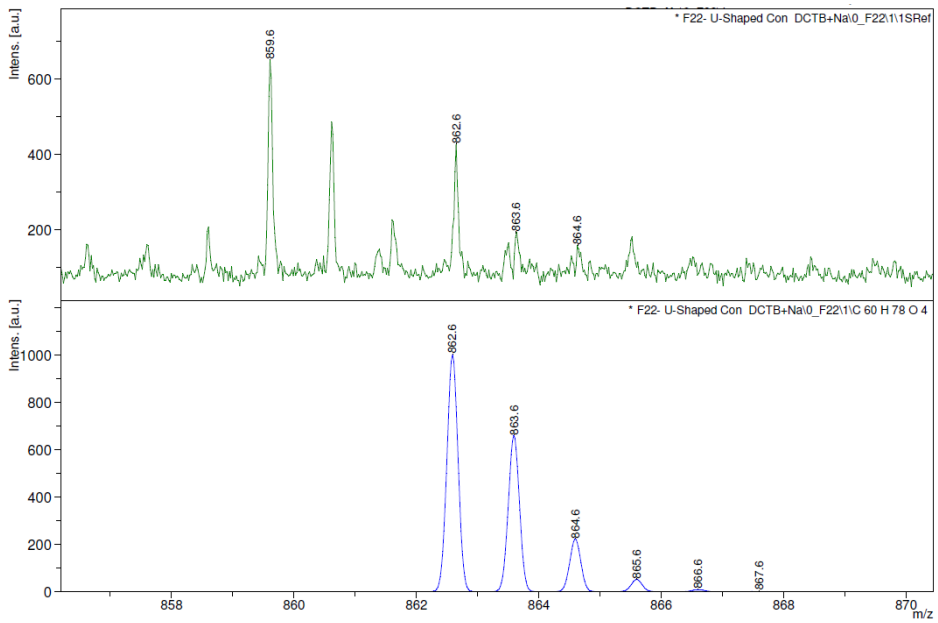

S3. Experimental titration procedure.

The guest molecules were dissolved in 1,1,2,2-tetrachloroethane (TCE). Then, 6,5-SWNTs were added (1 $mgmL^{-1}$) and the dispersion was mixed for 2 h at different temperatures (0 ºC, r.t., 50 ºC, 75 ºC). The suspension was filtered through a 0.2 µm-pore polytetrafluorethylene (PTFE) membrane and the supramolecular complex was dried under vacuum as a previous step of its characterization by thermogravimetric analysis (N_2, $30ºC \cdot min^{-1}$).

Depending on the solubility of the guest, several weights were used for the titration experiments: **1**: 5, 50, 200, 400, 600 mg; **2**: 5, 10, 25, 50 mg; **3**: 0.5, 1.9, 2.5, 5.0, 10.0 mg; **4**: 0.5, 1.0, 2.5, 5.0, 7.5, 10.0 ; **5**: 20, 40, 100, 200, 400 mg; **6**: 20, 50, 100, 200, 400 mg

Each experiment for each guest concentration at each temperature was repeated three times and the TGA results were averaged. In addition, to determine the solvent adsorbed or encapsulated in the nanotubes, blank experiments were performed at all temperatures studied. The results obtained were subtracted from all the sample analyses obtained.

S4. Adsorption isotherms not shown in the main text.

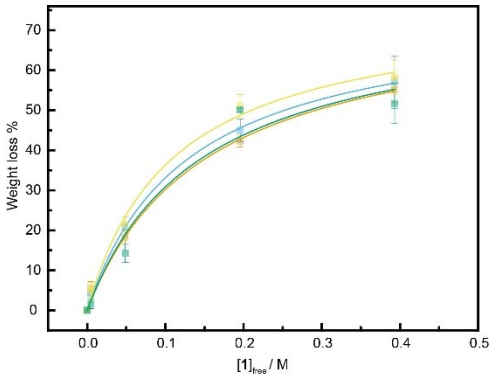

Figure S1. Titration of **1** vs 6,5-SWNTs in TCE at 273.15 K (blue line), 298.15 K (green line), 323.15 K (yellow line) and 348.15 K (orange line).

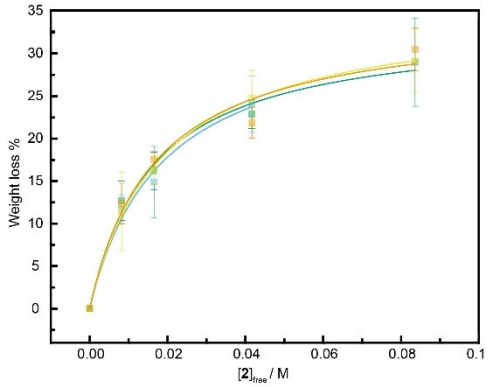

Figure S2. Titration of **2** vs 6,5-SWNTs in TCE at 273.15 K (blue line), 298.15 K (green line), 323.15 K (yellow line) and 348.15 K (orange line).

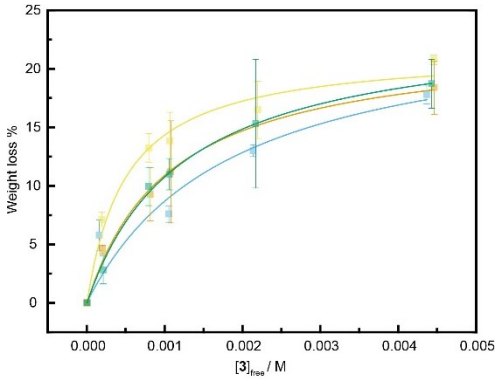

Figure S3. Titration of **3** vs 6,5-SWNTs in TCE at 273.15 K (blue line), 298.15 K (green line), 323.15 K (yellow line) and 348.15 K (orange line).

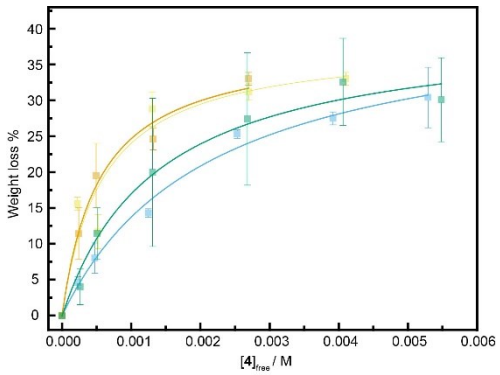

Figure S4. Titration of **4** vs 6,5-SWNTs in TCE at 273.15 K (blue line), 298.15 K (green line), 323.15 K (yellow line) and 348.15 K (orange line).

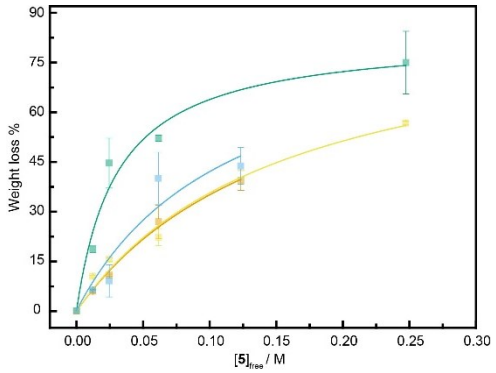

Figure S5. Titration of **5** vs 6,5-SWNTs in TCE at 273.15 K (blue line), 298.15 K (green line), 323.15 K (yellow line) and 348.15 K (orange line).

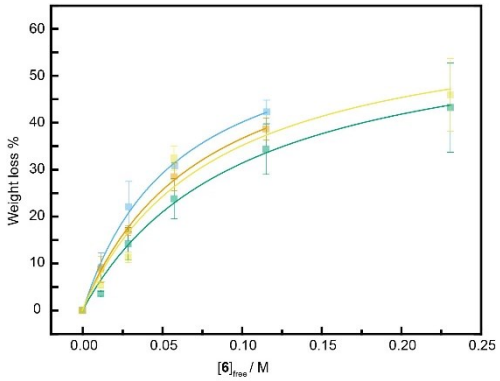

Figure S6. Titration of **6** vs 6,5-SWNTs in TCE at 273.15 K (blue line), 298.15 K (green line), 323.15 K (yellow line) and 348.15 K (orange line).

S5. Outline of the titration results at different temperatures.

Sample	T / K	K_a / M^{-1}	Error K_a / M^{-1}	S (%)	Error S (%)	R^2
1·6,5-SWNTs	273.15	7.87	0.71	68.56	2.23	1.00
	298.15	6.90	3.77	70.03	14.55	0.96
	323.15	9.11	1.80	71.26	4.76	0.99
	348.15	6.60	1.39	75.92	6.20	0.99
2·6,5-SWNTs	273.15	54.40	15.95	34.19	4.37	0.98
	298.15	62.55	12.36	33.39	2.15	0.99
	323.15	53.57	3.72	32.39	0.78	1.00
	348.15	59.50	17.63	30.48	2.99	0.97
3·6,5-SWNTs	273.15	542.09	415.48	24.67	7.97	0.88
	298.15	820.01	78.91	16.12	0.60	1.00
	323.15	1984.77	488.20	10.64	0.71	0.98
	348.15	935.94	138.17	11.92	0.67	0.99
4·6,5-SWNTs	273.15	465.81	81.10	43.22	3.11	0.99
	298.15	725.07	166.59	18.09	1.42	0.98
	323.15	1703.58	832.77	12.68	1.77	0.90
	348.15	1833.46	436.61	12.71	1.01	0.98
5·6,5-SWNTs	273.15	8.58	8.41	76.72	43.44	0.89
	298.15	32.93	9.67	34.33	3.27	0.96
	323.15	6.44	2.35	77.33	13.85	0.97
	348.15	6.24	1.57	91.68	14.71	0.99
6·6,5-SWNTs	273.15	16.79	2.21	64.03	3.96	1.00
	298.15	10.03	1.72	75.92	5.88	0.99
	323.15	12.08	5.65	59.37	11.83	0.94
	348.15	13.21	1.16	66.23	2.99	1.00

2.5. BIBLIOGRAPHY

(1) de Juan, A.; Pouillon, Y.; Ruiz-González, L.; Torres-Pardo, A.; Casado, S.; Martín, N.; Rubio, Á.; Pérez, E. M. Mechanically Interlocked Single-Wall Carbon Nanotubes. *Angew. Chem. Int. Ed.* **2014**, *53* (21), 5394–5400.

(2) López-Moreno, A.; Nieto-Ortega, B.; Moffa, M.; de Juan, A.; Bernal, M. M.; Fernández-Blázquez, J. P.; Vilatela, J. J.; Pisignano, D.; Pérez, E. M. Threading through Macrocycles Enhances the Performance of Carbon Nanotubes as Polymer Fillers. *ACS Nano* **2016**, *10* (8), 8012–8018.

(3) Blanco, M.; Nieto-Ortega, B.; de Juan, A.; Vera-Hidalgo, M.; López-Moreno, A.; Casado, S.; González, L. R.; Sawada, H.; González-Calbet, J. M.; Pérez, E. M. Positive and Negative Regulation of Carbon Nanotube Catalysts through Encapsulation within Macrocycles. *Nat. Commun.* **2018**, *9* (1), 2671.

(4) Wielend, D.; Vera-Hidalgo, M.; Seelajaroen, H.; Sariciftci, N. S.; Pérez, E. M.; Whang, D. R. Mechanically Interlocked Carbon Nanotubes as a Stable Electrocatalytic Platform for Oxygen Reduction. *ACS Appl. Mater. Interfaces* **2020**, *12* (29), 32615–32621.

(5) Zhang, W.; Guillén-Soler, M.; Silva, S. M.-D.; López-Moreno, A.; González, L. R.; Giménez-López, M. del C.; Pérez, E. M. Mechanical Interlocking of SWNTs with N-Rich Macrocycles for Efficient ORR Electrocatalysis. *Chem. Sci.* **2022**, *13* (33), 9706–9712.

(6) Moreno-Da Silva, S.; Martínez, J. I.; Develioglu, A.; Nieto-Ortega, B.; de Juan-Fernández, L.; Ruiz-Gonzalez, L.; Picón, A.; Oberli, S.; Alonso, P. J.; Moonshiram, D.; Pérez, E. M.; Burzurí, E. Magnetic, Mechanically Interlocked Porphyrin–Carbon Nanotubes for Quantum Computation and Spintronics. *J. Am. Chem. Soc.* **2021**, *143* (50), 21286–21293.

(7) de Juan, A.; López-Moreno, A.; Calbo, J.; Ortí, E.; Pérez, E. M. Determination of Association Constants towards Carbon Nanotubes. *Chem. Sci.* **2015**, *6* (12), 7008–7014.

(8) Calbo, J.; López-Moreno, A.; de Juan, A.; Comer, J.; Ortí, E.; Pérez, E. M. Understanding Noncovalent Interactions of Small Molecules with Carbon Nanotubes. *Chem. Eur. J.* **2017**, *23* (52), 12909–12916.

(9) López-Moreno, A.; Pérez, E. M. Pyrene-Based Mechanically Interlocked SWNTs. *Chem. Commun.* **2015**, *51* (25), 5421–5424.

(10) Leret, S.; Pouillon, Y.; Casado, S.; Navío, C.; Rubio, Á.; Pérez, E. M. Bimodal Supramolecular Functionalization of Carbon Nanotubes Triggered by Covalent Bond Formation. *Chem. Sci.* **2017**, *8* (3), 1927–1935.

(11) de Juan-Fernández, L.; Münich, P. W.; Puthiyedath, A.; Nieto-Ortega, B.; Casado, S.; Ruiz-González, L.; Pérez, E. M.; Guldi, D. M. Interfacing Porphyrins and Carbon Nanotubes through Mechanical Links. *Chem. Sci.* **2018**, *9* (33), 6779–6784.

(12) Chen, R. J.; Zhang, Y.; Wang, D.; Dai, H. Noncovalent Sidewall Functionalization of Single-Walled Carbon Nanotubes for Protein Immobilization. *J. Am. Chem. Soc.* **2001**, *123* (16), 3838–3839.

(13) Murphy, K. P.; Xie, D.; Thompson, K. S.; Amzel, L. M.; Freire, E. Entropy in Biological Binding Processes: Estimation of Translational Entropy Loss. *Proteins* **1994**, *18* (1), 63–67.

(14) Bannwarth, C.; Ehlert, S.; Grimme, S. GFN2-xTB—An Accurate and Broadly Parametrized Self-Consistent Tight-Binding Quantum Chemical Method with Multipole Electrostatics and Density-Dependent Dispersion Contributions. *J. Chem. Theory Comput.* **2019**, *15* (3), 1652–1671.

(15) Bannwarth, C.; Caldeweyher, E.; Ehlert, S.; Hansen, A.; Pracht, P.; Seibert, J.; Spicher, S.; Grimme, S. Extended Tight-Binding Quantum Chemistry Methods. *Comput. Mol. Sci.* **2021**, *11* (2), e1493. 3.

(16) Becke, A. D. Perspective: Fifty Years of Density-Functional Theory in Chemical Physics. *J. Chem. Phys.* **2014**, *140* (18), 18A301.

(17) Becke, A. D. Density-Functional Thermochemistry. V. Systematic Optimization of Exchange-Correlation Functionals. *J. Chem. Phys.* **1997**, *107* (20), 8554–8560.

(18) Schmider, H. L.; Becke, A. D. Optimized Density Functionals from the Extended G2 Test Set. *J. Appl. Phys.* **1998**, *108* (23), 9624–9631.

(19) Grimme, S.; Antony, J.; Ehrlich, S.; Krieg, H. A Consistent and Accurate Ab Initio Parametrization of Density Functional Dispersion Correction (DFT-D) for the 94 Elements H-Pu. *J. Chem. Phys.* **2010**, *132* (15), 154104.

(20) Rassolov, V. A.; Ratner, M. A.; Pople, J. A.; Redfern, P. C.; Curtiss, L. A. 6-31G* Basis Set for Third-Row Atoms. *J. Comp. Chem.* **2001**, *22* (9), 976–984.

(21) Gaussian 16, Revision A.03, Frisch, M. J.; Trucks, G. W.; Schlegel, H. B.; Scuseria, G. E.; Robb, M. A.; Cheeseman, J. R.; Scalmani, G.; Barone, V.; Petersson, G. A.; Nakatsuji, H.; Li, X.; Caricato, M.; Marenich, A. V.; Bloino, J.; Janesko, B. G.; Gomperts, R.; Mennucci, B.; Hratchian, H. P.; Ortiz, J. V.; Izmaylov, A. F.; Sonnenberg, J. L.; Williams-Young, D.; Ding, F.; Lipparini, F.; Egidi, F.; Goings, J.; Peng, B.; Petrone, A.; Henderson, T.; Ranasinghe, D.; Zakrzewski, V. G.; Gao, J.; Rega, N.; Zheng, G.; Liang, W.; Hada, M.; Ehara, M.; Toyota, K.; Fukuda, R.; Hasegawa, J.; Ishida, M.; Nakajima, T.; Honda, Y.; Kitao, O.; Nakai, H.; Vreven, T.; Throssell, K.; Montgomery, J. A., Jr.; Peralta, J. E.; Ogliaro, F.; Bearpark, M. J.; Heyd, J. J.; Brothers, E. N.; Kudin, K. N.; Staroverov, V. N.; Keith, T. A.; Kobayashi, R.; Normand, J.; Raghavachari, K.; Rendell, A. P.; Burant, J. C.; Iyengar, S. S.; Tomasi, J.; Cossi, M.; Millam, J. M.; Klene, M.; Adamo, C.; Cammi, R.; Ochterski, J. W.; Martin, R. L.; Morokum.

(22) Caldeweyher, E.; Bannwarth, C.; Grimme, S. Extension of the D3 Dispersion Coefficient Model. *J. Chem. Phys.* **2017**, *147* (3), 034112.

(23) Ehlert, S.; Stahn, M.; Spicher, S.; Grimme, S. Robust and Efficient Implicit Solvation Model for Fast Semiempirical Methods. *J. Chem. Theory Comput.* **2021**, *17* (7), 4250–4261.

(24) Ribeiro, J.; Ríos-Vera, C.; Melo, F.; Schüller, A. Calculation of Accurate Interatomic Contact Surface Areas for the Quantitative Analysis of Non-Bonded Molecular Interactions. *Bioinformatics* **2019**, *35* (18), 3499–3501.

(25) Pettersen, E. F.; Goddard, T. D.; Huang, C. C.; Couch, G. S.; Greenblatt, D. M.; Meng, E. C.; Ferrin, T. E. UCSF Chimera--a Visualization System for Exploratory Research and Analysis. *J. Comput. Chem.* **2004**, *25* (13), 1605–1612.

(26) Boto, R. A.; Peccati, F.; Laplaza, R.; Quan, C.; Carbone, A.; Piquemal, J.-P.; Maday, Y.; Contreras-García, J. NCIPLOT4: Fast, Robust, and Quantitative

Analysis of Noncovalent Interactions. *J. Chem. Theory Comput.* **2020**, *16* (7), 4150–4158.

(27) Ozawa, H.; Ide, N.; Fujigaya, T.; Niidome, Y.; Nakashima, N. One-Pot Separation of Highly Enriched (6,5)-Single-Walled Carbon Nanotubes Using a Fluorene-Based Copolymer. *Chem. Lett.* **2011**, *40* (3), 239–241.

(28) Canevet, D.; Gallego, M.; Isla, H.; de Juan, A.; Pérez, E. M.; Martín, N. Macrocyclic Hosts for Fullerenes: Extreme Changes in Binding Abilities with Small Structural Variations. *J. Am. Chem. Soc.* **2011**, *133* (9), 3184–3190.

Chapter 3

Magnetic, Mechanically Interlocked Porphyrin–Carbon Nanotubes for Quantum Computation and Spintronics

Moreno-Da Silva, S.; Martínez, J. I.; Develioglu, A.; Nieto-Ortega, B.; de JuanFernández, L.; Ruiz-Gonzalez, L.; Picón, A.; Oberli, S.; Alonso, P. J.; Moonshiram, D.; Pérez, E. M.; Burzurí, E. *J. Am. Chem. Soc.* **2021**, *143* (50), 21286–21293

Atomic-scale reproducibility and tunability endorse magnetic molecules as candidates for spin qubits and spintronics. A major challenge is to implant those molecular spins into circuit geometries that may allow one, two or a few spins to be addressed in a controlled way. Here, the formation of mechanically bonded magnetic porphyrin dimeric rings around carbon nanotubes (mMINTs) is presented. The mechanical bond places the porphyrin magnetic cores in close contact with the carbon nanotube without disturbing their structures. A combination of spectroscopic techniques shows that the magnetic geometry of the dimers is preserved upon formation of the macrocycle and the mMINT. Moreover, the metallic core selection determines the spin location in the mMINT. The suitability of mMINTs as qubits is explored by measuring their quantum coherence times (T_m). Formation of the dimeric ring preserves T_m found in the monomer, which remains in the µs scale for mMINTs. The carbon nanotube is used as vessel to place the molecules in complex circuits. This strategy can be extended to other families of magnetic molecules. The size and composition of the macrocycle can be tailored to modulate magnetic interactions between the cores and to introduce magnetic asymmetries (heterometallic dimers) for more complex molecule-based qubits.

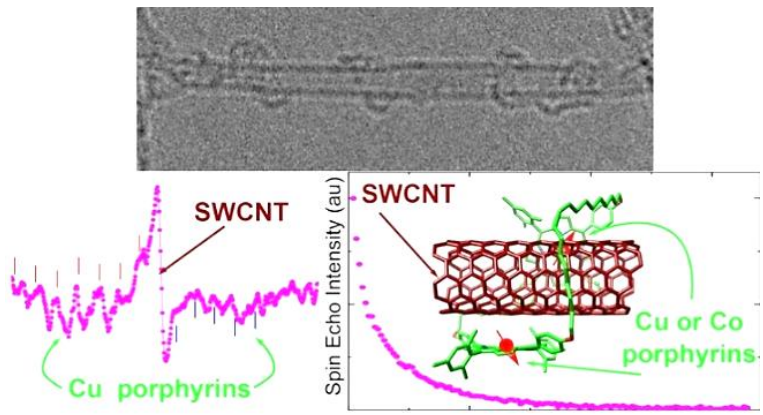

3.1. INTRODUCTION

Magnetic molecules have been proposed as versatile building blocks for quantum computing[1,2] and molecular spintronics[3] devices. The molecular spin can be used to encode quantum information in qubits[1,2] or even perform logic operations as quantum gates[4–6] with unmatched reproducibility and scalability.[7] In spintronics, that same molecular spin can be used to generate spin currents in molecular-based spin filters,[8,9] spin switches[10,11] or spin valves in carbon-nanotube/molecule hybrids[12] among other applications.

The adaptability in chemical synthesis provides a wide variety of customized magnetic molecules. Some of the most studied families, specifically designed for quantum information and spintronics applications, are porphyrins,[13–15] organic radicals[16–18] and single-ion magnets like phthalocyanines[6,12,19] or

[1] Leuenberger, M. N.; Loss, D. *Nature* **2001**, *410* (6830), 789–793.
[2] Gaita-Ariño, A.; Luis, F.; Hill, S.; Coronado, E. *Nat. Chem.* **2019**, *11* (4), 301–309.
[3] Sanvito, S. *Chem. Soc. Rev.* **2011**, *40* (6), 3336–3355.
[4] Luis, F.; Repollés, A.; Martínez-Pérez, M. J.; Aguilà, D.; Roubeau, O.; Zueco, D.; Alonso, P. J.; Evangelisti, M.; Sesé, J.; Barrios, L. A.; Aromí, G. *Phys. Rev. Lett.* **2011**, *107* (11), 117203.
[5] Aguilà, D.; Barrios, L. A.; Velasco, V.; Roubeau, O.; Repollés, A.; Alonso, P. J.; Sesé, J.; Teat, S. J.; Luis, F.; Aromí, G. *J. Am. Chem. Soc.* **2014**, *136* (40), 14215–14222.
[6] Godfrin, C.; Ferhat, A.; Ballou, R.; Klyatskaya, S.; Ruben, M.; Wernsdorfer, W.; Balestro, F. *Phys. Rev. Lett.* **2017**, *119* (18), 187702.
[7] Moreno-Pineda, E.; Godfrin, C.; Balestro, F.; Wernsdorfer, W.; Ruben, M. *Chem. Soc. Rev.* **2018**, *47* (2), 501–513.
[8] Herrmann, C.; Solomon, G. C.; Ratner, M. A. *J. Am. Chem. Soc.* **2010**, *132* (11), 3682–3684.
[9] Pal, A. N.; Li, D.; Sarkar, S.; Chakrabarti, S.; Vilan, A.; Kronik, L.; Smogunov, A.; Tal, O. *Nat. Commun.* **2019**, *10* (1), 5565.
[10] Zhang, J. L.; Zhong, J. Q.; Lin, J. D.; Hu, W. P.; Wu, K.; Xu, G. Q.; Wee, A. T. S.; Chen, W. *Chem. Soc. Rev.* **2015**, *44* (10), 2998–3022.
[11] Burzurí, E.; García-Fuente, A.; García-Suárez, V.; Kumar, K. S.; Ruben, M.; Ferrer, J.; Zant, H. S. J. van der. *Nanoscale* **2018**, *10* (17), 7905–7911.
[12] Urdampilleta, M.; Klyatskaya, S.; Cleuziou, J.-P.; Ruben, M.; Wernsdorfer, W. *Nature Mater.* **2011**, *10* (7), 502–506.
[13] Urtizberea, A.; Natividad, E.; Alonso, P. J.; Andrés, M. A.; Gascón, I.; Goldmann, M.; Roubeau, O. *Adv. Funct. Mat.* **2018**, *28* (31), 1801695.
[14] Yu, C.-J.; Krzyaniak, M. D.; Fataftah, M. S.; Wasielewski, M. R.; Freedman, D. E. *Chem. Sci.* **2019**, *10* (6), 1702–1708.
[15] von Kugelgen, S.; Krzyaniak, M. D.; Gu, M.; Puggioni, D.; Rondinelli, J. M.; Wasielewski, M. R.; Freedman, D. E. *J. Am. Chem. Soc.* **2021**, *143* (21), 8069–8077.
[16] Mas-Torrent, M.; Crivillers, N.; Mugnaini, V.; Ratera, I.; Rovira, C.; Veciana, J. *J. Mater. Chem.* **2009**, *19* (12), 1691–1695.
[17] Gaudenzi, R.; de Bruijckere, J.; Reta, D.; Moreira, I. de P. R.; Rovira, C.; Veciana, J.; van der Zant, H. S. J.; Burzurí, E. *ACS Nano* **2017**, *11* (6), 5879–5883.
[18] Dai, Y.-Z.; Dong, B.-W.; Kao, Y.; Wang, Z.-Y.; Un, H.-I.; Liu, Z.; Lin, Z.-J.; Li, L.; Xie, F.-B.; Lu, Y.; Xu, M.-X.; Lei, T.; Sun, Y.-J.; Wang, J.-Y.; Gao, S.; Jiang, S.-D.; Pei, J. *ChemPhysChem* **2018**, *19* (22), 2972–2977.
[19] Atzori, M.; Tesi, L.; Morra, E.; Chiesa, M.; Sorace, L.; Sessoli, R. *J. Am. Chem. Soc.* **2016**, *138* (7), 2154–2157.

polyoxometalates.[20,21] One of the more daunting obstacles that remains to be removed is to place and address such molecular spins in solid-state devices in a controlled way while preserving their properties. A technically challenging approach involves in the direct contact of the individual molecule to nanospaced electrodes in a transistor geometry.[22] Pioneer works using this technique have demonstrated control over a spin qubit[23] and the realization of the first quantum algorithm in terbium phthalocyanines.[6] Alternative approaches make use of Cu porphyrins to self-assemble 2D molecular networks on surfaces[13] or in metal-organic frameworks (MOFs).[14] In both examples, Cu porphyrins preserve quantum coherence to be used as qubits. The access to each molecular spin qubit would be performed through local superconducting circuits.[24,25]

Interestingly, an indirect method, mainly used in molecular spintronics, involves using a one-dimensional single-wall carbon nanotube (SWNT) as an intermediate channel onto which the magnetic molecule is attached.[12,26,27] The current flowing through the SWNT backbone probes the spin without disturbing its state. *Vice versa*, a combination of molecular spins on a carbon nanotube can be used to alter the current flow in a controlled way. This geometry has been used to fabricate supramolecular spin valves based on double-decker phthalocyanines.[12,26]

---

[6] Godfrin, C.; Ferhat, A.; Ballou, R.; Klyatskaya, S.; Ruben, M.; Wernsdorfer, W.; Balestro, F. *Phys. Rev. Lett.* **2017**, *119* (18), 187702.

[12] Urdampilleta, M.; Klyatskaya, S.; Cleuziou, J.-P.; Ruben, M.; Wernsdorfer, W. *Nature Mater.* **2011**, *10* (7), 502–506.

[13] Urtizberea, A.; Natividad, E.; Alonso, P. J.; Andrés, M. A.; Gascón, I.; Goldmann, M.; Roubeau, O. *Adv. Funct. Mat.* **2018**, *28* (31), 1801695.

[14] Yu, C.-J.; Krzyaniak, M. D.; Fataftah, M. S.; Wasielewski, M. R.; Freedman, D. E. *Chem. Sci.* **2019**, *10* (6), 1702–1708.

[20] Clemente-Juan, J. M.; Coronado, E.; Gaita-Ariño, A. *Chem. Soc. Rev.* **2012**, *41* (22), 7464–7478.

[21] Lehmann, J.; Gaita-Ariño, A.; Coronado, E.; Loss, D. *Nature Nanotech.* **2007**, *2* (5), 312–317.

[22] Perrin, M. L.; Burzurí, E.; Zant, H. S. J. van der. Single-Molecule Transistors. *Chem. Soc. Rev.* **2015**, *44* (4), 902–919.

[23] Thiele, S.; Balestro, F.; Ballou, R.; Klyatskaya, S.; Ruben, M.; Wernsdorfer, W. *Science* **2014**, *344* (6188), 1135–1138.

[24] Jenkins, M. D.; Zueco, D.; Roubeau, O.; Aromí, G.; Majer, J.; Luis, F. *Dalton Trans.* **2016**, *45* (42), 16682–16693.

[25] Carretta, S.; Zueco, D.; Chiesa, A.; Gómez-León, Á.; Luis, F. *Appl. Phys. Lett.* **2021**, *118* (24), 240501.

[26] Urdampilleta, M.; Nguyen, N.-V.; Cleuziou, J.-P.; Klyatskaya, S.; Ruben, M.; Wernsdorfer, W. *Int. J. Mol. Sci.* **2011**, *12* (10), 6656–6667.

[27] Villalva, J.; Develioglu, A.; Montenegro-Pohlhammer, N.; Sánchez-de-Armas, R.; Gamonal, A.; Rial, E.; García-Hernández, M.; Ruiz-Gonzalez, L.; Costa, J. S.; Calzado, C. J.; Pérez, E. M.; Burzurí, E. *Nat. Commun.* **2021**, *12*, 1578.

Several strategies have been followed to couple the magnetic molecules to carbon nanotubes: the most straightforward one is the direct physisorption of the molecules with or without specific anchoring groups to enhance van der Waals interactions with the SWNTs.[28–30] A less explored case is the covalent bonding of the magnetic molecule.[31] Additional, more exotic approaches include the encapsulation of the magnetic molecules.[27,32,33] The first case provides a soft although weak anchoring that helps preserve the spin state in the molecule and the carbon nanotube sp^2 hybridization. The second case is a stronger bond that, in turn, may create local defects on the nanotube or transform the magnetic properties of the target molecule, affecting its quantum coherence.

More recently, the synthesis of mechanically interlocked rotaxane-like SWNT derivatives (MINTs) was developed in our group, in which the ring-closing metathesis of a U-shape molecule around SWNTs is templated using suitable SWNT recognition motifs.[34] Importantly, the number of macrocycles around the SWNT can be controlled.[35,36] Rotaxane-like structures have recently shown their potential to form magnetic mechanically interlocked derivatives.[37] Alternatively, we have also explored the use of self-assembled H-bonded macrocycles, in collaboration with Gonzalez-Rodríguez.[38] Miki and Ohe have used pre-formed macrocycles to directly encapsulate SWNTs in solution.[39] Very recently, von Delius

[27] Villalva, J.; Develioglu, A.; Montenegro-Pohlhammer, N.; Sánchez-de-Armas, R.; Gamonal, A.; Rial, E.; García-Hernández, M.; Ruiz-Gonzalez, L.; Costa, J. S.; Calzado, C. J.; Pérez, E. M.; Burzurí, E. *Nat. Commun.* **2021**, *12*, 1578.

[28] Kyatskaya, S.; Galán Mascarós, J. R.; Bogani, L.; Hennrich, F.; Kappes, M.; Wernsdorfer, W.; Ruben, M. *J. Am. Chem. Soc.* **2009**, *131* (42), 15143–15151.

[29] Ganzhorn, M.; Klyatskaya, S.; Ruben, M.; Wernsdorfer, W. *Nature Nanotech.* **2013**, *8* (3), 165–169.

[30] Garrido, M.; Volland, M. K.; Münich, P. W.; Rodríguez-Pérez, L.; Calbo, J.; Ortí, E.; Herranz, M. Á.; Martín, N.; Guldi, D. M. *J. Am. Chem. Soc.* **2020**, *142* (4), 1895–1903.

[31] Schnee, M.; Besson, C.; Frielinghaus, R.; Lurz, C.; Kögerler, P.; Schneider, C. M.; Meyer, C. *Phys. Status Solidi (b)* **2016**, *253* (12), 2424–2427.

[32] del Carmen Giménez-López, M.; Moro, F.; La Torre, A.; Gómez-García, C. J.; Brown, P. D.; van Slageren, J.; Khlobystov, A. N. *Nat. Commun.* **2011**, *2* (1), 407.

[33] Domanov, O.; Weschke, E.; Saito, T.; Peterlik, H.; Pichler, T.; Eisterer, M.; Shiozawa, H. *Nanoscale* **2019**, *11* (22), 10615–10621.

[34] Pérez, E. M. *Chem. Eur. J.* **2017**, *23* (52), 12681–12689.

[35] de Juan, A.; Pouillon, Y.; Ruiz-González, L.; Torres-Pardo, A.; Casado, S.; Martín, N.; Rubio, Á.; Pérez, E. M. *Angew. Chem. Int. Ed.* **2014**, *53* (21), 5394–5400.

[36] de Juan, A.; Mar Bernal, M.; Pérez, E. M. *ChemPlusChem* **2015**, *80* (7), 1153–1157.

[37] Cirulli, M.; Salvadori, E.; Zhang, Z.-H.; Dommett, M.; Tuna, F.; Bamberger, H.; Lewis, J. E. M.; Kaur, A.; Tizzard, G. J.; van Slageren, J.; Crespo-Otero, R.; Goldup, S. M.; Roessler, M. M. *Angew. Chem. Int. Ed.* **2021**, *60* (29), 16051–16058.

[38] Chamorro, R.; Juan-Fernández, L. de; Nieto-Ortega, B.; Mayoral, M. J.; Casado, S.; Ruiz-González, L.; Pérez, E. M.; González-Rodríguez, D. *Chem. Sci.* **2018**, *9* (17), 4176–4184.

[39] Miki, K.; Saiki, K.; Umeyama, T.; Baek, J.; Noda, T.; Imahori, H.; Sato, Y.; Suenaga, K.; Ohe, K. *Small* **2018**, *14* (26), 1800720.

et al. have demonstrated that reversible S-S bond formation can also be used to make MINTs.[40] The mechanical bond imparts MINTs with stability comparable to covalent SWNT derivatives.

Here, we apply the mechanical bond to anchor magnetic molecules around carbon nanotubes. Magnetic porphyrins are selected due to their recently proved suitability as qubits,[13–15] even preserving their magnetic properties[41] and quantum coherence[13] on surfaces. Moreover, we have already shown that porphyrins are valid recognition motifs to synthesize MINTs.[42] In particular, we fabricate Cu^{2+} and Co^{2+} (S = 1/2) metalloporphyrin dimer rings mechanically interlocked around carbon nanotubes to form magnetic MINTs (hereafter mMINT), as shown in Figure 1. The mechanical bond places the porphyrin magnetic cores in close contact with the SWNT without disturbing the molecular spin nor the carbon nanotube structure, combining thus the advantages of van der Waals and covalent approaches. We show that the magnetic properties of the metallic dimers are preserved upon formation of the macrocycle and the mechanically interlocked hybrid. Quantum coherence times (T_m), which measure the coherence loss rate and thus the quality of a qubit, are found to be in the order of 25 μs in the porphyrin monomer and the dimeric rings. Quantum relaxation is therefore not altered by the formation of the ring. Importantly, T_m remains in the μs range in the mMINT, indicating a roughly preserved quantum coherence of the porphyrin spin. The carbon nanotube can be used as vessel to position the molecules in nanoscale spintronics and quantum devices.[27] A proof-of-concept field-effect transistor device containing a single mMINT is fabricated. This strategy based on the mechanical bond can be extended to other families of magnetic molecules. Furthermore, the size of the macrocycle can be tailored to promote or suppress magnetic interactions between magnetic

[13] Urtizberea, A.; Natividad, E.; Alonso, P. J.; Andrés, M. A.; Gascón, I.; Goldmann, M.; Roubeau, O. *Adv. Funct. Mat.* **2018**, *28* (31), 1801695.
[14] Yu, C.-J.; Krzyaniak, M. D.; Fataftah, M. S.; Wasielewski, M. R.; Freedman, D. E. *Chem. Sci.* **2019**, *10* (6), 1702–1708.
[15] von Kugelgen, S.; Krzyaniak, M. D.; Gu, M.; Puggioni, D.; Rondinelli, J. M.; Wasielewski, M. R.; Freedman, D. E. *J. Am. Chem. Soc.* **2021**, *143* (21), 8069–8077.
[27] Villalva, J.; Develioglu, A.; Montenegro-Pohlhammer, N.; Sánchez-de-Armas, R.; Gamonal, A.; Rial, E.; García-Hernández, M.; Ruiz-Gonzalez, L.; Costa, J. S.; Calzado, C. J.; Pérez, E. M.; Burzurí, E. *Nature Commun.* **2021**, *12*, 1578.
[40] Balakrishna, B.; Menon, A.; Cao, K.; Gsänger, S.; Beil, S. B.; Villalva, J.; Shyshov, O.; Martin, O.; Hirsch, A.; Meyer, B.; Kaiser, U.; Guldi, D. M.; von Delius, M. *Angew. Chem. Int. Ed.* **2020**, *59* (42), 18774–18785.
[41] Auwärter, W.; Écija, D.; Klappenberger, F.; Barth, J. V. *Nature Chem.* **2015**, *7* (2), 105–120.
[42] de Juan-Fernández, L.; Münich, P. W.; Puthiyedath, A.; Nieto-Ortega, B.; Casado, S.; Ruiz-González, L.; Pérez, E. M.; Guldi, D. M. *Chem. Sci.* **2018**, *9* (33), 6779–6784.

cores in the ring, or to introduce asymmetries. Our experimental findings are supported by density functional theory (DFT) calculations.

3.2. RESULTS AND DISCUSSION

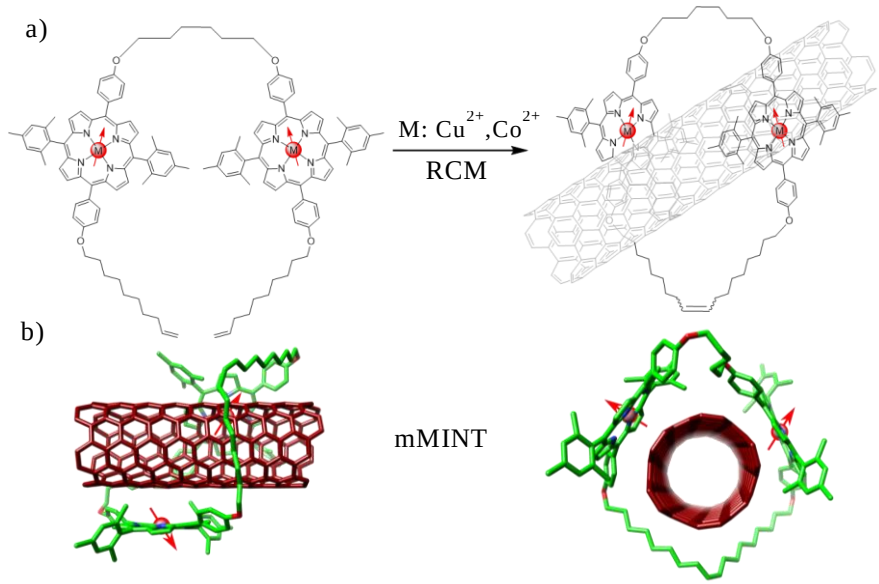

Figure 1. a) Synthetic route to obtain the magnetic MINT (mMINT). The open porphyrin-based macrocycle (U-por) closes through a ring closing metathesis (RCM) and forms the mac-por around the SWNT. b) Relaxed mMINT structure obtained by density functional theory (DFT) calculations. The magnetic centers are placed at about 3.4-3.8 Å from the SWNT surface. No bending of the porphyrin plane is observed.

The synthetic route to obtain the target Co and Cu mMINTs is summarized in Figure 1a. The initial steps to obtain the free-base U-por are described in detail in our previous work.[42] The last step was the metalation of the linear precursor with cobalt and copper acetates. The formation of the metalated porphyrin is proved by infrared spectroscopy and mass spectrometry (see S2, S7). Once the metalated U-por is obtained, the metalated porphyrin macrocycle (metalated mac-por) was synthesized through ring-closing metathesis (RCM) reaction. The target Cu and Co metalated mMINTs are obtained by RCM but using (6,5)-SWNTs as a template for the formation of the metalated mac-por around the carbon nanotube. Briefly, the nanotubes were suspended in tetrachloroethane (TCE) via ultrasonication, mixed with Co/Cu U-por compounds, and N_2-bubbled for 20 min. They were then mixed

[42] de Juan-Fernández, L.; Münich, P. W.; Puthiyedath, A.; Nieto-Ortega, B.; Casado, S.; Ruiz-González, L.; Pérez, E. M.; Guldi, D. M. *Chem. Sci.* **2018**, *9* (33), 6779–6784.

with Grubbs second-generation catalyst, and the dispersion was stirred at room temperature for 72h, filtered through a polytetrafluoroethylene membrane with a pore size of 0.2 µm, and washed with dichloromethane until complete elimination of physisorbed byproducts and catalyst. Figure 1b shows different perspectives of the final mMINTs calculated by relaxing their structure by DFT (see S8). A control sample was prepared by following the same experimental procedure but without the catalyst (see S3, S4).

The mMINT derivatives were analyzed with different characterization techniques to prove the formation of the mechanical bond and the structural stability. Thermogravimetric analysis (TGA) on the mMINTs shows an initial weight loss of 20% and 24% for Co and Cu por-MINTs respectively at 320 ºC, not present in pristine SWNT nor the control samples (See S3, S4, S5). This has been associated before to organic material not simply physisorbed but forming mechanical bonds around the nanotubes.[34,42] Raman spectroscopy on the mMINT complexes shows no significant energy shifts (<4 cm^{-1}) nor modification of the relative height in the SWNT bands (see S6). No significant defects nor electronic modulation respectively are therefore introduced in the SWNTs with the formation of the mMINTs, as expected for a mechanical bond.[34]

Additional proofs of the formation of the mMINTs are provided by microscopy. Figure 2a shows a high-resolution transmission electron microscope image (HR-TEM) of an individual Co-mMINT. Four rings embracing the SWNT can be clearly observed. Their size agrees with the expected for the mac-por in the mMINT.[42] In addition, the shape of some of them can be correlated with specific orientations of the macrocycle, as modeled by DFT (See S9). Figure 2b shows an atomic force microscopy (AFM) image taken on an individual Co-mMINT. The image is obtained by drop casting of a sample suspension in TCE onto a mica plate. The results reveal the presence of isolated carbon nanotubes (~1 nm high) covered by a few brighter spots of ~2.3-2.6 nm high, as seen in the selected profiles in Figure 2c. The height is in good agreement with the size estimated by DFT for the mMINTs (see S8)

[34] Pérez, E. M. *Chem. Eur. J.* **2017**, *23* (52), 12681–12689.
[42] de Juan-Fernández, L.; Münich, P. W.; Puthiyedath, A.; Nieto-Ortega, B.; Casado, S.; Ruiz-González, L.; Pérez, E. M.; Guldi, D. M. *Chem. Sci.* **2018**, *9* (33), 6779–6784.

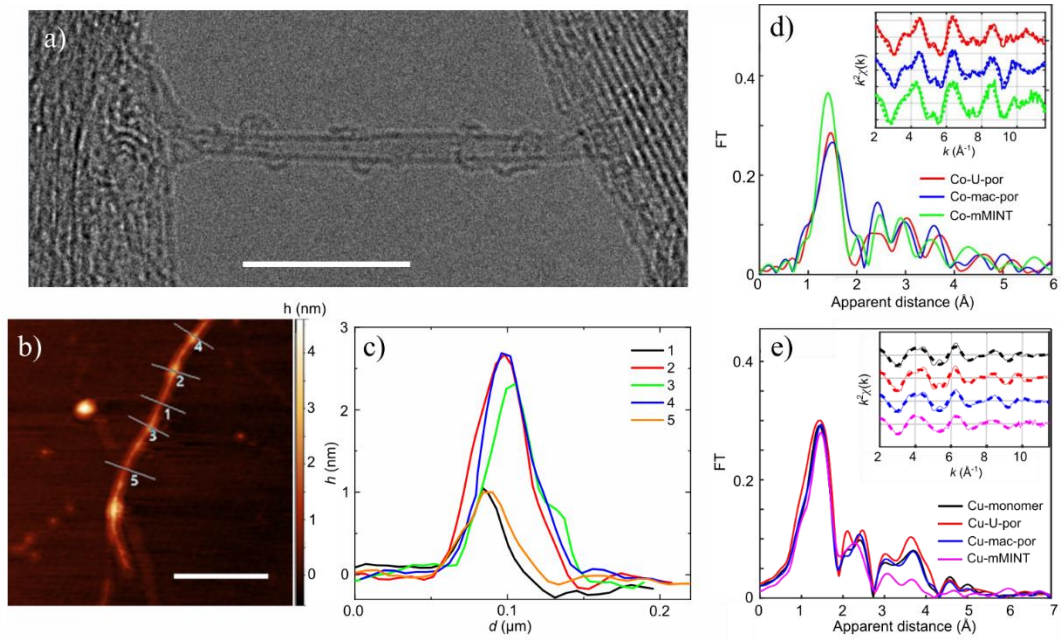

Figure 2. a) HR-TEM image showing a single Co-mMINT. Four Co-mac-por rings can be seen embracing the SWNT. Scale bar: 10 nm. b) AFM image taken on an individual Co-mMINT. Several bright spots appear along the SWNT. Scale bar: 400 nm. c) Height profiles taken across the bright spots (2, 3, and 4). Profiles 1 and 5 are taken on the darker areas as a reference. The reference profiles match with the height of the SWNT (~1 nm). The brighter area profiles are in good agreement with the height of the mMINT expected from DFT calculations. d) and e) Experimental Fourier transforms of k^2-weighted Co and Cu EXAFS of the different complexes. The experimental spectra were calculated for k values of 2-11.5 $Å^{-1}$. Inset: Back Fourier transformed experimental (solid lines) and fitted (dashed lines) $k^2[\chi(k)]$ of the different derivatives.

The integrity of the coordination sphere around the metals in the mMINTs and the molecular precursors is studied by X-ray absorption near edge structure (XANES) and extended X-ray absorption fine structure (EXAFS) spectroscopic techniques. The normalized XANES spectra show that all Co and Cu porphyrin derivatives, including the mMINTs, are four-coordinated and in the +2 oxidation state (See S10 for full details). The analysis of the EXAFS spectra, shown in Figure 2(d,e), provides a direct probe of possible changes in the Co-N and Cu-N bond lengths. All four Cu-porphyrin complexes demonstrate very similar Cu-N bond lengths 1.99-2.04 Å, indicating the close to intact coordination sphere of the Cu mMINT complex (See S10). In turn, the Co porphyrin derivatives exhibit small deviations from a square planar geometry with Co-N bond distances between 1.91 and 1.95 Å and an additional lengthened Co-O distance, as explained below.

The magnetism of all porphyrin derivatives has been analyzed by continuous-wave electron paramagnetic resonance (EPR) spectroscopy. shows the X-band EPR spectra of the Cu a) monomer, b) U-por, and c) mac-por derivatives (See S11 for more EPR details). The molecules are dispersed in a chloroform/tetrachloroethane mixture to promote glass-like solids at cryogenic temperatures while avoiding aggregates. The Cu-monomer spectrum is then well described by an $S = 1/2$ species with an axial Zeeman interaction and a hyperfine coupling with an $I = 3/2$ nuclear spin (dotted line in a). This corresponds with a Cu^{2+} ion ($3d^9$ configuration) in a square planar environment, with the unpaired electron placed in the in-plane $d_{x^2-y^2}$ copper orbital, (see S11) and showing a resolved hyperfine coupling with the nuclei of the two naturally abundant Cu isotopes. The additional splitting corresponds to super hyperfine couplings with the ligands´ nitrogen nuclei ($I_N = 1$), which are not included in our simulations. The Cu-U-por (b) and Cu-mac-por (c) EPR spectra show no significant differences of the EPR spectral features with the monomer spectrum, indicating that the spin state and the ligands´ geometry characterizing the Cu magnetic properties are preserved upon cycling the U-por molecule into the mac-por structure. Only changes in the width of the super hyperfine lines are seen, surely originated by the well-known aggregation/freezing problems with Cu-porphyrins that lead to variations in the distribution of dipolar fields.[43] Besides, the U-por and mac-por spectra can be fitted with negligible exchange coupling between the spins, indicating a negligible magnetic coupling between the two copper centers. This result is expected, given the long atomic bridges connecting both metallic species, as very recently demonstrated.[15]

Similar conclusions can be extracted from the EPR spectra measured on the Co derivatives, as seen in (d-f). The EPR spectra of the three derivatives can be interpreted as coming from an $S = 1/2$ showing a hyperfine interaction with a $I = 7/2$ nuclear spin. This is the typical situation for a low spin Co^{2+} center. However, there are some subtle differences with respect to the Cu derivatives. The EPR spectra can be explained using quasi-axial gyromagnetic and hyperfine tensors. Simulation of the EPR spectrum using parameters $g_\perp = 1.998$, $g_\parallel = 2.1025$, $A_\perp = 52$ MHz, $A_\parallel = 86$ MHz (dotted line in d) shows a fair fit to the experiments, but it is

[15] von Kugelgen, S.; Krzyaniak, M. D.; Gu, M.; Puggioni, D.; Rondinelli, J. M.; Wasielewski, M. R.; Freedman, D. E. *J. Am. Chem. Soc.* **2021**, *143* (21), 8069–8077.

[43] Cunningham, K. L.; McNett, K. M.; Pierce, R. A.; Davis, K. A.; Harris, H. H.; Falck, D. M.; McMillin, D. R. *Inorg. Chem.* **1997**, *36* (4), 608–613.

also evident that orthorhombic tensors ($g_x \neq g_y$, $A_x \neq A_y$) could be necessary for a better fitting.

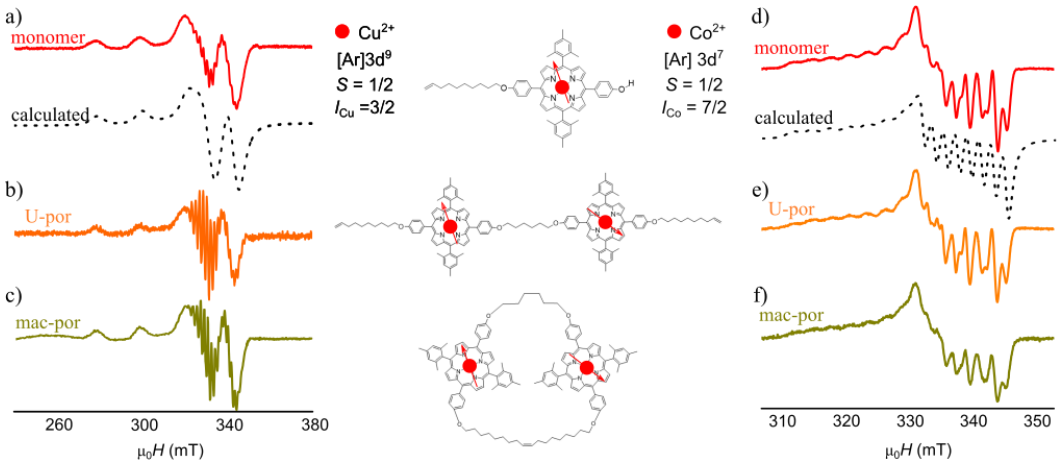

Figure 3. X-band electron paramagnetic resonance (EPR) spectra measured at T = 20 K on the Cu a) porphyrin monomer, b) U-por, and c) mac-por, and the Co d) porphyrin monomer, e) U-por, and f) mac-por. The dotted lines are simulations of the monomer spectra with Cu: $g_\perp$ = 2.055, $g_\parallel$ = 2.19, $A_\perp$ = 40 MHz, and $A_\parallel$ = 620 MHz, and with Co: $g_\perp$ = 1.998, $g_\parallel$ = 2.1025, $A_\perp$ = 52 MHz, and $A_\parallel$ = 86 MHz. The superhyperfine interaction is not included in the simulations.

An out-of-plane pseudo-axial geometry has been reported before for cobalt porphyrins where Co^{2+} can easily bond to molecular oxygen or other small molecules in the axial direction.[44–48] The mass spectroscopy analysis performed in the three derivatives points indeed to the presence of small molecules coordinated to the porphyrin (See S2). In addition, EXAFS shows an improvement in the fit quality upon addition of a Co-O bond at 2.34-2.57 Å (See S10). In this configuration, the unpaired electron resides mainly in the d_z^2 orbital out of the porphyrin plane formed by the N ligands.[49,50] The absence of super hyperfine interactions with the four surrounding N nuclei, observed in contrast for the Cu derivatives, supports this scenario.

[44] Walker, F. Ann. *J. Am. Chem. Soc.* **1970**, *92* (14), 4235–4244.
[45] Hoffman, B. Mark.; Diemente, D. L.; Basolo, Fred. *J. Am. Chem. Soc.* **1970**, *92* (1), 61–65.
[46] Baumgarten, M.; Winscom, C. J.; Lubitz, W. *Appl. Magn. Reason.* **2001**, *20* (1–2), 35–70.
[47] Van Doorslaer, S.; Schweiger, A. *J. Phys. Chem. B* **2000**, *104*, 2919–2927.
[48] Collman, J. P.; Berg, K. E.; Sunderland, C. J.; Aukauloo, A.; Vance, M. A.; Solomon, E. I. *Inorg. Chem.* **2002**, *41* (25), 6583.
[49] Skrzypek, D.; Madejska, I.; Habdas, J. *Solid State Sci.* **2007**, *9* (3–4), 295–302.
[50] Jones, R. D.; Summerville, D. A.; Basolo, Fred. *Chem. Rev.* **1979**, *79* (2), 139–179.

Differences in widths of the spectral feature are found between Co derivatives. In particular, the in-plane components for the Co-mac-por (see S12 for a direct comparison between spectra). There could be several causes for this: mechanical strain induced to accommodate the adsorbed molecules in both porphyrins when the macrocycle is closed could produce slightly higher distortion of the in-plane rings, and/or the two Co porphyrins are not completely equivalent. EXAFS shows a slight deviation as well from the square planar geometry in the Co mac-por and mMINT due to bonding of an additional Co-O distance (see Figure 2d). Additional strain coming from frozen solvent or broadening caused by a higher aggregation tendency of mac-por as compared to the U-por molecules cannot be discarded either.

Next, the EPR spectra of the Cu-mMINT and Co-mMINT can be seen in Figure 4(a,b) and the section S12, respectively. A clear $S = 1/2$, $g = 2$ resonance is observed in both mMINT derivatives. This spectrum has been described as originated by itinerant spins in the carbon nanotube.[51] Interestingly, a spectral feature coming from the Cu porphyrin centers, similar to Cu-mac-por, appears (Figure 4b). Only small variations of position and intensity of the nitrogen hyperfine pattern is detected, indicating minor (if any) differences of the molecular symmetry around the spin. This would point to a soft contact between porphyrins and SWNTs introducing only a slight distortion to the square planar geometry, in agreement with the bond distances obtained by EXAFS (Figure 2d,e) and the DFT calculations. No significant distortions of the metallic coordination spheres are predicted by DFT when in close proximity to the SWNT (around 3.5 Å and 3.8 Å for the two metallic centers). The porphyrin structure does not bend towards the carbon nanotube, prevailing the U-por planar geometry, in agreement with other reports of porphyrins on surfaces.[13,41] Note that we can safely discard that this EPR signal could be originated by residual closed macrocycles not embraced around the carbon nanotube. First, the TGA analysis does not show non-attached supramolecular remnant after washing of the mMINTs. In addition, EXAFS do not indicate signatures of other more distorted coordination spheres or oxidized Cu/Co metal centers that could be potentially ascribed to distorted porphyrins embracing the SWNT.

[13] Urtizberea, A.; Natividad, E.; Alonso, P. J.; Andrés, M. A.; Gascón, I.; Goldmann, M.; Roubeau, O. *Adv. Funct. Mat.* **2018**, *28* (31), 1801695.
[41] Auwärter, W.; Écija, D.; Klappenberger, F.; Barth, J. V. *Nature Chem.* **2015**, *7* (2), 105–120.
[51] Chen, Y.; Chen, J.; Hu, H.; Hamon, M. A.; Itkis, M. E.; Haddon, R. C. *Chem. Phys. Lett.* **1999**, *299* (6), 532–535.

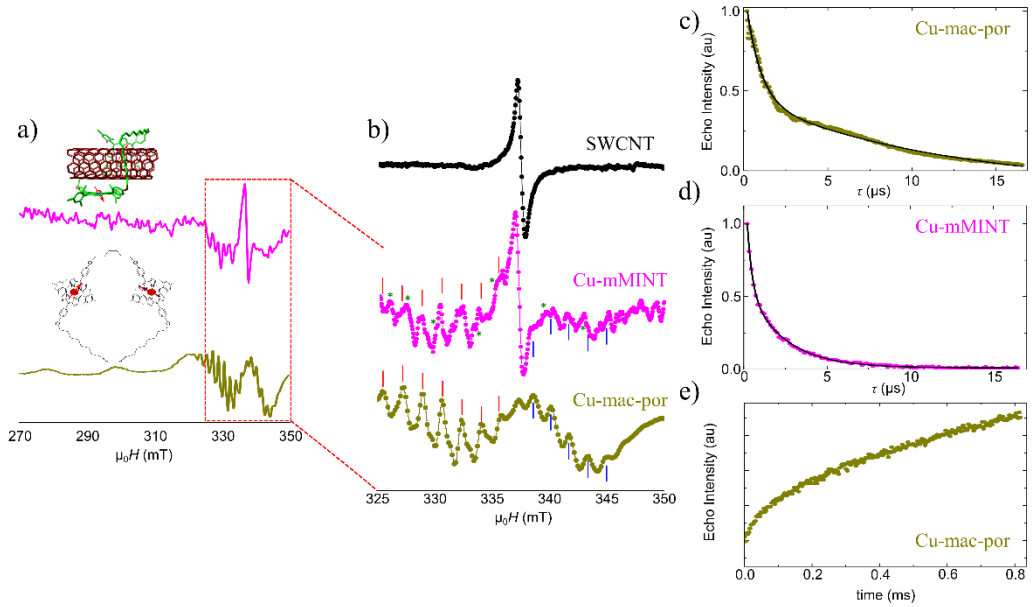

Figure 4. a) X-band EPR spectra measured at T = 20 K on the Cu-mMINT (Upper trace) and the Cu-mac-por (lower trace). b) Zoom on the highest magnetic field region, showing spectra from pristine SWNTs (upper trace), Cu-mMINT (medium trace) and Cu-mac-por (lower trace) samples. Cu-mMINT spectra show the signal corresponding to the SWNT, as well as the nitrogen hyperfine coupling pattern from the Cu centers in the mac-por (see text). The colored lines are guides to the eye to the most representative resonances observed in both the Cu-mMINT and the Cu mac-por. Asterisks mark resonances observed in both the Cu-mMINT and the Cu mac-por. c) and d) Echo intensity decay measured after Hahn sequence of pulses at 11 K and 331 mT for the Cu mac-por c) and mMINT d) respectively. Solid lines are fit to exponential decays (see text). e) Inversion-recovery curve measured at 11 K and 331 mT for the Cu mac-por.

Strikingly, the spectrum measured on the Co-mMINT does not show any clear contribution from Co porphyrins (see S12). This is surprising since EXAFS unambiguously shows the presence of Co^{2+} in a roughly preserved coordination sphere in the mMINT. The spin geometry is therefore expected to remain unaltered. A possible explanation for this difference between Co- and Cu-based mMINTs is a lower proportion of magnetic molecules per carbon nanotube in the Co-mMINTs that buries their EPR signal under the SWNT contribution. However, the TGA points to a relatively similar functionalization of the Co-mMINT and Cu-mMINT (see S5). Alternatively, the different molecular orbitals occupied by the unpaired electron for Cu and Co, $d_{x^2-y^2}$ and d_{z^2} respectively, may determine the proximity and interaction of the spin with the SWNT, and therefore its EPR spectrum. A similar scenario has been previously reported for vanadyl phthalocyanines on a superconducting substrate. The orientation of the orbitals occupied by the spin determines the degree of spin delocalization over the substrate. Molecule in-plane

orbitals, like in the Cu-mMINT, tend to establish weak interactions and limited spin delocalization over the substrate, whereas out-of-plane orbitals, like the occupied by the spin in the Co-mMINT, may create strong bound states with electrons in the substrate.[52]

Pulse EPR spectroscopy has been performed on the Cu derivatives to probe the impact of the dimer and mMINT formation on the phase memory time (T_m). This parameter comprises the intrinsic relaxation T_2 and the extrinsic interactions with the environment. T_m parametrizes the quantum coherence loss rate and therefore the quality of a physical system to serve as a qubit. Figure 4c shows the spin echo intensity measured in the Cu mac-por after applying a $\pi/2 - \tau - \pi - \tau -$ echo sequence of pulses, known as the Hahn-echo sequence, at 11 K and 331 mT. The echo intensity decay can be fitted with a bi-exponential decay to obtain T_m (see S13). Measurements at different temperatures shows that T_m reaches a maximum of $T_m \approx 25$ µs for the monomer, U-por, and mac-por at around 10 K. These values are consistent with previous reports on porphyrins.[15] Therefore, the formation of the dimeric mac-por does not limit T_m obtained for the monomer. Interestingly, a clear though weaker spin echo is also observed in the Cu mMINT. The fit to the echo intensity decay with time (Figure 4d) provides $T_m = 4$ µs. Quantum coherence remains therefore in the microsecond scale. This value is consistent with reports of porphyrins on surfaces.[13] The drop in T_m may be due to the interaction between the Cu spin and the SWNT itinerant electronic spins, which in turn may give us the handle to read the quantum state of the spin in the porphyrin. The spin-lattice relaxation time (T_1) can be obtained from the spin echo decay measured after applying a sequence of inversion-recovery pulses (see S13). Figure 4e shows the saturation-recovery curve measured in the Cu-mac-por at 11 K and 331 mT. The fit to an exponential decay provides $T_1 = 0.8$ ms. This value remains roughly constant from the monomer to the mac-por and is consistent with reports for porphyrins found in the literature.[13,15] The echo obtained in the mMINT is too weak to obtain T_1.

[13] Urtizberea, A.; Natividad, E.; Alonso, P. J.; Andrés, M. A.; Gascón, I.; Goldmann, M.; Roubeau, O. *Adv. Funct. Mat.* **2018**, *28* (31), 1801695.

[15] von Kugelgen, S.; Krzyaniak, M. D.; Gu, M.; Puggioni, D.; Rondinelli, J. M.; Wasielewski, M. R.; Freedman, D. E. *J. Am. Chem. Soc.* **2021**, *143* (21), 8069–8077.

[52] Malavolti, L.; Briganti, M.; Hänze, M.; Serrano, G.; Cimatti, I.; McMurtrie, G.; Otero, E.; Ohresser, P.; Totti, F.; Mannini, M.; Sessoli, R.; Loth, S. *Nano Lett.* **2018**, *18* (12), 7955–7961.

Finally, as proof-of-concept, a field-effect transistor containing a single mMINT has been fabricated by dielectrophoresis.[27,53] See S14 for details and an SEM image of the device. This preliminary device shows the feasibility of dispersing and deterministically placing individual mMINTs in specific positions of nanoscale devices.

3.3. CONCLUSIONS

We have mechanically interlocked magnetic Co^{2+} and Cu^{2+} porphyrin dimers with carbon nanotubes into mMINTs. We show by means of different structural and spectroscopic techniques that the metal centers in the mac-por and mMINT porphyrins preserve the coordination sphere and structure when cycled with only slight distortions of the square planar geometry. We show that the spin geometry is preserved in the Cu-mMINT, whereas no EPR signature of the Co-mMINT has been observed, although EXAFS unambiguously shows the presence of Co^{2+} in a slightly distorted square planar coordination sphere. The selection of metal determines the orbital the spin will occupy and thus its interaction with the SWNT. This is of great relevance for the design of mMINTs since it provides a handle to modulate the interaction between spin and conduction electros, which may be used to read the molecular spin. Besides, quantum coherence times of 25 µs are found to be robust from the Cu monomer to the mac-por dimer, indicating that the formation of the dimer does not limit T_m. Importantly, T_m remains in the microsecond scale in the Cu-mMINT derivative. A small drop in T_m may be indicative of spin interaction with the SWNT, which would give the key to read the quantum state of the molecular spin. We propose mMINTs as robust hybrid candidates for molecular spintronics and molecular spin qubits. These molecular hybrids are deterministically placed into nanoscale devices by dielectrophoresis. A detailed study of its electronic properties will be the subject of a further study.

[27] Villalva, J.; Develioglu, A.; Montenegro-Pohlhammer, N.; Sánchez-de-Armas, R.; Gamonal, A.; Rial, E.; García-Hernández, M.; Ruiz-Gonzalez, L.; Costa, J. S.; Calzado, C. J.; Pérez, E. M.; Burzurí, E. *Nature Commun.* **2021**, *12*, 1578.

[53] Nieto-Ortega, B.; Villalva, J.; Vera-Hidalgo, M.; Ruiz-González, L.; Burzurí, E.; Pérez, E. M. *Angew. Chem. Int. Ed.* **2017**, *56* (40), 12240–12244.

3.4. SUPPORTING INFORMATION

S1. Experimental section.

Reagents were obtained from usual commercial sources and used without further purification. Solvents were dried following standard procedures. Air-sensitive reactions were carried out under argon atmosphere. Analytical TLC were performed using aluminium-coated Merck Kiesel silica gel 60 F254 plates or aluminium-coated Macherey-Nagel aluminium oxide F254 plates. Column chromatography purification was performed using silica gel (Scharlau 60, 70-230 mesh) or aluminium oxide (Merck, Kieselgel 60, 230-240 mesh).

NMR spectra were recorded on a BrukerAvance 400 (^{1}H: 400 MHz; COSY: 400 MHz) at 298K, using partially deuterated solvents as internal standards. TGA spectra were performed using a TA Instruments TGAQ500 with a ramp of 10 °C/min under air and nitrogen conditions from 100 to 1000 °C. FT-ATR-IR spectra were measured with a Bruker ALPHA FT-IR spectrometer. Raman spectra were obtained with a Bruker Senterra confocal Raman microscope (Bruker Optic, Ettlingen, Germany, resolution 9-15 cm^{-1}) using the following parameters: objective NA 0.75, 50V; laser excitation: 532 nm, 0.2 mW; 633 nm, 0.2 mW and 785 nm, 1 mW. The samples were dispersed in tetrachloroethane and drop-casted onto glass slides. UV/Vis/NIR spectra were achieved using a Cary 5000 UV/Vis/NIR spectrophotometer (Varian) and 10x10 mm quartz cuvettes (path length = 1 cm). Mass spectra were recorded through FAB and MALDI-TOF experiments on a VG AutoSpec spectrometer, and a Bruker REFLEX spectrometer, respectively. AFM images were acquired using a JPK NanoWizard II AFM working in dynamic mode coupled to an inverted optical microscope Nikon Eclipse Ti-U. NT-MDT NSG01 silicon cantilevers, with typical values of 5.1 $N \cdot m^{-1}$ spring constant and 150 kHz resonant frequency, were employed under ambient conditions in air. The samples were dispersed in TCE, and spin coated onto mica slides. TEM images were obtained in a JEOL-JEM 2100F (2.5 Å resolution) instrument operating at 200 kV. HR-TEM images were obtained in an imaging aberration corrected microscope JEOL JEM GRAND ARM300cF operating at 60 kV. Images were recorded on a slow-CCD camera GATAN Oneview. Approximately 0.2 mg of MINT was ultrasonic dispersed in 2 mL of TCE for ten minutes. Few drops of this dispersion were deposited onto a 200 square mesh grid covered by holey carbon. EPR measurements were carried out on a Bruker Elexsys spectrometer operating at X-Band (microwave frequency approx. 9.5 GHz). Low temperature experiments were performed by means of a He gas-flow cryostat and a temperature controller, both

form Oxford Instruments. Microwave power was adjusted to ensure that there was no saturation.

S2. Synthetic details and characterization.

1. Scheme of the porphyrin synthesis

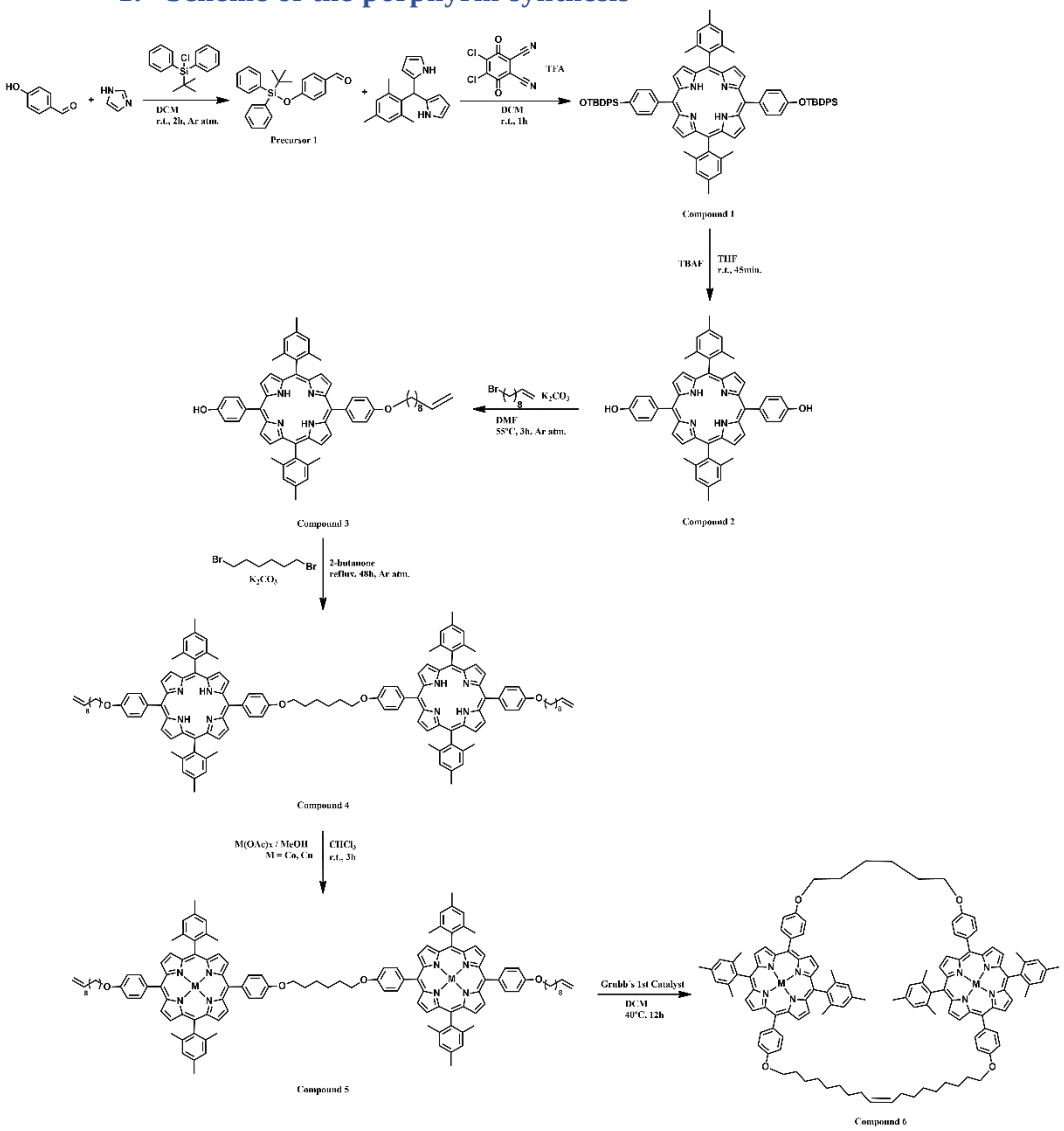

2. Non-metalated porphyrins

4-((tert-butyldiphenylsilyl)oxy)benzaldehyde

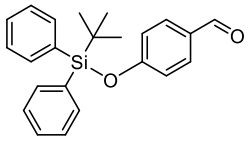

Precursor **1**

4-hydroxybenzaldehyde (2.0 g, 16.4 mmol, 1.0 equiv) was dissolved in DCM (50 mL) in a dry flask under inert atmosphere. Then, the solution was stirred at room temperature and imidazole (5.6 g, 40.9 mmol, 2.5 equiv) was added. The reaction mixture was stirred for one hour before the addition of TBDPSCl (4.7 mL, 18.0 mmol, 1.1 equiv). After 2h, the solution was washed with brine and dried over anhydrous Na_2SO_4. The crude product was purified by column chromatography using silica gel by eluting with hexane/EtOAc (9:1) to afford desired white product (71%) (4.2 g, 11.6 mmol). **^{1}H NMR (400 MHz, $CDCl_3$) δ (ppm)**: 9.81 (s, 1H, H_a), 7.72 – 7.68 (m, 4H, H_d, H_e), 7.64 (d, J = 8.6 Hz, 2H, H_b), 7.49 – 7.34 (m, 6H, H_f, H_g, H_h), 6.86 (d, J = 8.6 Hz, 2H, H_c), 1.11 (s, 9H, H_i).

^{1}H NMR (400 MHz, $CDCl_3$)

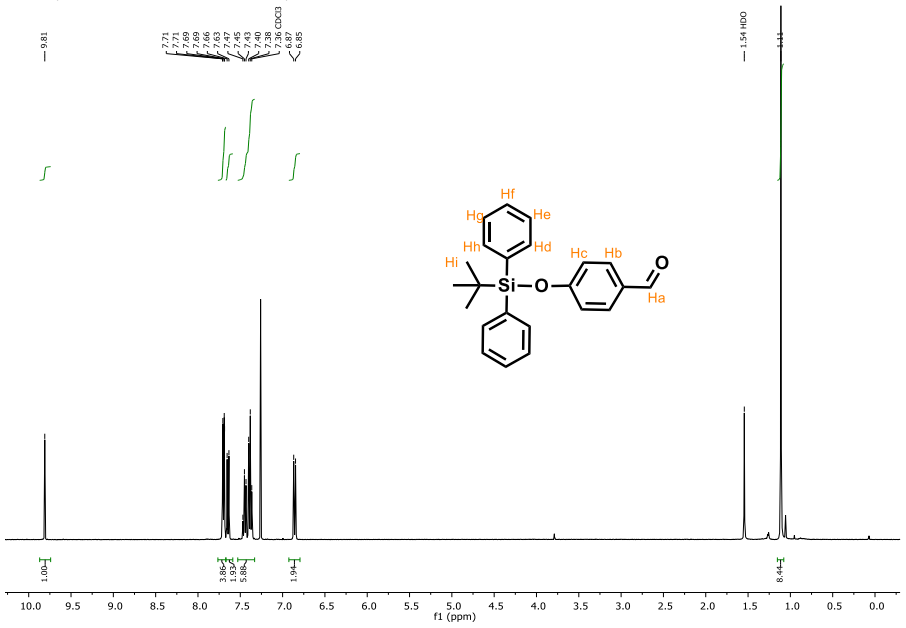

5,15-bis(4-((tert-butyldiphenylsilyl)oxy)phenyl)-10,20-dimesitylporphyrin

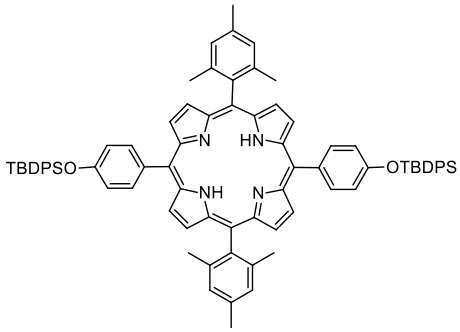

Compound **1**

4-((tertbutyldiphenylsilyl)oxy)benzaldehyde (409.3 mg, 1.1 mmol) and 5-mesityldipyrromethane (300.1 mg, 1.1 mmol) were dissolved in DCM (120 mL). Then, TFA (163 µL, 2.1 mmol) was added slowly and the reaction was stirred at room temperature for 30 min. Hereafter DDQ (516.4 mg, 2.3 mmol) was added, and the solution was stirred at room temperature for 1 h to oxidize all chlorin molecules. The solvent was removed under vacuum and the crude product was subjected to a quick percolate (aluminium oxide, DCM) to remove a big amount of impurities. Finally, it was purified by column chromatography (aluminium oxide, Hex/DCM 1:1). Removal of the solvent under vacuum gave a shiny purple solid, compound 1 in a 39% yield (268.2 mg, 0.2 mmol). **^{1}H NMR (400 MHz, $CDCl_3$) δ (ppm)**: 8.70 (d, J = 4.7 Hz, 2H, H_e), 8.63 (d, J = 4.7 Hz, 2H, H_d), 7.97 – 7.83 (m, 6H, H_i, H_j, H_g), 7.58 – 7.45 (m, 6H, H_k, H_l, H_m), 7.27 (s, 2H, H_b), 7.11 (d, J = 8.5 Hz, 2H, H_h), 2.63 (s, 3H, H_a), 1.80 (s, 6H, H_c), 1.26 (d, J = 2.8 Hz, 9H, H_n, H_o, H_p), -2.69 (s, 1H, H_f).

^{1}H NMR (400 MHz, $CDCl_3$)

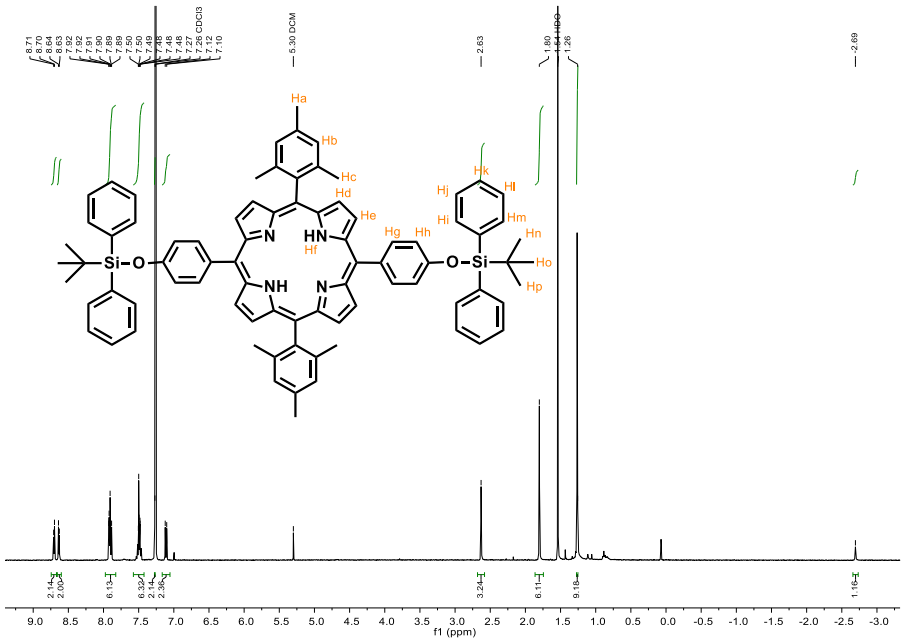

4,4'-(10,20-dimesitylporphyrin-5,15-diyl)diphenol

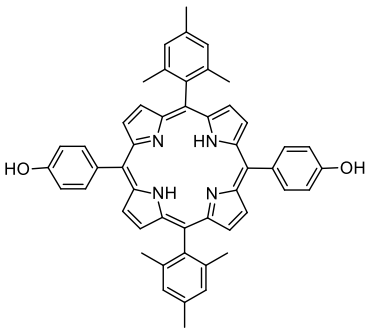

Compound **2**

Compound **1** (212.0 mg, 0.2 mmol) was dissolved in THF (71 mL), and TBAF (1.0 M in THF) (0.2 mL, 0.9 mmol) was added at room temperature. After completion of the reaction, the reaction mixture was hydrolyzed with deuterated water and extracted with DCM. The organic phase was washed with brine, dried over Na_2SO_4, and filtered. Solvents were removed by evaporation under reduced pressure. The crude product was washed with cold hexane, filtered getting compound **2** as a purple solid (quantitative yield) and used directly in the next step

reaction. The compound **2** (131.6 mg, 0.18mmol, 99%). **^{1}H NMR (400 MHz, DMSO-d_6) δ (ppm)**: 9.95 (s, 1H, H_i), 8.85 (d, *J* = 4.8 Hz, 2H, H_e), 8.61 (d, *J* = 4.7 Hz, 2H, H_d), 8.00 (d, *J* = 8.3 Hz, 2H, H_g), 7.35 (s, 2H, H_b), 7.18 (d, *J* = 8.3 Hz, 2H, H_h), 2.59 (s, 3H, H_a), 1.76 (s, 6H, H_c), -2.74 (s, 1H, H_f).

^{1}H NMR (400 MHz, $CDCl_3$)

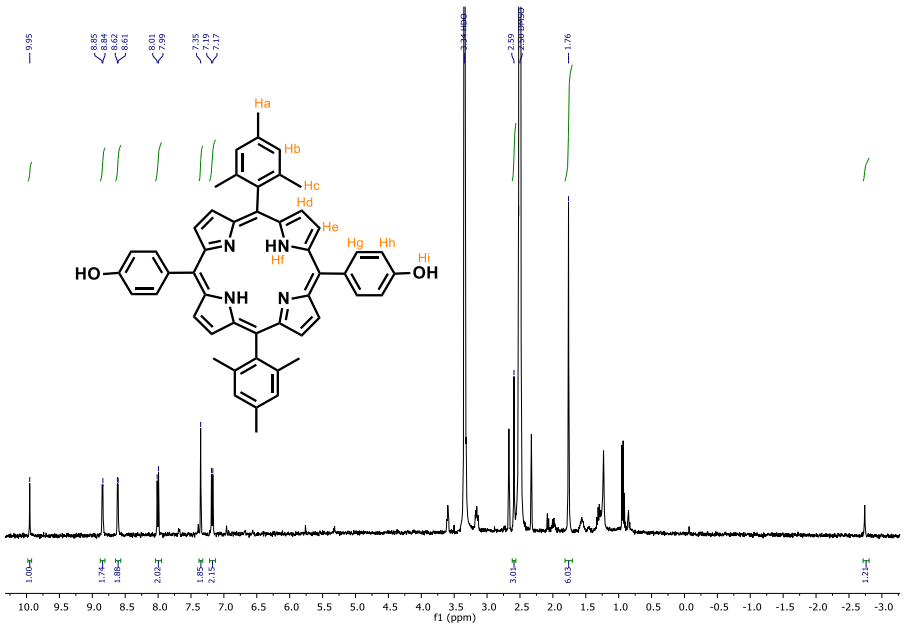

4-(15-(4-(dec-9-en-1-yloxy)phenyl)-10,20-dimesitylporphyrin-5-yl)phenol

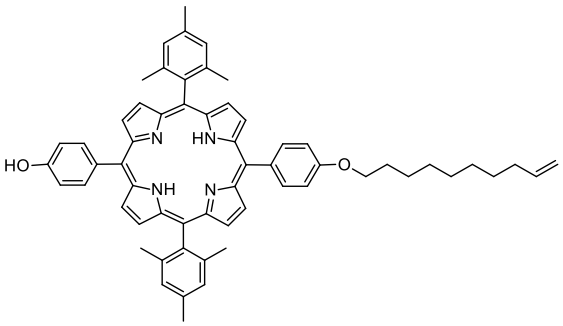

Compound **3**

Compound **2** (198.5 mg, 0.3 mmol) was dissolved in dry DMF (53 mL) under Ar atmosphere at room temperature. Then, dry K_2CO_3 (450.4 mg, 3.3 mmol) was added to the previous solution. The reaction was heated at 55 ºC and a solution of 10-

bromo-1-decene (11 µL, 0.05 mmol) in dry DMF (2 mL) was added dropwise. After 10 min stirring, 0.05 mmol more of 10-bromo-1-decene in dry DMF were added, and the resulting mixture was stirred at 55 ºC for 3 h. The completed reaction was poured onto cold HCl 1M. The result solid was isolated by filtration, dissolved in $CHCl_3$ and extracted with $CHCl_3$. The organic phase was washed with brine, dried over Na_2SO_4 and filtered. The solvent was removed under vacuum and the crude product was purified by column chromatography (silica gel, $CHCl_3$) to furnish compound **3** (55.1 mg, 0.06mmol, 55.5% yield). **^{1}H NMR (400 MHz, $CDCl_3$)** δ **(ppm)**: 8.81 (dd, J = 20.8, 4.7 Hz, 4H, H_e, $H_{e'}$, H_m, $H_{m'}$), 8.68 (dd, J = 4.8, 3.5 Hz, 4H, H_d, $H_{d'}$, H_l, $H_{l'}$), 8.10 (d, J = 8.4 Hz, 2H, H_g, $H_{g'}$), 7.99 (d, J = 8.4 Hz, 2H, H_n, $H_{n'}$), 7.26 – 7.14 (m, 6H, H_h, $H_{h'}$, H_j, $H_{j'}$, H_b, $H_{b'}$), 6.98 (d, J = 8.4 Hz, 2H, H_o, $H_{o'}$), 5.84 (m, *J* = 16.9, 10.2, 6.7 Hz, 1H, H_x), 5.07 – 4.88 (m, 2H, H_y), 4.20 (t, *J* = 6.5 Hz, 2H, H_p), 2.60 (s, 6H, H_a, $H_{a'}$), 2.12 - 2.04 (m, 2H, H_w), 1.99 – 1.90 (m, 2H, H_q), 1.83 (s, 12H, H_c, $H_{c'}$, H_k, $H_{k'}$), 1.59 (m, 2H, H_v), 1.44 – 1.38 (m, 6H, H_r, H_s, H_t), 0.87 – 0.81 (m, 2H, H_u), -2.60 (s, 2H, H_f, $H_{f'}$).

^{1}H NMR (400 MHz, $CDCl_3$)

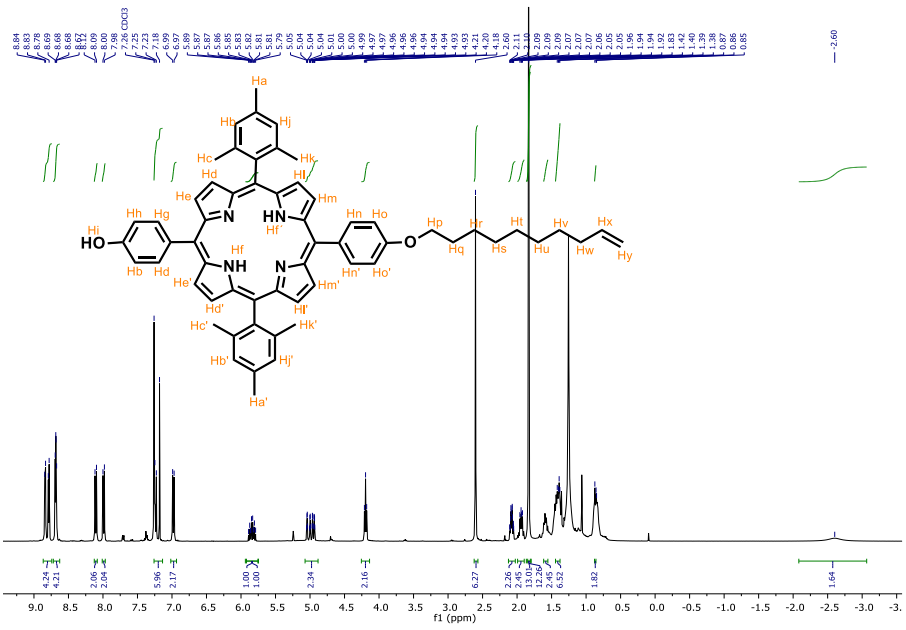

1,6-bis(4-(15-(4-(dec-9-en-1-yloxy)phenyl)-10,20-dimesitylporphyrin-5-yl)phenoxy)hexane (U-shape porphyrin – U-por)

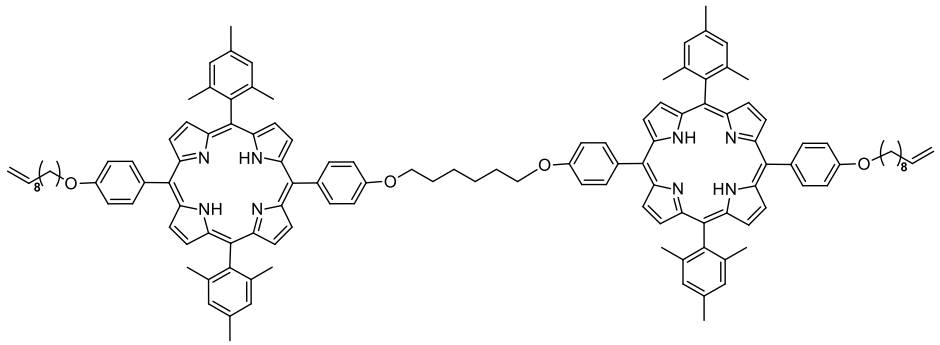

Compound **4**

Compound **3** (50.2 mg, 0.06 mmol) was dissolved in dry 2- butanone (9 mL) under Ar atmosphere. Then, dry K_2CO_3 (84.3 mg, 0.6 mmol) and 1,6-dibromohexane (2 µL, 0.01 mmol) were added. The resulting mixture was stirred under reflux for 48 h, quenched with water and extracted with $CHCl_3$. The organic phase was washed with brine, dried over Na_2SO_4 and the solvent was removed under vacuum. The crude product was purified by column chromatography (silica gel, Hex/DCM 1:1) giving a purple product (23.4 mg, 0.01mmol, 86%). **^{1}H NMR (400 MHz, $CDCl_3$)** δ **(ppm)**: 8.87 (dd, *J* = 8.4, 4.8 Hz, 4H, H_e, $H_{e'}$, H_m, $H_{m'}$), 8.71 (t, *J* = 4.3 Hz, 4H, H_d, $H_{d'}$, H_l, $H_{l'}$), 8.16 (dd, *J* = 12.1, 8.3 Hz, 4H, H_g, $H_{g'}$, H_n, $H_{n'}$), 7.34 (d, *J* = 8.2 Hz, 2H, H_h, $H_{h'}$), 7.30 (s, 4H, H_b, $H_{b'}$, H_j, $H_{j'}$), 7.27 (m, 2H, H_o, $H_{o'}$), 5.88 (m, *J* = 16.9, 10.2, 6.7 Hz, 1H, H_x), 5.11 – 4.94 (m, 2H, H_y), 4.35 (t, *J* = 6.4 Hz, 2H, H_i), 4.26 (t, *J* = 6.5 Hz, 2H, H_p), 2.64 (s, 6H, H_a, $H_{a'}$), 2.12 (m, *J* = 7.0 Hz, 4H, H_q, H_z), 1.98 (m, *J* = 7.1 Hz, 2H_w), 1.87 (s, 12H, H_c, $H_{c'}$, H_k, $H_{k'}$), 1.63 (m, 2H, H_v), 1.47 (m, 4H, H_r, H_A), 1.00 – 0.76 (m, 6H, H_s, H_t, H_u), -2.58 (s, 2H, H_f, $H_{f'}$).

^{1}H NMR (400 MHz, $CDCl_3$)

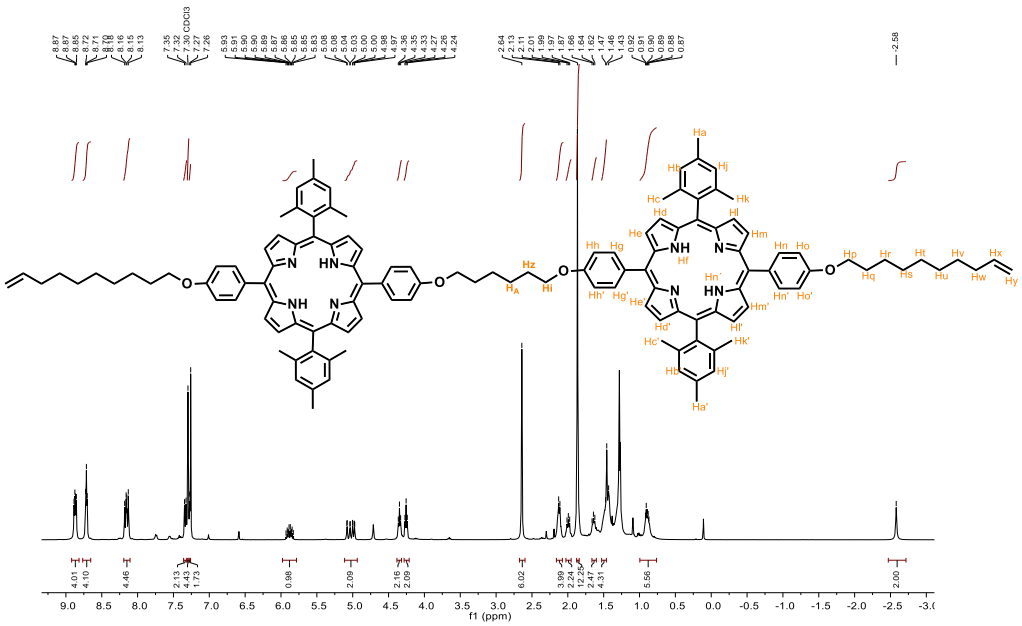

3. Metalated porphyrins

Metallated linear porphyrin (Metallated U-por)

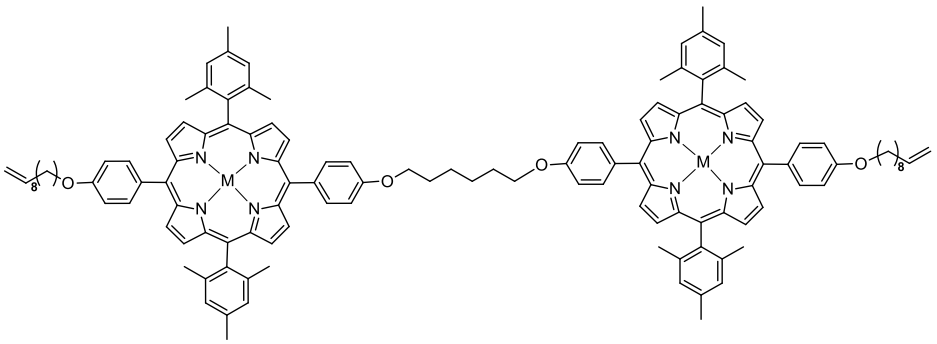

Compound 5

Compound **4** (34.1 mg, 0.019 mmol) was dissolved in $CHCl_3$ (7.1 mL) and a solution of cobalt acetate (13.45 mg, 0.076 mmol) in MeOH (1.4 mL) was added. The reaction mixture was stirred at room temperature. After completion of the reaction, the solvent was removed under vacuum and the crude product was extracted with $CHCl_3$. Then, it was washed with brine, and dried over Na_2SO_4. Evaporation of the solvent gives an orange product (Compound **5a**) (34.9 mg, 0.02mmol, 95%) is obtained. **^{1}H NMR (400 MHz, $CDCl_3$) δ (ppm)**: 15.96 (d, 4H,

H_e, $H_{e'}$, H_m, $H_{m'}$), 15.35 (d, *J* = 53.3 Hz, 4H, H_d, $H_{d'}$, H_l, $H_{l'}$), 12.55 (d, *J* = 71.7 Hz, 4H, H_g, $H_{g'}$, H_n, $H_{n'}$), 9.39 (t, *J* = 61.2 Hz, 8H, H_b, $H_{b'}$, H_j, $H_{j'}$, H_h, $H_{h'}$, H_o, $H_{o'}$), 6.19 – 5.92 (c, 1H, H_x), 5.85 (t, 2H, H_i), 5.40 (t, 2H, H_p), 5.26 – 5.07 (m, 2H, H_y), 4.04 (s, 6H, H_a, $H_{a'}$), 3.77 (s, 10H, H_q, H_z, H_w, H_v, H_r), 3.35 (s, 2H, H_A), 3.07 (s, 2H, H_s), 2.77 (s, 2H, H_t), 2.33 (s, 2H, H_u), 2.02 (s, 3H, H_c), 1.86 (s, 3H, $H_{c'}$), 1.76 (s, 6H, H_k, $H_{k'}$). **MS m/z**: calculated for $C_{126}H_{126}Co_2N_8O_4$ [M] 1932.8561, found MALDI 1932.8522. λ_{abs} ($CHCl_3$) 413, 531 nm.

^{1}H NMR (400 MHz, $CDCl_3$)

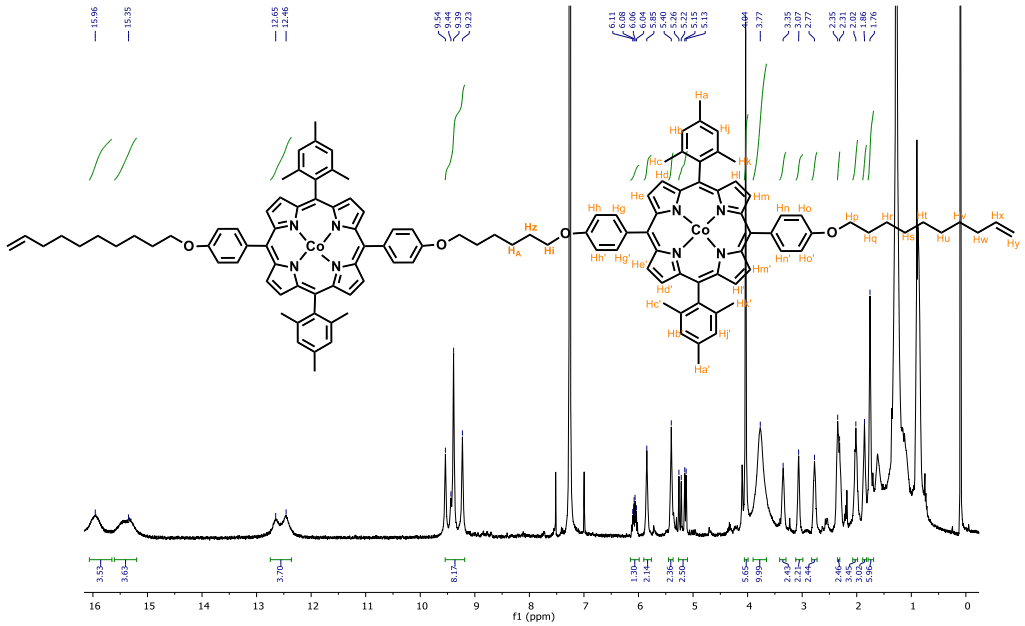

COSY (400 MHz, $CDCl_3$)

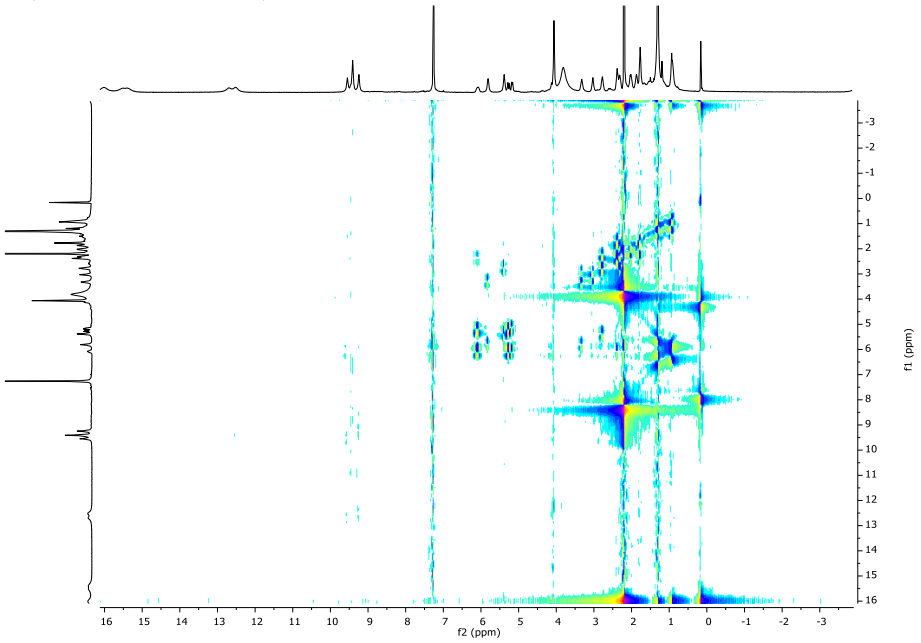

MS MALDI

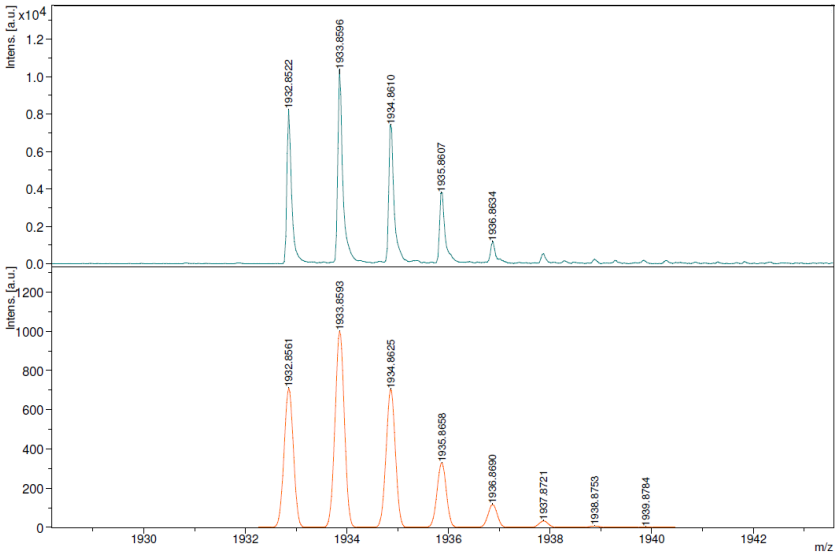

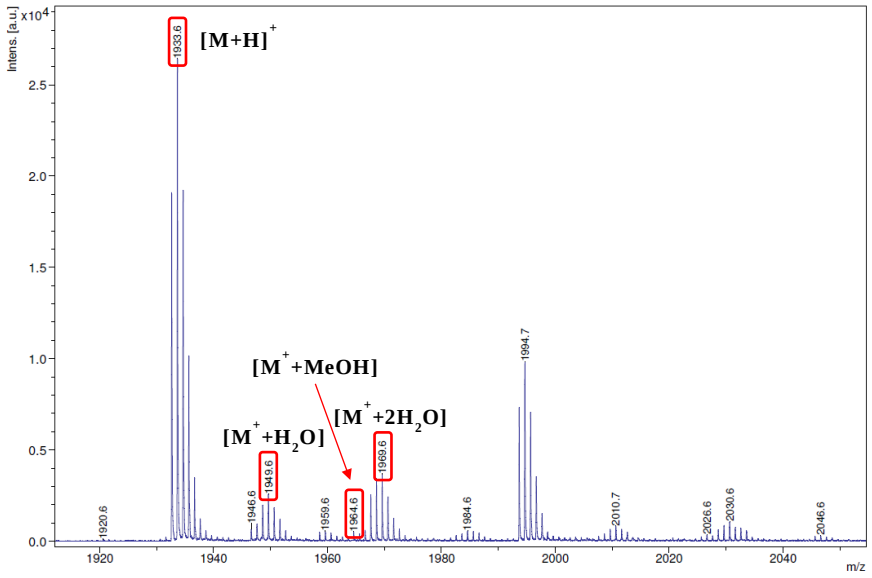

UV-vis ($CHCl_3$)

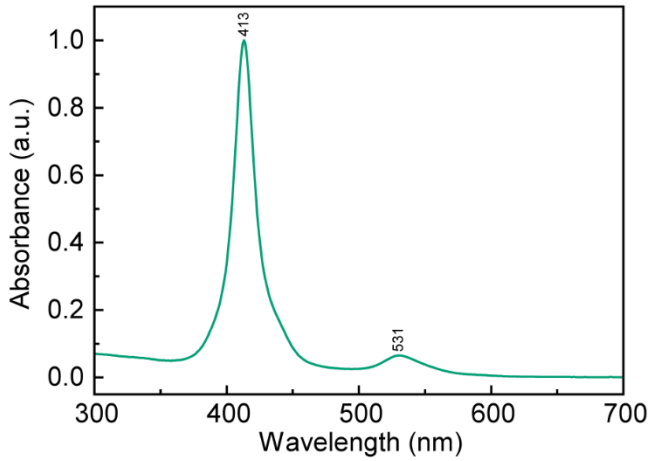

The experimental procedure for the synthesis of copper **U-por** (Compound **5b**) is the same explained above. The quantities used are:

Compound **4**: 7.2 mg, $3.94 \cdot 10^{-3}$ mmol; $CHCl_3$: 3 mL; Cobalt acetate: 5.6 mg, 0.03 mmol; MeOH: 2 mL. Final product: reddish pink solid (7.4 mg, $3.8 \cdot 10^{-3}$ mmol, 97%). **MS m/z**: calculated for $C_{126}H_{126}Cu_2N_8O_4$ [M] 1940.8489, found MALDI 1940.8527. λ_{abs} ($CHCl_3$) 418, 541 nm.

MS MALDI

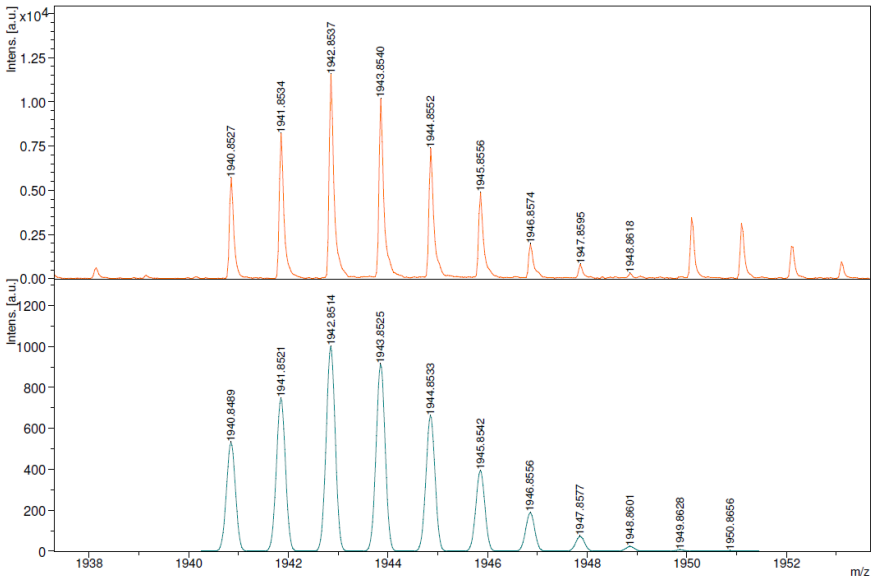

UV-vis ($CHCl_3$)

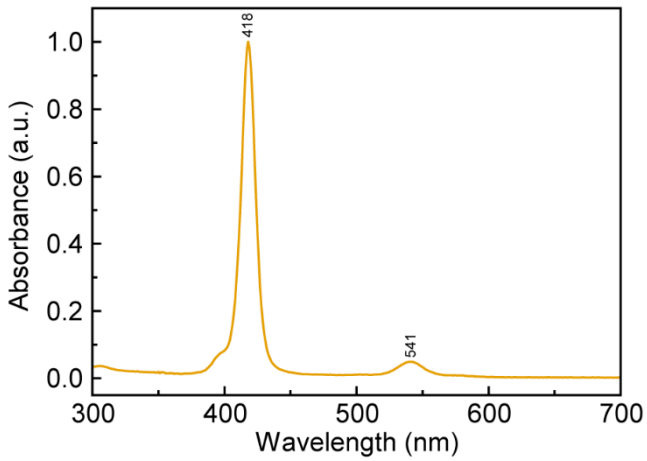

Metallated macrocycle porphyrin (Metallated mac-por)

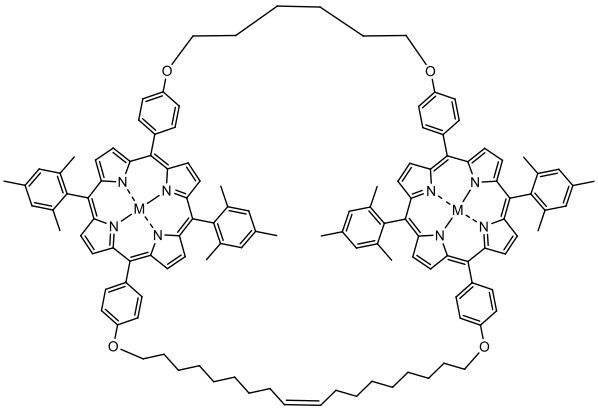

Compound 6

Compound **5a** (20.1 mg, $10.3 \cdot 10^{-3}$ mmol) was dissolved in dry DCM (100 mL) and degassed for 30 min. under N_2 atmosphere. Grubbs' 1st generation catalyst (1.8 mg, $2.1 \cdot 10^{-3}$ mmol) was added and the solution was stirred under reflux for 12h. After completion of the reaction, the crude product was purified by column chromatography (silica gel, DCM) giving the orange product (Compound **6a**) (7.2 mg, $3.8 \cdot 10^{-3}$ mmol, 38%). **MS m/z**: calculated for $C_{124}H_{122}Co_2N_8O_4$ [M] 1904.8248, found MALDI 1904.8254. λ_{abs} ($CHCl_3$) 412, 533 nm.

MS MALDI

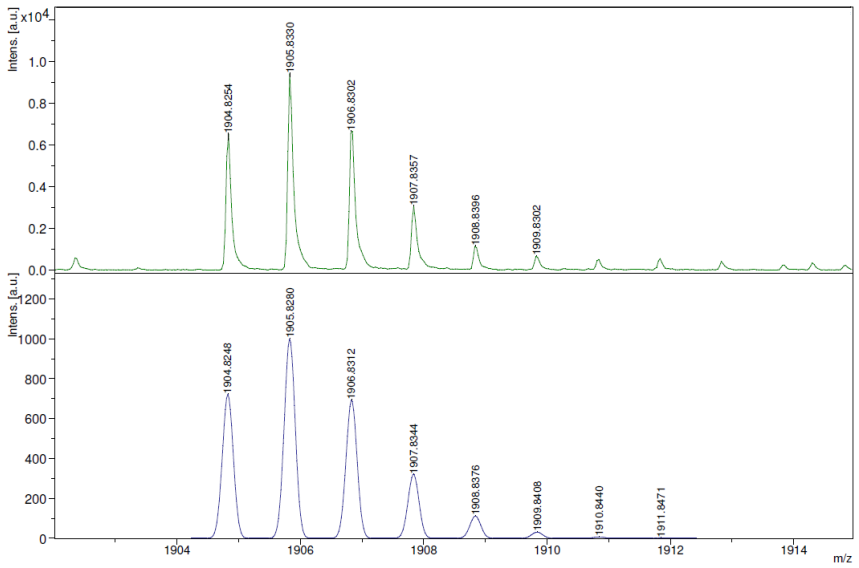

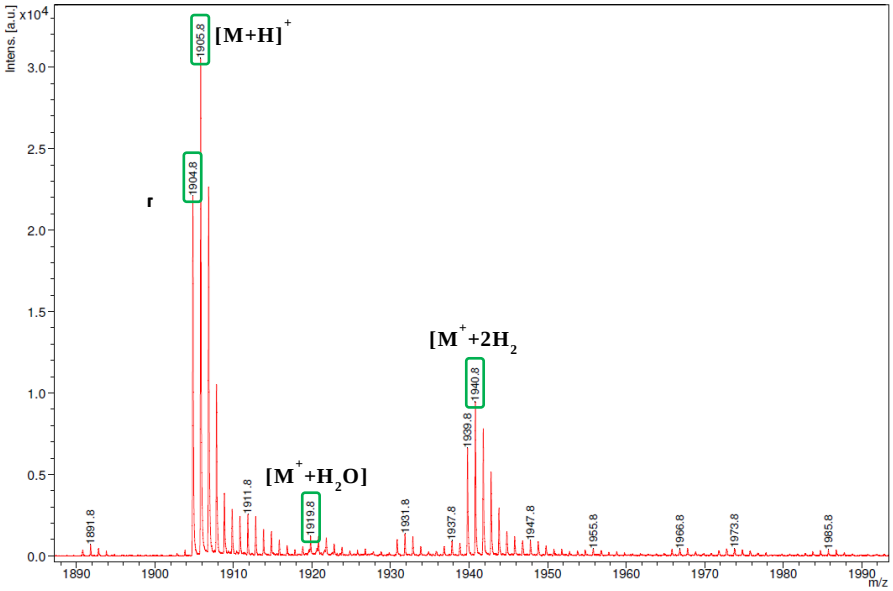

UV-vis ($CHCl_3$)

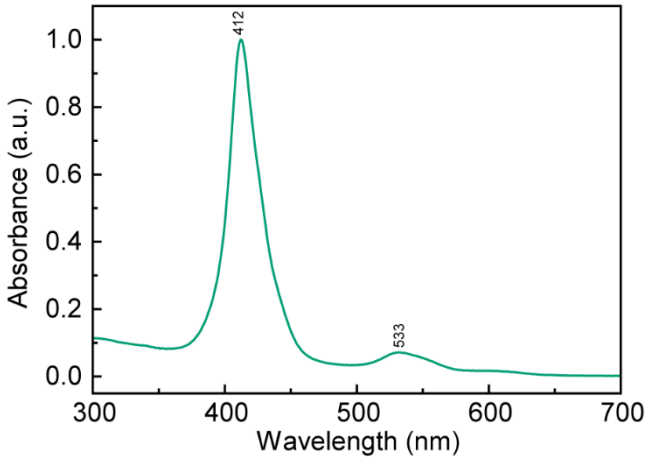

The experimental procedure for the synthesis of copper **mac-por** (Compound **6b**) is the same explained above. The quantities that were used are:

Compound **5b**: 15.7 mg, $8.1 \cdot 10^{-3}$ mmol; DCM: 81 mL; Grubbs´s 1st generation catalyst: 1.4 mg, $1.6 \cdot 10^{-3}$ mmol. Final product:reddish pink solid (6.2 mg, $7.9 \cdot 10^{-3}$ mmol, 40%) **MS m/z**: calculated for $C_{124}H_{122}Cu_2N_8O_4$ [M] 1912.8176, found MALDI 1912.8140. λ_{abs} ($CHCl_3$) 417, 540 nm.

MS MALDI

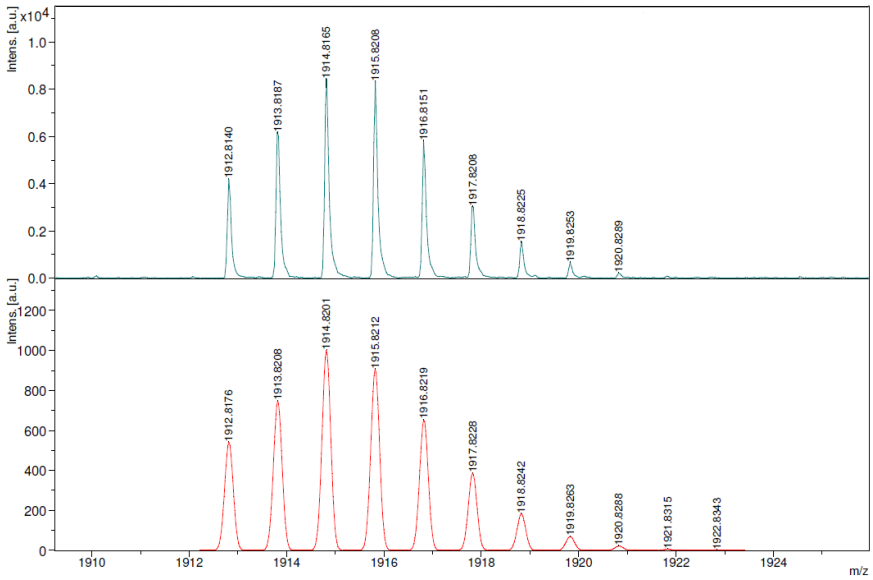

UV-vis ($CHCl_3$)

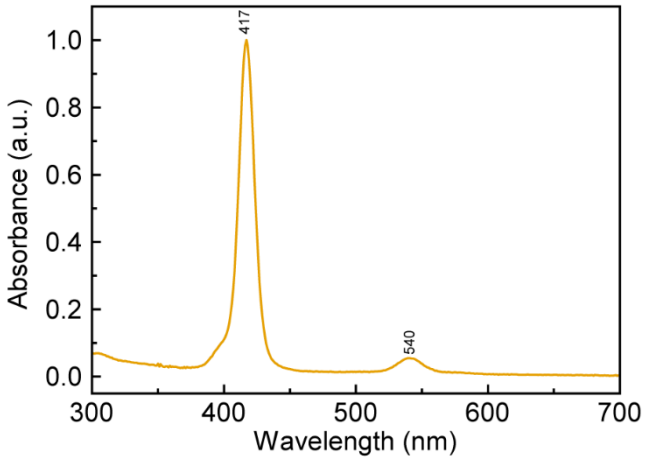

Metallated dialkylated porphyrin

In the synthesis of **compound 3** the dialkylated porphyrin was obtain as a by-product (**compound 3b**). This derivative was used to compare the mono with the linear porphyrin.

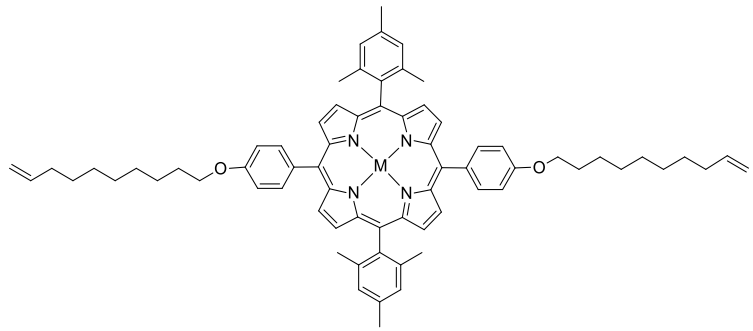

Compound 3b

Compound **3b** (35.0 mg, $9.9 \cdot 10^{-3}$ mmol) was dissolved in $CHCl_3$ (5 mL) and a solution of cobalt acetate (7.1 mg, 0.04 mmol) in MeOH (0.5 mL) was added. The reaction mixture was stirred under reflux for 24h. After completion of the reaction, the solvent was removed under vacuum and the crude product was extracted with $CHCl_3$. Then, it was washed with brine, and dried over Na_2SO_4. The solvent is removed under vacuum and an orange product (Compound 7a) (9.5 mg, $8.9 \cdot 10^{-3}$ mmol, 90%) is obtained. **^{1}H NMR (400 MHz, $CDCl_3$)** δ (ppm): 16.01 (d, 2H, H_e), 15.39 (d, 2H, H_d), 12.53 (d, 2H, H_f), 9.36 (d, *J* = 88.1 Hz, 4H, H_b, H_g), 6.09 (c, 1H, H_p), 5.30 - 5.18 (m, *J* = 35.6, 13.4 Hz, 2H, H_q), 4.77 (t, 1H, H_h), 4.14 (s, 3H, H_a), 3.83 (s, 4H, H_i, H_o), 2.78 (s, 2H, H_n), 2.40 (s, 2H, H_j), 2.31 (s, 2H, H_k), 2.03 - 1.88 (s, 6H, H_c), 1.78 (s, 4H, H_l, H_m). **MS m/z**: calculated for $C_{70}H_{76}CoN_4O_2$ [M] 1063.5295, found MALDI 1063.5285. λ_{abs} ($CHCl_3$) 413, 531 nm.

^{1}H NMR (400 MHz, $CDCl_3$)

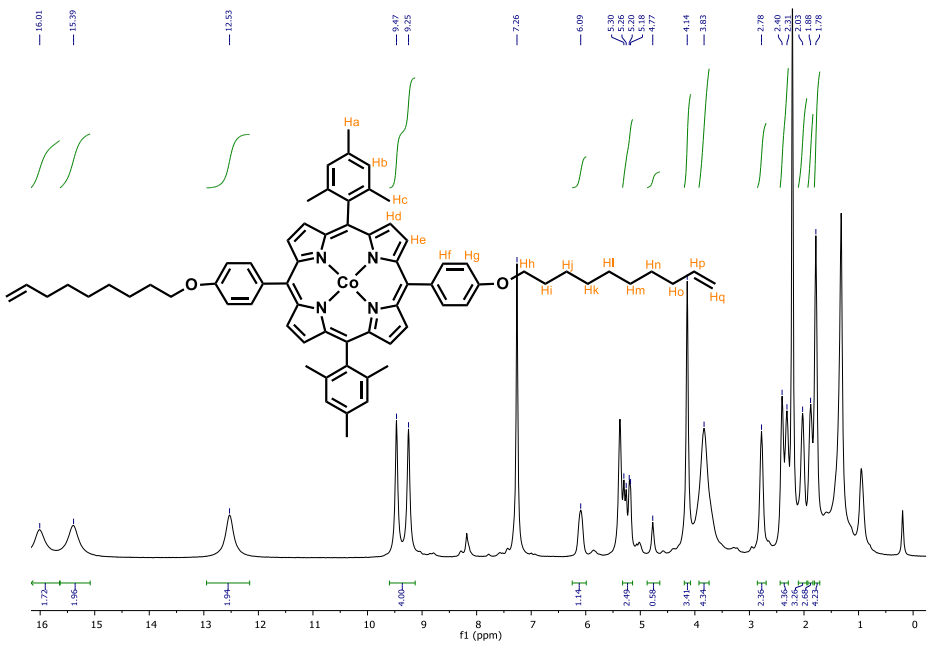

COSY (400 MHz, $CDCl_3$)

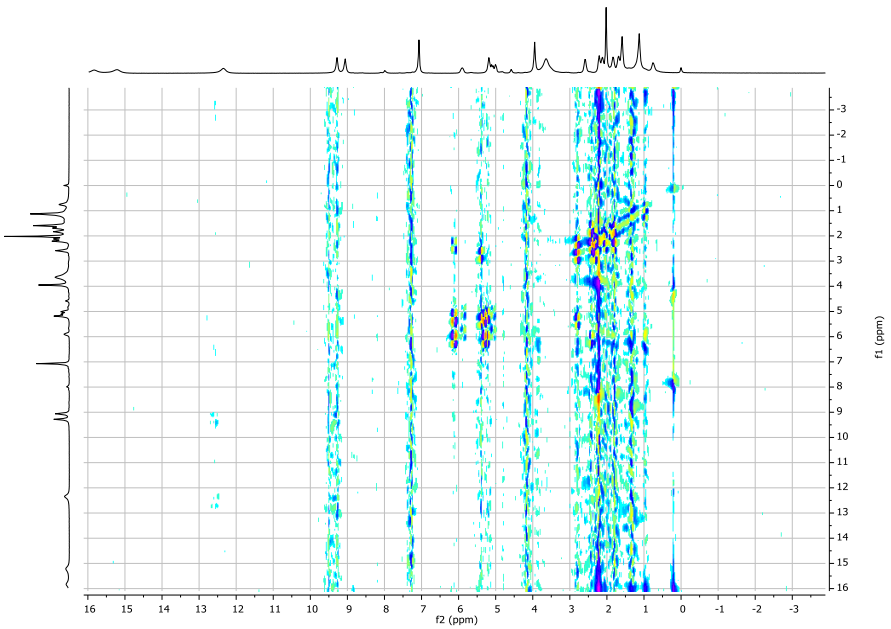

MS MALDI

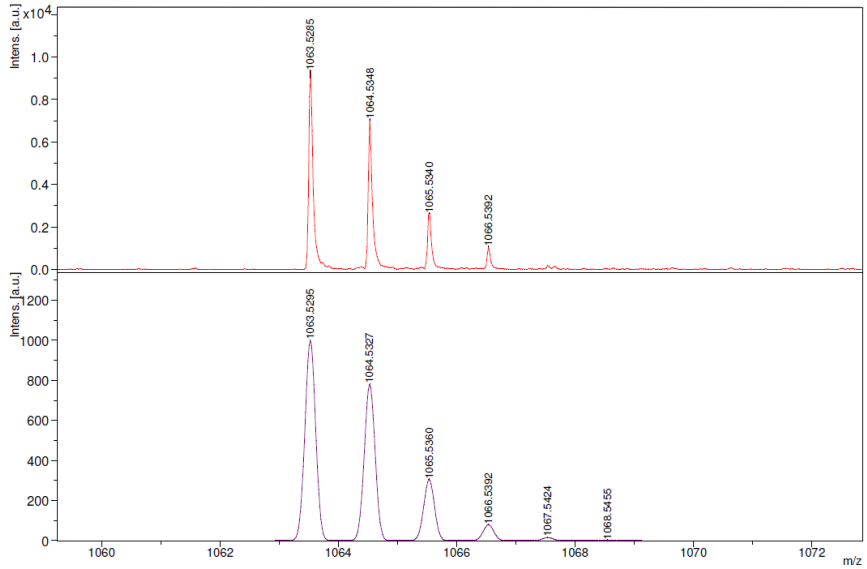
Intens. [a.u.]
x10^4
1.0
0.8
0.6
0.4
0.2
0.0
1063.5285
1064.5348
1065.5340
1066.5392
Intens. [a.u.]
1200
1000
800
600
400
200
0
1063.5295
1064.5327
1065.5360
1066.5392
1067.5424
1068.5455
1060
1062
1064
1066
1068
1070
1072
m/z

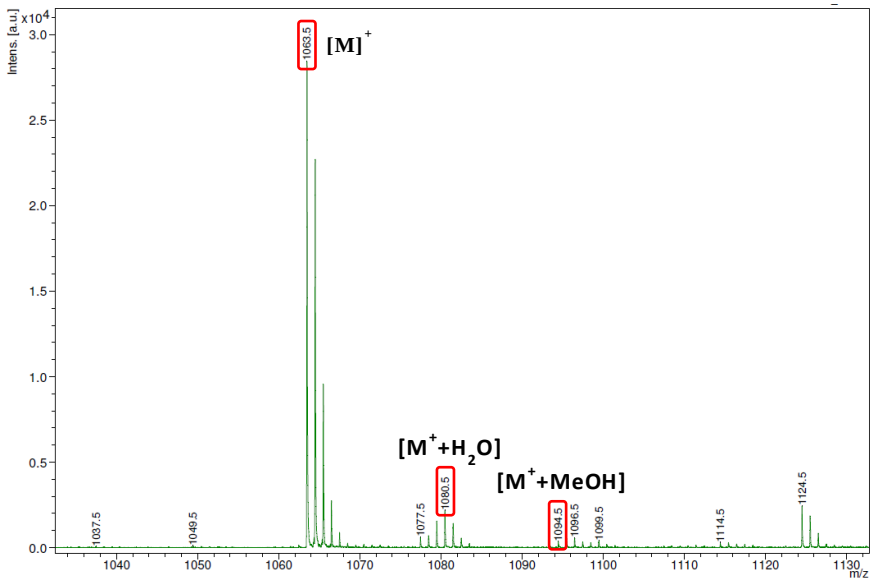
Intens. [a.u.]
x10^4
3.0
2.5
2.0
1.5
1.0
0.5
0.0
1063.5
[M]+
[M+H2O]
1080.5
[M+MeOH]
1094.5
1037.5
1049.5
1077.5
1096.5
1099.5
1114.5
1124.5
1040
1050
1060
1070
1080
1090
1100
1110
1120
1130
m/z

UV-vis ($CHCl_3$)

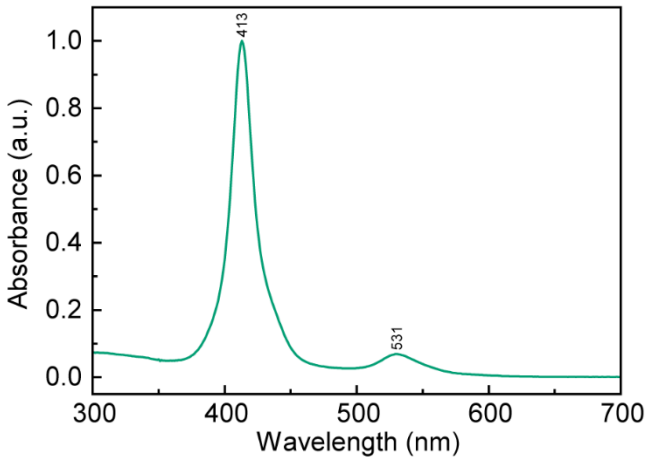

The experimental procedure for the synthesis of copper dialkylated porphyrin (Compound **7b**) is the same explained above. The quantities that were used are:

Compound **3b**: 20.0 mg, 0.02 mmol; $CHCl_3$: 10 mL; Cobalt acetate: 14.4 mg, 0.08 mmol; MeOH: 1 mL. Final product: reddish pink solid (35.7 mg, 0.02 mmol, 92%) **^{1}H NMR (400 MHz, $CDCl_3$)** δ (ppm): **MS m/z**: calculated for $C_{70}H_{76}CuN_4O_2$ [M] 1067.5259, found MALDI 1067.5244. λ_{abs} ($CHCl_3$) 418, 541 nm.

MS MALDI

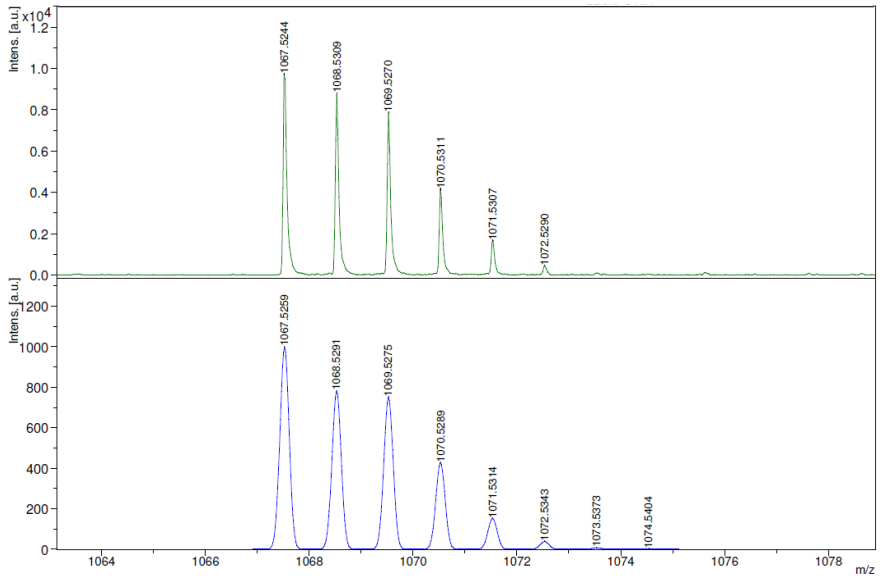

UV-vis ($CHCl_3$)

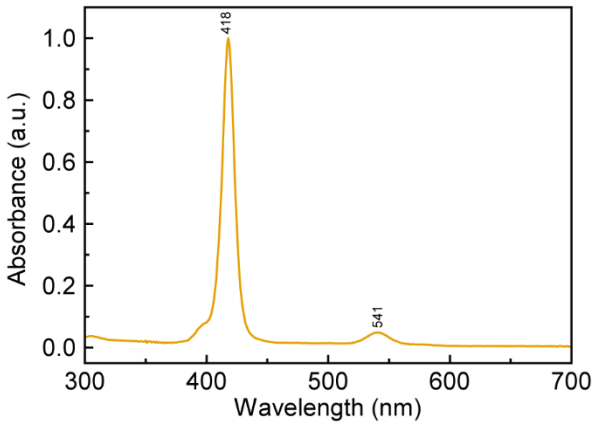

S3. Experimental procedure for SWNTs functionalization

For the synthesis of mMINT, we used a clipping strategy in which the SWNTs serve as template for the formation of the metallated mac-por around the nanotubes, as described in de Juan-Fernandez et al.[42]

The first step is the purification of the nanotubes from metallic particles. To this end, 50 mg of ((6,5))- SWNTs were suspended in 34 mL of 35% HCl and sonicated for 15 min. The mixture was poured onto milliQ water and filtered through a polycarbonate membrane of 0.2 µm pore size. The solid was washed with water to neutral pH and then dried in an oven at 350 °C for 30 min.

The purified ((6,5))-SWNTs (3.2 mg) were suspended in tetrachloroethane (3.2 mL) through sonication for 10min and mixed with linear precursor (metallated U-por) (cobalt and copper U-por 25.0 mg, 0.01 mmol) and Grubbs' 2nd catalyst (11.0 mg, 0.01mmol) at room temperature for 72 h. After this time, the suspension was filtered through a polytetrafluoroethylene membrane with a pore size of 0.2 mm, and the solid was washed with dichloromethane (DCM). The solid was redispersed in DCM (20 mL) through 10 min of sonication and filtered through a PTFE membrane of 0.2 µm pore size again. This purification step was repeated three times to remove any remaining U-por precursor, non-threaded macrocycles, and catalyst.

[42] de Juan-Fernández, L.; Münich, P. W.; Puthiyedath, A.; Nieto-Ortega, B.; Casado, S.; Ruiz-González, L.; Pérez, E. M.; Guldi, D. M. *Chem. Sci.* **2018**, *9* (33), 6779–6784.

S4. Control experiments for SWNTs functionalization.

The purified ((6,5))-SWNTs (2 mg) were suspended in tetrachloroethane TCE (2 mL) through sonication for 10 min and mixed with metallated U-por (16.3 mg) at room temperature for 72 hours. After this time, the suspension was filtered through a PTFE membrane with a pore size of 0.2 µm, and the solid was washed with DCM. The solid was redispersed in DCM (20 mL) through 10 min of sonication and filtered through a PTFE membrane of 0.2 µm pore size again. This purification step was repeated three times to remove any remaining linear precursor, and non-threaded macrocycles.

S5. TGA of SWNTs and mMINTs.

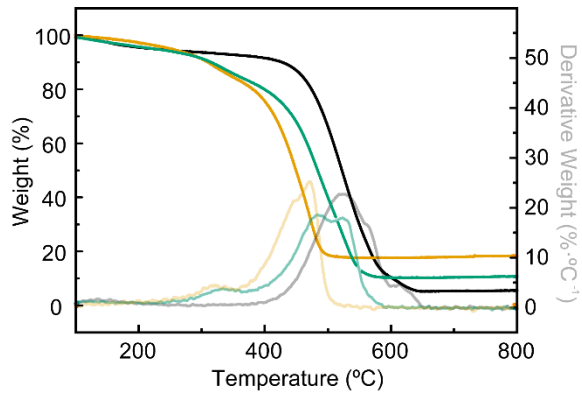

Figure S1. TGA (Air, 10 °C·min^{-1}) of control single wall carbon nanotubes (SWNT) in black, cobalt mMINT in green and copper mMINT in orange. The first derivatives are shown in thinner lines.

Using thermogravimetric analysis (TGA) the functionalization was estimated at *ca*. 20 wt. % for the Co-mMINT and *ca*. 24 wt. % for the Cu-mMINT. For a rigorous analysis, a control SWNT sample was treated following the exact same procedure described for the mMINT synthesis (see previous section), but without addition of the macrocyclic precursor. This control sample presents an initial weight loss at around 100 °C which can correspond to adsorbed solvent; then it is thermally stable until 450 °C approximately, where it starts to decompose. The organic material loss appears at around 320 °C for both metallated mMINT samples. This is an indication that the organic material is not simply physisorbed onto the surface but forming mechanical bonds around the nanotubes.

S6. Raman spectra of SWNTs and mMINTs.

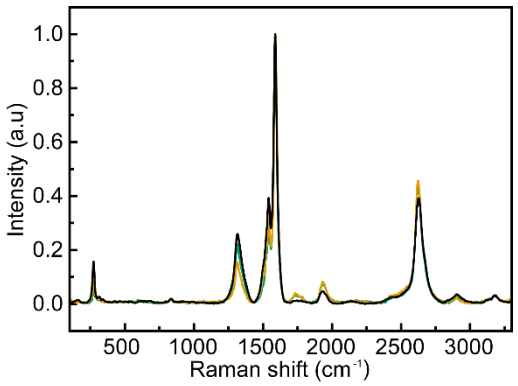

Figure S2. Normalized Raman spectra obtained for the control SWNT in black, cobalt mMINT in green and copper mMINT in orange using a 532 nm laser.

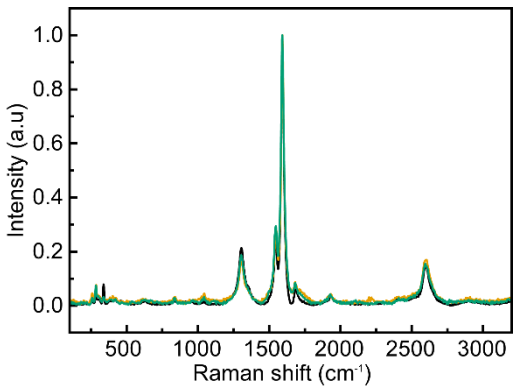

Figure S3. Normalized Raman spectra obtained for the control SWNT in black, cobalt mMINT in green and copper mMINT in orange using a 633 nm laser.

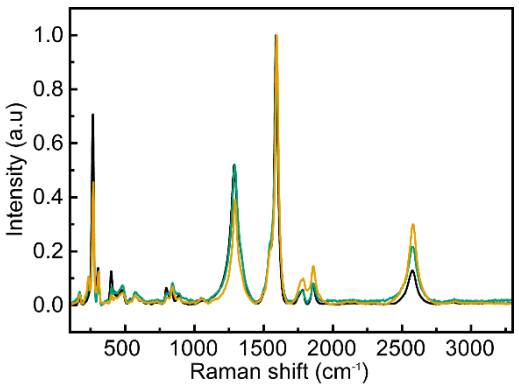

Figure S4. Normalized Raman spectra obtained for the control SWNT in black, cobalt mMINT in green and copper mMINT in orange using a 785 nm laser.

The Raman spectra obtained under all three excitations share some common features, most significantly, the negligible increase or even slight decrease of the I_D/I_G ratio, the lack of a significant shift of the G or 2D band Raman shifts. These observations confirm that the porphyrin rings are not covalently connected to the SWNTs and that there is no observable doping of the SWNTs upon functionalization. Both observations are in line with our previous report.[42].

S7. FTIR spectra of SWNTs and mMINTs

Single wall carbon nanotubes and both synthesized mMINTs were analyzed by FTIR spectroscopy. In order to facilitate the mMINTs spectra study, all the metallated porphyrins were also characterized by this technique.

The spectrum of the free metal base porphyrin was very similar in comparison with the metallated ones. The only obvious difference was the disappearance of the N-H (3316 cm^{-1}) vibration frequency of free base porphyrin indicating the formation of cobalt (II) and copper (II) porphyrin compounds. The alkyl and alkenyl C-H vibrations can be located around 3000 cm^{-1}, and the peaks observed about 1000 cm^{-1} can be associated with the CCH vibration modes of the skeletal porphyrin ring.

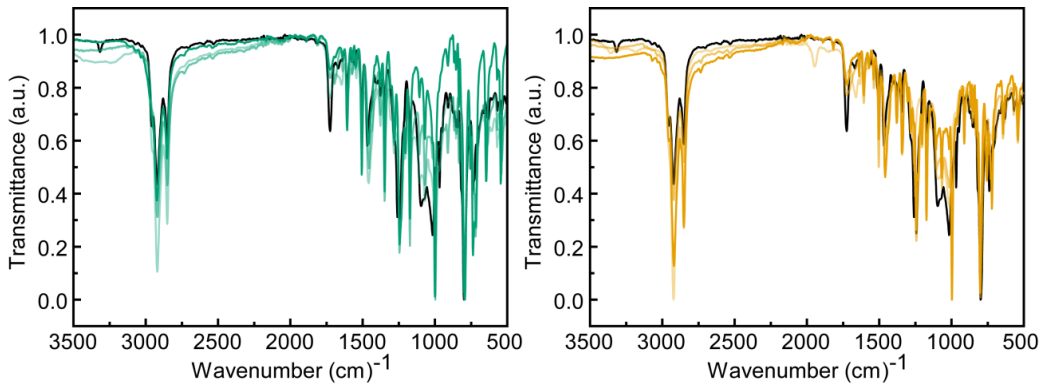

Figure S5. Normalized FTIR spectra of free-base, cobalt and copper porphyrin derivatives: (a) Free-base porphyrin in black, Co-monomer in green, Co-U-por in lighter green and Co-mac-por in the lightest green, (b) Free-base porphyrin in black, Cu-monomer in orange, Cu-U-por in lighter orange and Cu-mac-por in the lightest orange.

The FTIR spectra of the SWNTs is fundamentally featureless. After the ring-closing metathesis of a U-shape molecule around nanotube, stretching vibrations of C-H group (about 2860 cm^{-1} and 2680 cm^{-1}) can be observed. These vibrational modes can be comparable with the peaks observed in the cobalt and copper

macrocycle porphyrin (2920 and 2851 cm^{-1} for Co-mac-por, and 2922 and 2852 cm^{-1} for Cu-mac-por). Finally, the broad band at 1000 cm^{-1} corresponds with the CCH vibration modes of the skeletal porphyrin ring.

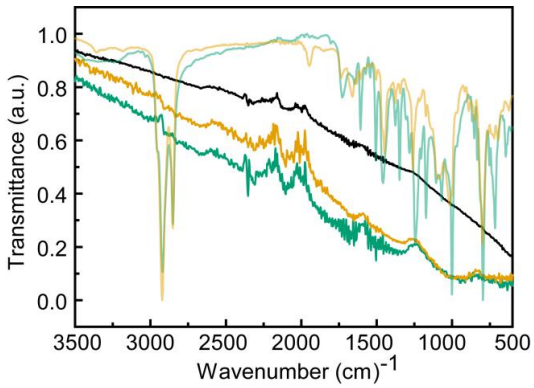

Figure S6. Normalized FTIR spectra of SWNTs in black, Co-mMINT in green, Cu-mMINT in orange and the respective cobalt and copper macrocycle porphyrins in lighter green and orange.

S8. Density functional theory (DFT) calculations.

We have modelled the cobalt mac-por by employing the unrestricted B3LYP hybrid functional using the Gaussian 16 Revision A.03[54], package. The method used was Becke's three-parameter hybrid exchange functional the nonlocal correlation provided by the Lee, Yang, and Parr expression[55,56]. The basis set was LanL2DZ. The optimized geometry of a Co mac-por is shown in Figure S7.

[54] Frisch, M. J.; Trucks, G. W.; Schlegel, H. B.; Scuseria, G. E.; Robb, M. A.; Cheeseman, J. R.; Scalmani, G.; Barone, V.; Mennucci, B.; Petersson, G. A.; Nakatsuji, H.; Caricato, M.; Li, X.; Hratchian, H. P.; Izmaylov, A. F.; Bloino, J.; Zheng, G.; Sonnenberg, J. L.; Hada, M.; Ehara, M.; Toyota, K.; Fukuda, R.; Hasegawa, J.; Ishida, M.; Nakajima, T.; Honda, Y.; Kitao, O.; Nakai, H.; Vreven, T.; Montgomery, J. A., J.; Peralta, J. E.; Ogliaro, F.; Bearpark, M.; Heyd, J. J.; Brothers, E.; Kudin, K. N.; Staroverov, V. N.; Kobayashi, R.; Normand, J.; Raghavachari, K.; Rendell, A.; Burant, J. C.; Iyengar, S. S.; Tomasi, J.; Cossi, M.; Rega, N.; Millam, J. M.; Klene, M.; Knox, J. E.; Cross, J. B.; Bakken, V.; Adamo, C.; Jaramillo, J.; Gomperts, R.; Stratmann, R. E.; Yazyev, O.; Austin, A. J.; Cammi, R.; Pomelli, C.; Ochterski, J. W.; Martin, R. L.; Morokuma, K.; Zakrzewski, V. G.; Voth, G. A.; Salvador, P.; Dannenberg, J. J.; Dapprich, S.; Daniels, A. D.; Farkas, Ö.; Foresman, J. B.; Ortiz, J. V.; Cioslowski, J.; Fox, D. J. Gaussian **2009**.

[55] Becke, A. D. *J. Chem. Phys.* **1993**, *98* (7), 5648.

[56] Lee, C.; Yang, W.; Parr, R. G. *Phys. Rev. B* **1988**, *37* (2), 785–789.

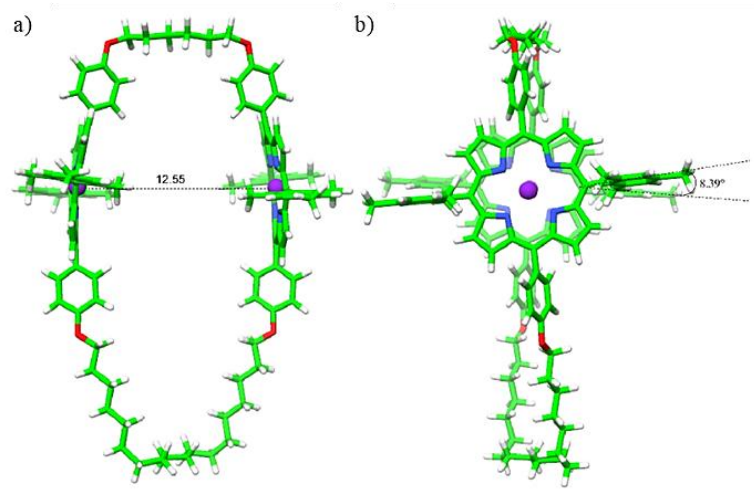

Figure S7. UB3LYP optimized geometries of Co mac-por as obtained by using LanL2DZ basis. The distances are measured in Å.

The corresponding Co mMINT was also stabilized. In this case, the theory used was: ub3lyp/lanl2dz for the macrocycle and hf/3-21g* for the carbon nanotube. The Cartesian coordinates of the carbon nanotube were freeze upon optimization of the nanotube isolated. The measured distances between the cobalt atom and the nanotube were: 3.479 Å and 3.765 Å for each cobalt atom respectively. Interestingly, the porphyrin structure is not bending itself towards the carbon nanotube, prevailing the pre-existing planar geometry, anterior to the mMINT formation (see Figure 1 in the main text).

S9. Additional TEM image.

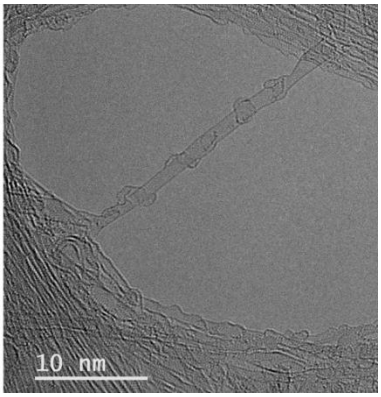

Figure S8. High resolution TEM images showing several mac-por units mechanically bonded to a SWNT.

S10. X-ray absorption Near Edge Structure (XANES) and Extended X-ray Absorption Fine Structure (EXAFS) spectroscopy.

a. X-ray Absorption Spectroscopy (XAS) Methods.

X-ray absorption spectra on the cobalt-based porphyrin complexes were collected at the Advanced Photon Source (APS) at Argonne National Laboratory on bending magnet beamline 20 at electron energy 7.7 KeV and average current of 100 mA source. The radiation at APS was monochromatized by a Si (110) crystal monochromator. The intensity of the X-rays were monitored by three ion chambers (I_0, I_1 and I_2) filled with 80% nitrogen and 20% helium and placed before the sample (I_0) and after the sample (I_1 and I_2). Co metal was placed between ion chambers I_1 and I_2 and its absorption was recorded with each scan for energy calibration. The samples were kept at 20 K in a He atmosphere at ambient pressure. The solution complexes and diluted mMINT complex with Boron Nitride (BN) were recorded as fluorescence excitation spectra using a 13-element energy-resolving detector. All samples were measured in a continuous helium flow cryostat in fluorescence mode with a 13-element Germanium detector. Around 30 XAS spectra were collected for each sample.

The X-ray absorption spectra on the Cu porphyrin solid complexes were by contrast carried out at the Petra P64 beamline[57] (Hamburg, Germany) and at the ELETTRA light source on the XAFS beamline at electron energy 8.98 KeV and average current 100 mA. The radiation was monochromatized at Petra and Elettra by a Si (111) crystal monochromator. The intensity of the X-ray was monitored by I_0, I_1 and I_2 filled with 70% nitrogen and 30% helium. A Cu metal foil was placed between the I_1 and I_2 and its absorption once again recorded with each scan for energy calibration. The solid complexes were similarly mixed with BN powder, pressed into a pellet, and subsequently inserted into a pre-cooled cryostat. The XAS data were recorded as fluorescence excitation spectra at both the P64 (Petra) and XAFS (ELETTRA) beamlines using a 4-element silicon drift detector.

All samples were also protected from the x-ray beam during spectrometer movements by a shutter synchronized with the scan program. Co and Cu XAS energy was calibrated by the first maxima in the second derivative of the cobalt and copper metal X-ray Absorption Near Edge Structure (XANES) spectrum respectively. No more than 5 scans were taken at each sample position at any condition. In order to reduce the risk of sample damage by x-ray radiation, 80%

[57] Gupta, M.; Kumar, Y.; Tayal, A.; Pandey, N.; Caliebe, W.; Stahn, J. *SN Appl. Sci.* **2020**, *2* (1), 1–11.

flux was used in the defocused mode (beam size 5500 µm (Horizontal) x 600 µm (Vertical)) and no damage was observed scan after scan to any samples.

b. Extended X-ray Absorption Fine Structure (EXAFS) Analysis.

Athena software[58] was used for data processing. The energy scale for each scan was normalized using the cobalt and copper metal standards. Data in energy space were pre-edge corrected, normalized, deglitched (if necessary), and background corrected. The processed data were next converted to the photoelectron wave vector (k) space and weighted by k^2. The electron wave number is defined as $k = [2m(E - E_0)/\hbar^2]^{1/2}$, E_0 is the energy origin or the threshold energy. K-space data were truncated near the zero crossings k = 2 to 11.6 $Å^{-1}$ for the solution and the mMINT complex, in Co and Cu EXAFS before Fourier transformation. The k-space data were transferred into the Artemis Software for curve fitting. In order to fit the data, the Fourier peaks were isolated separately, grouped together, or the entire (unfiltered) spectrum was used. The individual Fourier peaks were isolated by applying a Hanning window to the first and last 15% of the chosen range, leaving the middle 70% untouched. Curve fitting was performed using *ab initio*-calculated phases and amplitudes from the FEFF8[59] program from the University of Washington. *Ab initio*-calculated phases and amplitudes were used in the EXAFS equation

$$\chi(k) = S_0^2 \sum_j \frac{N_j}{kR_j^2} f_{eff_j}(\pi, k, R_j) e^{-2\sigma_j^2 k^2} e^{\frac{-2R_j}{\lambda_j(k)}} \sin(2kR_j + \phi_{ij}(k)) \qquad \text{(S1)}$$

where N_j is the number of atoms in the j^{th} shell; R_j the mean distance between the absorbing atom and the atoms in the j^{th} shell; $f_{eff_j}(\pi, k, R_j)$ is the *ab initio* amplitude function for shell *j*, and the Debye-Waller term $e^{-2\sigma_j^2 k^2}$ accounts for damping due to static and thermal disorder in absorber-backscatterer distances. The mean free path term $e^{\frac{-2R_j}{\lambda_j(k)}}$ reflects losses due to inelastic scattering, where $\lambda_j(k)$, is the electron mean free path. The oscillations in the EXAFS spectrum are reflected in the sinusoidal term $\sin(2kR_j + \phi_{ij}(k))$, where $\phi_{ij}(k)$ is the *ab initio* phase function for shell *j*. This sinusoidal term shows the direct relation between the frequency of the EXAFS oscillations in k-space and the absorber-backscatterer distance. S_0^2 is an amplitude reduction factor.

[58] Ravel, B.; Newville, M. *J. Synchrotron Rad.*; IUCrJ, **2005**, 12, 537–541.
[59] Rehr, J. J.; Albers, R. C. *Rev. Mod. Phys*. **2000**, *72* (3), 621–654.

The EXAFS equation[60] (Eq. S1) was used to fit the experimental Fourier isolated data (q-space) as well as unfiltered data (k-space) and Fourier transformed data (R-space) using N, S_0^2, E_0, R, and σ^2 as variable parameters (Table S1). N refers to the number of coordination atoms surrounding Co and Cu for each shell. The quality of fit was evaluated by R-factor and the reduced Chi^2 value. The deviation in E_0 ought to be less than or equal to 10 eV. R-factor less than 2% denotes that the fit is good enough whereas R-factor between 2 and 5% denotes that the fit is correct within a consistently broad model. The reduced Chi^2 value is used to compare fits as more absorber-backscatter shells are included to fit the data. A smaller reduced Chi^2 value implies a better fit. Similar results were obtained from fits done in k, q, and R-spaces.

c. XANES Simulations analysis.

TD-DFT Calculations for the XAS spectrum of the Co pre-edge and rising edge were performed using ORCA[61] , and HF-3C as functional. The pre-edge absorption spectra from the TD-DFT calculations were shifted in energy by +11 eV relative to the experimental data and a broadening of 1.0 eV was applied to all calculated spectra. The donor orbitals for XAS calculations were chosen as Co1s and all virtual orbitals were selected as acceptor orbitals. Up to 150 roots were calculated. The calculated pre-edge spectrum contains contributions from electric quadrupole, electric dipole and magnetic dipole transitions.

i. Co porphyrin complexes.

The XANES spectra of the U-por, mac-por and mMINT complexes show a prominent shoulder peak at 7715 eV characteristic of a Co(II) four-coordinated porphyrin complex[62]. Although the normalized XANES spectra show all 4 porphyrin complexes to have oxidation state +2, distinct changes are observed along the rising edge confirming small changes in the coordination spheres and local symmetries around the Co atom (Figure S9) as further illustrated through the EXAFS spectra in Figure 2d in the main text.

EXAFS studies provide a direct probe of changes in the Co-N and Co-C bond lengths. A prominent peak is observed in the EXAFS spectra of the U-por, mac-por and mMINT porphyrin complexes corresponding to the Co-N distances from 1.91-

[60] Koningsberg, D. C.; Prins R. *Wiley*; Koningsberg, D. C., Prins R, Eds.; John Wiley & Sons, **1988**.
[61] Neese, F. *Wiley Interdiscip. Rev. Comput. Mol. Sci.* **2012**, *2*, 73–78.
[62] Yamamoto, K.; Nakazawa, S.; Matsufuji, A.; Taguchi, T. *J. Chem. Soc., Dalton Trans.* **2001**, No. 3, 251–258.

-1.95 Å (See Figure 2d in the main text). Addition of an additional Co-O distance at 2.57 Å, 2.34 Å, and 2.36 Å improves the quality of the fit in the U-por, mac-por and mMINT porphyrin complexes respectively (Table S2) as illustrated by the decreased R-factors and reduced $\chi 2$ values. This finding confirms the out-of-plane pseudo-axial geometry observed from EPR spectroscopic measurements with an additional Co-O bond distance.

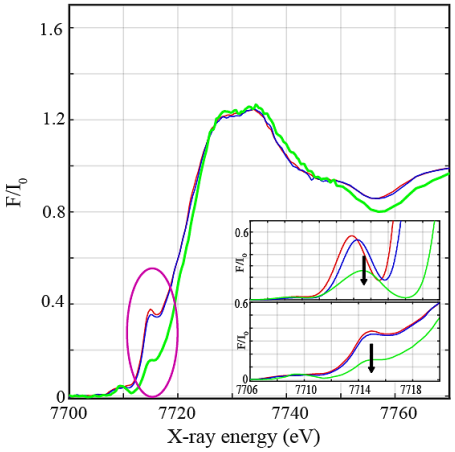

Figure S9. Normalized Cu K-edges XANES of the Co, U-por (red), mac-por (blue) dissolved in dichloromethane together with Co-mMINT solid complex (green) grinded with Boron Nitride all measured frozen at 20 K. Inset. Top. Theoretically calculated XANES simulations using the DFT optimized geometries as input. Bottom. Zoom-in of the experimental pre-edge and rising-edge features.

Table S1. Summary of Structural Parameters derived from EXAFS fits for the first coordination shell of the Co porphyrin complexes.

Complex	EXAFS Parameters	Distances (Å)
U-por	Co-N,4	1.94
	Co-O, 1	2.57
mac-por	Co-N,4	1.95
	Co-O, 1	2.34
mMINT	Co-N,4	1.91
	Co-O, 1	2.36

Table S2. EXAFS Fits parameters for the Co U-por, mac-por and mMINT complexes.

Sample	Fit	Region	Shell, N	R, Å	E_0	ss.^{2} (10^{-3})	R-factor	Reduced Chi-square
Co U-por	1	I	Co-N,4	1.93	-5.4	3.6	0.0280	75
	2	I, II	Co-N,4 Co-C,8 Co-C,16	1.92 2.50 2.98	-8.7	3.2 16.8 44.7	0.0333	66
	3	I, II	Co-N,4 Co-C/O,9 Co-C,16	1.92 2.50 2.96	-9.3	3.2 17.7 40.3	0.0328	65
	4	All	Co-N,4 Co-C/O,9 Co-C, 16 Co-C,12 Co-C,24	1.94 2.57 3.04 3.42 4.25	-5.1	3.7 24.5 17.5 8.0 32.2	0.0106	14
Co mac-por	5	I	Co-N,4	1.97	-2.2	3.5	0.0634	129
	6	I	Co-N,4 Co-O,1	1.97 2.40	-2.1	3.4 3.0	0.0104	53
	7	I, II	Co-N,4 Co-O,1 Co-C,8 Co-C,16	1.93 2.33 2.57 2.97	-10.4	4.5 6.9 9.8 29.2	0.0451	350
	8	All	Co-N,4 Co-O,1 Co-C,8 Co-C,16 Co-C,12 Co-C,24	1.95 2.34 2.62 3.02 3.38 4.20	-7.0	4.7 6.3 10.9 12.9 7.1 32.3	0.0116	17
Co mMINT	9	I	Co-N,4	1.93	-8.5	0.1	0.0092	105
	10	I	Co-N,4 Co-O,1	1.92 2.37	-11.8	0.2 6.6	0.0054	54
	11	I, II	Co-N,4 Co-O,1 Co-C,8 Co-C,16	1.91 2.36 2.61 2.95	-12.8	3.8 11.8 3.3 21.1	0.003	130
	12	All	Co-N,4 Co-O,1 Co-C,8 Co-C,16 Co-C,12 Co-C,24	1.91 2.36 2.66 3.01 3.36 4.20	-13.2	0.4 7.9 8.4 12.6 11.1 34.9	0.0071	23

* The amplitude reduction factor S02 was fixed to 1. Region I refers to the EXAFS spectra region between apparent distances 1-2.1 Å. Regions I, II to that between 1-3.3 Å and All to apparent distances between 1-4.1 Å.

ii. Cu porphyrin complexes.

XANES and EXAFS were additionally used to characterize the electronic and structural properties of the Cu-based porphyrin complexes. The Cu K-edge XANES spectra of Cu(II) square planar or tetrahedral complexes are generally characterized by a main peak along the rising edge from 8980 to 9000 eV at ~ 8986-8988 eV[63] (Figure S10). This transition is assigned to a metal localized 1s → 4 p transition with "shakedown" contribution arising from a coupled ligand to metal charge transfer (LMCT) transition.[64] The Cu monomeric, U-por and mac-por complexes demonstrate the 1s → (4 p+shakedown) transition at ~8988 eV whereas the mMINT complex exhibits this transition at ~8986 eV. The XANES spectra (Figure S10) show small changes in the rising-edge features indicating small variations in the local symmetries and coordination spheres of the four Cu(II) porphyrin complexes. A prominent peak at apparent distance of 1.5 Å (Figure 2e in the main manuscript) is observed in the EXAFS spectra of the four porphyrin complexes, corresponding to the averaged contribution of the Cu-N bond distances. The EXAFS fits for the extraction of the actual bond distances of all four complexes are shown in Figure 2(e) of the main manuscript and Table S3 and Table S4.

Analysis of the EXAFS spectra in the porphyrin complexes clearly resolved four Cu-N distances for the Cu monomeric, U-por, mac-por and mMINT complexes at 1.99 $\pm$ 0.02 Å, 2.04 $\pm$ 0.02 Å, 2.00 $\pm$ 0.01 Å and 1.99 $\pm$ 0.01 Å respectively. The close agreements observed in the experimental EXAFS for the Cu monomeric complex agree well with the local structural data extracted from XRD analysis showing that the EXAFS analysis can be reliably used for understanding the structural conformations of the four Cu-based porphyrins. Importantly, all four Cu-porphyrin complexes demonstrate very similar structural arrangements indicating the close to intact nature of the structural conformations of the Cu mMINT complex.

[63] Gaur, A.; Klysubun, W.; Joshi, S. K.; Soni, B.; Shrivastava, B. D.; Prasad, J.; Srivastava, K. In *J. Conf. Ser*. IOP **2016**, 712, 012084.

[64] DeBeer, S.; Randall, D. W.; Nersissian, A. M.; Valentine, J. S.; Hedman, B.; Hodgson, K. O.; Solomon, E. I. *J. Phys. Chem. B* **2000**, *104* (46), 10814–10819.

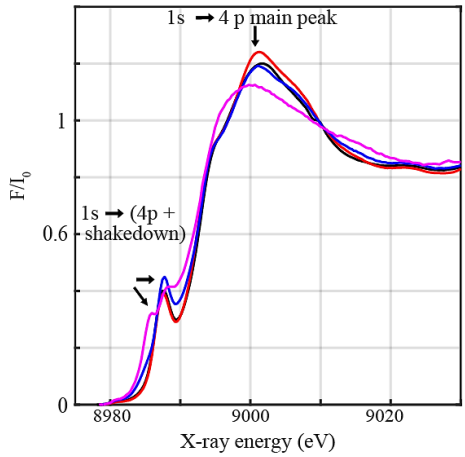

Figure S10. Normalized Cu K-edges XANES of the Cu monomer (black), U-por (red), mac-por (blue) porphyrin complexes together with the Cu mMINT complex (pink) grinded with Boron Nitride all measured frozen at 20 K.

Table S3. Summary of Structural Parameters derived from EXAFS fits for the first coordination shell.

Complex	EXAFS Parameters	Distances (Å)
Monomer	Cu-N,4	1.99
U-por	Cu-N,4	2.04
mac-por	Cu-N,4	2.00
mMINT	Cu-N,4	1.99

Table S4. EXAFS Fits parameters for the copper porphyrin complexes.

Sample	Fit	Region	Shell, N	R, Å	E_0	ss.^{2} (10^{-3})	R-factor	Reduced Chi-square
Cu Monomer	1	I	Cu-N,4	1.98	-1.1	4.1	0.0085	657
	2	I, II	Cu-N,4 Cu-C,8	1.99 3.05	1.7	3.9	0.0380	1093
	3	I, II	Cu-N,4 Cu-C,8 Cu-C,20	1.99 3.01 3.20	1.5	27.6	0.0070	323
Cu U-por	5	I	Cu-N,4	2.00	2.3	3.9	0.0265	751
	6	I, II	Cu-N,4 Cu-C,8	2.01 3.08	5.1	4.9 15.5	0.0432	452
	7	I, II	Cu-N,4 Cu-C,8 Cu-C,20	2.04 3.05 3.18	8.4	4.2 2.5 14.4	0.0168	268

Cu Mac-por	8	I	Cu-N,4	1.98	-0.75	3.9	0.0098	756
	9	I, II	Cu-N,4 Cu-C,8	1.99 3.07	2.7	4.7 25.1	0.0345	898
	10	I, II	Cu-N,4 Cu-C,8 Cu-C,20	2.00 3.01 3.18	2.6	3.6 3.9 18.0	0.0012	43
Cu mMINT	11	I	Cu-N,4	1.98	-0.34	5.0	0.0036	23
	12	I, II	Cu-N,4 Cu-C,8	1.98 2.78	-0.80	5.1 104	0.0228	50
	13	I, II	Cu-N,4 Cu-C,8 Cu-C,20	1.99 2.98 3.18	1.5	4.8 8.9 15.6	0.0039	12

* The amplitude reduction factor $S0^2$ was fixed to 1. Region I refers to the EXAFS spectra region between apparent distances 1.1-2 Å whereas regions I and II refer to that between 1.1-3 Å.

S11. Electronic configuration and crystal symmetry.

a. Cobalt porphyrin complexes.

The EPR spectra of Co derivatives is rather complex and typically involves a combination of orbital degeneracy, coupling to excited states and non-trivial modification of the coordination environment.[49]

The out-of-plane pseudoaxial geometry obtained for Co-porphyrins in the main text is, in principle, not expected for a d^7 electron in a square planar molecular field in porphyrin molecules. A possible explanation for the out-of-plane pseudo-axial geometry is that the Co-porphyrin is weakly penta or hexa-coordinated (see schematics in Figure S11b). It has been previously reported that Co porphyrins experience an enhanced affinity to molecular oxygen when in the presence of bases capable of H-bonding (like amides)[44,46–48] or even water[45]. Electron transfer from cobalt to molecular oxygen is promoted thus creating a bond between them, either if Co-O_2 superoxides or $Co^{3+}O_2$ species remains under debate[44–48]. In this scenario, the electronic level structure and electronic orbital filling of the d^7 Co^{2+} changes

[44] Walker, F. Ann. *J. Am. Chem. Soc.* **1970**, *92* (14), 4235–4244.
[45] Hoffman, B. Mark.; Diemente, D. L.; Basolo, Fred. *J. Am. Chem. Soc.* **1970**, *92* (1), 61–65.
[46] Baumgarten, M.; Winscom, C. J.; Lubitz, W. *Appl. Magn. Reason.* **2001**, *20* (1–2), 35–70.
[47] Van Doorslaer, S.; Schweiger, A. *J. Phys. Chem. B* **2000**, *104*, 2919–2927.
[48] Collman, J. P.; Berg, K. E.; Sunderland, C. J.; Aukauloo, A.; Vance, M. A.; Solomon, E. I. *Inorg. Chem.* **2002**, *41* (25), 6583.
[49] Skrzypek, D.; Madejska, I.; Habdas, J. *Solid State Sci.* **2007**, *9* (3–4), 295–302.

from a square planar geometry (where the unpaired electron would reside in the xy plane, Figure S11c) to a pyramidal or bi-pyramidal tetragonal symmetry that can be approximated to elongated octahedral symmetry (Figure S11b). The presence of adducts would induce more complex rhombic distortions that could explain as well some orthorhombicity of the g tensor.

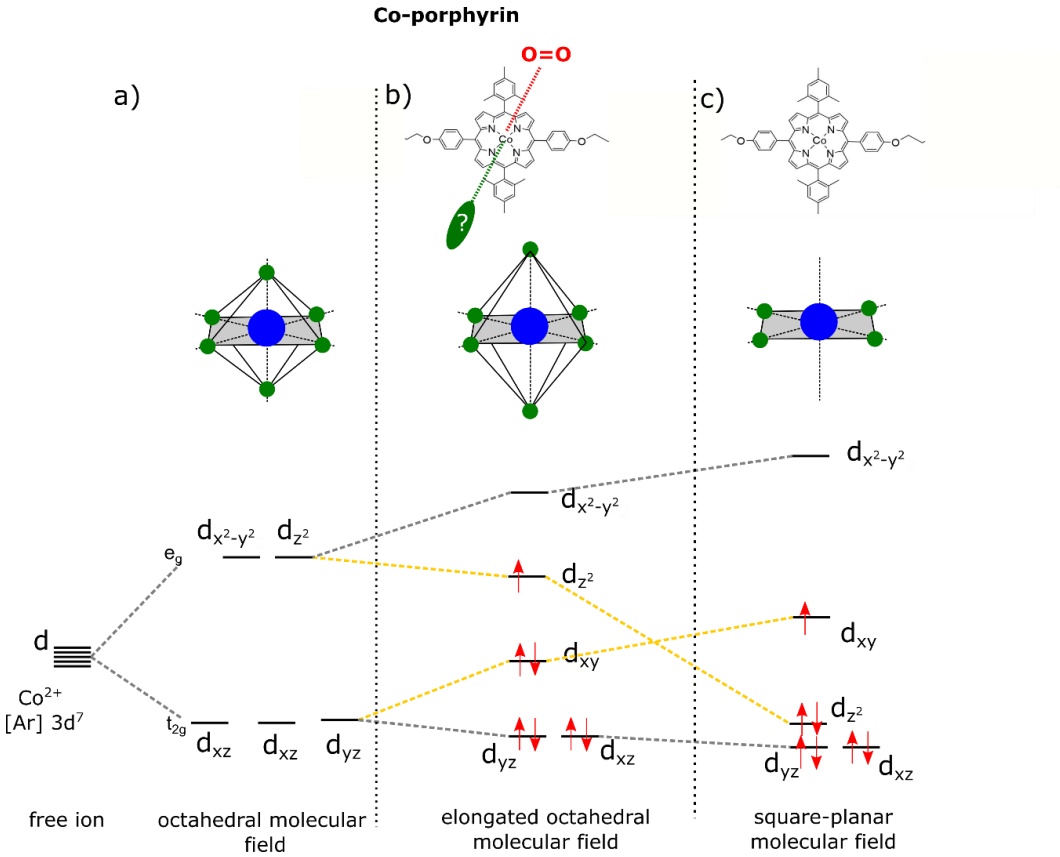

Figure S11. Energy level structure of Co^{2+} in a) an octahedral molecular field, b) elongated octahedral molecular field (or bi-pyramidal tetragonal field) and a c) square-planar molecular field. The elongated octahedral geometry occurs in cobalt porphyrins hexa/penta coordinated to molecular oxygen and other solvents.

b. Copper porphyrin complexes.

In contrast to the cobalt derivatives, the absence of adducts in the copper dimers results in a more straightforward analysis. Figure S12 shows the electronic level structure and orbital filling of a d^9 Cu^{2+} ion in a square planar geometry. The unpaired electron resides in the d_{x2-y2} orbital.

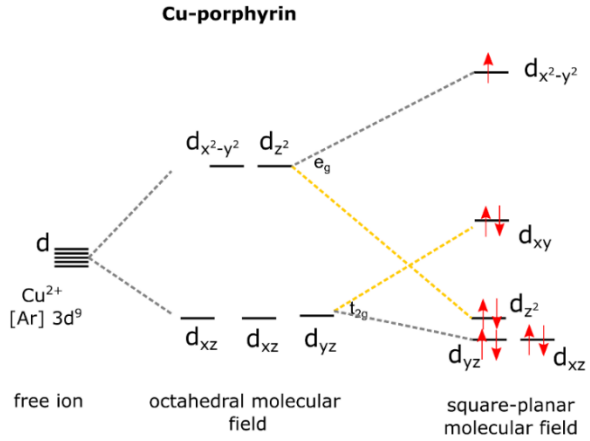

Figure S12. Energy level structure of Cu^{2+} in square-planar molecular field.

S12. Additional EPR Spectra.

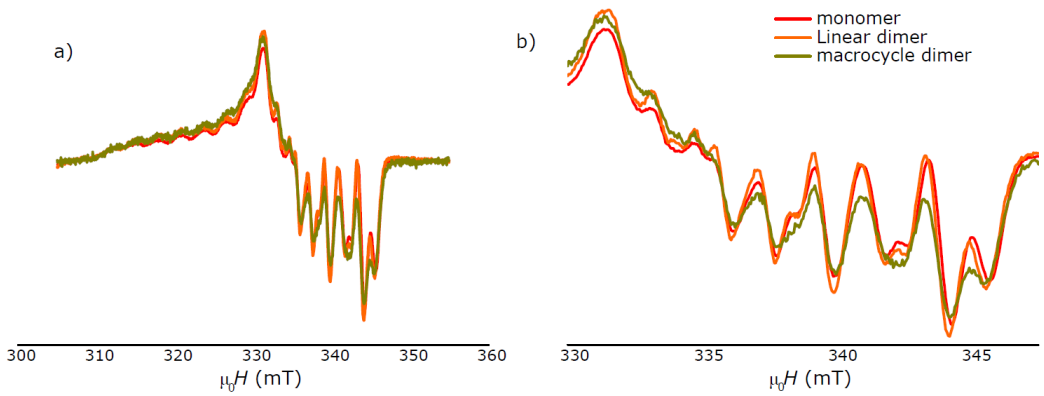

Figure S13. shows the EPR spectrum measured in a Co-mMINT sample. A clear g = 2, S = ½ resonance is observed that corresponds to the itinerant spins in the carbon nanotube. However, no clear signature from the Co porphyrins is observed.

Figure S13 shows a comparison of the Co monomer, U-por and mac-por EPR spectra normalized to the maximum signal. The monomer and the U-por spectra are

almost identical in number, intensity, and position of the resonances. The mac-por presents a diminished intensity and slightly increased width of the *x-y* components

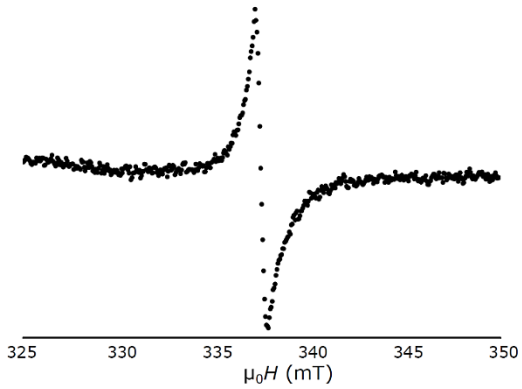

Figure S13. X-band Electron Paramagnetic Resonance EPR spectra measured at T = 20 K on Co-porphyrin mMINT powder sample. A_g = 3, S =1/2 resonance is observed. It can be assigned to the free spins in the carbon nanotube. No clear spectrum from the Co porphyrins is observed.

S13. Pulse EPR spectroscopy.

a. Phase memory time.

Phase memory times (T_M) are measured for all the Cu compounds via a two-pulse Hahn echo sequence: π/2-τ-π-τ-echo, where τ is the time between pulses and echo measurement. The echo intensity decay, shown in Figure 4(c) and Figure 4(d) of the main manuscript for the Cu mac-por and mMINT respectively, can be fitted with a bi-exponential that accounts for an initial 'fast' decay and a subsequent 'slow' decay. The initial decay is almost independent of the temperature whereas a drop in T_M with increasing temperature would be expected for the porphyrin samples. This decay could be therefore an experimental artefact originated by a residual ringing or impurities in the cavity. On the other hand, it cannot be discarded a faster relaxation due to a less favourable environment of part of the paramagnetic centers in the samples.

The slow mode relaxation, in turn, shows a clear dependence with temperature. The evolution of the T_M with temperature is shown in Figure S15(a) for B = 331 mT. T_M reaches a maximum of about T_M = 25 μs at around 10 K for monomer, U-por and mac-por. This value decreases to about 5 μs for the mMINT as explained in the main text. A similar behaviour is observed for other magnetic fields.

The presence of a T_M maximum value in temperature is not unusual for a paramagnetic molecular system. T_M depends on spin-spin decoherence processes.

Such processes can be indirectly affected by the activation/freezing of vibrational modes or other thermal mechanisms. It has been recently reported that the freezing of vibrational modes (rotational mode) of non-deuterated solvent molecules used in ESR experiments can originate a maximum in T_M.[15] A similar effect is most likely originating the peak in the molecular system presented in this manuscript.

b. Spin-lattice relaxation time

The spin-lattice relaxation time (T_1) is obtained via a 3-pulse inversion-recovery sequence. T_1 is obtained by fitting the echo intensity decay (Figure 4e in the main text) with an exponential decay. Figure S15(b) shows the evolution of T_1 as a function of temperature for the monomer, the U-por and the mac-por derivatives at 331 mT. The echo intensity after 3 pulses for the mMINT was too weak to be measured. The three derivatives show $T_1 \approx 0.8$ ms below 20 K. Note that the apparent maximum around 10 K in T_1 is probably an experimental artefact or part of the uncertainty in the determination of T_1.

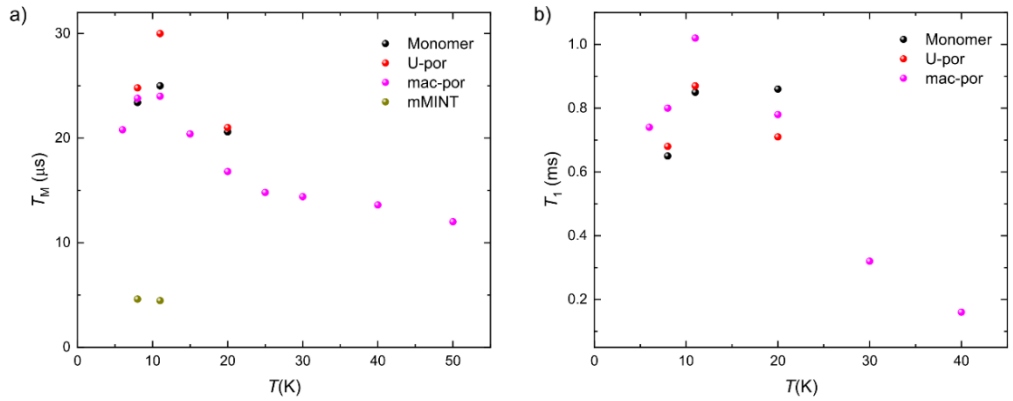

Figure S14. a) Phase memory time T_m obtained at different temperatures and at 331 mT from the echo intensity decay measured after a two-pulse Hahn sequence in EPR. b) Spin-lattice time T_1 obtained at different temperatures and at 331 mT from the echo intensity decay after a three-pulse inversion-recovery sequence. The echo in the mMINT was too weak to obtain T_1.

[15] von Kugelgen, S.; Krzyaniak, M. D.; Gu, M.; Puggioni, D.; Rondinelli, J. M.; Wasielewski, M. R.; Freedman, D. E. *J. Am. Chem. Soc.* **2021**, *143* (21), 8069–8077.

The raw spin echo relaxation measurements used to obtain Tm at different temperatures are shown in Figures S16-S20.

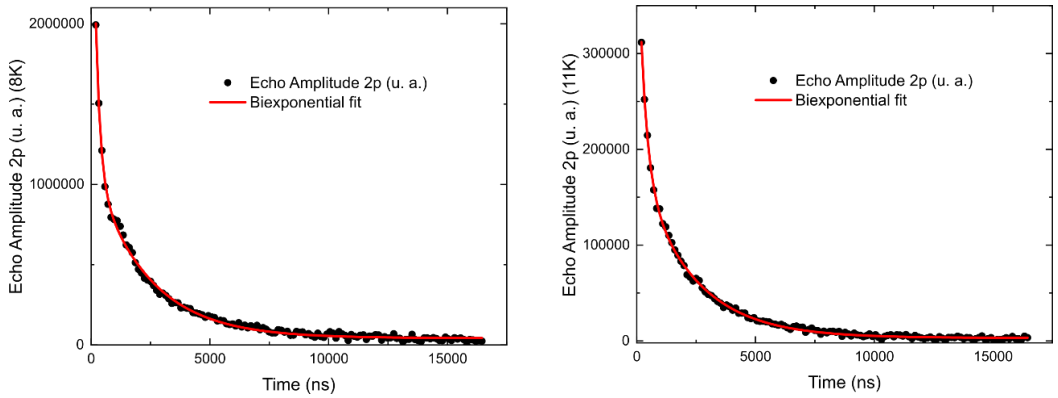

Figure S15. Echo intensity decay measured after a Hahn sequence of pulses and at different temperatures (8K, 11K) at 331 mT for the Cu mMINT derivative. The lines are fits to a biexponential with the Tm shown in Figure S15.

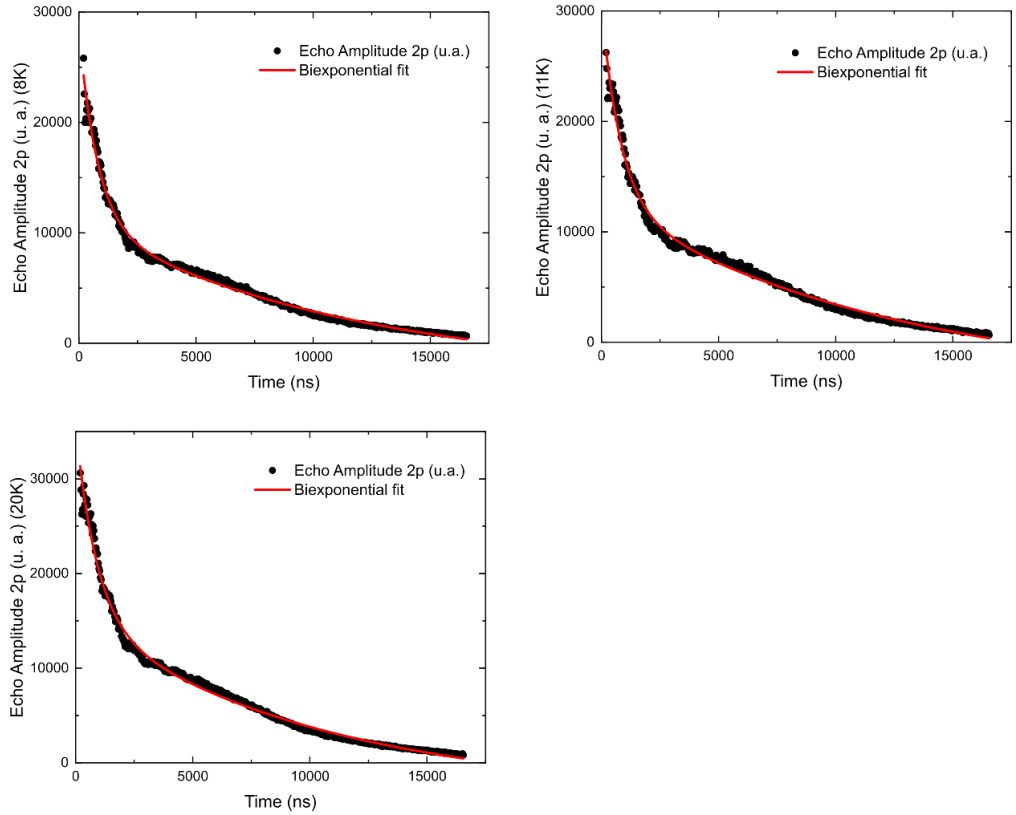

Figure S16. Echo intensity decay measured after a Hahn sequence of pulses and at different temperatures (8K, 11K, 20K) at 331 mT for the Cu monomer. The lines are fits to a biexponential with the Tm shown in Figure S15.

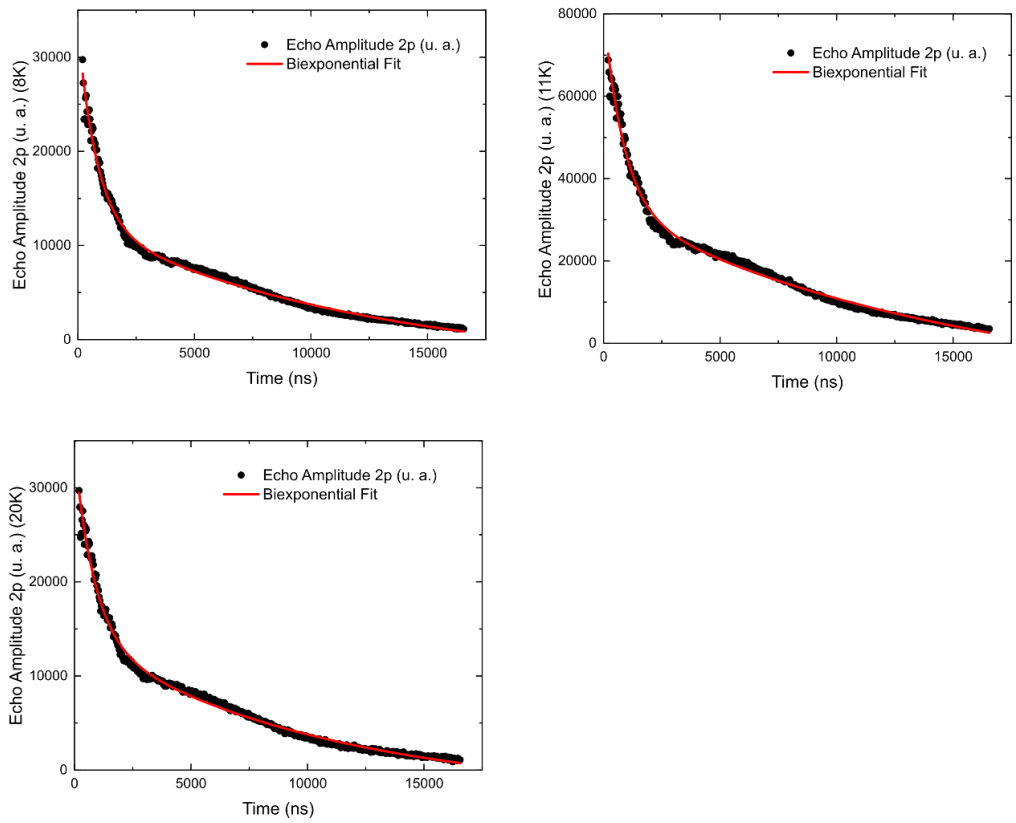

Figure S17. Echo intensity decay measured after a Hahn sequence of pulses and at different temperatures (8K, 11K, 20K) at 331 mT for the Cu-U-por molecule. The lines are fits to a biexponential with the Tm shown in Figure S15.

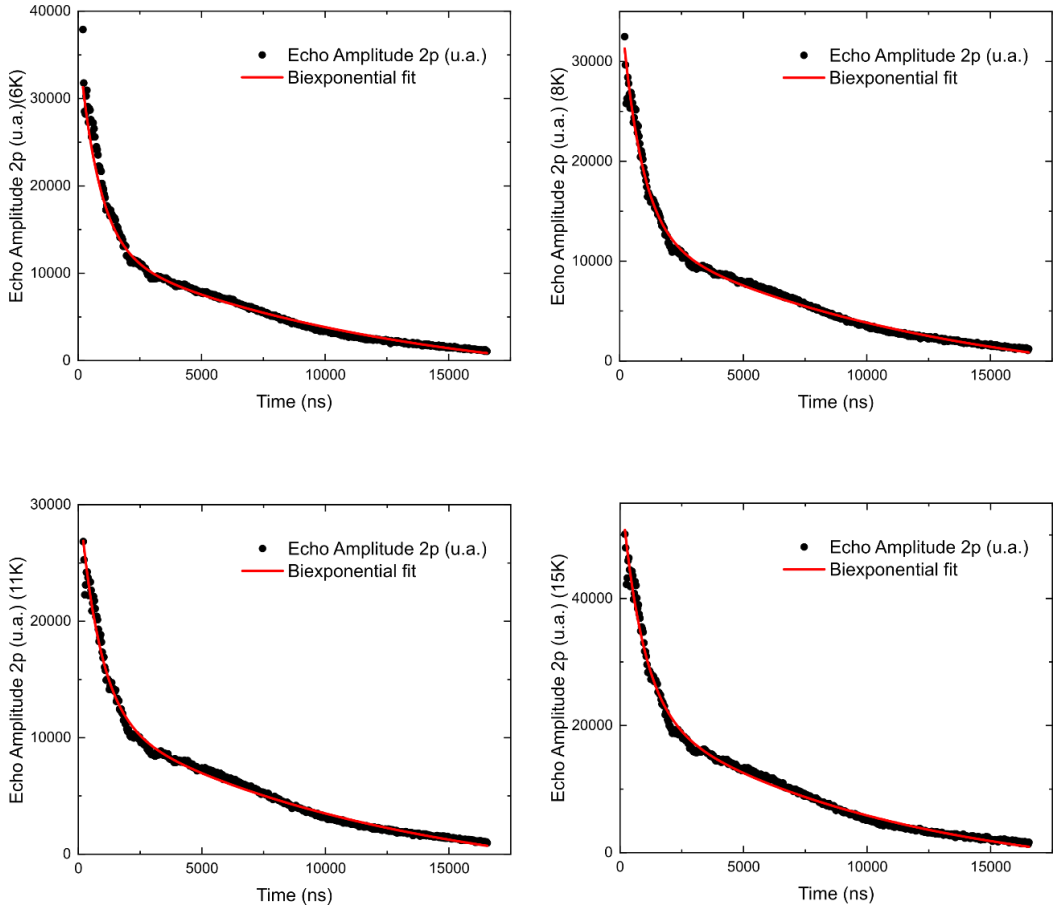

Figure S18. Echo intensity decay measured after a Hahn sequence of pulses and at different temperatures (6K, 8K, 11K, 15K) at 331 mT for the Cu-mac-por molecule. The lines are fits to a biexponential with the Tm shown in Figure S15.

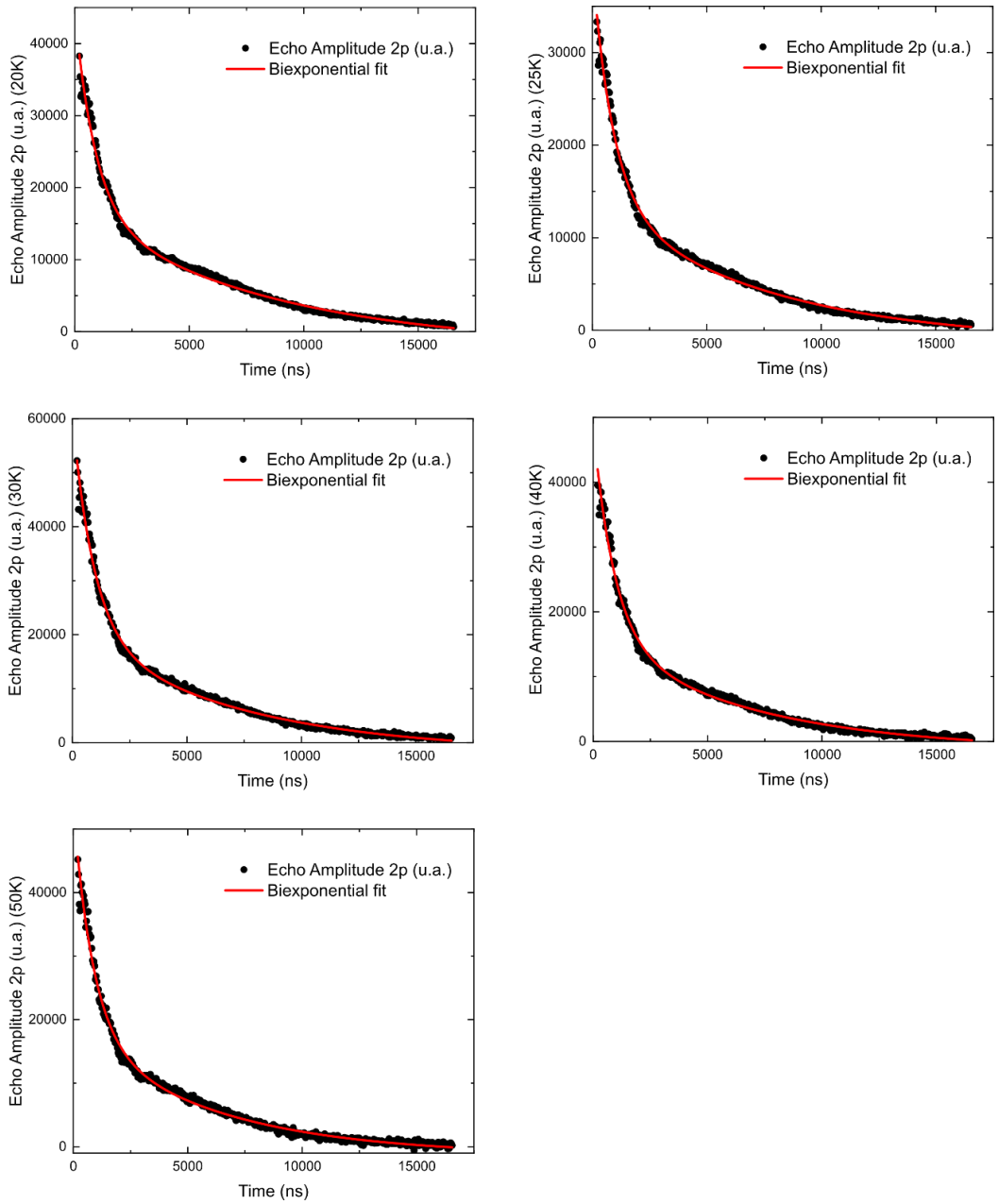

Figure S19. Echo intensity decay measured after a Hahn sequence of pulses and at different temperatures (20K, 25K, 30K, 40K, 50K) at 331 mT for the Cu-mac-por molecule. The lines are fits to a biexponential with the Tm shown in Figure S15.

S14. Fabrication of devices based on mMINTs.

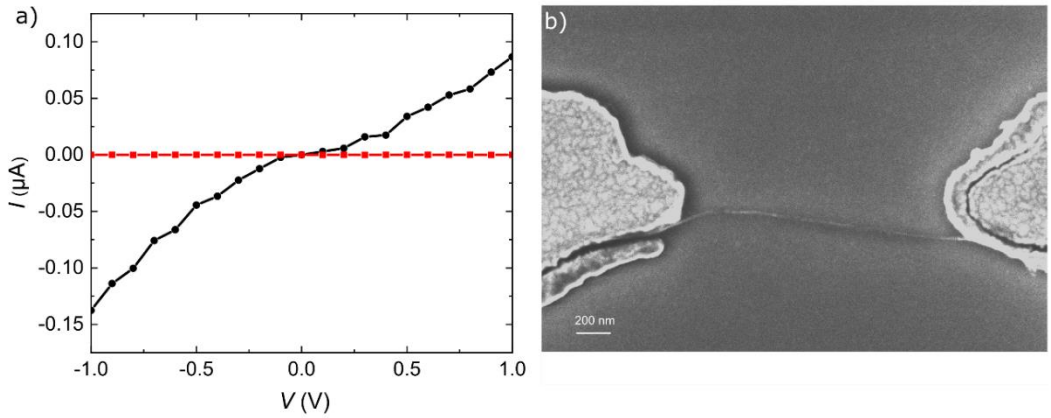

Figure S20. (a) Current I – Voltage V curve measured at room temperature on a solid-state transistor before (red) and after (black) positioning of the mMINTs by dielectrophoresis. A sharp increment in the conductance indicates that a mMINT has bridged the gap between the electrodes. (b) Scanning Electron Microscopy (SEM) image of a pair of electrodes containing a mMINT trapped by dielectrophoresis.

Field effect-like devices are fabricated in a cleanroom environment. Sets of 1 µm-spaced gold electrodes are fabricated on a Si/SiO_2 substrate by mask-less laser lithography and subsequent evaporation of metals (Figure S16b). mMINTs are deterministically placed between the electrodes by dielectrophoresis[27,53]. In short, an AC bias voltage (v = 3 MHz, V_{AC} = 4 V, t = 60 s) is applied between the electrodes while immersed in an isopropanol droplet containing dispersed mMINTs. The concentration to obtain individual mMINTs is roughly 0.013mg/ml. The device is annealed at 200 Celsius and 10^{-6} mbar for 4 hours after dielectrophoresis. Figure S21a shows the current measured at room temperature in a solid-state device before and after dielectrophoresis. A sharp increment in the conductance after dielectrophoresis is indicative of the presence of a mMINT bridging the gap between the electrodes. The scanning electron microscopy image in Figure S21b confirms the presence of a single mMINT aligned in between the electrodes.

[27] Villalva, J.; Develioglu, A.; Montenegro-Pohlhammer, N.; Sánchez-de-Armas, R.; Gamonal, A.; Rial, E.; García-Hernández, M.; Ruiz-Gonzalez, L.; Costa, J. S.; Calzado, C. J.; Pérez, E. M.; Burzurí, E. *Nature Commun.* **2021**, *12*, 1578.

[53] Nieto-Ortega, B.; Villalva, J.; Vera-Hidalgo, M.; Ruiz-González, L.; Burzurí, E.; Pérez, E. M. *Angew. Chem. Int. Ed.* **2017**, *56* (40), 12240–12244.

3.5. BIBLIOGRAPHY

(1) Leuenberger, M. N.; Loss, D. Quantum Computing in Molecular Magnets. *Nature* **2001**, *410* (6830), 789–793.

(2) Gaita-Ariño, A.; Luis, F.; Hill, S.; Coronado, E. Molecular Spins for Quantum Computation. *Nat. Chem.* **2019**, *11* (4), 301–309.

(3) Sanvito, S. Molecular Spintronics. *Chem. Soc. Rev.* **2011**, *40* (6), 3336–3355.

(4) Luis, F.; Repollés, A.; Martínez-Pérez, M. J.; Aguilà, D.; Roubeau, O.; Zueco, D.; Alonso, P. J.; Evangelisti, M.; Camón, A.; Sesé, J.; Barrios, L. A.; Aromí, G. Molecular Prototypes for Spin-Based CNOT and SWAP Quantum Gates. *Phys. Rev. Lett.* **2011**, *107* (11), 117203.

(5) Aguilà, D.; Barrios, L. A.; Velasco, V.; Roubeau, O.; Repollés, A.; Alonso, P. J.; Sesé, J.; Teat, S. J.; Luis, F.; Aromí, G. Heterodimetallic [LnLn′] Lanthanide Complexes: Toward a Chemical Design of Two-Qubit Molecular Spin Quantum Gates. *J. Am. Chem. Soc.* **2014**, *136* (40), 14215–14222.

(6) Godfrin, C.; Ferhat, A.; Ballou, R.; Klyatskaya, S.; Ruben, M.; Wernsdorfer, W.; Balestro, F. Operating Quantum States in Single Magnetic Molecules: Implementation of Grover's Quantum Algorithm. *Phys. Rev. Lett.* **2017**, *119* (18), 187702.

(7) Moreno-Pineda, E.; Godfrin, C.; Balestro, F.; Wernsdorfer, W.; Ruben, M. Molecular Spin Qudits for Quantum Algorithms. *Chem. Soc. Rev.* **2018**, *47* (2), 501–513.

(8) Herrmann, C.; Solomon, G. C.; Ratner, M. A. Organic Radicals As Spin Filters. *J. Am. Chem. Soc.* **2010**, *132* (11), 3682–3684.

(9) Pal, A. N.; Li, D.; Sarkar, S.; Chakrabarti, S.; Vilan, A.; Kronik, L.; Smogunov, A.; Tal, O. Nonmagnetic Single-Molecule Spin-Filter Based on Quantum Interference. *Nat. Commun.* **2019**, *10* (1), 5565.

(10) Zhang, J. L.; Zhong, J. Q.; Lin, J. D.; Hu, W. P.; Wu, K.; Xu, G. Q.; Wee, A. T. S.; Chen, W. Towards Single Molecule Switches. *Chem. Soc. Rev.* **2015**, *44* (10), 2998–3022.

(11) Burzurí, E.; García-Fuente, A.; García-Suárez, V.; Kumar, K. S.; Ruben, M.; Ferrer, J.; Zant, H. S. J. van der. Spin-State Dependent Conductance Switching in Single Molecule-Graphene Junctions. *Nanoscale* **2018**, *10* (17), 7905–7911.

(12) Urdampilleta, M.; Klyatskaya, S.; Cleuziou, J.-P.; Ruben, M.; Wernsdorfer, W. Supramolecular Spin Valves. *Nature Mater.* **2011**, *10* (7), 502–506.

(13) Urtizberea, A.; Natividad, E.; Alonso, P. J.; Andrés, M. A.; Gascón, I.; Goldmann, M.; Roubeau, O. A Porphyrin Spin Qubit and Its 2D Framework Nanosheets. *Adv. Funct. Mat.* **2018**, *28* (31), 1801695.

(14) Yu, C.-J.; Krzyaniak, M. D.; Fataftah, M. S.; Wasielewski, M. R.; Freedman, D. E. A Concentrated Array of Copper Porphyrin Candidate Qubits. *Chem. Sci.* **2019**, *10* (6), 1702–1708.

(15) von Kugelgen, S.; Krzyaniak, M. D.; Gu, M.; Puggioni, D.; Rondinelli, J. M.; Wasielewski, M. R.; Freedman, D. E. Spectral Addressability in a Modular Two Qubit System. *J. Am. Chem. Soc.* **2021**, *143* (21), 8069–8077.

(16) Mas-Torrent, M.; Crivillers, N.; Mugnaini, V.; Ratera, I.; Rovira, C.; Veciana, J. Organic Radicals on Surfaces: Towards Molecular Spintronics. *J. Mater. Chem.* **2009**, *19* (12), 1691–1695.

(17) Gaudenzi, R.; de Bruijckere, J.; Reta, D.; Moreira, I. de P. R.; Rovira, C.; Veciana, J.; van der Zant, H. S. J.; Burzurí, E. Redox-Induced Gating of the Exchange Interactions in a Single Organic Diradical. *ACS Nano* **2017**, *11* (6), 5879–5883.

(18) Dai, Y.-Z.; Dong, B.-W.; Kao, Y.; Wang, Z.-Y.; Un, H.-I.; Liu, Z.; Lin, Z.-J.; Li, L.; Xie, F.-B.; Lu, Y.; Xu, M.-X.; Lei, T.; Sun, Y.-J.; Wang, J.-Y.; Gao, S.; Jiang, S.-D.; Pei, J. Chemical Modification toward Long Spin Lifetimes in Organic Conjugated Radicals. *ChemPhysChem* **2018**, *19* (22), 2972–2977.

(19) Atzori, M.; Tesi, L.; Morra, E.; Chiesa, M.; Sorace, L.; Sessoli, R. Room-Temperature Quantum Coherence and Rabi Oscillations in Vanadyl Phthalocyanine: Toward Multifunctional Molecular Spin Qubits. *J. Am. Chem. Soc.* **2016**, *138* (7), 2154–2157.

(20) Clemente-Juan, J. M.; Coronado, E.; Gaita-Ariño, A. Magnetic Polyoxometalates: From Molecular Magnetism to Molecular Spintronics and Quantum Computing. *Chem. Soc. Rev.* **2012**, *41* (22), 7464–7478.

(21) Lehmann, J.; Gaita-Ariño, A.; Coronado, E.; Loss, D. Spin Qubits with Electrically Gated Polyoxometalate Molecules. *Nature Nanotech.* **2007**, *2* (5), 312–317.

(22) Perrin, M. L.; Burzurí, E.; Zant, H. S. J. van der. Single-Molecule Transistors. *Chem. Soc. Rev.* **2015**, *44* (4), 902–919.

(23) Thiele, S.; Balestro, F.; Ballou, R.; Klyatskaya, S.; Ruben, M.; Wernsdorfer, W. Electrically Driven Nuclear Spin Resonance in Single-Molecule Magnets. *Science* **2014**, *344* (6188), 1135–1138.

(24) Jenkins, M. D.; Zueco, D.; Roubeau, O.; Aromí, G.; Majer, J.; Luis, F. A Scalable Architecture for Quantum Computation with Molecular Nanomagnets. *Dalton Trans.* **2016**, *45* (42), 16682–16693.

(25) Carretta, S.; Zueco, D.; Chiesa, A.; Gómez-León, Á.; Luis, F. A Perspective on Scaling up Quantum Computation with Molecular Spins. *Appl. Phys. Lett.* **2021**, *118* (24), 240501.

(26) Urdampilleta, M.; Nguyen, N.-V.; Cleuziou, J.-P.; Klyatskaya, S.; Ruben, M.; Wernsdorfer, W. Molecular Quantum Spintronics: Supramolecular Spin Valves Based on Single-Molecule Magnets and Carbon Nanotubes. *Int. J. Mol. Sc.i* **2011**, *12* (10), 6656–6667.

(27) Villalva, J.; Develioglu, A.; Montenegro-Pohlhammer, N.; Sánchez-de-Armas, R.; Gamonal, A.; Rial, E.; García-Hernández, M.; Ruiz-Gonzalez, L.; Costa, J. S.; Calzado, C. J.; Pérez, E. M.; Burzurí, E. Spin-State-Dependent

Electrical Conductivity in Single-Walled Carbon Nanotubes Encapsulating Spin-Crossover Molecules. *Nature Commun.* **2021**, *12*, 1578.

(28) Kyatskaya, S.; Galán Mascarós, J. R.; Bogani, L.; Hennrich, F.; Kappes, M.; Wernsdorfer, W.; Ruben, M. Anchoring of Rare-Earth-Based Single-Molecule Magnets on Single-Walled Carbon Nanotubes. *J. Am. Chem. Soc.* **2009**, *131* (42), 15143–15151.

(29) Ganzhorn, M.; Klyatskaya, S.; Ruben, M.; Wernsdorfer, W. Strong Spin–Phonon Coupling between a Single-Molecule Magnet and a Carbon Nanotube Nanoelectromechanical System. *Nature Nanotech.* **2013**, *8* (3), 165–169.

(30) Garrido, M.; Volland, M. K.; Münich, P. W.; Rodríguez-Pérez, L.; Calbo, J.; Ortí, E.; Herranz, M. Á.; Martín, N.; Guldi, D. M. Mono- and Tripodal Porphyrins: Investigation on the Influence of the Number of Pyrene Anchors in Carbon Nanotube and Graphene Hybrids. *J. Am. Chem. Soc.* **2020**, *142* (4), 1895–1903.

(31) Schnee, M.; Besson, C.; Frielinghaus, R.; Lurz, C.; Kögerler, P.; Schneider, C. M.; Meyer, C. Quantum Transport in Carbon Nanotubes Covalently Functionalized with Magnetic Molecules. *physica status solidi (b)* **2016**, *253* (12), 2424–2427.

(32) del Carmen Giménez-López, M.; Moro, F.; La Torre, A.; Gómez-García, C. J.; Brown, P. D.; van Slageren, J.; Khlobystov, A. N. Encapsulation of Single-Molecule Magnets in Carbon Nanotubes. *Nat. Commun.* **2011**, *2* (1), 407.

(33) Domanov, O.; Weschke, E.; Saito, T.; Peterlik, H.; Pichler, T.; Eisterer, M.; Shiozawa, H. Exchange Coupling in a Frustrated Trimetric Molecular Magnet Reversed by a 1D Nano-Confinement. *Nanoscale* **2019**, *11* (22), 10615–10621.

(34) Pérez, E. M. Putting Rings around Carbon Nanotubes. *Chem. Eur. J.* **2017**, *23* (52), 12681–12689.

(35) de Juan, A.; Pouillon, Y.; Ruiz-González, L.; Torres-Pardo, A.; Casado, S.; Martín, N.; Rubio, Á.; Pérez, E. M. Mechanically Interlocked Single-Wall Carbon Nanotubes. *Angew. Chem. Inter. Ed.* **2014**, *53* (21), 5394–5400.

(36) de Juan, A.; Mar Bernal, M.; Pérez, E. M. Optimization and Insights into the Mechanism of Formation of Mechanically Interlocked Derivatives of Single-Walled Carbon Nanotubes. *ChemPlusChem* **2015**, *80* (7), 1153–1157.

(37) Cirulli, M.; Salvadori, E.; Zhang, Z.-H.; Dommett, M.; Tuna, F.; Bamberger, H.; Lewis, J. E. M.; Kaur, A.; Tizzard, G. J.; van Slageren, J.; Crespo-Otero, R.; Goldup, S. M.; Roessler, M. M. Rotaxane CoII Complexes as Field-Induced Single-Ion Magnets. *Angew. Chem. Inter. Ed.* **2021**, *60* (29), 16051–16058.

(38) Chamorro, R.; Juan-Fernández, L. de; Nieto-Ortega, B.; Mayoral, M. J.; Casado, S.; Ruiz-González, L.; Pérez, E. M.; González-Rodríguez, D. Reversible Dispersion and Release of Carbon Nanotubes via Cooperative Clamping Interactions with Hydrogen-Bonded Nanorings. *Chem. Sci.* **2018**, *9* (17), 4176–4184.

(39) Miki, K.; Saiki, K.; Umeyama, T.; Baek, J.; Noda, T.; Imahori, H.; Sato, Y.; Suenaga, K.; Ohe, K. Unique Tube–Ring Interactions: Complexation of Single-Walled Carbon Nanotubes with Cycloparaphenyleneacetylenes. *Small* **2018**, *14* (26), 1800720.

(40) Balakrishna, B.; Menon, A.; Cao, K.; Gsänger, S.; Beil, S. B.; Villalva, J.; Shyshov, O.; Martin, O.; Hirsch, A.; Meyer, B.; Kaiser, U.; Guldi, D. M.; von Delius, M. Dynamic Covalent Formation of Concave Disulfide Macrocycles Mechanically Interlocked with Single-Walled Carbon Nanotubes. *Angew. Chem. Inter. Ed.* **2020**, *59* (42), 18774–18785.

(41) Auwärter, W.; Écija, D.; Klappenberger, F.; Barth, J. V. Porphyrins at Interfaces. *Nature Chem.* **2015**, *7* (2), 105–120.

(42) de Juan-Fernández, L.; Münich, P. W.; Puthiyedath, A.; Nieto-Ortega, B.; Casado, S.; Ruiz-González, L.; Pérez, E. M.; Guldi, D. M. Interfacing Porphyrins and Carbon Nanotubes through Mechanical Links. *Chem. Sci.* **2018**, *9* (33), 6779–6784.

(43) Cunningham, K. L.; McNett, K. M.; Pierce, R. A.; Davis, K. A.; Harris, H. H.; Falck, D. M.; McMillin, D. R. EPR Spectra, Luminescence Data, and Radiationless Decay Processes of Copper(II) Porphyrins. *Inorg. Chem.* **1997**, *36* (4), 608–613.

(44) Walker, F. Ann. Electron Spin Resonance Study of Coordination to the Fifth and Sixth Positions of .Alpha.,.Beta.,.Gamma.,.Delta.-Tetra(p-Methoxyphenyl)Porphinatocobalt(II). *Journal of the American Chemical Society* **1970**, *92* (14), 4235–4244.

(45) Hoffman, B. Mark.; Diemente, D. L.; Basolo, Fred. Electron Paramagnetic Resonance Studies of Some Cobalt(II) Schiff Base Compounds and Their Monomeric Oxygen Adducts. *J. Am. Chem. Soc.* **1970**, *92* (1), 61–65.

(46) Baumgarten, M.; Winscom, C. J.; Lubitz, W. Probing the Surrounding of a Cobalt(II) Porphyrin and Its Superoxo Complex by EPR Techniques. *Appl. Magn. Reson.* **2001**, *20* (1–2), 35–70.

(47) Van Doorslaer, S.; Schweiger, A. Continuous Wave and Pulse EPR and ENDOR Study of Oxygenated Cobalt(II) Heme Model Systems. *J. Phys. Chem. B* **2000**, *104*, 2919–2927.

(48) Collman, J. P.; Berg, K. E.; Sunderland, C. J.; Aukauloo, A.; Vance, M. A.; Solomon, E. I. Distal Metal Effects in Cobalt Porphyrins Related to CcO. *Inorg. Chem.* **2002**, *41* (25), 6583..

(49) Skrzypek, D.; Madejska, I.; Habdas, J. The Characterization of Cobalt(II) Derivatives of Selected Substituted Meso-Tetraphenyl and Tetrapyridyl Porphyrins by EPR Spectroscopic Study. *Solid State Sci.* **2007**, *9* (3–4), 295–302.

(50) Jones, R. D.; Summerville, D. A.; Basolo, Fred. Synthetic Oxygen Carriers Related to Biological Systems. *Chem. Rev.* **1979**, *79* (2), 139–179.

(51) Chen, Y.; Chen, J.; Hu, H.; Hamon, M. A.; Itkis, M. E.; Haddon, R. C. Solution-Phase EPR Studies of Single-Walled Carbon Nanotubes. *Chem. Phys. Lett.* **1999**, *299* (6), 532–535.

(52) Malavolti, L.; Briganti, M.; Hänze, M.; Serrano, G.; Cimatti, I.; McMurtrie, G.; Otero, E.; Ohresser, P.; Totti, F.; Mannini, M.; Sessoli, R.; Loth, S. Tunable Spin–Superconductor Coupling of Spin 1/2 Vanadyl Phthalocyanine Molecules. *Nano Lett.* **2018**, *18* (12), 7955–7961.

(53) Nieto-Ortega, B.; Villalva, J.; Vera-Hidalgo, M.; Ruiz-González, L.; Burzurí, E.; Pérez, E. M. Band-Gap Opening in Metallic Single-Walled Carbon Nanotubes by Encapsulation of an Organic Salt. *Angew. Chem. Inter. Ed.* **2017**, *56* (40), 12240–12244.

(54) Frisch, M. J.; Trucks, G. W.; Schlegel, H. B.; Scuseria, G. E.; Robb, M. A.; Cheeseman, J. R.; Scalmani, G.; Barone, V.; Mennucci, B.; Petersson, G. A.; Nakatsuji, H.; Caricato, M.; Li, X.; Hratchian, H. P.; Izmaylov, A. F.; Bloino, J.; Zheng, G.; Sonnenberg, J. L.; Hada, M.; Ehara, M.; Toyota, K.; Fukuda, R.; Hasegawa, J.; Ishida, M.; Nakajima, T.; Honda, Y.; Kitao, O.; Nakai, H.; Vreven, T.; Montgomery, J. A., J.; Peralta, J. E.; Ogliaro, F.; Bearpark, M.; Heyd, J. J.; Brothers, E.; Kudin, K. N.; Staroverov, V. N.; Kobayashi, R.; Normand, J.; Raghavachari, K.; Rendell, A.; Burant, J. C.; Iyengar, S. S.; Tomasi, J.; Cossi, M.; Rega, N.; Millam, J. M.; Klene, M.; Knox, J. E.; Cross, J. B.; Bakken, V.; Adamo, C.; Jaramillo, J.; Gomperts, R.; Stratmann, R. E.; Yazyev, O.; Austin, A. J.; Cammi, R.; Pomelli, C.; Ochterski, J. W.; Martin, R. L.; Morokuma, K.; Zakrzewski, V. G.; Voth, G. A.; Salvador, P.; Dannenberg, J. J.; Dapprich, S.; Daniels, A. D.; Farkas, Ö.; Foresman, J. B.; Ortiz, J. V.; Cioslowski, J.; Fox, D. J. Gaussian, **2009**, Inc., Wallingford CT.

(55) Becke, A. D. Density-Functional Thermochemistry. III. The Role of Exact Exchange. *J. Chem. Phys* **1993**, *98* (7), 5648.

(56) Lee, C.; Yang, W.; Parr, R. G. Development of the Colle-Salvetti Correlation-Energy Formula into a Functional of the Electron Density. *Phys. Rev. B* **1988**, *37* (2), 785–789.

(57) Gupta, M.; Kumar, Y.; Tayal, A.; Pandey, N.; Caliebe, W.; Stahn, J. X-Ray Absorption Spectroscopy Study of Cobalt Mononitride Thin Films. *SN Appl. Sci.* **2020**, *2* (1), 1–11.

(58) Ravel, B.; Newville, M. ATHENA, ARTEMIS, HEPHAESTUS: Data Analysis for X-Ray Absorption Spectroscopy Using IFEFFIT. *J. Synchrotron Rad.;* IUCrJ, **2005**; 12, 537–541.

(59) Rehr, J. J.; Albers, R. C. Theoretical Approaches to X-Ray Absorption Fine Structure. *Rev. Mod. Phys.* **2000**, *72* (3), 621–654.

(60) Koningsberg, D. C.; Prins R. *X-Ray Absorption: Principles, Applications, Techniques of EXAFS, SEXAFS and XANES | Wiley*; Koningsberg, D. C., Prins R, Eds.; John Wiley & Sons, **1988**.

(61) Neese, F. The ORCA Program System. *Wiley Interdiscip. Rev. Comput. Mol. Sci.* **2012**, *2*, 73–78.

(62) Yamamoto, K.; Nakazawa, S.; Matsufuji, A.; Taguchi, T. Spectroelectrochemical Investigation of a Dinuclear Cobalt Porphyrin Complex with Ionic Groups in DMSO. *J. Chem. Soc.; Dalton Trans.* **2001**, No. 3, 251–258.

(63) Gaur, A.; Klysubun, W.; Joshi, S. K.; Soni, B.; Shrivastava, B. D.; Prasad, J.; Srivastava, K. XAFS Study of Copper(II) Diethylenetriamine Complexes Having Different Coordination Geometries. *J. Phys. Conf. Ser.*; IOP, **2016**, 712, 012084.

(64) DeBeer, S.; Randall, D. W.; Nersissian, A. M.; Valentine, J. S.; Hedman, B.; Hodgson, K. O.; Solomon, E. I. X-Ray Absorption Edge and EXAFS Studies of the Blue Copper Site in Stellacyanin: Effects of Axial Amide Coordination. *J. Phys. Chem. B* **2000**, *104* (46), 10814–10819.

Chapter 4

Single-Walled Carbon Nanotubes Encapsulated within Metallacycles

López-Moreno, A.; Ibáñez, S.; Moreno-Da Silva, S.; Ruiz-González, L.; M. Sabanés, N.; Peris, E.; Pérez, E. M. *Angew. Chem. Int. Ed.* **2022**, 61, e202208189; *Angew. Chem.* **2022**, 134, e202208189

Mechanically interlocked derivatives of carbon nanotubes (MINTs) are interesting nanotube products since they show high stability without altering the carbon nanotube structure. So far, MINTs have been synthesized using ring-closing metathesis, disulfide exchange reaction, H-bonding or direct threading with macrocycles. Here, we describe the encapsulation of single-walled carbon nanotubes within a palladium-based metallosquare. The formation of MINTs was confirmed by a variety of techniques, including high-resolution electron microscopy. We find the making of these MINTs is remarkably sensitive to structural variations of the metallo-assemblies. When a metallosquare with a cavity of appropriate shape and size is used, the formation of the MINT proceeds successfully by both template clipping and direct threading. Our studies also show indications on how supramolecular coordination complexes can help expanding the potential applications of MINTs.

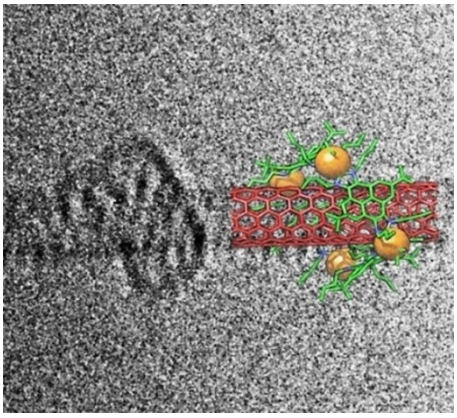

4.1. INTRODUCTION

Chemical modification of single-wall carbon nanotubes (SWNTs)[1,2] is a critical step to exploit their properties.[3] To name just two recent prominent examples, the covalent modification of the SWNTs can be used to change their surface properties and enhance their performance as optical sensors in biologically relevant environments.[4] In 2019, a series of cleverly designed processes based on the noncovalent functionalization of SWNTs (pretreatment with hexamethyldisilazane and bis(trimethylsilyl)amine to promote adhesion to a silicon wafer, adhesion coating with polymethylglutarimide, and mechanical exfoliation), were key in the fabrication of the first functioning modern microprocessor based on carbon nanotube field-effect transistors.[5] In 2014, some of us described a clipping strategy to synthesize mechanically interlocked derivatives of SWNTs (MINTs), which can be viewed as rotaxane-like species in which the SWNTs act as threads.[6] In our original method, the nanotube was first trapped supramolecularly within the two recognition motifs of a U-shaped molecule featuring two terminal alkenes, which were subsequently coupled via a ring-closing metathesis (RCM) producing the annulation of the molecule around the SWNT.[7] Thanks to the mechanical link, the resulting MINTs show similar stability as covalently-modified carbon nanotubes but preserving its structure.[8]

Since these initial works, we found that this method can be extended to numerous types of recognition motifs for SWNTs.[9–12] We also provided evidence that the formation of MINTs shows promise in various applications, such as for reinforcing

[1] Singh, P.; Campidelli, S.; Giordani, S.; Bonifazi, D.; Bianco, A.; Prato, M. *Chem. Soc. Rev.* **2009**, *38* (8), 2214–2230.
[2] Karousis, N.; Tagmatarchis, N.; Tasis, D. *Chem. Rev.* **2010**, *110* (9), 5366–5397.
[3] De Volder, M. F. L.; Tawfick, S. H.; Baughman, R. H.; Hart, A. J. *Science* **2013**, *339* (6119), 535–539.
[4] Chio, L.; Pinals, R. L.; Murali, A.; Goh, N. S.; Landry, M. P. *Adv. Funct. Mat.* **2020**, *30* (17), 1910556.
[5] Hills, G.; Lau, C.; Wright, A.; Fuller, S.; Bishop, M. D.; Srimani, T.; Kanhaiya, P.; Ho, R.; Amer, A.; Stein, Y.; Murphy, D.; Arvind; Chandrakasan, A.; Shulaker, M. M. *Nature* **2019**, *572* (7771), 595–602.
[6] de Juan, A.; Pouillon, Y.; Ruiz-González, L.; Torres-Pardo, A.; Casado, S.; Martín, N.; Rubio, Á.; Pérez, E. M. *Angew. Chem. Int. Ed.* **2014**, *53* (21), 5394–5400.
[7] de Juan, A.; Mar Bernal, M.; Pérez, E. M. *ChemPlusChem* **2015**, *80* (7), 1153–1157.
[8] Mena-Hernando, S.; Pérez, E. M. *Chem. Soc. Rev.* **2019**, *48* (19), 5016–5032.
[9] López-Moreno, A.; Pérez, E. M. *Chem. Commun.* **2015**, *51* (25), 5421–5424.
[10] de Juan-Fernández, L.; Münich, P. W.; Puthiyedath, A.; Nieto-Ortega, B.; Casado, S.; Ruiz-González, L.; Pérez, E. M.; Guldi, D. M. *Chem. Sci.* **2018**, *9* (33), 6779–6784.
[11] Leret, S.; Pouillon, Y.; Casado, S.; Navío, C.; Rubio, Á.; Pérez, E. M. *Chem. Sci.* **2017**, *8* (3), 1927–1935.
[12] Martínez-Periñán, E.; Juan, A. de; Pouillon, Y.; Schierl, C.; Strauss, V.; Martín, N.; Rubio, Á.; Guldi, D. M.; Lorenzo, E.; Pérez, E. M. *Nanoscale* **2016**, *8* (17), 9254–9264.

polymers,[13] and for designing metal-free catalysts[14,15] or qubits.[16] In the last years, several groups described different strategies towards the synthesis of MINTs, such as the reversible formation of macrocycles through disulfide bonds,[17] hydrogen bond self-assembled macrocycles,[18] or the direct threading through rigid macrocycles.[19]

Although the chemistry of MINTs experienced a significant development in the last few years, we are unaware of examples of MINTs made by the threading of SWNTs through the cavity of supramolecular coordination complexes (SCCs).[20] Compared to MINTs built with purely organic supramolecular assemblies, SCCs may introduce a new dimension in the resulting MINT, as the presence of the metal can provide enhanced photoelectrochemical properties that can help expanding their applications. During the past few years, some of us described a series of N-heterocyclic-carbene (NHC) based supramolecular organometallic complexes (SOCs), which were used as hosts for encapsulating a variety of organic and inorganic guests.[21] In particular, we found that some of our Ni-[22,23] and Pd-containing[24–26] metallosupramolecular assemblies based on a pyrene-bis-imidazolylidene ligand (**1** and **2** in Figure 1a), were able to adapt their shapes to the size of the encapsulated fullerenes (C_{60} or C_{70}). This guest-induced fitting effect

[13] López-Moreno, A.; Nieto-Ortega, B.; Moffa, M.; de Juan, A.; Bernal, M. M.; Fernández-Blázquez, J. P.; Vilatela, J. J.; Pisignano, D.; Pérez, E. M. *ACS Nano* **2016**, *10* (8), 8012–8018.

[14] Blanco, M.; Nieto-Ortega, B.; de Juan, A.; Vera-Hidalgo, M.; López-Moreno, A.; Casado, S.; González, L. R.; Sawada, H.; González-Calbet, J. M.; Pérez, E. M. *Nat. Commun.* **2018**, *9* (1), 2671.

[15] Wielend, D.; Vera-Hidalgo, M.; Seelajaroen, H.; Sariciftci, N. S.; Pérez, E. M.; Whang, D. R. *ACS Appl. Mater. Interfaces* **2020**, *12* (29), 32615–32621.

[16] Moreno-Da Silva, S.; Martínez, J. I.; Develioglu, A.; Nieto-Ortega, B.; de Juan-Fernández, L.; Ruiz-Gonzalez, L.; Picón, A.; Oberli, S.; Alonso, P. J.; Moonshiram, D.; Pérez, E. M.; Burzurí, E. *J. Am. Chem. Soc.* **2021**, *143* (50), 21286–21293.

[17] Balakrishna, B.; Menon, A.; Cao, K.; Gsänger, S.; Beil, S. B.; Villalva, J.; Shyshov, O.; Martin, O.; Hirsch, A.; Meyer, B.; Kaiser, U.; Guldi, D. M.; von Delius, M. *Angew. Chem. Int. Ed.* **2020**, *59* (42), 18774–18785.

[18] Chamorro, R.; Juan-Fernández, L. de; Nieto-Ortega, B.; Mayoral, M. J.; Casado, S.; Ruiz-González, L.; Pérez, E. M.; González-Rodríguez, D. *Chem. Sci.* **2018**, *9* (17), 4176–4184.

[19] Miki, K.; Saiki, K.; Umeyama, T.; Baek, J.; Noda, T.; Imahori, H.; Sato, Y.; Suenaga, K.; Ohe, K. *Small* **2018**, *14* (26), 1800720.

[20] Pöthig, A.; Casini, A. *Theranostics* **2019**, *9* (11), 3150–3169.

[21] Ibáñez, S.; Poyatos, M.; Peris, E. *Acc. Chem. Res.* **2020**, *53* (7), 1401–1413.

[22] Martínez-Agramunt, V.; Ruiz-Botella, S.; Peris, E. *Chem. Eur. J.* **2017**, *23* (27), 6675–6681.

[23] Martínez-Agramunt, V.; Gusev, D. G.; Peris, E. *Chem. Eur. J.* **2018**, *24* (55), 14802–14807.

[24] Martínez-Agramunt, V.; Peris, E. *Chem. Commun.* **2019**, *55* (99), 14972–14975.

[25] Martínez-Agramunt, V.; Eder, T.; Darmandeh, H.; Guisado-Barrios, G.; Peris, E. *Angew. Chem. Int. Ed.* **2019**, *58* (17), 5682–5686.

[26] Vicent, C.; Martinez-Agramunt, V.; Gandhi, V.; Larriba-Andaluz, C.; Gusev, D. G.; Peris, E. *Angew. Chem. Int. Ed.* **2021**, *60* (28), 15412–15417.

was manifested by the compression or the expansion of the metallacycles, and by the bending of the pyrene moieties of the bis-NHC ligand for maximizing the face-to-face overlap with the convex surface of the fullerenes. We thought that the high binding affinities of our metallo-assemblies to fullerenes, together with their great shape adaptability, could make these hosts perfect candidates for the mechanical interlocking of SWNTs and give access to a new class of transition metal-doped MINTs.

Considering all the above, herein we describe the preparation metallacycle-containing MINTs, which can be performed by templated self-assembly of the molecular components around the SWNTs, or by direct encapsulation of the nanotube in the cavity of the preformed metallacycle (Figure 1c).

4.2. RESULTS AND DISCUSSION

To attempt the preparation of MINTs we chose a collection of building blocks that would lead to macrocycles **1** or **2** (Figure 1a). The metallosquare **1** is bound by four pyrene-bis-imidazolylidene ligands that confer its structure with a great level of stability, due to the strong NHC-Pd bonds. In addition, this structure can be regarded as 'static', in the sense that it does not reversibly assemble and dissemble. The nickel-conjoined metallacycle **2** is more dynamic, as the two more labile bipyridine ligands can reversibly dissociate, but it shows a slightly smaller cavity (Figure 1b). As described above, both **1** and **2** can associate fullerenes C_{60} and C_{70}, which are equivalent in size to the diameter of the (6,5)-SWNTs used in this work.

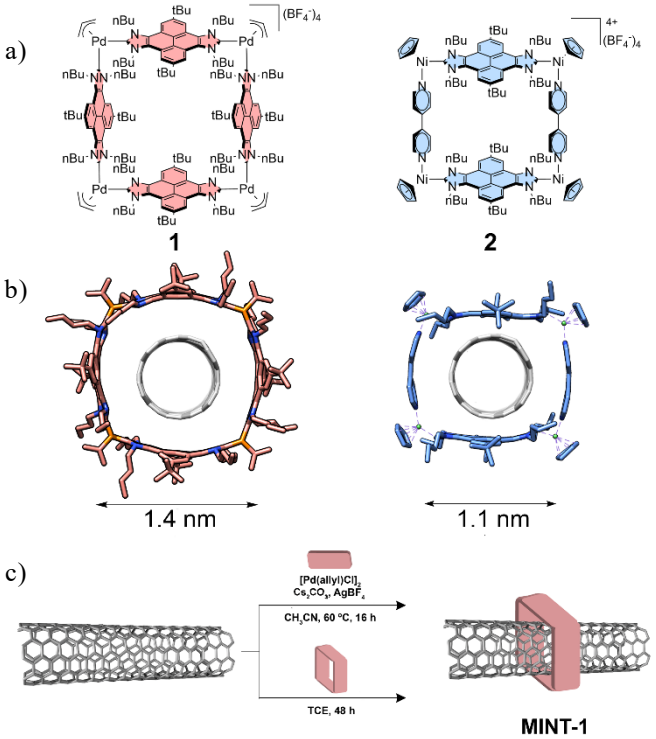

Figure 1. a) Chemical structure of metallosquare **1** and **2**. b) Energy-minimized (UFF) model of MINT-**1** and MINT-**2**. c) Schematic representation of MINT-**1** through two different routes.

The templated preparation of MINT-**1** was performed as follows. To a suspension of (6,5)-SWNTs in anhydrous acetonitrile were added the pyrene-bis(imidazolium) salt, $[Pd(allyl)Cl]_2$, $AgBF_4$ and Cs_2CO_3 (see Supporting Information for full details), and the suspension was allowed to react for 16 h at 60 ºC. The resulting MINT-**1** was recovered by filtration through a polytetrafluoroethylene (PTFE) membrane with a pore size of 0.2 μm and washed with CH_3CN and CH_2Cl_2 to remove all non-interlocked materials. After purification, the samples were subjected to thermogravimetric analysis (TGA) in order to quantify the degree of functionalization. In three separate experiments, MINT-**1** showed weight losses of 26-28%, which correspond to a reasonable degree of functionalization for MINTs.[8] We also carried out control experiments in which we mixed the pyrene-bis(imidazolium) salt with (6,5)-SWNTs without Cs_2CO_3, under otherwise identical conditions to the MINT-forming reaction. These samples showed less than 5% functionalization after the washing step. Likewise, when the reaction was performed in absence of the $[Pd(allyl)Cl]_2$ under the same conditions, (6,5)-SWNTs were also recovered without physisorbed products on the SWNTs.

[8] Mena-Hernando, S.; Pérez, E. M. *Chem. Soc. Rev.* **2019**, *48* (19), 5016–5032.

Finally, a control experiment with preformed metallosquare-**1** (0.0014 mmol) in a suspension of 10 mg of (6,5)-SWNTs in 10 mL of anhydrous acetonitrile resulted in a lower but significant functionalization of 13%. Considering these results, we optimized the preparation of MINTs by direct encapsulation within **1** taking inspiration from the results of Ohe et al.[19] Preformed metallosquare **1** was added to a dispersion of (6,5)-SWNTs in 1,1',2,2'-tetrachloroethane (TCE), and the mixture was stirred at room temperature for 48h at room temperature. After this time MINT-**1** was recovered by filtration and washed profusely. The sample was analyzed by TGA showing 29% of functionalization and proving that both methods are effective and comparable (Figure S1).

We previously reported that MINTs show remarkable stability, comparable to that of covalently modified nanotubes while maintaining the native covalent structure of the SWNTs.[6–13] To test the stability of functionalization and remove any non-interlocked material that might have survived the initial purification process, we subjected all samples to 30 min of reflux in TCE (bp = 147 °C), followed by a thorough rinse with CH_3CN and CH_2Cl_2. TGA of the resulting samples showed no decrease in the degree of functionalization confirming the high stability of these new MINTs.

To study the structural requirements for the success of the method, and in particular its sensitivity to the size complementarity between the cavity of the macrocycle and the diameter of the SWNT, we investigated the preparation of MINTs with a macrocycle of slightly different size. Reactions were set-up as follows for the attempted formation of MINT-**2**: $[NiCpCl]_2$(pyrene-di-NHC) (1 eq.), 4,4'-bipyridine (1 eq.) and $AgBF_4$ (2 eq.) were added to a suspension of (6,5)-SWNTs in TCE or CH_2Cl_2 (see Supporting Information for full details). TGA showed very low functionalization (<5%), indicating that the formation of MINT-

[6] de Juan, A.; Pouillon, Y.; Ruiz-González, L.; Torres-Pardo, A.; Casado, S.; Martín, N.; Rubio, Á.; Pérez, E. M. *Angew. Chem. Int. Ed.* **2014**, *53* (21), 5394–5400.
[7] de Juan, A.; Mar Bernal, M.; Pérez, E. M. *ChemPlusChem* **2015**, *80* (7), 1153–1157.
[8] Mena-Hernando, S.; Pérez, E. M. *Chem. Soc. Rev.* **2019**, *48* (19), 5016–5032.
[9] López-Moreno, A.; Pérez, E. M. *Chem. Commun.* **2015**, *51* (25), 5421–5424.
[10] de Juan-Fernández, L.; Münich, P. W.; Puthiyedath, A.; Nieto-Ortega, B.; Casado, S.; Ruiz-González, L.; Pérez, E. M.; Guldi, D. M. *Chem. Sci.* **2018**, *9* (33), 6779–6784.
[11] Leret, S.; Pouillon, Y.; Casado, S.; Navío, C.; Rubio, Á.; Pérez, E. M. *Chem. Sci.* **2017**, *8* (3), 1927–1935.
[12] Martínez-Periñán, E.; Juan, A. de; Pouillon, Y.; Schierl, C.; Strauss, V.; Martín, N.; Rubio, Á.; Guldi, D. M.; Lorenzo, E.; Pérez, E. M. *Nanoscale* **2016**, *8* (17), 9254–9264.
[13] López-Moreno, A.; Nieto-Ortega, B.; Moffa, M.; de Juan, A.; Bernal, M. M.; Fernández-Blázquez, J. P.; Vilatela, J. J.; Pisignano, D.; Pérez, E. M. *ACS Nano* **2016**, *10* (8), 8012–8018.
[19] Miki, K.; Saiki, K.; Umeyama, T.; Baek, J.; Noda, T.; Imahori, H.; Sato, Y.; Suenaga, K.; Ohe, K. *Small* **2018**, *14* (26), 1800720.

2 is negligible, and suggesting that the formation of the MINT species is extremely sensitive to the fit between macrocycle cavity and SWNT diameter (Figure S2). Similar results have been found for the supramolecular association of fullerenes,[27] and are understood on the basis of a dispersion-dominated interaction, where maximizing van der Waals contacts is essential.[28]

To fully characterize MINT-**1**, we carried out UV/Vis/NIR spectroscopy, photoluminescence excitation intensity mapping (PLE), and Raman spectroscopy, all of which are in agreement with the noncovalent functionalization of the (6,5)-SWNTs with **1**. In the absorption spectra (D_2O, 1% sodium dodecyl sulphate, 298 K, Figure 2a), the UV region is dominated by the nanotube absorption. The absorption features of **1** (blue in Figure 2a) are distinguishable in the spectrum of MINT-**1** (red in Figure 2a), for the transitions at 268, 302, and 359 nm. The S22 and S11 transitions of the (6,5)-SWNTs are prominent in the vis-NIR, appearing at λ_{max} = 584 and 1016 nm for the pristine nanotubes (black in Figure 2a). As expected for an intimate metallacycle–SWNT supramolecular interaction, both transitions are shifted hypsochromically to λ_{max} = 578 and 1001 nm, respectively, upon derivatization to form MINT-**1**. Identical shifts were found for the MINT-**1** sample formed by direct encapsulation (Figure S4). The S22 transition suffers a quantitatively smaller shift due to its higher energy.

Figure 2b contains Raman spectra of the (6,5)-SWNT (black), and MINT-**1** prepared by self-assembly(red) (532 nm excitation, 2 mW). The spectra are an average of 100 individual spectra taken over the sample. Detailed statistical analysis of peak position and intensity ratios are included in SI section (Figure S3). The spectral features after MINT formation are rather similar to those obtained for (6,5)-SWNT. In particular, radial breathing modes (RBM, 200-400 cm^{-1}), D (ca. 1300 cm^{-1}), G^- (ca. 1535 cm^{-1}) and G^+ (1590 cm^{-1}) modes do not show any relevant shift (see Figure S3), indicating that the electronic structure and the aggregation state of the tubes is mostly preserved upon encapsulation using both methods. Moreover, I_D/I_G ratios, often used to identify structural changes in carbon-based materials due to the increase of defects[29,30] is identical within error for (6,5)-SWNT (0.035±0.009) and MINT-**1** synthesized by self-assembly (0.038±0.009), and remains very low (0.087±0.007) for the MINT-**1** sample synthesized by direct

[27] Canevet, D.; Gallego, M.; Isla, H.; de Juan, A.; Pérez, E. M.; Martín, N. *J. Am. Chem. Soc.* **2011**, *133* (9), 3184–3190.
[28] Pérez, E. M.; Martín, N. *Chem. Soc. Rev.* **2015**, *44* (18), 6425–6433.
[29] Dresselhaus, M. S.; Dresselhaus, G.; Saito, R.; Jorio, A. *Phys. Rep.* **2005**, *409* (2), 47–99.
[30] Jorio, A.; Saito, R. *J. Appl. Phy.* **2021**, *129* (2), 021102.

encapsulation. This difference in the I_D/I_G ratio between the different synthetic methods is too small to indicate an increase of covalent defects when using the encapsulation method, and we believe it is better ascribed to differences in the sample preparation method that might lead to, for instance encapsulation of more or less solvent.[31]

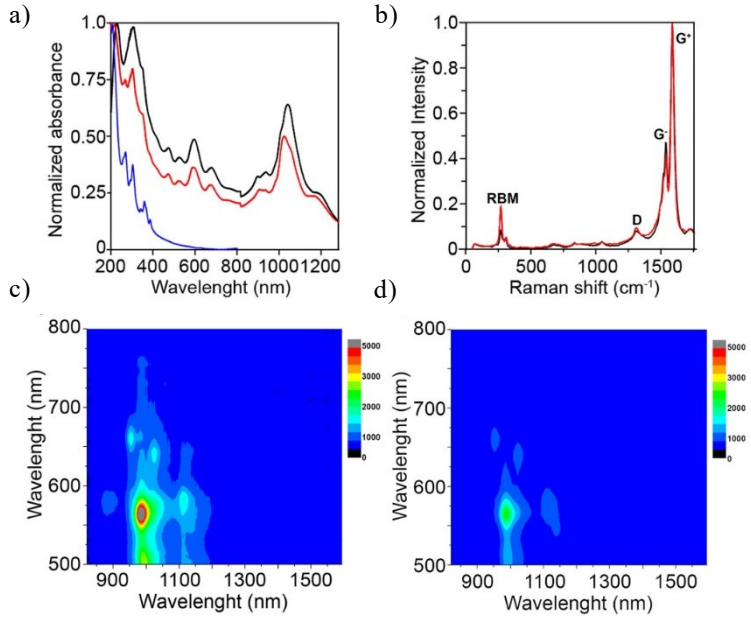

Figure 2. a) UV/Vis/NIR spectra (D_2O, 1 % sodium dodecyl sulfate (SDS), 298 K) of pristine (6,5)-SWNTs (black), metallacycle-**1** (blue), and MINT-**1** (red) prepared by self-assembly; b) Raman spectra (λ_{exc} = 532 nm) of (6,5)-SWNTs (black), MINT-**1** (red). All spectra are the average of 100 different measurements. PLE intensity maps (D_2O, 1 % SDS, 298 K) of c) pristine (6,5)-SWNTs and d) MINT-**1**.

The photoluminescence excitation (PLE) maps of the (6,5)- SWNTs in the visible-NIR region (Figure 2c) shows an intense peak at λ_{exc} = 565 nm, λ_{em} = 984 nm characteristic of the (6,5) chirality, and residual peaks at λ_{exc} = 643 nm, λ_{em} = 1021 nm and λ_{exc} = 665, λ_{em} = 948 nm, corresponding to (7,5) and (8,3) chiralities. In the MINT-**1** sample synthesized by self-assembly (Figure 2d), the luminescence of the (6,5) nanotubes is quenched to approximately 40% and suffers a bathochromic shift to λ_{em} = 984 nm, compared to a sample of (6,5)-SWNTs with identical optical density. In the MINT-**1** sample synthesized by direct encapsulation (Figure S5b), the luminescence of the (6,5) nanotubes is quenched less efficiently, to approximately 18% and suffers a bathochromic shift to λ_{em} = 993 nm, compared

[31] Dresselhaus, M. S.; Jorio, A.; Hofmann, M.; Dresselhaus, G.; Saito, R. *Nano Lett.* **2010**, *10* (3), 751–758.

to the pristine (6,5)-SWNTs. These results might reflect the non-negligible presence of non-interlocked **1** in this sample. With regards to the emission of the pyrene chromophore, in the UV/Vis region, we observe that the fluorescence of metallacycle **1** is blue-shifted from λ_{em} = 403 nm to λ_{em} = 393 nm, and quenched by 85 % (Figure S5) upon information of MINT-**1**.

Finally, the analysis of a sample of MINT-**1** under atomic force microscopy (AFM, dynamic mode) is in clear agreement with the formation of the rotaxane-type species. Figure 3a shows a topographic image of a single SWNT with a height of approximately 1 nm, on which three elevations of approximately 2.5-3 nm are observed (Figure 3a, b). The dimensions and the regularity of these elevations are consistent with the formation of **1** around a SWNT and rules out the possibility of physisorption of **1** on the SWNT walls. HR-TEM analysis (200 kV) of samples of MINT-**1** drop casted from a TCE suspension shows mostly bundled nanotubes with heavily functionalized sidewalls, in agreement with the TGA data, although at several instances we can find individualized tubes with objects of adequate size and shape to correspond to cage **1** (see Figures S7 and S8 in the Supporting Information).The chemical composition analysis of these micrographs, as obtained by energy-dispersive spectroscopy, confirms the presence of Pd (see Figure S9). However, under these conditions the organic addends get quickly damaged,[32] and atomic resolution cannot be obtained. A more structurally informative micrograph, obtained in an image aberration corrected microscope at 60 kV is shown in Figure 3c. An isolated SWNT encapsulated within a macrocycle-shaped organic residue is distinguishable with close to atomic resolution. For the free nanotube, a diameter of 0.68 nm was measured, in perfect accordance with a (6,5)-SWNT. Meanwhile, while the macrocycle addend shows a diameter of 1.55 nm, again in great agreement with the dimensions of metallosquare **1** (Figure 3d). Four individual atomic contrasts are also visible, that can be tentatively assigned to the four Pd corners.[33] by comparison with the energy-minimized molecular model superimposed in Figure 3c (see the Supporting Information for more micrographs).

[32] Skowron, S. T.; Chamberlain, T. W.; Biskupek, J.; Kaiser, U.; Besley, E.; Khlobystov, A. N. *Acc. Chem. Res.* **2017**, *50* (8), 1797–1807.

[33] Cao, K.; Zoberbier, T.; Biskupek, J.; Botos, A.; McSweeney, R. L.; Kurtoglu, A.; Stoppiello, C. T.; Markevich, A. V.; Besley, E.; Chamberlain, T. W.; Kaiser, U.; Khlobystov, A. N. *Nat. Commun.* **2018**, *9* (1), 3382.

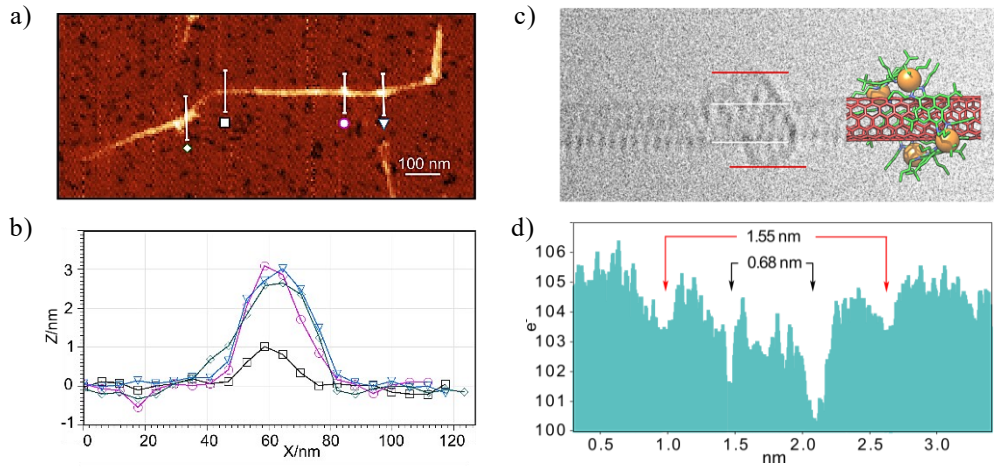

Figure 3. a) AFM topographic image of MINT-1 as obtained from a dropcast from a suspension in in TCE; b) Height profiles along the lines depicted in a); c) ac-HRTEM image of MINT-**1**. An energy-minimized molecular model (molecular mechanics, UFF) of MINT-1 is superimposed on the right side to serve as visual reference. d) Profile graph of c), showing the dimensions of the SWNT and the macrocycle, in perfect accordance with expectations. Four darker atoms are visible and tentatively assigned to the Pd centers by comparison with the model.

4.3. CONCLUSIONS

In conclusion, we have introduced a new type of MINT consisting of the threading of a SWNT through the well-defined cavity of a palladium-based supramolecular organometallic complex. The preparation of this metallo-MINT can be performed either by the template-formation of the metallacycles around the surface of the SWNT, or by encapsulating the SWNT into the cavity of the preformed metallacycle. To our knowledge, this is the first time that a metallo-MINT is obtained by interlocking a SWNT, thus exemplifying how metal-ligand binding and the directional control of coordination geometries can be used for the preparation of self-assembly structures beyond the molecular level. We also proved that the incorporation of metal atoms into the structure of the MINT has important implications that affect to the electronic nature of these functionalized nanotubes. In particular, PLE maps suggest that a charge-transfer process occurs from the metallo-square to the nanotubes upon photoexcitation. Interlocked structures based on metal coordination have played a prominent role from the early days of the field,[34] including supramolecular functionalization of SWNT,[35] and up till now, where some of the most complex structures are synthesized using this kind of

[34] Fujita, M.; Ibukuro, F.; Hagihara, H.; Ogura, K. *Nature* **1994**, *367* (6465), 720–723.
[35] Chichak, K. S.; Star, A.; Altoé, M. V. P.; Stoddart, J. F. *Small* **2005**, *1* (4), 452–461.

interactions.[36–38] We think that our work opens a new field of opportunities for MINTs. We now intend to extend our strategy for threading other types of metallocycles, and to investigate their potential properties in catalysis.

4.4. SUPPORTING INFORMATION

S1. Equipment.

Thermogravimetric Analyses (TGA) were performed using a TA Instruments TGAQ500 with a ramp of 10 °C/min under air and nitrogen conditions from 100 to 1000 °C. Raman spectra were recorded with a Bruker Senterra confocal Raman microscope (Bruker Optic, Ettlingen, Germany, resolution 9-15 cm^{-1}). Ultraviolet/Visible/Near Infrared Spectroscopy (UV/Vis/NIR) spectra were performed using a Cary 5000 UV/Vis/NIR spectrophotometer (Varian) and 10x10 mm quartz cuvettes (path length = 1 cm). Atomic Force Microscopy (AFM) images were acquired using a JPK NanoWizard II AFM working in dynamic mode coupled to an inverted optical microscope Nikon Eclipse Ti-U. NT-MDT NSG01 silicon cantilevers, with typical values of 5.1 $N \cdot m^{-1}$ spring constant and 150 kHz resonant frequency, were employed under ambient conditions in air. The samples were dispersed in tetrachloroethane, and spin coated onto mica slides. Transmission Electron Microscopy (TEM) images were obtained in a JEOL-JEM 2100F (2.5 Å resolution) instrument operating at 200 kV. High resolution-transmission electron microscopy (HR-TEM) images were obtained in an imaging aberration corrected microscope JEOL JEM GRAND ARM300cF operating at 60 kV. Images were recorded on a slow-CCD camera GATAN Oneview. Approximately 0.2 mg of MINT was ultrasonic dispersed in 2 mL of tetrachloroethane for ten minutes. Few drops of this dispersion were deposited onto a 200 square mesh grid covered by holey carbon. After solvent evaporation in air, the grid was ready to use.

S2. Synthesis of 1 and 2.

Metallosquares **1**[25] and **2**[22] were synthesized as described in the literature.

---

[22] Martínez-Agramunt, V.; Ruiz-Botella, S.; Peris, E. *Chem. Eur. J.* **2017**, *23* (27), 6675–6681.
[25] Martínez-Agramunt, V.; Eder, T.; Darmandeh, H.; Guisado-Barrios, G.; Peris, E. *Angew. Chem. Int. Ed.* **2019**, *58* (17), 5682–5686.
[36] Ashbridge, Z.; Kreidt, E.; Pirvu, L.; Schaufelberger, F.; Stenlid, J. H.; Abild-Pedersen, F.; Leigh, D. A. *Science* **2022**, *375* (6584), 1035–1041.
[37] Wu, Y.; Guo, Q.-H.; Qiu, Y.; Weber, J. A.; Young, R. M.; Bancroft, L.; Jiao, Y.; Chen, H.; Song, B.; Liu, W.; Feng, Y.; Zhao, X.; Li, X.; Zhang, L.; Chen, X.-Y.; Li, H.; Wasielewski, M. R.; Stoddart, J. F. *Proc. Nat. Acad. Sci.* **2022**, *119* (12), e2118573119.
[38] Huang, S.-L.; Hor, T. S. A.; Jin, G.-X. *Coord. Chem. Rev.* **2017**, *333*, 1–26

S3. Procedure for SWNTs Functionalization.

1. MINT-1 (Route A)

(6,5)-SWNTs (5 mg) were dispersed in 5 mL of anhydrous acetonitrile by sonication in a bathsonicator. Then the pyrene-bis(imidazolium) salt (0.006 mmol, 2 eq.), $[Pd(allyl)Cl]_2$ (0.003 mmol, 1 eq.), $AgBF_4$ (0.006 mmol, 2 eq.) and Cs_2CO_3 (0.012 mmol, 4 eq.) were added. After 16 h at 60 ºC, MINT-**1** was recovered by filtration through a polytetrafluoroethylene (PTFE) membrane with a pore size of 0.2 μm and washed with CH_3CN and CH_2Cl_2 to remove all non-interlocked materials. The samples were dried under vacuum and subjected to thermogravimetric analysis (TGA) to quantify the degree of functionalization.

2. MINT-1 (Route B)

(6,5)-SWNTs (5 mg) were dispersed in 5 mL of TCE by sonication in a bathsonicator. Preformed metallosquare-**1** (0.0014 mmol) dissolved in 20 mL of TCE and 3 mL of CH_3CN was added. After 48 h at r.t. under dark, nanotubes were recovered by filtration through a polytetrafluoroethylene (PTFE) membrane with a pore size of 0.2 μm and washed with CH_3CN and CH_2Cl_2 to remove all non-interlocked materials. The samples were dried under vacuum and subjected to thermogravimetric analysis (TGA) to quantify the degree of functionalization.

3. Metallosquare 2 + (6,5)-SWNTs

(6,5)-SWNTs (5 mg) were dispersed in 5 mL of TCE by sonication in a bath sonicator. Then bis-nickel-pyrene-di-imidazolylidene complex (5 mg, 1 eq.), 4,4'-bipyridine (0.66 mg, 1 eq.) and $AgBF_4$ (1.8 mg, 2 eq.) were added. After 16 h at r.t, nanotubes were recovered by filtration through a polytetrafluoroethylene (PTFE) membrane with a pore size of 0.2 μm and washed with and CH_2Cl_2 and THF to remove all non-interlocked materials. The samples were dried under vacuum and subjected to thermogravimetric analysis (TGA) to quantify the degree of functionalization.

Reaction was also carried out in dry CH_2Cl_2 using same conditions.

S4. Control experiments.

(6,5)-SWNTs (5 mg) were dispersed in 5 mL of anhydrous acetonitrile by sonication in a bath sonicator. Then the pyrene-bis(imidazolium) salt (0.006 mmol, 2 eq.), $[Pd(allyl)Cl]_2$ (0.003 mmol, 1 eq.), and $AgBF_4$ (0.006 mmol, 2 eq.) were added. After 16 h at 60 ºC, nanotubes were recovered by filtration through a polytetrafluoroethylene (PTFE) membrane with a pore size of 0.2 μm and washed with CH_3CN and CH_2Cl_2 to remove all non-interlocked materials. The samples were dried under vacuum and subjected to thermogravimetric analysis (TGA) to quantify the degree of functionalization.

(6,5)-SWNTs (5 mg) were dispersed in 5 mL of anhydrous acetonitrile by sonication in a bath sonicator. Then the pyrene-bis(imidazolium) salt (0.006 mmol, 2 eq.), $AgBF_4$ (0.006 mmol, 2 eq.) and Cs_2CO_3 (0.012 mmol, 4 eq.) were added. After 16 h at 60 ºC, nanotubes were recovered by filtration through a polytetrafluoroethylene (PTFE) membrane with a pore size of 0.2 μm and washed with CH_3CN and CH_2Cl_2 to remove all non-interlocked materials. The samples were dried under vacuum and subjected to thermogravimetric analysis (TGA) to quantify the degree of functionalization.

(6,5)-SWNTs (10 mg) were dispersed in 10 mL of anhydrous acetonitrile by sonication in a bath sonicator and preformed metallo-square-**1** (0.0014 mmol) was added. After 16 h at 60 ºC, nanotubes were recovered by filtration through a polytetrafluoroethylene (PTFE) membrane with a pore size of 0.2 μm and washed with CH_3CN and CH_2Cl_2 to remove all non-interlocked materials. The samples were dried under vacuum and subjected to thermogravimetric analysis (TGA) to quantify the degree of functionalization.

S5. TGA of MINT-1, control experiments and metallosquares-1 and 2.

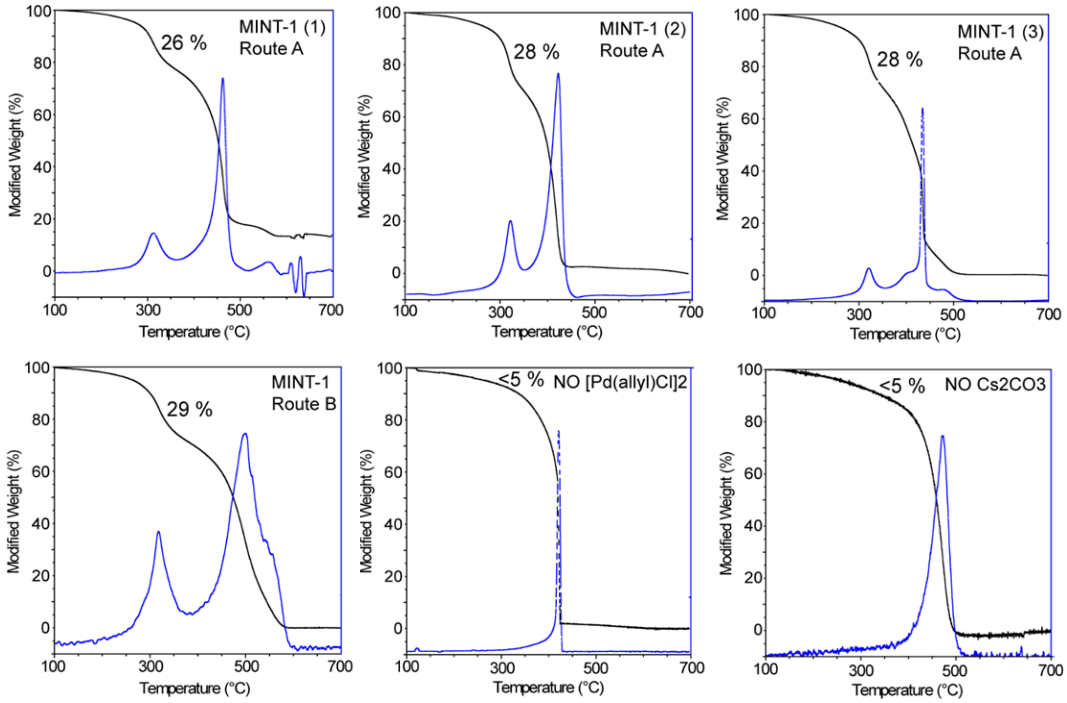

Figure S1. TGA analysis (under air, 10 ºC / min) of MINT-**1** (self-assembly), MINT-**1** (preformed cage), and control experiments.

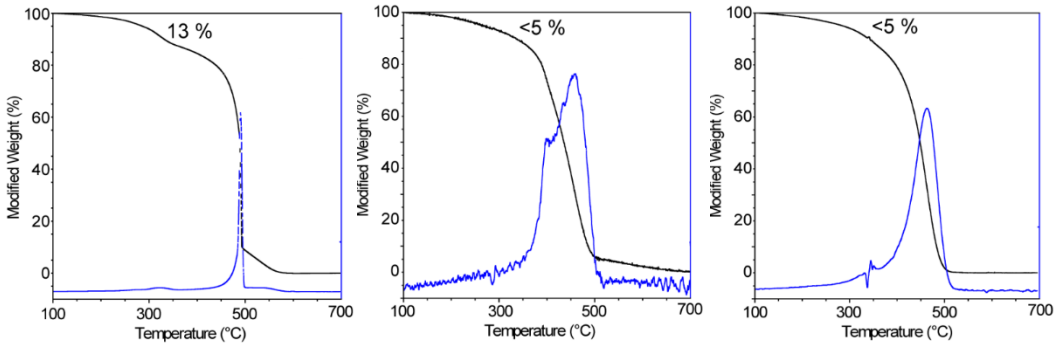

Figure S2. TGA analysis (under air, 10 ºC / min) of control experiment with preformed metallosquare-**1** (left), and metallosquare-**2** in CH_2Cl_2 (centre) and TCE (right).

S6. Other Raman spectra.

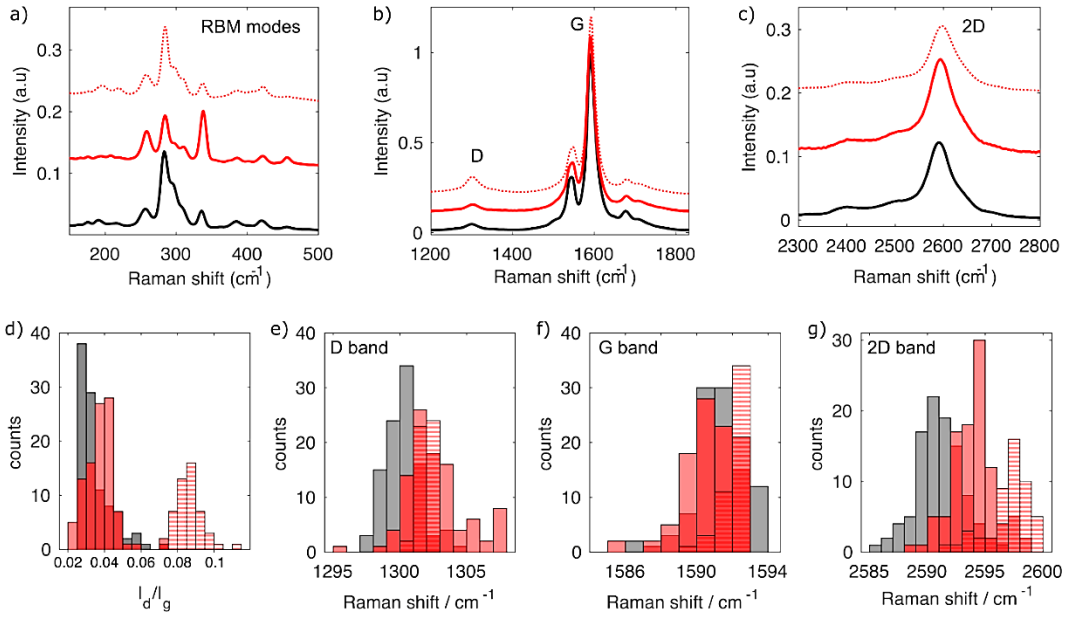

Figure S3. (a)-(c) Zoom into specific regions of the Raman spectra shown in Fig. 2b in main text, showing a detail of the RBM (radial breathing modes), D and G (defect-induced and in-plane stretching, respectively) and 2D (overtone of D mode, also denoted G' by some authors) for (6,5)-SWNT (black), MINT-**1** (self-assembly, red), and MINT-**1** (preformed metallosquare, dotted red). The displayed spectra are an average of 100 individual spectra acquired at different sample spots, statistical analysis of the spectral features of the individual spectra are displayed in: (d) intensity ratio (I_D/I_G); (e) D band position; (f) G^+ band position; (g) 2D band position for (6,5)-SWNT (gray), MINT-**1** (self-assembly, solid red), and MINT-**1** (preformed metallosquare, dashed red). Spectra are acquired with 633 nm excitation light, 100x objective, 2 mW incident power, 5 sec acquisition time.

Raman spectra of the (6,5)-SWNT (black) compared to the MINT-**1** (by self-assembly, red) and MINT-**1** (by encapsulation with preformed metallosquare, dotted red) are included in Figure 2b of the main text. Zoom into specific spectral regions are included in Figure S3a to c. Figures S3 d to g contain histograms of intensity ratio (I_D/I_G), D, G and 2D band position of the individual spectra used for the averages ((6,5)-SWNT gray, MINT-**1** (self-assembly, solid red) and MINT-**1** (preformed metallosquare, dashed red). The histograms are obtained by extracting for each individual spectrum used in the averages, the position of the bands and the intensity ratio between D and G modes.

The radial breathing modes (RBM) are related with the contraction and expansion of the tubes, and hence, associated to the diameter and aggregation state. The same frequencies and approximately relative intensity are observed in all RBM

modes, indicating same diameter distribution and aggregation state before and after encapsulation following both methods. Similarly, no notable shift of the D and G modes is found between the pristine tubes and the MINTs (Figure S3 b, e and f). The intensity ratio between D and G bands (I_D/I_G) is identical within error between (6,5)-SWNT (0.035±0.009) and MINT-**1** (self-assembly) (0.038±0.009) and increases slightly for MINT-**1** (preformed cage) (0.087±0.007), as discussed in the main text.

S7. UV/Vis/NIR and fluorescence spectra.

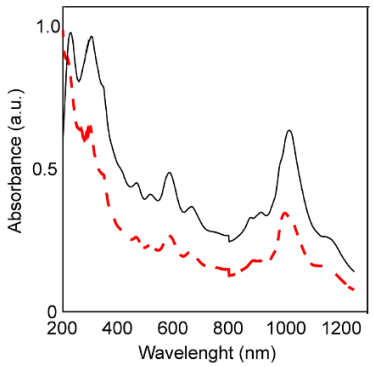

Figure S4. UV/Vis/NIR spectra (D2O, 1 % sodium dodecyl sulfate (SDS), 298 K) of pristine (6,5)-SWNTs (black) and MINT-**1** (dashed red) prepared using the preformed metallosquare.

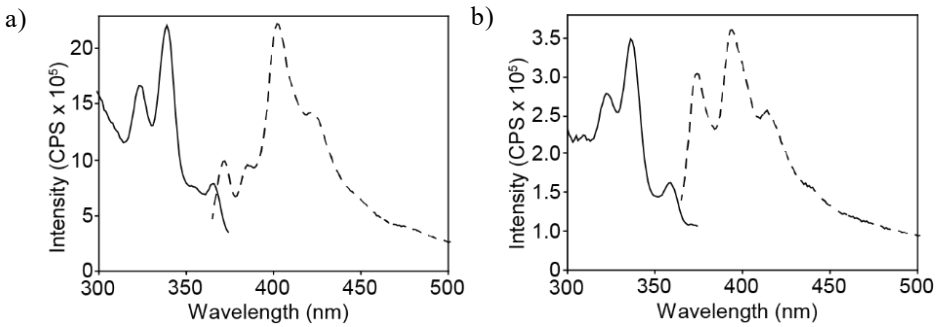

Figure S5. Excitation (black line) and emission (dashed) spectra (D_2O, 1 % sodium dodecyl sulfate (SDS), 298 K) of a) Metallosquare **1** and b) MINT-**1**.

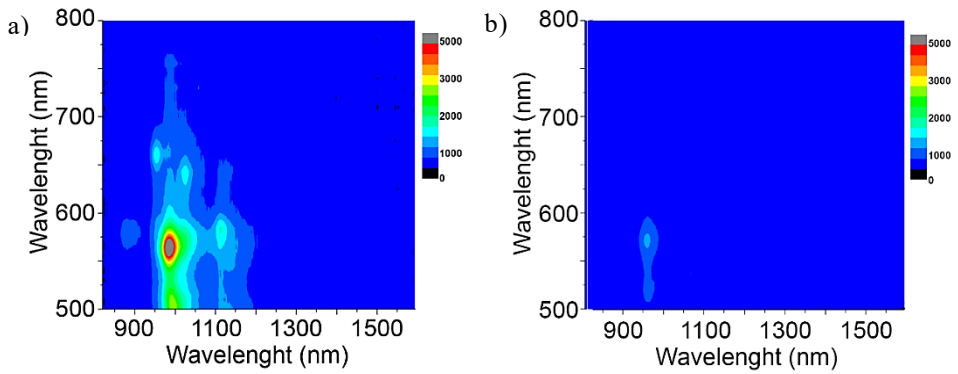

Figure S6. PLE intensity maps (D_2O, 1 % SDS, 298 K) of a) pristine (6,5)-SWNTs and d) MINT-**1** prepared using the preformed metallosquare.

S8. Additional TEM images and EDX of MINT-1.

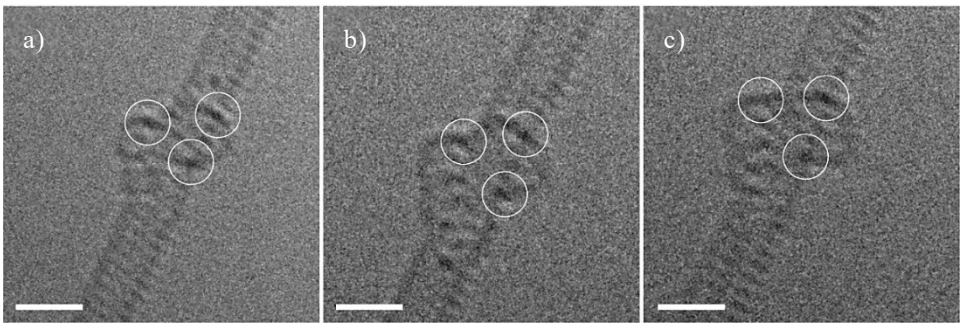

Figure S7. ac-HRTEM micrographs of MINT-**1** showing several Pd atoms. Scale bars are 1 nm.

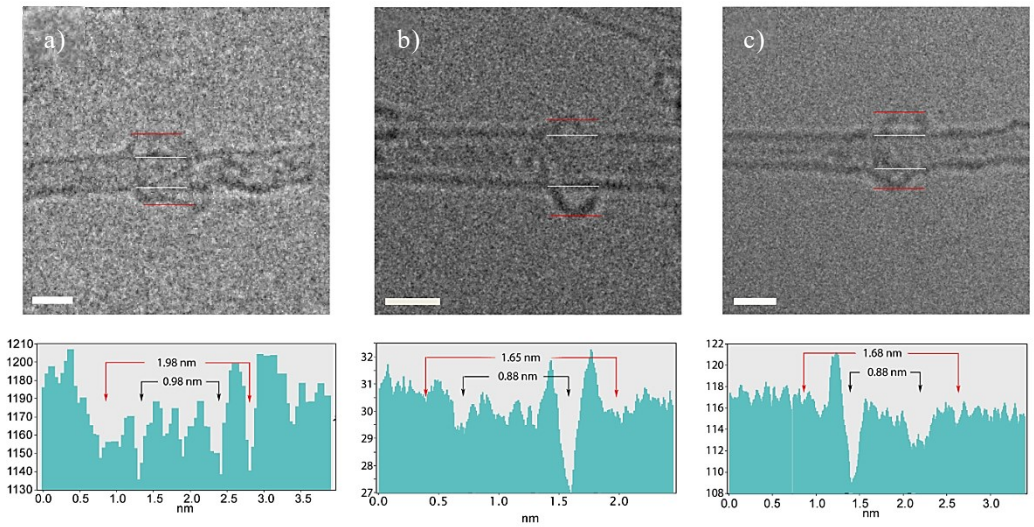

Figure S8. HRTEM micrographs of MINT-**1** showing several SWNT with 1.6-19 nm metallosquares around them. Scale bars are 1 nm.

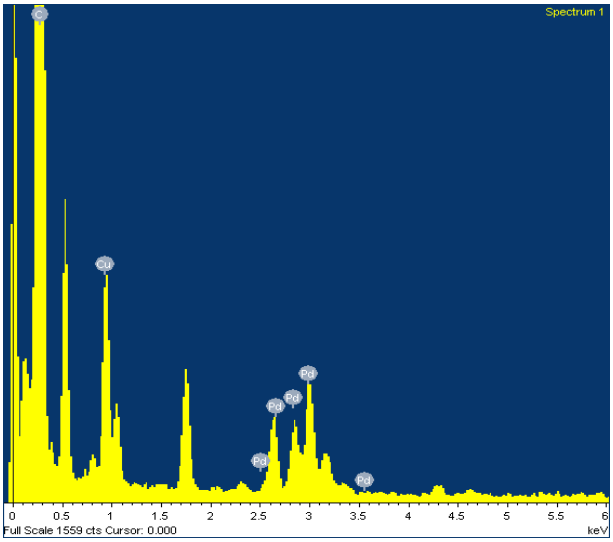

Figure S9. Energy Dispersive X-ray (EDX) spectra of MINT-**1**.

4.5. BIBLIOGRAPHY

(1) Singh, P.; Campidelli, S.; Giordani, S.; Bonifazi, D.; Bianco, A.; Prato, M. Organic Functionalisation and Characterisation of Single-Walled Carbon Nanotubes. *Chem. Soc. Rev.* **2009**, *38* (8), 2214–2230.

(2) Karousis, N.; Tagmatarchis, N.; Tasis, D. Current Progress on the Chemical Modification of Carbon Nanotubes. *Chem. Rev.* **2010**, *110* (9), 5366–5397.

(3) De Volder, M. F. L.; Tawfick, S. H.; Baughman, R. H.; Hart, A. J. Carbon Nanotubes: Present and Future Commercial Applications. *Science* **2013**, *339* (6119), 535–539.

(4) Chio, L.; Pinals, R. L.; Murali, A.; Goh, N. S.; Landry, M. P. Covalent Surface Modification Effects on Single-Walled Carbon Nanotubes for Targeted Sensing and Optical Imaging. *Adv. Funct. Mat* **2020**, *30* (17), 1910556.

(5) Hills, G.; Lau, C.; Wright, A.; Fuller, S.; Bishop, M. D.; Srimani, T.; Kanhaiya, P.; Ho, R.; Amer, A.; Stein, Y.; Murphy, D.; Arvind; Chandrakasan, A.; Shulaker, M. M. Modern Microprocessor Built from Complementary Carbon Nanotube Transistors. *Nature* **2019**, *572* (7771), 595–602.

(6) de Juan, A.; Pouillon, Y.; Ruiz-González, L.; Torres-Pardo, A.; Casado, S.; Martín, N.; Rubio, Á.; Pérez, E. M. Mechanically Interlocked Single-Wall Carbon Nanotubes. *Angew. Chem. Int. Ed* **2014**, *53* (21), 5394–5400.

(7) de Juan, A.; Mar Bernal, M.; Pérez, E. M. Optimization and Insights into the Mechanism of Formation of Mechanically Interlocked Derivatives of Single-Walled Carbon Nanotubes. *ChemPlusChem* **2015**, *80* (7), 1153–1157.

(8) Mena-Hernando, S.; Pérez, E. M. Mechanically Interlocked Materials. Rotaxanes and Catenanes beyond the Small Molecule. *Chem. Soc. Rev.* **2019**, *48* (19), 5016–5032.

(9) López-Moreno, A.; Pérez, E. M. Pyrene-Based Mechanically Interlocked SWNTs. *Chem. Commun.* **2015**, *51* (25), 5421–5424.

(10) de Juan-Fernández, L.; Münich, P. W.; Puthiyedath, A.; Nieto-Ortega, B.; Casado, S.; Ruiz-González, L.; Pérez, E. M.; Guldi, D. M. Interfacing Porphyrins and Carbon Nanotubes through Mechanical Links. *Chem. Sci.* **2018**, *9* (33), 6779–6784.

(11) Leret, S.; Pouillon, Y.; Casado, S.; Navío, C.; Rubio, Á.; Pérez, E. M. Bimodal Supramolecular Functionalization of Carbon Nanotubes Triggered by Covalent Bond Formation. *Chem. Sci.* **2017**, *8* (3), 1927–1935.

(12) Martínez-Periñán, E.; Juan, A. de; Pouillon, Y.; Schierl, C.; Strauss, V.; Martín, N.; Rubio, Á.; Guldi, D. M.; Lorenzo, E.; Pérez, E. M. The Mechanical Bond on Carbon Nanotubes: Diameter-Selective Functionalization and Effects on Physical Properties. *Nanoscale* **2016**, *8* (17), 9254–9264.

(13) López-Moreno, A.; Nieto-Ortega, B.; Moffa, M.; de Juan, A.; Bernal, M. M.; Fernández-Blázquez, J. P.; Vilatela, J. J.; Pisignano, D.; Pérez, E. M. Threading through Macrocycles Enhances the Performance of Carbon Nanotubes as Polymer Fillers. *ACS Nano* **2016**, *10* (8), 8012–8018. 04028.

(14) Blanco, M.; Nieto-Ortega, B.; de Juan, A.; Vera-Hidalgo, M.; López-Moreno, A.; Casado, S.; González, L. R.; Sawada, H.; González-Calbet, J. M.; Pérez, E. M. Positive and Negative Regulation of Carbon Nanotube Catalysts through Encapsulation within Macrocycles. *Nat. Commun.* **2018**, *9* (1), 2671.

(15) Wielend, D.; Vera-Hidalgo, M.; Seelajaroen, H.; Sariciftci, N. S.; Pérez, E. M.; Whang, D. R. Mechanically Interlocked Carbon Nanotubes as a Stable Electrocatalytic Platform for Oxygen Reduction. *ACS Appl. Mater. Interfaces* **2020**, *12* (29), 32615–32621.

(16) Moreno-Da Silva, S.; Martínez, J. I.; Develioglu, A.; Nieto-Ortega, B.; de Juan-Fernández, L.; Ruiz-Gonzalez, L.; Picón, A.; Oberli, S.; Alonso, P. J.; Moonshiram, D.; Pérez, E. M.; Burzurí, E. Magnetic, Mechanically Interlocked Porphyrin–Carbon Nanotubes for Quantum Computation and Spintronics. *J. Am. Chem. Soc.* **2021**, *143* (50), 21286–21293.

(17) Balakrishna, B.; Menon, A.; Cao, K.; Gsänger, S.; Beil, S. B.; Villalva, J.; Shyshov, O.; Martin, O.; Hirsch, A.; Meyer, B.; Kaiser, U.; Guldi, D. M.; von Delius, M. Dynamic Covalent Formation of Concave Disulfide Macrocycles Mechanically Interlocked with Single-Walled Carbon Nanotubes. *Angew. Chem. Int. Ed* **2020**, *59* (42), 18774–18785.

(18) Chamorro, R.; Juan-Fernández, L. de; Nieto-Ortega, B.; Mayoral, M. J.; Casado, S.; Ruiz-González, L.; Pérez, E. M.; González-Rodríguez, D. Reversible Dispersion and Release of Carbon Nanotubes via Cooperative Clamping Interactions with Hydrogen-Bonded Nanorings. *Chem. Sci.* **2018**, *9* (17), 4176–4184.

(19) Miki, K.; Saiki, K.; Umeyama, T.; Baek, J.; Noda, T.; Imahori, H.; Sato, Y.; Suenaga, K.; Ohe, K. Unique Tube–Ring Interactions: Complexation of Single-Walled Carbon Nanotubes with Cycloparaphenyleneacetylenes. *Small* **2018**, *14* (26), 1800720.

(20) Pöthig, A.; Casini, A. Recent Developments of Supramolecular Metal-Based Structures for Applications in Cancer Therapy and Imaging. *Theranostics* **2019**, *9* (11), 3150–3169.

(21) Ibáñez, S.; Poyatos, M.; Peris, E. N-Heterocyclic Carbenes: A Door Open to Supramolecular Organometallic Chemistry. *Acc. Chem. Res.* **2020**, *53* (7), 1401–1413.

(22) Martínez-Agramunt, V.; Ruiz-Botella, S.; Peris, E. Nickel-Cornered Molecular Rectangles as Polycyclic Aromatic Hydrocarbon Receptors. *Chem. Eur. J.* **2017**, *23* (27), 6675–6681.

(23) Martínez-Agramunt, V.; Gusev, D. G.; Peris, E. A Shape-Adaptable Organometallic Supramolecular Coordination Cage for the Encapsulation of Fullerenes. *Chem. Eur. J.* **2018**, *24* (55), 14802–14807.

(24) Martínez-Agramunt, V.; Peris, E. A Palladium-Hinged Organometallic Square with a Perfect-Sized Cavity for the Encapsulation of Three Heteroguests. *Chem. Commun.* **2019**, *55* (99), 14972–14975.

(25) Martínez-Agramunt, V.; Eder, T.; Darmandeh, H.; Guisado-Barrios, G.; Peris, E. A Size-Flexible Organometallic Box for the Encapsulation of Fullerenes. *Angew. Chem. Int. Ed* **2019**, *58* (17), 5682–5686.

(26) Vicent, C.; Martinez-Agramunt, V.; Gandhi, V.; Larriba-Andaluz, C.; Gusev, D. G.; Peris, E. Ion Mobility Mass Spectrometry Uncovers Guest-Induced Distortions in a Supramolecular Organometallic Metallosquare. *Angew. Chem. Int. Ed* **2021**, *60* (28), 15412–15417.

(27) Canevet, D.; Gallego, M.; Isla, H.; de Juan, A.; Pérez, E. M.; Martín, N. Macrocyclic Hosts for Fullerenes: Extreme Changes in Binding Abilities with Small Structural Variations. *J. Am. Chem. Soc.* **2011**, *133* (9), 3184–3190.

(28) Pérez, E. M.; Martín, N. π–π Interactions in Carbon Nanostructures. *Chem. Soc. Rev.* **2015**, *44* (18), 6425–6433.

(29) Dresselhaus, M. S.; Dresselhaus, G.; Saito, R.; Jorio, A. Raman Spectroscopy of Carbon Nanotubes. *Phys. Rep.* **2005**, *409* (2), 47–99.

(30) Jorio, A.; Saito, R. Raman Spectroscopy for Carbon Nanotube Applications. *J. Appl. Phys.* **2021**, *129* (2), 021102.

(31) Dresselhaus, M. S.; Jorio, A.; Hofmann, M.; Dresselhaus, G.; Saito, R. Perspectives on Carbon Nanotubes and Graphene Raman Spectroscopy. *Nano Lett.* **2010**, *10* (3), 751–758.

(32) Skowron, S. T.; Chamberlain, T. W.; Biskupek, J.; Kaiser, U.; Besley, E.; Khlobystov, A. N. Chemical Reactions of Molecules Promoted and Simultaneously Imaged by the Electron Beam in Transmission Electron Microscopy. *Acc Chem Res* **2017**, *50* (8), 1797–1807.

(33) Cao, K.; Zoberbier, T.; Biskupek, J.; Botos, A.; McSweeney, R. L.; Kurtoglu, A.; Stoppiello, C. T.; Markevich, A. V.; Besley, E.; Chamberlain, T. W.; Kaiser, U.; Khlobystov, A. N. Comparison of Atomic Scale Dynamics for the Middle and Late Transition Metal Nanocatalysts. *Nat. Commun.* **2018**, *9* (1), 3382.

(34) Fujita, M.; Ibukuro, F.; Hagihara, H.; Ogura, K. Quantitative Self-Assembly of a [2]Catenane from Two Preformed Molecular Rings. *Nature* **1994**, *367* (6465), 720–723.

(35) Chichak, K. S.; Star, A.; Altoé, M. V. P.; Stoddart, J. F. Single-Walled Carbon Nanotubes Under the Influence of Dynamic Coordination and Supramolecular Chemistry. *Small* **2005**, *1* (4), 452–461.

(36) Ashbridge, Z.; Kreidt, E.; Pirvu, L.; Schaufelberger, F.; Stenlid, J. H.; Abild-Pedersen, F.; Leigh, D. A. Vernier Template Synthesis of Molecular Knots. *Science* **2022**, *375* (6584), 1035–1041.

(37) Wu, Y.; Guo, Q.-H.; Qiu, Y.; Weber, J. A.; Young, R. M.; Bancroft, L.; Jiao, Y.; Chen, H.; Song, B.; Liu, W.; Feng, Y.; Zhao, X.; Li, X.; Zhang, L.; Chen, X.-Y.; Li, H.; Wasielewski, M. R.; Stoddart, J. F. Syntheses of Three-Dimensional Catenanes under Kinetic Control. *Proc. Nat. Acad. Sci. U.S.A* **2022**, *119* (12), e2118573119.

(38) Huang, S.-L.; Hor, T. S. A.; Jin, G.-X. Metallacyclic Assembly of Interlocked Superstructures. *Coord. Chem. Rev.* **2017**, *333*, 1–26.

Chapter 5

Transmission Electron Microscopy

In the last few decades, materials science has attracted a great deal of attention in the different fields. The later boom has been facilitated by the development of advanced transmission electron microscopy (TEM), which allows accurate identification of atomic configuration, intrinsic defect composition and local structures, and has improved the fundamental understanding of nanomaterials and their properties, such as electronic, mechanical, thermal and chemical potential. Therefore, this chapter is divided into three parts. The first part is theoretical and gives an introduction to electron microscopy, focusing on explaining what transmission electron microscopes are and how they work. It also discusses the possible aberrations that lenses can have, as well as the use of different correctors to compensate them, with the consequent acquisition of atomic resolved images.

The second and third parts consists of two examples of the use of electron microscopy to study 1D and 2D materials.

One is the confirmation of the non-covalent functionalization of carbon nanotubes with nitrogen-rich macrocycles. The substitutional N-doping of single-walled carbon nanotubes (SWNTs) is a common strategy to enhance their electrocatalytic properties in the oxygen reduction reaction (ORR). On the other hand, it is demonstrated that covalent functionalization of a van der Waals heterostructure (Franckeite) with organic molecules can be performed without altering the structure of the material. This strategy opens up the possibility of synthesising multidimensional 2D-2D-0D heterostructures that consist of ultrathin materials with tailored properties.

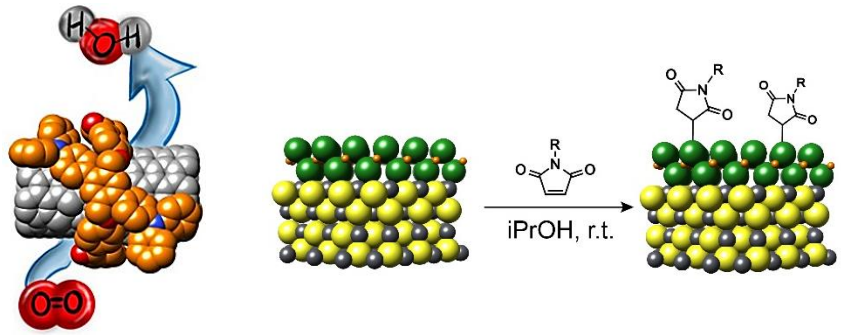

5.1. INTRODUCTION TO ELECTRON MICROSCOPY

Electron microscopy is a powerful technique that allows direct imaging of samples compared to other characterization tools which provide indirect data. Electron microscopes (EM) facilitates the study of a wide range of species, providing information such as their topography (surface characteristics of a sample), morphology (shape and size of the particles that constitute the material), composition (elements and compounds that compose the sample and their relative amount) and crystallography (how the atoms are arranged in the specimen). In the constant search for improvement in imaging accuracy, it became clear that the resolution was limited not only by the number and quality of the optics, also by the wavelength of the light source. While conventional light microscopes have a magnification of around 1000x, allowing the human eye to distinguish objects as close as 0.2µm,[1] EM uses a beam of electrons, particles with a very small wavelength that results in an improvement of the resolution getting images at the atomic level. As a conclusion, EM can produce images that show much finer details than regular light microscopes revealing information that would be difficult to obtain in any other way.

5.1.1. Electron beam - specimen interactions.

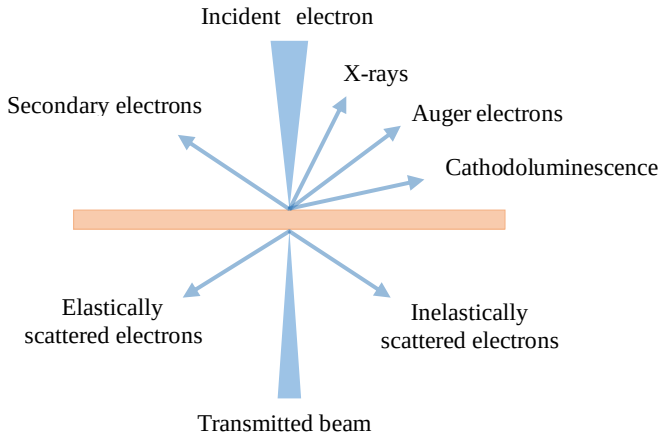

Figure 1. Electron beam scattering diagram.

Electrons are negative charged particles that have very strong interactions with both, the electrons, and the nuclei of the sample. As the electrons pass through it, they can either be scattered or remain unaffected generating signals which can be detected in different instruments like the transmission or scanning electron microscopes, or surface analysis devices (Figure 1). When the electron passes through the sample without interacting at all, no energy is transferred. These electrons are the transmitted direct beam, which includes the electrons that are still moving in the same direction as the incident beam. On the other

[1] Kubitscheck, U. John Wiley & Sons, Ltd, **2017**, 23–83.

hand, the scattered electrons can be divided into elastic or inelastic according to their energy loss.

a. Elastic scattering/diffraction: in elastic interaction, there is no transfer of energy from the incident electron to the specimen and, as a consequence, the electron that leaves the sample preserves its original energy. Essentially, elastic scatter affects the path of the electron beam within the sample without modifying the kinetic energy of the electron. It is mostly caused by the interaction of an incident electron with the atomic nucleus or with the electrostatic field of the atom. Since the mass of the nucleus exceeds that of the electron, the energy exchange (loss) is minimal and hardly measurable. In addition, it is responsible for the formation of a diffraction pattern in crystalline specimens, which is used to reveal structure. These interactions are employed to study thin specimens by transmission electron microscopy, TEM.

b. Inelastic scattering: in inelastic interaction, some of the incoming electrons are absorbed by the sample and other collide with the electrons present in the material, removing them from their shells (secondary electrons) and leaving the atoms in an excited (unstable) state. When these secondary electrons are generated far from the surface of the sample, they do not escape, they recombine with the holes formed in the scattering process creating phonons of energy. As a result of the ejection of an electron, the ionize atom rearranges and fills the vacancy with an electron from a higher energy level emitting X-rays because of the transition. This X-ray may also be absorbed by a second electron from one of the outer shells, resulting the ejection of a third electron (Auger electron). In both cases, the energy released is characteristic of the emitting element. The similar mass between the incident electron and the atomic electron allows the energy exchange (loss) to be noticeable. The scattered energy will then be transferred to the specimen and the energy of the incoming electron will be reduced. Inelastic scattering generates signals that can be studied by energy dispersive X-ray or electron energy loss spectroscopies. This type of interactions is mainly used for analysis of thick or bulk species by scanning electron microscopy, SEM.

5.1.1.1. Inelastic scattering-based EM spectroscopic techniques.

1. Energy Dispersive X-ray Spectroscopy.

Energy dispersive spectroscopy (EDS) is a technique based on the analysis of X-rays emitted by a specimen. When a high energetic electron impacts the sample, an inner shell electron of an atom can be promoted leaving a vacancy. An electron from an outer shell drops down to fill the hole emitting a photon of energy equal to the energy difference between the two shells (Figure 2a). Because the difference in atomic energy levels is characteristic of a particular element, a measurement of this X-ray energy provides a

'fingerprint' of the element. There is another kind of X-ray that is always present besides the characteristic X-rays, known as 'continuum' or 'Bremsstrahlung' X-rays, which are produced by the incident electrons interacting with the Coulomb field of the atomic nuclei. The incoming electron loses energy in the process, and this is emitted as a continuum X-ray. The different energy peaks allow the qualitative analysis, while the measurement of the intensities (phonon counts) of the signals, are useful for the semiquantitative determination of the elements.

2. Electron Energy Loss Spectroscopy.

Electron energy loss spectroscopy (EELS) is a useful technique since it identifies all the energy lost by the incident electrons, not just a small amount of inelastic scatter. The transmitted beam passes through the microscope column and is focused into the EELS spectrometer, which scatters the electrons according to their energy. Electrons in the incoming beam that have undergone inelastic diffraction are deflected to larger angles than those that have not lost energy. They are then imaged using a charge-coupled device (CCD), resulting in an EELS spectrum. An EELS spectrum is composed of a continuous background on which the characteristic signals or absorption maxima are superimposed. It can be divided into three energy regions depending on the type of the interaction: i) zero-loss, ii) low-loss and iii) core-loss, as shown schematically in Figure 2b.

i. Zero-loss peak: is the most intense signal in the spectrum and includes all elastically and quasi-elastically (vibrational or phonon) scattered electron contributions, i.e., those electrons that have not lost energy or whose loss is too small to be detected.

ii. Low-loss range: extends from the zero loss peak to an energy loss of about 50 eV and represents the collective excitation of electrons in the most outer atomic orbitals. The smallest energy losses result from phonon excitation and are usually confined in the zero-loss peak. The most significant peaks in the low-loss spectrum are caused by collective, resonant plasmon oscillations of the valence electrons and (interband) transitions from the valence to the conduction bands. These latter transitions allow the band gap of some elements in the sample to be determined.

iii. Core-loss range: includes all transitions above 50 eV energy loss. That is, the excitation of electrons from localized orbitals in the most inner layers of the atom to extended, unoccupied electron energy levels above the Fermi level of the sample. As a result, this region of energy provides detailed information about the electronic structure, chemical bonding and density of states of the elements in the specimen. Peaks in the core loss region are mostly generated by the inelastic electron interactions within the core shells of the atoms, and as the binding energy of the core electrons depends on the atomic number, each element has a specific ionisation edge energy onset in the energy loss spectrum.

Electron energy loss spectroscopy (EELS) and energy dispersive X-ray spectroscopy (EDS) provide (within their limitations) useful qualitative and quantitative elemental analysis. While EELS is more specific for light (low Z) elements, EDS is not, but can identify a broad set of elements.

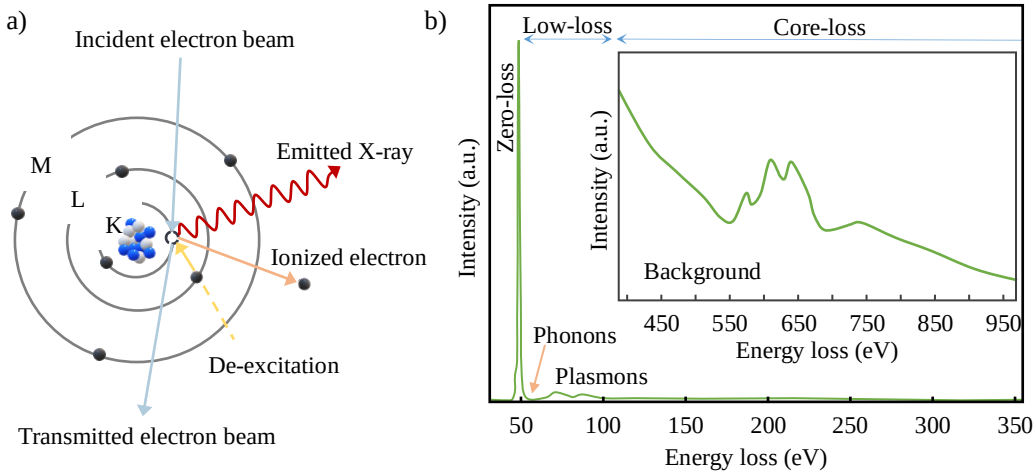

Figure 2. a) Schematic representation of X-ray process. b) Schematic diagram of an EELS spectrum.

5.2. TRANSMISSION ELECTRON MICROSCOPY

As it was mentioned earlier, electron microscopy is a technique that allows the acquisition of high-resolution images of a wide variety of samples. There are two major types of electron microscopes, transmission (TEM)[2] and scanning (SEM)[3] which work in the same manner. In short, a beam of electrons is accelerated in vacuum, cross a set of lenses and apertures, and reaches the sample, interacting with it to create an image. The main difference between both is that in TEM, the image is generated when the electrons are transmitted through a thin specimen, giving information about the morphology and the crystal structure. On the other hand, SEMs use the scattered electrons which arise from the surface of thick and bulk specimens creating topological images. The different among the images are due to the fact that SEM uses focused scattered electrons for scanning the surface of the sample in the x-y directions. For this reason, the sample can be thick, the only limitation being the ability to be fitted into the analysis chamber. In the case of TEM, a parallel beam is transmitted through the specimen, not scanned, unlike when used in scanning transmission electron microscopy. In addition, the sample needs to be thin to allow the electron beam to pass through it. Finally, the magnification of TEM is high compared to SEM and shows a 2D image whereas SEM provides 3D image.

[2] Goodhew, P. J.; Humphreys, J.; Beanland, R. CRC Press, **2000**.
[3] Erdman, N.; Bell, D. C.; Reichelt, R. Springer Handbooks; Springer International Publishing: Cham, **2019,** 229–318.

Transmission EM is a technique used to study the atomic and nanoscale structure, composition, and properties of materials. It is therefore a useful tool for understanding and correlating the physical and chemical characteristics associated to the microstructure with the macroscopic features of the material. This technology uses a device called a transmission electron microscope, which has two operating modes, conventional and scanning. The first, invented by Knoll and Ruska in 1931 and commonly known as TEM, is the direct electron image microscope which a parallel incident beam, illuminates the specimen (Figure 3a).[4–6] On the other hand, in the scanning transmission electron microscope (STEM), invented by von Ardenne in 1937,[7] the sample is scanned with a finely focused beam, the diameter of which also determines the resolution (Figure 3b). In both modes, the source emits a beam of electrons which, after being reduced in size by passing through the condenser lenses, produces an output wave which incidents on the sample. That beam is diffracted by the sample and a diffraction pattern is created in the back focal plane: selected area electron diffraction (SAED) in TEM mode and convergent beam electron diffraction (CBED) in STEM mode. In TEM, the image is created when the beam passed through the sample producing an exit wave that contains information about its structure. Then, it travels through the objective to the back focal plane where a diffraction patter is generated and later, to the image plane where the image is obtained. In STEM, while scanning, an image is created successively from transmitted electrons detected by different detectors located behind the sample. In both cases, the quality of the electron microscope image is compromised by the aberrations of the electron optical lenses used. This chapter is based on the analysis and characterization of materials using conventional transmission electron microscopes. Therefore, only information concerning this microscope will be given. A detailed study of the STEM technique is explained in the handbook of microscopy published in 2019.[8]

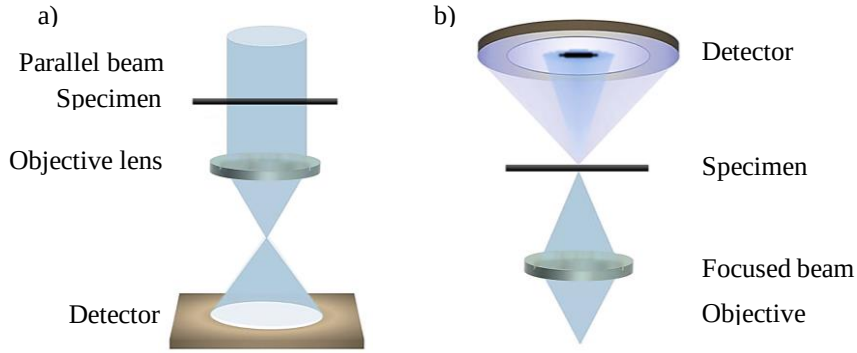

Figure 3. Schematic imaging modes of a) TEM, and b) STEM.

[4] Knoll, M.; Ruska, E. I. *Ann. Phys.* **1932**, *404* (5), 607–640.
[5] Knoll, M.; Ruska, E. *Ann. Phys.* **1932**, *404* (6), 641–661.
[6] Knoll, M.; Ruska, E. *Z. Physik* **1932**, *78* (5–6), 318–339.
[7] Von Ardenne, M. D *Z. Physik* **1938**, *109* (9–10), 553–572.
[8] Nellist, P. D. Springer Handbooks; Springer International Publishing: Cham, **2019**; 49–99.

5.2.1. Components of a TEM.

Transmission electron microscope consists of three functional components: the illumination system, the image producing system, and the image recording system (Figure 4):

a. The illumination system: It contains two parts, the electron gun, and the condenser system. The electron gun is the generator of the electron beam, i.e., it emits and accelerates electrons. The electrons are produced by a cathode, which is a thermionic or a field emission gun (FEG), either cold or thermally activated.

   A condensing lens system is used to focus the electron beam onto a sample by controlling its energy intensity and angular opening. TEMs use two condenser lenses to produce an image. The first lens is strong and controls the reduction in size of the beam (and therefore the final size of the illuminated area), producing a crossover of the electrons. The smaller source is then projected onto the sample by the second lens, which controls the convergence angle to form a parallel or convergent electron beam depending on the desired operating mode (image or diffraction, respectively). In addition, most microscopes have one or more condenser apertures placed under the first condenser lens. They limit the number of electrons passing through the column by trapping those travelling at high angles and reducing the X-rays produced. Using a small spot size minimises sample disturbance from heating and irradiation.

b. Image producing system: It consists of objective, intermediate and projector lenses, a moving sample holder, and an objective and selected-area apertures. They purpose is to focus the electrons as they pass through the specimen to produce a highly magnified image. The specimen is surrounded by two objective lenses. The one just below the sample has a short focal length and produces an initial inverted image that is transmitted to the projector lenses for enlarging. There are two types of projector lens: the intermediate, which allows the formation of both an image (image mode) and a diffraction pattern (diffraction mode), and the projector, which allows a generally higher magnification than the intermediate lens and displays the final image or the final diffraction pattern into the image recording system. These lenses make it possible to amplify the image without increasing the physical length of the microscope column. On the other hand, the objective aperture is in the back focal plane of the objective lens (where a pattern of diffraction can be produced) to permit the selection of specific diffracted rays. The selected-area aperture is located in the image plane of the objective lens (where an image can be generated) to enable specific areas to be selected.

c. Image recording system: It consists of a fluorescent screen has and a digital camera. The image generated is monochromatic (greyish or black and white) and must be visible to the human eye, either by directing the electrons onto a fluorescent screen

fixed to the base of the microscope column, or by acquiring the image digitally for display on a computer monitor.

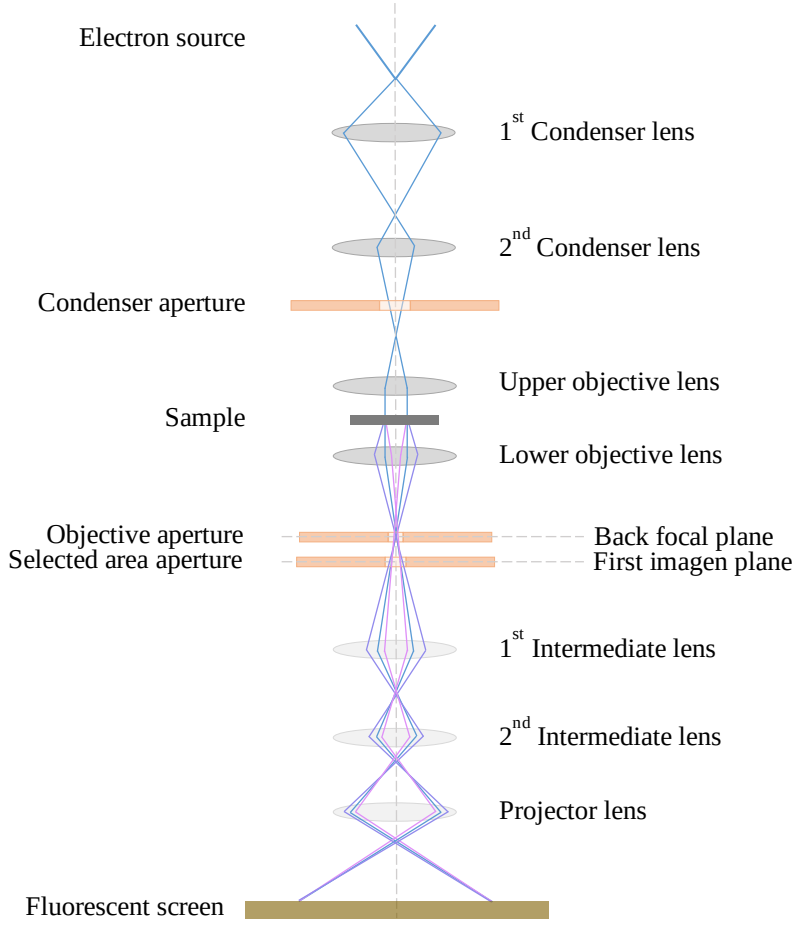

Figure 4. Diagram of a TEM in imaging mode. The intermediate lens moves its object plane to either the image plane, forming an image on the screen, or the back focal plane, forming a diffraction pattern.

5.2.2. Image formation in a TEM.

Image formation in a conventional TEM starts with a coherent parallel electron beam passing through a thin specimen. Electrons are scattered and a diffraction pattern is formed at the back focal plane of the objective lens. Finally, an image is formed in the image plane. In this way, the diffracted and transmitted electrons contribute to the final image. However, by placing an objective aperture into the back focal plane it is possible to select the information in the image to the transmitted or specific diffracted beams. From a SAED diagram, the image can be form in three different modes: 1. Bright field (BF): the objective aperture selects only the transmitted beam which contains most intensity of electron beams and all strongly diffracted regions in the sample appear dark. 2. Dark field (DF): an

objective aperture selects only one (or a few) diffracted beams without the contribution of the direct beam and this diffracted beam of electrons then appears bright in the DF image. 3. High resolution (HREM): the objective aperture selects the transmitted and several diffracted beams being the mode which allows the study of the samples at higher resolution. Contrast is created when the diffraction conditions for the electrons vary locally, e.g., owing to variations in the sample thickness, bending the crystal, or the presence of crystal defects. Nevertheless, the intensity pattern of the image is not just influenced by the interaction of the electron beam with the sample, it also depends on the illumination parameters and on the objective lens and its apertures. It is therefore more meaningful to use diffracted electrons rather than the transmitted beam, as they have interacted with the sample and the image contrast is then typically enhanced. The more common imaging technique is amplitude contrast. This means that the phases of the transmitted and scattered waves are not recombined, as in BF and DF modes. Conversely, the contrast in HREM is called phase contrast, due to the images is the result of the combination of the transmitted and diffracted beams which are in different phase.

The acquisition of HRTEM images has been an important aspect in the development of this thesis, thus the whole process of their formation is briefly explained. For more detailed information on this topic, please have a look at ref. 9 and 10.

An incident parallel electron beam, ideally a plane wave (ψ_i) interacts with a sample undergoing multiple diffraction processes. After passing through it, an exit wave is created and is mathematically described by the Fourier transform of the object wave function (ψ_o). For thin samples there is no absorption of the beam, the scattering produces a phase shift but not amplitude shift, which is known as weak phase object approximation (WPOA). Such samples result in weak scattering with a very small phase shift. This exit wave includes the information about the structure of the specimen and can be expressed in terms of the projected potential ϕ (x,y):

$$\psi_o(r) = 1 - i\sigma\phi_{p(x,y)}$$

where σ represents an interaction constant given by $\sigma = 2m_e(\lambda_r/h^2)$ in which m_e and λ_r are the relativistic electron mass and wavelength. $\phi_{p(x,y)}$ is the 2D projection of the sample potential along the beam direction. After leaving the sample, the object wave function propagates across the objective lens to the back focal plane (reciprocal space) creating a diffraction pattern ψ_d (K), or to the image plane (real space) forming the HRTEM, ψ_i (r). The exit wave function ψ_i (r) is affected by the imperfections of the objective lens. Thus, its expression is described by taking into account the contrast transfer function, CTF(K).

$$\psi_i(r) = F^{-1}[\psi_d(K) \times CTF(K)]$$

[9] Kirkland, A. I.; Chang, S. L.-Y.; Hutchison, J. L. Springer Handbooks; Springer International Publishing: Cham, **2019**; 3–47.
[10] Wagner, G. Oxford University Press: Oxford, New York, **1989**.

where F^{-1} is the inverse Fourier transform. In this way, the intensity observed in the HRTEM is represented by: $I(r) = |\psi_i(r)|^2$

CTF(K) considers the factors that limit the resolution and is given by:

$$CTF(K) = 2A(K)E(K)\sin\gamma(K)$$

where A(K) contemplates the limiting effects of the apertures related to the geometrical position and its size, E(K) covers the factors that cause instability such as the vibration or the displacement of the sample, and γ(K), is the aberration function, which shows the distortion of the beam due to imperfections in the lens. The aberrations in the objective lens are the responsible for the phase shifts of the diffracted waves. The degree of phase shift depends on the distance from the optical axis and therefore on the angle of diffraction. As a result, each diffracted ray is subjected to a different phase shift and is modified in its spatial frequencies. The aberration function is influenced by the defocus (Δf), the wavelength (λ), the astigmatism (C_a) and the spherical aberration (C_s) and it is represented as:

$$\sin\gamma(K) = (2\pi/\lambda)W(K)$$

where W(K) is the wave aberration function which is written considering the different aberrations as follows:[11]

$$W(K/\phi) = 2\pi/\lambda\,(|A_0|\lambda k\cos(\phi-\alpha_0) + 1/2|A_1|\lambda^2k^2\cos2(\phi-\alpha_1) + 1/2C_1\lambda^2k^2 + 1/3|A_2|\lambda^3k^3\cos3(\phi-\alpha_2) + 1/3|B_2|\lambda^3k^3\cos3(\phi-\beta_2) + 1/4|A_3|\lambda^4k^4\cos4(\phi-\alpha_3) + 1/4|S_3|\lambda^4k^4\cos2(\phi-\sigma_3) + 1/4C_3\lambda^4k^4 + \ldots)$$

where A_0 is the image shift, A_1 the two-fold astigmatism, C_1 the defocus, A_2 the three-fold astigmatism, B_2 the axial comma, A_3 the four-fold astigmatism, S_3 the axial star, and C_3 the spherical aberration. In this way, the contrast transfer function is oscillatory due to its dependence with sinγ, depends on the focus and affects the observed contrast in the image. It can be plotted as a function of the frequency, K (Figure 5). When the sine function is zero, there is no information transferred. However, it changes for different values of K, giving regions with positive contrast where all the information is transferred. This shows the scattering centres of the specimen appear as dark spots (dark contrast). In this way, the smaller number of zeros, the best contrast transfer. In 1949, Scherzer described the focus setting for optimum phase contrast transfer.[12] Scherzer defocus (Δf_S) gets the best conditions for optimizing the focus of the images and it is given by:

$$\Delta f_S = 1.2(C_s\lambda)^{1/2}$$

At this focal point, all the electron rays have approximately the same phase until the first crossover with the x axis, known as the point resolution. Until this frequency (spatial frequency, Ki), it is possible to directly interpret the information in the HRTEM image. While increasing the frequency, the CFT difficulties the interpretation of the information

[11] Brooks, S. Wiley, **2011**.
[12] Scherzer, O. *J. Appl. Phys.* **1949**, *20* (1), 20–29.

due to contrast oscillatory reversals. The CTF can fluctuate widely with the defocus. In addition, at higher values of K, the CFT is strongly attenuated from effects of chromatic aberration, focus scattering and energy instabilities until it arrives at the spatial frequency K_t, which indicates the point beyond which no information can be transferred. It therefore defines the absolute limit of the transferred information. Finally, the spatial resolution, ρ(r), between two points, for the Scherzer focus is expressed as:

$$\rho(r) = 0.6(C_s\lambda^3)^{1/4}$$

Therefore, HREM is a phase contrast imaging technique that needs high coherence and compensation of aberrations to obtain the best resolution of an image. The point resolution depends on the defocus level. As this is a parameter that can be adjusted on the microscope, it is feasible to optimize it, resulting in maximizing the CTF over a wider range of frequencies.

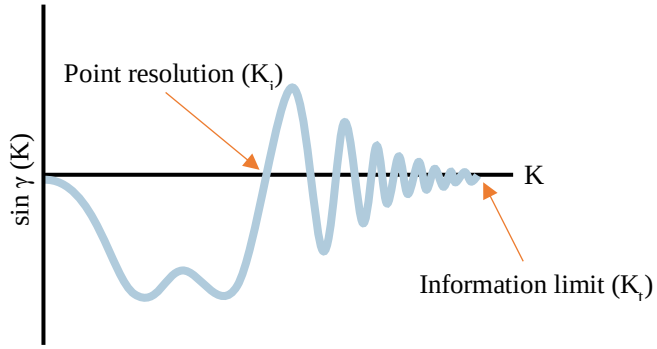

Figure 5. Representation of the contrast transfer function.

5.2.3. Aberrations.

The resolution of the electron microscope is affected by the aberrations of the optics used. Microscope lenses are never perfect and will always produce some image distortion. An ideal lens will perfectly reproduce every single point of an object in the image (Figure 6a). However, the real ones have aberrations. These cause the rays coming from a single point to be focused on different points. Aberrations are imperfections or distortions in the electron optics that can affect the quality and resolution of images obtained in a TEM. By reducing the ability to resolve fine details, these artifacts can cause blurring, distortion, or loss of contrast in the final image. The aberration is defined as the phase difference between a perfect wave and a wave that has experimented aberration and is represented by the equation:

$$\gamma = (2\pi/\lambda)\, W$$

where W is the distance between where the wavefront is and where it would be for an ideal lens. The aberrations in a microscope can be expressed as a polynomial function with the lowest order terms being the easiest to correct.[11] Lens aberrations can be divided into

[11] Brooks, S. Wiley, **2011**.

two categories: geometrical, which result in phase changes and do not involve changes in beam energy, and chromatic, which are due to changes in beam energy.

a. Geometrical aberrations.

Of the geometric aberrations, spherical aberration is the main one that limits resolution, but there are others such as coma and astigmatism.

Spherical aberration (Cs) occurs when parallel rays passing through the lens system are focused on different focal planes depending on how close or far they are from the optical axis. The different rays are focused on different points, but always along the optical axis. The result is a circular cross section instead of a point that produces a blurry image. This reduces the ability to resolve small features and limits overall image quality. In other words, it decreases the resolution of the image (Figure 6b).

Coma aberration is associated with ray emissions arising from a point on the object slightly off the optical axis. The rays that pass through the centre of the lens will be focused off the optical axis but at the same location, whereas those that pass through the edge of the lens will be focused on different places. Unlike spherical aberration, in which the images from an on-axis point are circular, of different sizes and superimposed around a shared centre, in coma the images from an off-axis point are also circular, of different sizes but displaced from each other (Figure 6c).

Astigmatism, in contrast to spherical aberration and coma, is the result of the error of a single zone of a lens in focusing the image of an off-axis point to a unique focal point. It is caused by the existence of multiple focal points along the optical axis in such a way that the rays meet as perpendicular planes, creating images with an elliptical shape (Figure 6d).

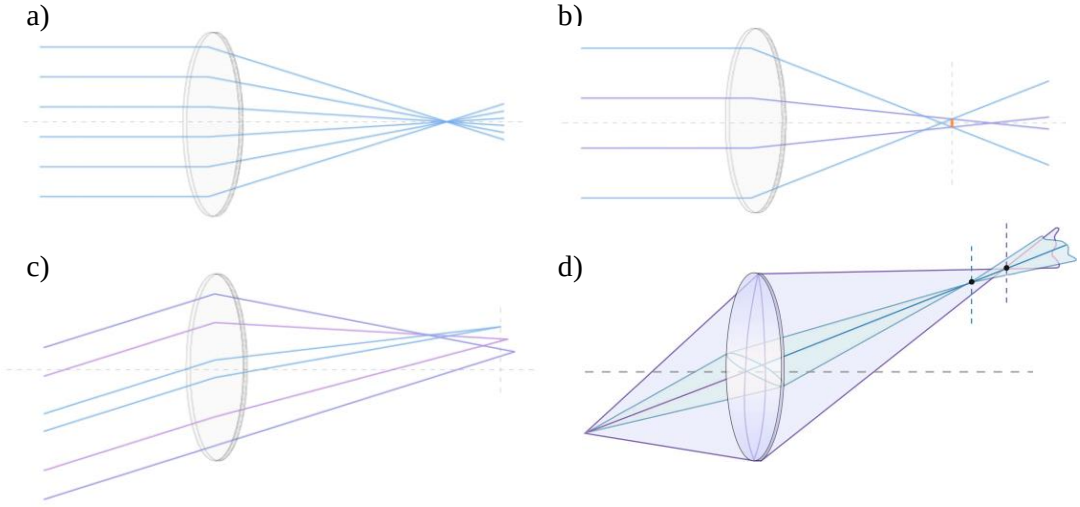

Figure 6. Simplified representation of lenses: a) Ideal. b) Lens with spherical aberration (in orange, minimum confusion disc). c) Lens with comma aberration. d) Lens with astigmatism.

b. Chromatic aberrations.

Chromatic aberration (Cc) is caused by the fact that the electrons in the beam are not completely monochromatic. The lens is unable to focus all the electron rays on the same plane (higher energy electrons are faster and less affected by the electromagnetic field than lower energy ones). It generates waves of variable wavelength and energy which are focused at different points along the optical axis. The lower the acceleration voltage used, the more important this aberration becomes (Figure 7b)

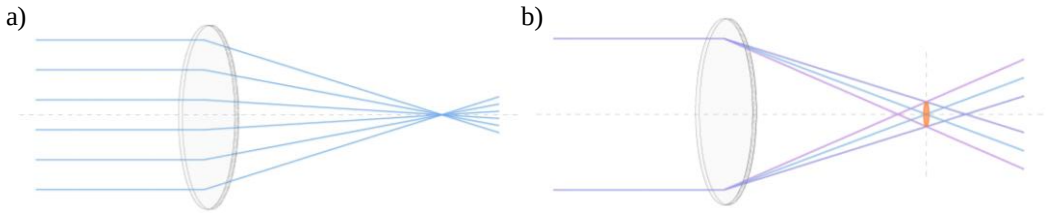

Figure 7. Comparison between an ideal lens, a) and a lens with chromatic aberration, b) (in orange, minimum confusion plane).

Most aberrations can be reduced or eliminated by proper design and alignment of the microscope stage. However, spherical and chromatic aberrations are inherent in static, rotationally symmetric electromagnetic fields. The effect of Cs and Cc aberrations can be overcome in two ways:

1. Acquisition of aberrated images to be processed a posteriori: this can be done using the through-focus series reconstruction method,[13,14] or super-resolution techniques.[15]
2. Addition of multipole correctors to compensate for aberrations (Figure 8): This method is based on the construction of non-round lenses that generate negative aberrations which, when combined with the positive aberrations of the objective lens, result in zero aberrations. To compensate for chromatic aberration, the correctors deflect the faster electrons in the direction of the optical axis and the slower electrons away from it. For spherical aberration, the correctors focus the side electrons at the same focal point as the electrons near the optical axis (paraxial electrons).

[13] Coene, W. M. J.; Thust, A.; Op de Beeck, M.; Van Dyck, D. *Ultramicroscopy* **1996**, *64* (1), 109–135.
[14] Kirkland, A. I.; Meyer, R. R. *Microsc. Microanal.* **2004**, *10* (4), 401–413.
[15] Rodenburg, J. M.; Bates, R. H. T. *Philos. trans., A Math. phys. eng. sci.* **1997**, *339* (1655), 521–553.

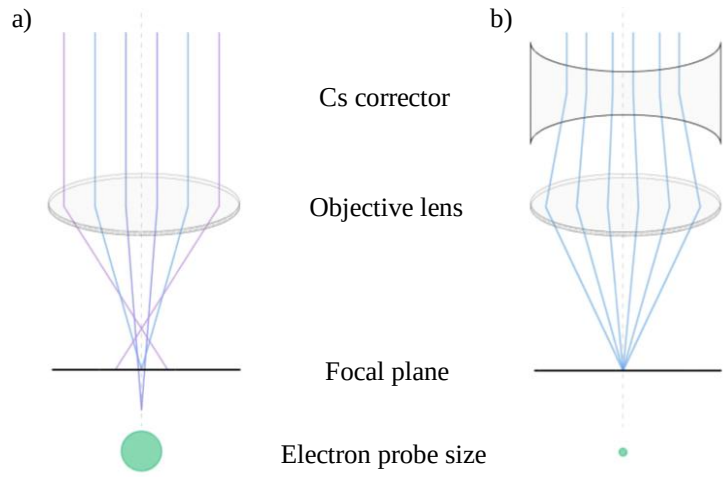

Figure 8. a) Simplified representation of a lens with spherical aberration. b) Electron beam focused by correcting spherical aberration using a corrector.

5.2.3.1. Improving resolution.

Since the first TEM prototype built by Ruska and Knoll,[6] progress in resolution has been slow, owing to the need to identify and overcome various instrumental limitations. In 1936, Scherzer demonstrated that it was not possible to avoid spherical and chromatic aberration in systems using round magnetic lenses.[16] And it was Scherzer who, in 1947, introduced the idea of correcting spherical aberration with multipole lenses.[17] Yet, it was to be more than 50 years before such systems were available for commercial use and thus actually achieved the purpose of this technology, i.e. higher resolution.[18,19] The first aberration corrected transmission electron microscope (AC-TEM) was built in 1998 by Haider et al. using a double hexapole corrector. [20,21] This immediately doubled the resolution compared to the uncorrected basic instrument. This discovery, together with the first aberration corrected scanning transmission electron microscope (AC-STEM) constructed by Krivanek *et al.* in 1997 using a quadrupole-octupole corrector, were the starting point for the progress of electron microscopy in both electron optics and its applications.[22,23]

[6] Knoll, M.; Ruska, E. *Z. Physik* **1932**, *78* (5–6), 318–339.
[16] Scherzer, O. *Z. Physik* **1936**, *101* (9), 593–603.
[17] Scherzer, O. Spharische Und Chromatische Korrektur von Elektronen-Linsen. *Optik* **1947**.
[18] Rose, H. Elsevier, **2008**, *153*, 3–39.
[19] Hawkes, P. W. *Philos. trans., A Math. phys. eng. sci.* **2009**, *367* (1903), 3637–3664.
[20] Haider, M.; Uhlemann, S.; Schwan, E.; Rose, H.; Kabius, B.; Urban, K. *Nature* **1998**, *392* (6678), 768–769.
[21] Haider, M.; Rose, H.; Uhlemann, S.; Schwan, E.; Kabius, B.; Urban, K. *Ultramicroscopy* **1998**, *75* (1), 53–60.
[22] Krivanek, O. L.; Dellby, N.; Spence, A. J.; Camps, R. A.; Brown, L. M. *Microsc. Microanal.* **1997**, *3* (S2), 1171–1172.
[23] Krivanek, O. L.; Dellby, N.; Lupini, A. R. *Ultramicroscopy* **1999**, *78* (1), 1–11.

Aberration corrected TEMs are advanced versions of transmission electron microscopes that incorporate sophisticated aberration correction technologies to improve imaging and analysis capabilities. TEM does not reach a resolution near to the wavelength of illumination because standard lenses are far from perfect. The resolution, crucial factor in AC-TEM, is the minimum distance between two points of a sample that can be distinguished as separate entities by the observer.[24] This parameter is limited by a number of factors such as: 1. the size of the source, which leads to restricted spatial coherence in the beam; 2. the instrumental instabilities, that make the incident electron beam to have a range of wavelengths: 3. the point resolution limit, given by the Scherzer expression ~ $0.66Cs^{¼}\lambda^{3/4}$, depending on the spherical aberration (Cs) and the wavelength (λ) of the electrons used,[25] and 4. the chromatic aberration of the electron lens, which results in misfocusing of the monochromatic beam. In conclusion, aberrations are key factors that need to be corrected in order to obtain a realistic image of the sample under examination.

5.2.3.1.1. Aberration correctors.

As mentioned above, the resolution-limiting aberrations can be corrected using multipole lenses, the hexapole and quadrupole-octupole correctors (Figure 9). In multipole lenses, the magnetic field is perpendicular to the beam and the deflection of the rays is just governed by the Lorentz force.

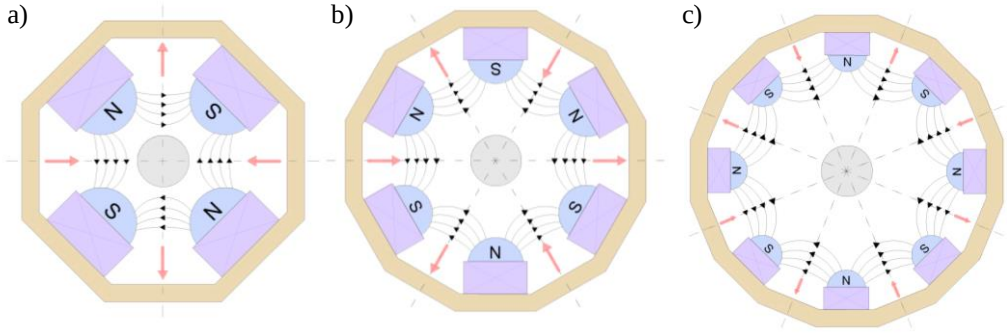

Figure 9. Magnetic lenses used to correct aberrations: a) quadrupole, b) hexapole and c) octupole.

i. Hexapole corrector

It is made up of a pair of strong hexapoles with opposite polarity and two transfer round lens doublets. The transfer doublet projects the first hexapole onto the second with a magnification of -1. Consequently, all second order aberrations introduced by the first hexapole are eliminated. The remaining secondary aberrations are of the same nature and are of the third order as those of the round lenses. In contrast, the sign of the spherical

[24] Born, M.; Wolf, E. Elsevier, **2013**.
[25] Ishikawa, R.; Morishita, S.; Tanigaki, T.; Shibata, N.; Ikuhara, Y. *Microsc.* **2023**, *72* (2), 78–96.

aberration of the hexapole corrector is the opposite. In this way the corrector achieves a negative Cs that exactly matches the positive Cs of the objective lens.

ii. Quadrupole-octupole corrector

It is a combination of octupole and quadrupole magnetic lenses. The QO corrector employs a quadrupole to create a line focus along the negative spherical aberration axis of an octupole, two more quadrupoles to produce a line focus in the perpendicular direction in a second octupole, and a fourth quadrupole to reform a round beam. The two octupoles introduce negative spherical aberration in x and y, but also generate some four-fold distortion of the beam. This requires a third octupole acting on a round beam to correct it. As with the hexapoles, the QO corrector must introduce compensating aberrations with rotational symmetry and must be in the opposite direction to those of the round lenses.

In summary, the hexapole corrector is only effective in the elimination of third-order spherical aberration and coma. On the other hand, the quadrupole-octupole corrector can also correct chromatic aberration. The QO corrector uses crossed electric and magnetic quadrupoles to correct chromatic aberration and octupoles to compensate for third-order spherical aberration.

5.3. MECHANICAL INTERLOCKING OF SWNTS WITH N-RICH MACROCYCLES FOR EFFICIENT ORR ELECTROCATALYSIS

The content of this second part consists of an example described in detail in reference 26 and is structured as follows. We begin with a brief introduction to understand why the supramolecular functionalization of SWNTs with N-rich macrocycles is interesting. This will be followed by an explanation on how to synthesize the MINTs and how to prepare them for transmission electron microscopy. Finally, high-resolution images obtained with JEOL instruments are shown.

For reasons of space and because the use of catalysts for the oxygen reduction reaction (ORR) belongs to a separate field, the electrocatalytic activity of mechanically interlocked carbon nanotubes (MINTs) is not discussed in this chapter. We recommend reading the full article for more detailed information on the research.

[26] Zhang, W.; Guillén-Soler, M.; Silva, S. M.-D.; López-Moreno, A.; González, L. R.; Giménez-López, M. del C.; Pérez, E. M. *Chem. Sci.* **2022**, *13* (33), 9706–9712.

5.3.1. Introduction.

Functionalization of single-walled carbon nanotubes (SWNTs) with molecular fragments using covalent or noncovalent chemistry is a common strategy to alter their physical properties for their further application.[27–30] Substitutional heteroatom doping of SWNTs is another strategy towards the same end.[31–33] Among possible dopants (B, N, S, F, and P), the N dopant is perhaps the most frequently studied, since the doping process is typically facile, and the N-doped SWNTs maintain high electrical conductivity and are typically easier to disperse in organic solvents.[34–37] As potentially negative outcomes, N-doping introduces defects into the SWNT structure, and the insertion of N groups produces changes in the energy band arrangements leading to creation of additional energy levels.

In this work, we investigate the formation of MINTs using N-rich macrocycles as a novel strategy for preparation of SWNT derivatives displaying N atoms on their surface and demonstrate their ability as electrocatalysts in the ORR.

5.3.2. Results and discussion.

The dibromo U-shape was prepared from bis(4-hydroxyphenyl) methane through two consecutive Williamson's etherifications with 11-bromoundecene and 1,4-dibromo-2,5-bis(-bromomethyl)benzene, respectively. Then, the U-shape molecule containing two triphenylamine (TPA) units (U-TPA, see S2 in SI) was prepared via Suzuki–Miyaura coupling in 72% yield in the presence of $Pd(PPh_3)_4$ from dibromo U-shape. Finally, the formation of MINT-TPA through templated ring closing metathesis (RCM) of U-TPA in the presence of (6,5)-enriched SWNTs (0.78 nm average diameter) was carried out (see S3 in SI). The chemical structure of MINT-TPA is shown in Figure 10.

[27] Sun, Y.-P.; Fu, K.; Lin, Y.; Huang, W. *Acc. Chem. Res.* **2002**, *35* (12), 1096–1104.
[28] Mallakpour, S.; Soltanian, S. Surface *RSC Adv.* **2016**, *6* (111), 109916–109935.
[29] Georgakilas, V.; Kordatos, K.; Prato, M.; Guldi, D. M.; Holzinger, M.; Hirsch, *J. Am. Chem. Soc.* **2002**, *124* (5), 760–761.
[30] Tasis, D.; Tagmatarchis, N.; Bianco, A.; Prato, M. *Chem. Rev.* **2006**, *106* (3), 1105–1136.
[31] Hu, C.; Dai, L. *Adv. Mater.* **2019**, *31* (7), 1804672.
[32] Li, J.-C.; Hou, P.-X.; Liu, C. *Small* **2017**, *13* (45), 1702002.
[33] Paraknowitsch, J. P.; Thomas, A. *Energy Environ. Sci.* **2013**, *6* (10), 2839–2855.
[34] Czerw, R.; Terrones, M.; Charlier, J.-C.; Blase, X.; Foley, B.; Kamalakaran, R.; Grobert, N.; Terrones, H.; Tekleab, D.; Ajayan, P. M.; Blau, W.; Rühle, M.; Carroll, D. L. *Nano Lett.* **2001**, *1* (9), 457–460.
[35] Xia, Y.; Mokaya, R. *Adv. Mater.* **2004**, *16* (17), 1553–1558.
[36] Panchakarla, L. S.; Govindaraj, A.; Rao, C. N. R. *Inorganica Chim. Acta* **2010**, *363* (15), 4163–4174.
[37] Steinmetz, M.; Lima, D.; Machado, R. R. L.; Sundararaj, U.; Arjmand, M.; da Silva, A. B.; Santos, J. P.; Pessôa, C. A.; Wohnrath, K. *Diam. Relat. Mater.* **2020**, *110*, 108093.

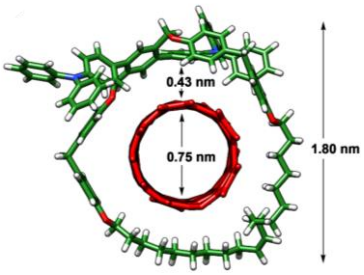

Figure 10. Energy-minimized (MM94) model of MINT-TPA. The MINT models are displayed with the alkene in *E* geometry arbitrarily, as the size of the cavity hardly changes in *Z* configuration. Note that, experimentally, MINTs are obtained as a mixture of *E/Z* isomers.

Analysis by HR-TEM of the samples of MINT-TPA drop cast from a TCE suspension (~ 0.2 mg of MINT-TPA in 2 mL of tetrachloroethane, see S4 in SI) shows mostly bundled nanotubes with heavily functionalized sidewalls. Figure 11 show images captured with the microscope JEOL JEM 2100, where SWNTs (0.7 nm in diameter) are densely covered with an organic material. Macrocycles of 1.7 nm in diameter are observed, in accordance with the expected size. To perform a more precise characterization, an aberration-corrected microscope was also employed. The microscope was operated at 60 kV under low dose conditions to prevent damage to the nanotubes and macrocycles as much as possible. Figure 12 and Figure 13 show the aberration-corrected HR-TEM images of macrocycles of diameters about 2.0 nm around SWNTs of 0.8 nm in diameter.

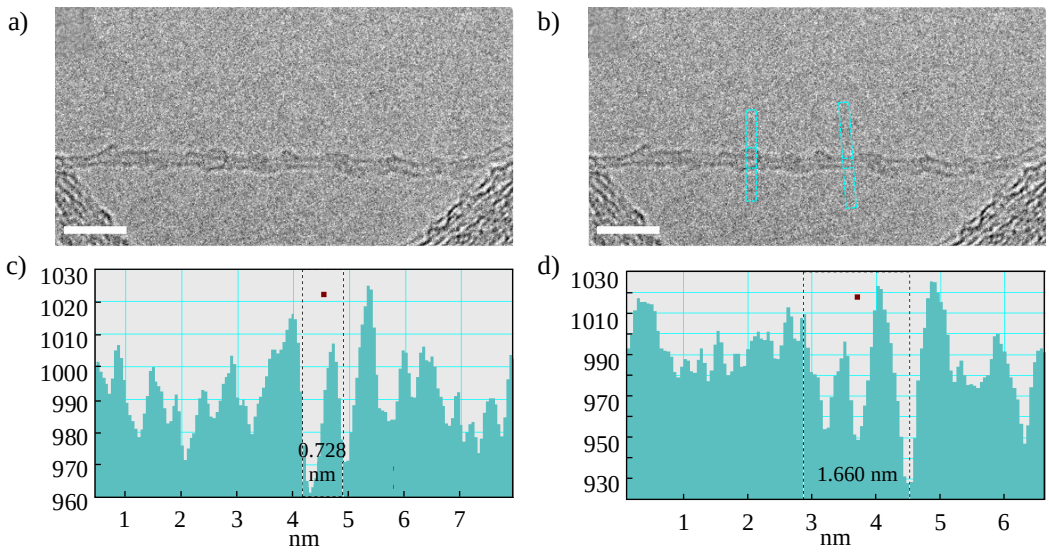

Figure 11. a) HR-TEM of MINT-TPA. b) Image a) with rectangles indicating the areas of interest. c) TEM profile of the SWNT. d) TEM profile of the TPA macrocycle. Scale bars are 5 nm for a) and b).

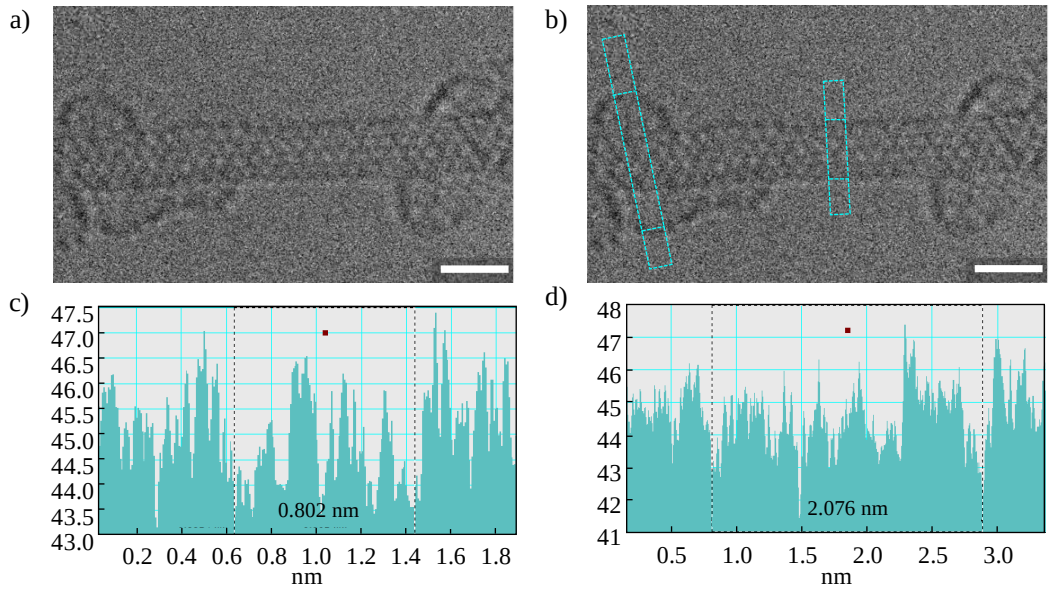

Figure 12. a) ac HR-TEM of MINT-TPA. b) Image a) with rectangles indicating the areas of interest. c) TEM profile of the SWNT. d) TEM profile of the TPA macrocycle. Scale bars are 1 nm for a) and b).

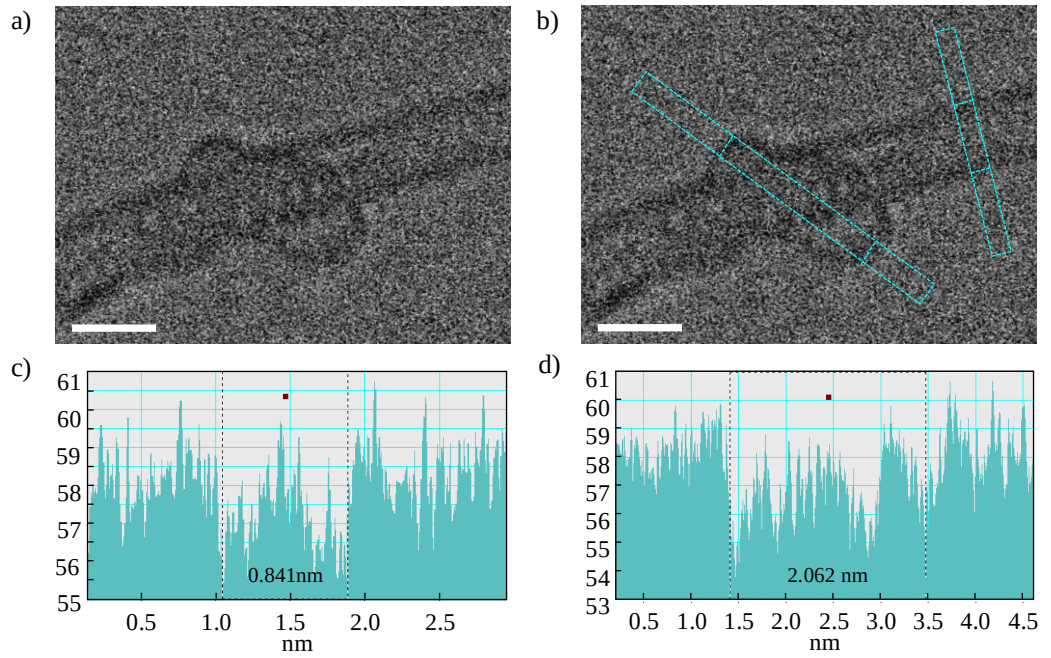

Figure 13. a) ac HR-TEM of MINT-TPA. b) Image a) with rectangles indicating the areas of interest. c) TEM profile of the SWNT. d) TEM profile of the TPA macrocycle. Scale bars are 1 nm for a) and b).

5.3.3. Conclusions.

We have synthesized MINTs containing TPA groups as a new strategy for displaying catalytically active N atoms on the surface of carbon nanotubes. Transmission electron microscopy was useful to check the formation of the MINT structure and to verify that the introduction of nitrogen atoms did not affect the integrity of the nanotube.

5.3.4. Supporting information.

S1. Equipment.

JEOL JEM 2100 - TEM microscope operating at 200 kV accelerating voltage and equipped with a LaB_6 thermionic electron gun. It is a built-in STEM unit with a bright field detector, and it is coupled to an ORIUS SC1000 CCD camera (model 832). The resolution between dots is 2.5 Å. It also has an XEDS microanalysis system (OXFORD INCA).

JEOL JEM GRAND ARM300cF - TEM microscope has an accelerating voltage of 60, 80, 120, and 300 kV and a cold cathode emission source. It is equipped with an aberration corrector on the objective lens with dodecapole symmetry manufactured by JEOL (ETA-JEOL). The control and alignment of the corrector is carried out by means of the JEOL COSMO software, which allows the measurement of the different aberrations. The equipment allows a resolution of 0.5 Å between dots. Images are captured by a high-resolution CCD camera GATAN Oneview (4096 x 4096 pixels). The microscope is complemented by a scanning transmission unit (STEM) and DF/BF/LADF detectors. A CENTURIO SDD detector for EDS microanalysis system, and an EELS ENFINIUM spectrometer for ELLS characterization. To avoid the sample damage, the microscope was used with an accelerating voltage of 60 kV.

S2. Synthesis of U-TPA.

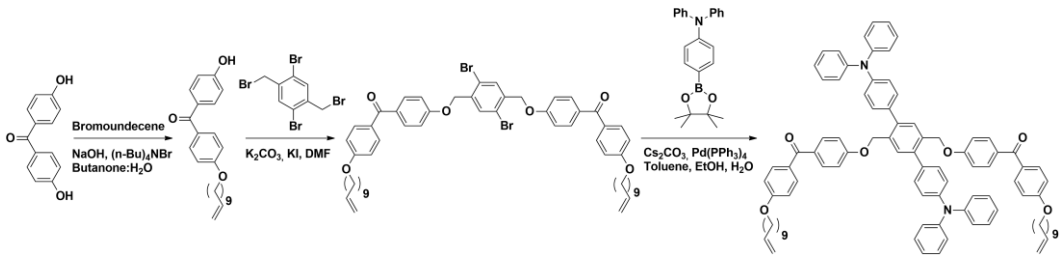

A detailed synthesis of U-TPA molecule is described in the reference 26.

[26] Zhang, W.; Guillén-Soler, M.; Silva, S. M.-D.; López-Moreno, A.; González, L. R.; Giménez-López, M. del C.; Pérez, E. M. *Chem. Sci.* **2022**, *13* (33), 9706–9712.

S3. Procedure for SWNTs functionalization.

SWNTs (20 mg) were dispersed in 20 mL of tetrachloroethane (TCE) by sonication in a bath sonicator. Subsequently, U-TPA (0.01 mmol) and 2nd generation Grubb´s catalyst (0.01 mmol, 17 mg) were added and the reaction was stirred at 60 ℃ under nitrogen for 96 hours. After this time, the suspension was filtered through a 0.2 μm pore-size polytetrafluoroethylene (PTFE) membrane and washed profusely with CH_2Cl_2 to remove any unreacted linear precursors, non-interlocked macrocycles, weakly adsorbed TPA materials, remaining catalyst, etc. This washing procedure was repeated three times, after which the samples were dried under vacuum.

S4. Protocol for TEM sample preparation.

Approximately 0.2 mg of MINT-TPA were ultrasonicated in 2 mL of tetrachloroethane for ten minutes. Then a few drops of this dispersion were deposited onto a 200 square mesh copper grid covered by holey carbon (100 micron). After the solvent evaporation in air, the grid was ready to use.

Note: Microstructural characterisation by transmission electron microscopy was carried out at the national centre for electron microscopy (ICTS-CNME) of the UCM.

5.4. COVALENT MODIFICATION OF FRANCKEITE WITH MALEIMIDES: CONNECTING MOLECULES AND VAN DER WALLS HETEROSTRUCTURES

The subject of this third section is based on an example described in detail in reference 38 and is structured as follows. First, we briefly introduce the reason for modifying a 2D material. This is followed by an explanation of how the covalent functionalization of Franckeite, Fk, is performed. Once this has been confirmed using high-resolution magic angle spinning NMR, we verify that the structure of the material has not been modified using electron microscopy.

The article also described time-resolved photoluminescence measurements of Fk functionalized with a maleimide derivative equipped with a chromophore (porphyrin). The steady-state photophysical properties of the 2D–2D–0D mixed-dimensional heterostructure obtained show that the organic chromophore retains its ground state character, whereas an energy transfer process between the porphyrin and the van der Waals heterostructure takes place. This part will not be explained here for reasons of space and

[38] Villalva, J.; Silva, S. M.-D.; Villa, P.; Ruiz-González, L.; Navío, C.; Garcia-Orrit, S.; Vega-Mayoral, V.; Cabanillas-González, J.; Castellanos-Gomez, A.; Giovanelli, E.; Pérez, E. M. *Nanoscale Horiz.* **2021**, *6* (7), 551–558.

because it concerns another area. We refer the reader to the full article for more information.

5.4.1 Introduction.

The chemistry of 2D materials is based on the idea that the decoration of the nanomaterials with functional molecular fragments will yield superior combined properties.[39] Besides this application-oriented point of view, the chemistry of 2D materials presents very interesting fundamental challenges, like obtaining chemical selectivity in materials where most atoms are chemically identical.[40,41]

In this work we describe the covalent functionalization of a naturally occurring van der Waals heterostructure, Franckeite, using maleimides. We achieve preferential reactivity of the sulphides in the SnS_2 layer to form S–C bonds, with sufficient selectivity to conserve the van der Waals heterostructure.

5.4.2. Results and discussion.

The structure of Franckeite and the idealized reaction scheme are shown in Figure 14. This naturally heterostructure is composed of the alternate layers of one pseudohexagonal (H) tin(IV) sulfide (SnS_2)-like layer and four pseudotetragonal (T) lead(II) sulfide (PbS)-like layers. For simplicity, only a minimal repetition unit is drawn. Few-layer Fk colloids were obtained using the liquid-phase exfoliation method previously described.[42] In order to perform the covalent functionalization, N-benzylmaleimide (Bn-mal in Figure 14) was added to a Fk dispersion and bonded to it via thiol-maleimide "click" reaction (see S2 in SI).

[39] Coronado, E.; Martí-Gastaldo, C.; Navarro-Moratalla, E.; Burzurí, E.; Camón, A.; Luis, F. *Adv. Mater*. **2011**, *23* (43), 5021–5026.

[40] Navarro, J. J.; Calleja, F.; Miranda, R.; Pérez, E. M.; Parga, A. L. V. de. *Chem. Commun*. **2017**, *53* (75), 10418–10421.

[41] Navarro, J. J.; Leret, S.; Calleja, F.; Stradi, D.; Black, A.; Bernardo-Gavito, R.; Garnica, M.; Granados, D.; Vázquez de Parga, A. L.; Pérez, E. M.; Miranda, R. *Nano Lett.* **2016**, *16* (1), 355–361.

[42] Molina-Mendoza, A. J.; Giovanelli, E.; Paz, W. S.; Niño, M. A.; Island, J. O.; Evangeli, C.; Aballe, L.; Foerster, M.; van der Zant, H. S. J.; Rubio-Bollinger, G.; Agraït, N.; Palacios, J. J.; Pérez, E. M.; Castellanos-Gomez, A. *Nat. Commun.* **2017**, *8* (1), 14409.

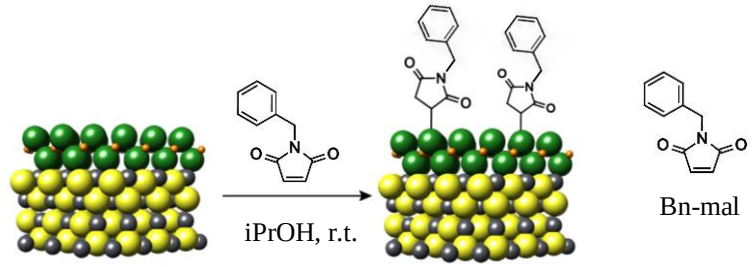

Figure 14. Chemical structure of Fk from its X-ray crystal structure,[43] and idealized reaction scheme with maleimides. Based on HR-TEM data we show SnS_2 as the reactive layer. The S atoms in the SnS_2-like layers are green, S atoms in the PbS-like layer are yellow, Sn atoms are orange and Pb atoms are gray. The structure of the maleimide reagent is also shown.

Conclusive evidence about the functionalization and its mechanism is obtained when the powder sample is analysed using high-resolution magic angle spinning (HR-MAS) NMR. Using deuterated water as the reference, the control Fk sample (orange in Figure 15) shows only weak signals in the alkane region, probably due to adsorbed hydrocarbons and residual iPrOH, and a broad and very weak signal centered around 7 ppm (most likely physisorbed iPrOH). In contrast, the benzylsuccinimide signals are clearly observed in the functionalized Bn-succ-Fk (blue in Figure 15), which can be unambiguously assigned to covalent functionalization of Fk through Michael addition by comparison with a Fk and N-benzylmaleimide mixture (green in Figure 15): the total depletion of the alkene signals at around 6.8 ppm (green triangle, ca. 6.8 ppm) is accompanied by the appearance of three new signals (marked with a square at ca. 3.4 ppm, an hexagon at ca. 2.3 ppm, and a star at ca. 1.9 ppm, in Figure 15) in the alkane region. The new signals correspond to the new aliphatic diastereotopic protons of the newly formed succinimide. Comparison with the experimental ^{1}H solution NMR spectrum of the product of the reaction between 1-propanethiol and N-benzylmaleimide ($CDCl_3$, 400 MHz, r.t., gray in Figure 15), where the signals can be unambiguously assigned, further confirms this observation: a consistent upfield shift is observed for all the succinimide signals due to the presence of Fk, while the aromatic protons, initially oriented away from Fk, are hardly affected. Unfortunately, the benzylic $–CH_2$ cannot be reliably identified in the different Fk samples, as spectra were acquired with water suppression.

[43] Makovicky, E.; Petříček, V.; Dušek, M.; Topa, D. *Am. Mineral.* **2011**, *96* (11–12), 1686–1702.

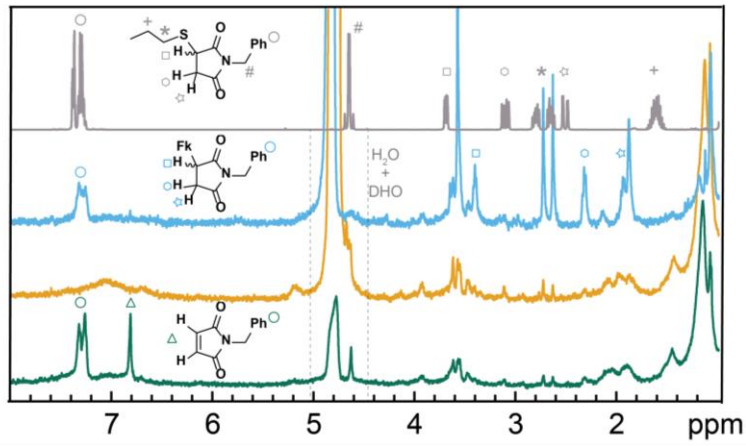

Figure 15. HR-MAS-^{1}H-NMR (500 MHz) spectra of Bn-succ-Fk (pale blue), control Fk (orange) and a mixture of Fk and Bn-maleimide (dark green) obtained using D_2O as the reference. The solution ^{1}H NMR ($CDCl_3$, 400 MHz, r.t.) of the product of the reaction between 1-propanethiol and N-benzylmaleimide is also shown for comparison (gray).

With the reaction effectiveness and mechanism clearly established, we went on to investigate if/how the Fk structure was affected by the covalent modification. High resolution transmission electron microscopy HR-TEM (200 kV) shows no major changes in the van der Waals heterostructure during functionalization. Figure 16a and b show the comparison of characteristic micrographs for Fk and Bn-succ-Fk along the [100] direction (see inset).[43] In both micrographs, the same Moire´ pattern is observed, which originates from the superposition of the H (SnS_2) and Q (PbS) layers (see S3 in SI for additional measurements). Figure 16c and d, correspond to an edge-on perspective (image plane perpendicular to the basal plane of Fk) of both samples. The measured periodicities, as better observed in the enhanced details (Figure 16e and f), are in agreement with the stacking of the H and Q layers of the Fk lattice. A closer look at the final layer (Figure 16e and f) suggests that the H layer, i.e., SnS_2, as proved by Velicky et al.[44] is the one exposed to ambient and is therefore most probably the one that reacts preferentially. This is consistent with the chemical intuition based on the lower electronegativity of Sn compared to Pb, and the smaller radius and higher charge of Sn(IV) compared to Pb(II): the combination of these properties should render SnS_2 more purely ionic compared to PbS[45] and, as a consequence, the sulphur atoms directly attached to Sn more anionic and more nucleophilic.

[43] Makovicky, E.; Petříček, V.; Dušek, M.; Topa, D. *Am. Mineral.* **2011**, *96* (11–12), 1686–1702.
[44] Velický, M.; Toth, P. S.; Rakowski, A. M.; Rooney, A. P.; Kozikov, A.; Woods, C. R.; Mishchenko, A.; Fumagalli, L.; Yin, J.; Zólyomi, V.; Georgiou, T.; Haigh, S. J.; Novoselov, K. S.; Dryfe, R. A. W. *Nat. Commun.* **2017**, *8* (1), 14410.
[45] Pauling, L. *J. Am. Chem. Soc.* **1932**, *54* (3), 988–1003.

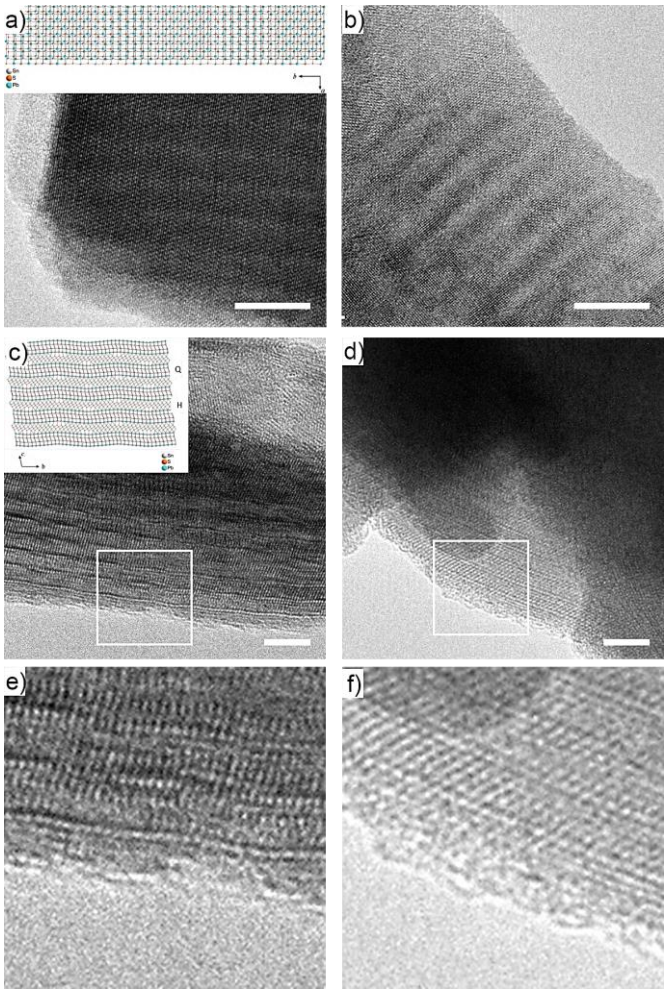

Figure 16. HR-TEM micrographs obtained for pristine Fk (a, c and e) and Bn-succ-Fk (b, d and f). The insets show the orientations that originate the Moiré pattern in a an b, and the edge-on perspective of c and d.[43] Scale bars are 10 nm for a and b and 5 nm for c and d. e) and f) show a zoom in on the edge areas highlighted with white squares in c) and d), respectively.

5.4.3. Conclusions.

We describe how the naturally occurring van der Waals heterostructure, Franckeite, can be functionalized covalently making use of the inherent soft electrophilicity of maleimides. The good quality of the ^{1}H HR-MAS NMR signals allows us to confirm the proposed thiol–maleimide ‘‘click’’ functionalization mechanism beyond reasonable doubt and serves as an encouraging example for the use of NMR techniques for the characterization of 2D materials. HR-TEM confirm that the functionalization is sufficiently mild to respect the native van der Waals heterostructure, occurring preferentially at the SnS_2 layer.

5.4.4. Supporting information.

S1. Equipment.

^{1}H-HR-MAS-NMR - ^{1}H high-resolution magic angle spinning (HRMAS) NMR spectroscopy (^{1}H-HR-MAS-NMR) experiments were performed on a vertical magnet Bruker AV500 operating at 500 MHz. The samples were introduced as solids in ZrO_2 rotors with 12 μL internal volume and a drop of D_2O was added. Standard solvent suppressed spectra (NOESYPRESAT) were acquired into 32 k data points, averaged over 512 acquisitions. The total acquisition time was ~26 min, with a spectral width of 8012 Hz. All spectra were processed using TOPSPIN software.

JEOL JEM 2100 - TEM microscope operating at 200 kV accelerating voltage and equipped with a LaB_6 thermionic electron gun. It is a built-in STEM unit with a bright field detector, and it is coupled to an ORIUS SC1000 CCD camera (model 832). The resolution between dots is 2.5 Å. It also has an XEDS microanalysis system (OXFORD INCA).

Note: Microstructural characterisation by transmission electron microscopy was carried out at the national centre for electron microscopy (ICTS-CNME) of the UCM.

S2. Procedure for Franckeite functionalization.

Franckeite was exfoliated by liquid phase exfoliation following the procedure previously described.[42]

10 mL of the obtained exfoliated Franckeite (the approximated concentration is 0.5 $mg \cdot mL^{-1}$ of Fk in iPrOH) are mixed with 100 mg of N-benzyl maleimide) previously dissolved in 10 mL $CHCl_3$. The mixture is sonicated for 5 min and stirred overnight at room temperature. For the cleaning procedure, the suspension was filtered through a polytetrafluoroethylene membrane with a pore size of 0.2 μm, and the solid was washed with $CHCl_3$ several times (around 15 times in this case) to remove excess reagents and physisorbed maleimide.

[42] Molina-Mendoza, A. J.; Giovanelli, E.; Paz, W. S.; Niño, M. A.; Island, J. O.; Evangeli, C.; Aballe, L.; Foerster, M.; van der Zant, H. S. J.; Rubio-Bollinger, G.; Agraït, N.; Palacios, J. J.; Pérez, E. M.; Castellanos-Gomez, A. *Nat. Commun.* **2017**, *8* (1), 14409.

S3. Additional HR-TEM images.

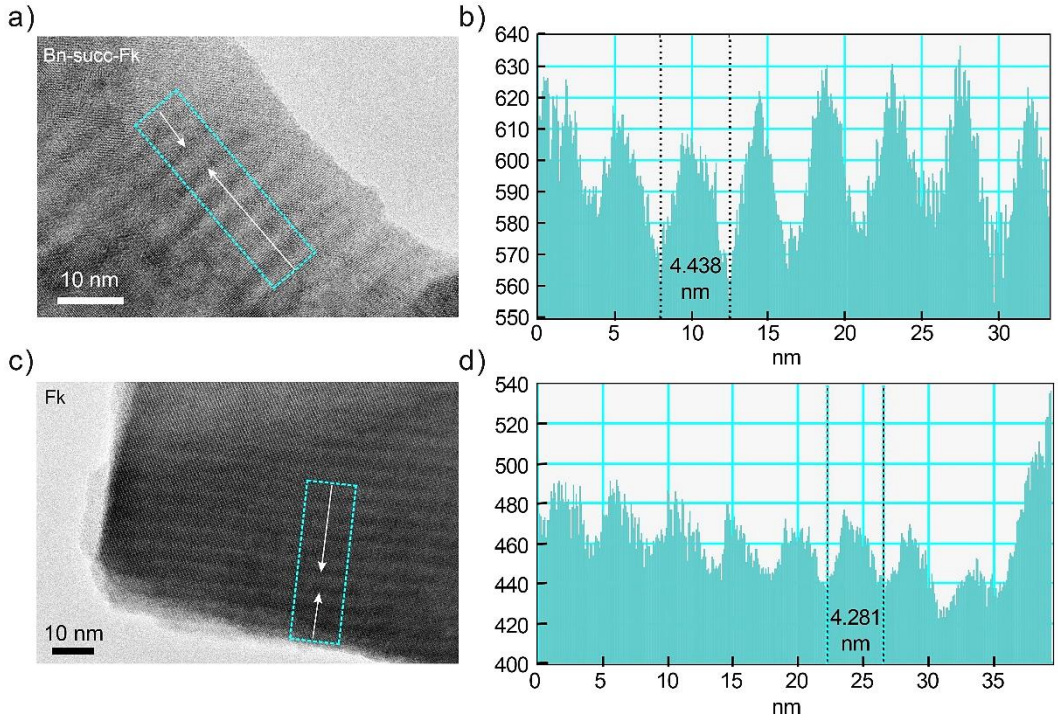

Figure S1. [100] HRTEM structure images of (a) Bn-succ-Fk and (c) Fk. b) Intensity profile along the blue square selected in (a), the periodicity corresponds to the one expected for the plane [100] and same happens for Fk (d).

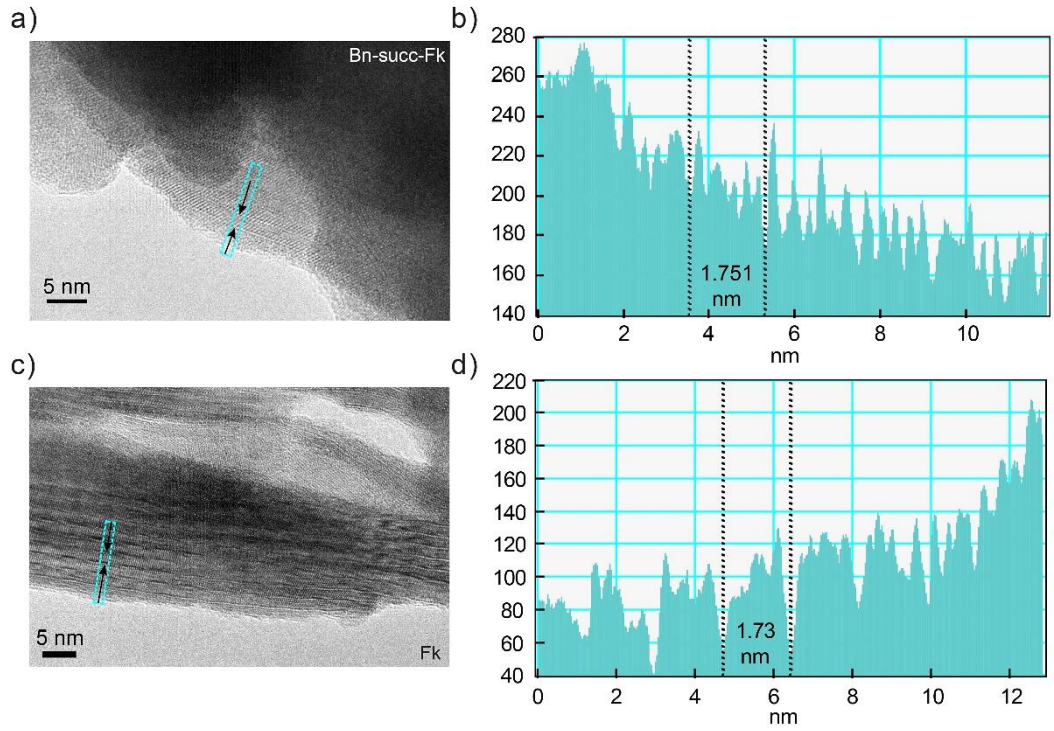

Figure S2. [001] HRTEM structure images of (a) Bn-succ-Fk and (c) Fk. b) Intensity profile along the blue square selected in (a), the periodic shade variations can be explained by the [001] projection. The same periodicity is observed for Fk (d).

5.5. BIBLIOGRAPHY

(1) Kubitscheck, U. Principles of Light Microscopy. In *Fluorescence Microscopy*; John Wiley & Sons, Ltd, **2017**; 23–83.

(2) Goodhew, P. J.; Humphreys, J.; Beanland, R. *Electron Microscopy and Analysis, Third Edition*; CRC Press, **2000**.

(3) Erdman, N.; Bell, D. C.; Reichelt, R. Scanning Electron Microscopy. In *Springer Handbook of Microscopy*; Hawkes, P. W., Spence, J. C. H., Eds.; Springer Handbooks; Springer International Publishing: Cham, **2019**; 229–318.

(4) Knoll, M.; Ruska, E. Beitrag Zur Geometrischen Elektronenoptik. I. *Ann. Phys.* **1932**, *404* (5), 607–640.

(5) Knoll, M.; Ruska, E. Beitrag Zur Geometrischen Elektronenoptik. II. *Ann. Phys.* **1932**, *404* (6), 641–661.

(6) Knoll, M.; Ruska, E. Das Elektronenmikroskop. *Z. Physik* **1932**, *78* (5–6), 318–339.

(7) Von Ardenne, M. Das Elektronen-Rastermikroskop: Theoretische Grundlagen. *Z. Physik* **1938**, *109* (9–10), 553–572.

(8) Nellist, P. D. Scanning Transmission Electron Microscopy. In *Springer Handbook of Microscopy*; Hawkes, P. W., Spence, J. C. H., Eds.; Springer Handbooks; Springer International Publishing: Cham, **2019**, 49–99.

(9) Kirkland, A. I.; Chang, S. L.-Y.; Hutchison, J. L. Atomic Resolution Transmission Electron Microscopy. In *Springer Handbook of Microscopy*; Hawkes, P. W., Spence, J. C. H., Eds.; Springer Handbooks; Springer International Publishing: Cham, **2019**; 3–47.

(10) Wagner, G. *High-Resolution Transmission Electron Microscopy and Associated Techniques*; Buseck, P. R., Cowley, J. M., Eyring, L., Eds.; Oxford University Press: Oxford, New York, **1989**.

(11) Brooks, S. *Aberration-Corrected Analytical Transmission Electron Microscopy*, 1st ed.; Brydson, R., Ed.; Wiley, **2011**.

(12) Scherzer, O. The Theoretical Resolution Limit of the Electron Microscope. *J. Appl. Phys.* **1949**, *20* (1), 20–29.

(13) Coene, W. M. J.; Thust, A.; Op de Beeck, M.; Van Dyck, D. Maximum-Likelihood Method for Focus-Variation Image Reconstruction in High Resolution Transmission Electron Microscopy. *Ultramicroscopy* **1996**, *64* (1), 109–135.

(14) Kirkland, A. I.; Meyer, R. R. "Indirect" High-Resolution Transmission Electron Microscopy: Aberration Measurement and Wavefunction Reconstruction. *Microsc. Microanal.* **2004**, *10* (4), 401–413.

(15) Rodenburg, J. M.; Bates, R. H. T. The Theory of Super-Resolution Electron Microscopy via Wigner-Distribution Deconvolution. *Philos. trans., A Math. phys. eng. sci.* **1997**, *339* (1655), 521–553.

(16) Scherzer, O. Über einige Fehler von Elektronenlinsen. *Z. Physik* **1936**, *101* (9), 593–603.

(17) Scherzer, O. Spharische Und Chromatische Korrektur von Elektronen-Linsen. *Optik* **1947**.

(18) Rose, H. CHAPTER 1 - History of Direct Aberration Correction. In *Advances in Imaging and Electron Physics*; Hawkes, P. W., Ed.; Aberration-Corrected Electron Microscopy; Elsevier, **2008**, 153, 3–39.

(19) Hawkes, P. W. Aberration Correction Past and Present. *Philos. trans., A Math. phys. eng. sci.* **2009**, *367* (1903), 3637–3664.

(20) Haider, M.; Uhlemann, S.; Schwan, E.; Rose, H.; Kabius, B.; Urban, K. Electron Microscopy Image Enhanced. *Nature* **1998**, *392* (6678), 768–769.

(21) Haider, M.; Rose, H.; Uhlemann, S.; Schwan, E.; Kabius, B.; Urban, K. A Spherical-Aberration-Corrected 200kV Transmission Electron Microscope. *Ultramicroscopy* **1998**, *75* (1), 53–60.

(22) Krivanek, O. L.; Dellby, N.; Spence, A. J.; Camps, R. A.; Brown, L. M. On-Line Aberration Measurement and Correction in STEM. *Microsc. Microanal.* **1997**, *3* (S2), 1171–1172.

(23)Krivanek, O. L.; Dellby, N.; Lupini, A. R. Towards Sub-Å Electron Beams. *Ultramicroscopy* **1999**, *78* (1), 1–11.

(24)Born, M.; Wolf, E. *Principles of Optics: Electromagnetic Theory of Propagation, Interference and Diffraction of Light*; Elsevier, **2013**.

(25)Ishikawa, R.; Morishita, S.; Tanigaki, T.; Shibata, N.; Ikuhara, Y. Spatial and Phase Resolution in Electron Microscopy. *Microsc.* **2023**, *72* (2), 78–96.

(26)Zhang, W.; Guillén-Soler, M.; Silva, S. M.-D.; López-Moreno, A.; González, L. R.; Giménez-López, M. del C.; Pérez, E. M. Mechanical Interlocking of SWNTs with N-Rich Macrocycles for Efficient ORR Electrocatalysis. *Chem. Sci.* **2022**, *13* (33), 9706–9712.

(27)Sun, Y.-P.; Fu, K.; Lin, Y.; Huang, W. Functionalized Carbon Nanotubes: Properties and Applications. *Acc. Chem. Res.* **2002**, *35* (12), 1096–1104.

(28)Mallakpour, S.; Soltanian, S. Surface Functionalization of Carbon Nanotubes: Fabrication and Applications. *RSC Adv.* **2016**, *6* (111), 109916–109935.

(29)Georgakilas, V.; Kordatos, K.; Prato, M.; Guldi, D. M.; Holzinger, M.; Hirsch, A. Organic Functionalization of Carbon Nanotubes. *J. Am. Chem. Soc.* **2002**, *124* (5), 760–761.

(30)Tasis, D.; Tagmatarchis, N.; Bianco, A.; Prato, M. Chemistry of Carbon Nanotubes. *Chem. Rev.* **2006**, *106* (3), 1105–1136.

(31)Hu, C.; Dai, L. Doping of Carbon Materials for Metal-Free Electrocatalysis. *Adv. Mater.* **2019**, *31* (7), 1804672.

(32)Li, J.-C.; Hou, P.-X.; Liu, C. Heteroatom-Doped Carbon Nanotube and Graphene-Based Electrocatalysts for Oxygen Reduction Reaction. *Small* **2017**, *13* (45), 1702002.

(33)Paraknowitsch, J. P.; Thomas, A. Doping Carbons beyond Nitrogen: An Overview of Advanced Heteroatom Doped Carbons with Boron, Sulphur and Phosphorus for Energy Applications. *Energy Environ. Sci.* **2013**, *6* (10), 2839–2855.

(34)Czerw, R.; Terrones, M.; Charlier, J.-C.; Blase, X.; Foley, B.; Kamalakaran, R.; Grobert, N.; Terrones, H.; Tekleab, D.; Ajayan, P. M.; Blau, W.; Rühle, M.; Carroll, D. L. Identification of Electron Donor States in N-Doped Carbon Nanotubes. *Nano Lett.* **2001**, *1* (9), 457–460.

(35)Xia, Y.; Mokaya, R. Synthesis of Ordered Mesoporous Carbon and Nitrogen-Doped Carbon Materials with Graphitic Pore Walls via a Simple Chemical Vapor Deposition Method. *Adv. Mater.* **2004**, *16* (17), 1553–1558.

(36)Panchakarla, L. S.; Govindaraj, A.; Rao, C. N. R. Boron- and Nitrogen-Doped Carbon Nanotubes and Graphene. *Inorganica Chim. Acta* **2010**, *363* (15), 4163–4174.

(37)Steinmetz, M.; Lima, D.; Machado, R. R. L.; Sundararaj, U.; Arjmand, M.; da Silva, A. B.; Santos, J. P.; Pessôa, C. A.; Wohnrath, K. Nitrogen-Doped Carbon Nanotubes towards Electrochemical Sensing: Effect of Synthesis Temperature. *Diam. Relat. Mater.* **2020**, *110*, 108093.

(38)Villalva, J.; Silva, S. M.-D.; Villa, P.; Ruiz-González, L.; Navío, C.; Garcia-Orrit, S.; Vega-Mayoral, V.; Cabanillas-González, J.; Castellanos-Gomez, A.; Giovanelli, E.;

Pérez, E. M. Covalent Modification of Franckeite with Maleimides: Connecting Molecules and van Der Waals Heterostructures. *Nanoscale Horiz.* **2021**, *6* (7), 551–558.

(39) Coronado, E.; Martí-Gastaldo, C.; Navarro-Moratalla, E.; Burzurí, E.; Camón, A.; Luis, F. Hybrid Magnetic/Superconducting Materials Obtained by Insertion of a Single-Molecule Magnet into TaS_2 Layers. *Adv. Mater.* **2011**, *23* (43), 5021–5026..

(40) Navarro, J. J.; Calleja, F.; Miranda, R.; Pérez, E. M.; Parga, A. L. V. de. High Yielding and Extremely Site-Selective Covalent Functionalization of Graphene. *Chem. Commun.* **2017**, *53* (75), 10418–10421.

(41) Navarro, J. J.; Leret, S.; Calleja, F.; Stradi, D.; Black, A.; Bernardo-Gavito, R.; Garnica, M.; Granados, D.; Vázquez de Parga, A. L.; Pérez, E. M.; Miranda, R. Organic Covalent Patterning of Nanostructured Graphene with Selectivity at the Atomic Level. *Nano Lett.* **2016**, *16* (1), 355–361.

(42) Molina-Mendoza, A. J.; Giovanelli, E.; Paz, W. S.; Niño, M. A.; Island, J. O.; Evangeli, C.; Aballe, L.; Foerster, M.; van der Zant, H. S. J.; Rubio-Bollinger, G.; Agraït, N.; Palacios, J. J.; Pérez, E. M.; Castellanos-Gomez, A. Franckeite as a Naturally Occurring van Der Waals Heterostructure. *Nat. Commun.* **2017**, *8* (1), 14409.

(43) Makovicky, E.; Petříček, V.; Dušek, M.; Topa, D. The Crystal Structure of Franckeite, Pb21.7Sn9.3Fe4.0Sb8.1S56.9. *Am. Mineral.* **2011**, *96* (11–12), 1686–1702.

(44) Velický, M.; Toth, P. S.; Rakowski, A. M.; Rooney, A. P.; Kozikov, A.; Woods, C. R.; Mishchenko, A.; Fumagalli, L.; Yin, J.; Zólyomi, V.; Georgiou, T.; Haigh, S. J.; Novoselov, K. S.; Dryfe, R. A. W. Exfoliation of Natural van Der Waals Heterostructures to a Single Unit Cell Thickness. *Nat. Commun.* **2017**, *8* (1), 14410.

(45) Pauling, L. The Nature of the Chemical Bond. III. The Transition from One Extreme Bond Type to Another. *J. Am. Chem. Soc.* **1932**, *54* (3), 988–1003.

GENERAL CONCLUSIONS

This thesis has been framed in the functionalization of nanomaterials. The starting point was the study of the thermodynamics that govern the non-covalent functionalization of carbon nanotubes with different organic molecules. The thermodynamic energies were calculated thanks to the prior knowledge of the values of the association constants. They were obtained with the measurement of the concentration of the free guest after subjecting the sample to thermogravimetric analysis. The results showed that the supramolecular functionalization of SWNTs is a spontaneous reaction favoured when rich conjugated compounds are used. The solvophobic behaviour of the nanotubes, joined to an increase of the π-π interactions, resulted in a tight binding between the species that increase the entropy of the system. The dynamics of these hybrids were also studied corroborating that the flexibility and aromaticity of the guest drives the association.

Parallel lines of work have been the synthesis of MINTs. On one side, Co^{2+} and Cu^{2+} porphyrin dimers were used to embrace SWNTs forming magnetic mechanically interlocked derivatives. With several characterization techniques, we proved that the porphyrins suffer just slight distortions preserving their coordination sphere and their structure after the cycling. Besides, these hybrids were incorporated into nanoscale devices by electrophoresis allowing their future use in spintronics and molecular spin qubits. Applications that are possible thanks to the possibility of changing the metal center and therefore, the interaction with the SWNT. On the other side, palladium-based metallosquare was used to encapsulate SWNTs. We found that the hybrid formation by both templated clipping and direct threading was sensitive to structural variations in the metallo-assemblies. This was demonstrated when a nickel-based metallosquare was used to perform the synthesis showing very low functionalization of the carbon nanotubes. Furthermore, we also shown charge-transfer process from the metallo-square to the nanotubes upon photoexcitation which could be considered for future applications.

To conclude this thesis, the last chapter has been dedicated to the electron microscopy. We started by describing the basic concepts of transmission electron microscopy, followed by two examples of nanomaterials´ functionalization. Firstly, TEM was used to confirm the synthesis of a MINT using N-rich macrocycles, verifying that the insertion of nitrogen atoms does not affect the integrity of the nanotube. Secondly, this technique was employed to verify that the covalent functionalization of a natural 2D material, franckeite, did not show any major changes in the van der Waals heterostructure upon functionalization.

CONCLUSIONES GENERALES

Esta tesis se ha centrado en la funcionalización de nanomateriales. Se ha estudiado la termodinámica que controla la modificación no covalente de nanotubos de carbono con diferentes moléculas orgánicas. Para ello, primero se han obtenido los valores de las constantes de asociación teniendo en cuenta la concentración de huésped libre tras someter las diferentes muestras a un análisis termogravimétrico. Con estos datos se han calculado los valores de las energías termodinámicas demostrando que la funcionalización supramolecular de los SWNTs es una reacción espontánea favorecida cuando se utilizan compuestos conjugados ricos en electrones. Además, el comportamiento solvofóbico de los nanotubos, unido a un aumento de las interacciones π-π, dio lugar a una unión estrecha entre las especies aumentando la entropía del sistema. Finalmente se estudió la dinámica de estos híbridos corroborando que la flexibilidad y aromaticidad del huésped impulsa la asociación.

En líneas paralelas se ha trabajado en la síntesis de MINTs. Por un lado, se utilizaron dímeros de porfirinas de Co^{2+} y Cu^{2+} para encapsular SWNTs formando derivados magnéticos mecánicamente entrelazados. Mediante diversas técnicas de caracterización, se comprobó que las porfirinas sólo sufren ligeras distorsiones conservando su esfera de coordinación y su estructura tras el ciclado. Además, estos híbridos se incorporaron a dispositivos en nano escala mediante electroforesis permitiendo su futuro uso en espintrónica y como qubits moleculares. Aplicaciones que son posibles gracias a la posibilidad de cambiar el centro metálico y, por tanto, la interacción con el SWNT. Por otro lado, se utilizó un macrociclo organometálico basado en paladio para encapsular SWNTs. Comprobamos que la formación de híbridos, tanto por síntesis directa templada por el nanotubo como por la formación del macrociclo antes de la funcionalización, está influenciada por las variaciones estructurales de los metalo ensamblajes. Esto se demostró cuando se utilizó un complejo organometálico basado en níquel para realizar la síntesis, mostrando una funcionalización muy baja de los nanotubos de carbono. Además, también demostramos el proceso de transferencia de carga desde el macrociclo a los nanotubos tras fotoexcitación, lo que podría tenerse en cuenta para futuras aplicaciones.

Para concluir esta tesis el último capítulo se ha dedicado a la microscopía electrónica. Comenzamos describiendo los conceptos básicos de la microscopía electrónica de transmisión, seguidos de dos ejemplos de funcionalización de nanomateriales. En primer lugar, se utilizó TEM para confirmar la síntesis de un

MINT utilizando macrociclos ricos en N, verificando que la inserción de átomos de nitrógeno no afecta a la integridad del nanotubo. En segundo lugar se empleó esta técnica para verificar que la funcionalización covalente de un material 2D natural, la Franckeita, no mostraba cambios importantes en la heteroestructura de van der Waals tras la funcionalización.

ANNEX I – List of publications

1. Naranjo, T.; Álvarez-Asencio, R.; Pedraz, P.; Nieto-Ortega, B.; **Moreno-Da Silva, S.**; Burzurí, E.; Rutland, M. W.; Pérez, E. M. Hydrogen-Bonded Host–Guest Systems Are Stable in Ionic Liquids. *Sci. Rep.* **2020**, *10* (1), 15414.

2. Villalva, J.; **Moreno-Da Silva, S.**; Villa, P.; Ruiz-González, L.; Navío, C.; Garcia-Orrit, S.; Vega-Mayoral, V.; Cabanillas-González, J.; Castellanos-Gomez, A.; Giovanelli, E.; Pérez, E. M. Covalent Modification of Franckeite with Maleimides: Connecting Molecules and van Der Waals Heterostructures. *Nanoscale Horiz.* **2021**, *6* (7), 551–558.

3. Xu, W.; D. Eaton, M.; **Moreno-Da Silva, S.**; M. Pérez, E. Functionalized Epoxy with Adjustable Fluorescence and UV-Shielding Enabled by Reactive Addition of 9-Anthracenemethoxyl Glycidyl Ether. *RSC Adv.* **2021**, *11* (58), 36719–36725.

4. **Moreno-Da Silva, S.**; Martínez, J. I.; Develioglu, A.; Nieto-Ortega, B.; de Juan-Fernández, L.; Ruiz-Gonzalez, L.; Picón, A.; Oberli, S.; Alonso, P. J.; Moonshiram, D.; Pérez, E. M.; Burzurí, E. Magnetic, Mechanically Interlocked Porphyrin–Carbon Nanotubes for Quantum Computation and Spintronics. *J. Am. Chem. Soc.* **2021**, *143* (50), 21286–21293.

5. López-Moreno, A.; Ibáñez, S.; **Moreno-Da Silva, S.**; Ruiz-González, L.; Sabanés, N. M.; Peris, E.; Pérez, E. M. Single-Walled Carbon Nanotubes Encapsulated within Metallacycles. *Angew. Chem. Int. Ed* **2022**, *61* (35), e202208189.

6. Zhang, W.; Guillén-Soler, M.; **Moreno-Da Silva, S.**; López-Moreno, A.; González, L. R.; Giménez-López, M. del C.; Pérez, E. M. Mechanical Interlocking of SWNTs with N-Rich Macrocycles for Efficient ORR Electrocatalysis. *Chem. Sci.* **2022**, *13* (33), 9706–9712.

7. Quirós-Ovies, R.; Laborda, M.; Sabanés, N. M.; Martín-Pérez, L.; **Moreno-Da Silva, S.**; Burzurí, E.; Sebastian, V.; Pérez, E. M.; Santamaría, J. Microwave-Driven Exfoliation of Bulk 2H-MoS2 after Acetonitrile Prewetting Produces Large-Area Ultrathin Flakes with Exceptionally High Yield. *ACS Nano* **2023**, *17* (6), 5984–5993.

8. Viela, F.; Ortega, I. V.; Hernández, J. J.; Rodríguez, I.; **Moreno-Da Silva, S.**; López-Moreno, A.; Pérez, E. M.; Flors, C. Real-Time Imaging of the Mechanobactericidal Action of Colloidal Nanomaterials and Nanostructured Topographies. *Small Sci.* **2023**, *3* (5), 2300002.

9. Martín, N.; Eaton, M.; **Moreno-Da Silva, S.**; Naranjo, A.; Perez, E. Automated Statistical Analysis of Raman Spectra of Nanomaterials. ChemRxiv, **2023**.